

**SYNTHESIS AND AGEING TRANSFORMATIONS
OF MANUFACTURED METAL OXIDE
NANOMATERIALS**

by

SOPHIE MARIE BRIFFA

A thesis submitted to the University of Birmingham

for the degree of DOCTOR OF PHILOSOPHY

School of Geography, Earth and Environmental Science

College of Life and Environmental Sciences

University of Birmingham

December 2016

UNIVERSITY OF
BIRMINGHAM

University of Birmingham Research Archive

e-theses repository

This unpublished thesis/dissertation is copyright of the author and/or third parties. The intellectual property rights of the author or third parties in respect of this work are as defined by The Copyright Designs and Patents Act 1988 or as modified by any successor legislation.

Any use made of information contained in this thesis/dissertation must be in accordance with that legislation and must be properly acknowledged. Further distribution or reproduction in any format is prohibited without the permission of the copyright holder.

Abstract

With the increased use of manufactured nanomaterials (MNMs) and increased environmental and human exposure, “nanosafety”, the assessment of hazards from MNMs, has become a major research objective. Despite this, the field has yet to advance sufficiently due to challenges in characterisation and in linking systematically physicochemical properties to toxicity. In order to understand what makes a nanomaterial harmful, toxicity studies need to be carried out. Yet these need to be performed on a range of well-characterised comparable MNMs with systematically varied properties. Furthermore, most nanoparticles undergo transformations and react in ways that change their behaviour and properties over time resulting in aged nanoparticles. These no longer have the same characteristics of their pristine counterparts, which in turn could influence their toxicity. Therefore thorough understanding of the behaviour and ageing processes that the MNMs can undergo is also necessary.

The aim of this work was to develop and fully characterise a library of comparable nanoparticles with a range of core chemistries, but the same capping. Following this behavioural and ageing studies of the MNMs in the different scenarios were carried out.

A library of metal oxide NMs based on a polyvinylpyrrolidone (PVP) capped ceria synthesis was developed and extensively characterised. The protocol was successfully modified to produce PVP capped zinc oxide and copper oxide of comparable sizes (c. 5, 7 and 20 nm). Characterisation was carried out by Dynamic Light Scattering (DLS), Zeta Potential, Ultra-Violet-Visible Light Spectroscopy (UV-VIS), Transmission Electron Microscopy (TEM), Scanning Transmission Electron Microscopy Electron Energy Loss Spectroscopy (STEM-EELS), Fourier Transform Infra-red (FT-IR), X-ray Photoelectron

Spectroscopy (XPS), X-ray Absorption Spectroscopy (XAS) and Inductively Coupled Plasma – Optical Emission Spectroscopy (ICP-OES) so as to confirm the success of the synthesis and gain valuable information on NM characteristics. Results suggest that the tested protocol was successful in creating stable PVP capped metal oxide NMs of reproducible sizes and that a common mechanism hypothesis holds true. The metal oxide core had mixed valency oxides when the metal was stable in multiple valency states. Additionally, PVP was found to play a significant role in the synthesis of the MNMs influencing both their physical and chemical properties.

The library nanoparticles along with commercially available uncoated ceria NMs were subjected to time and temperature dependent aqueous exposure studies in order to investigate their thermal transformations; in these experiments, temperature was used as a proxy for accelerated ageing over short periods of time. The work studied the physical and chemical changes occurring on exposure to various temperatures (25, 45, 65 and 80 °C) for a period of 4 weeks. Size, zeta potential, agglomeration/aggregation and valency state of the particles were studied through DLS, zeta potential, UV-VIS, TEM and XPS, as a function of time. The influence of temperature resulted in increased aggregation, changes in metal valency state and a decrease in stability with increasing temperature and time most likely due to deterioration in the efficiency of the capping. Differences were noted both based on core composition and on whether the samples were capped or not.

Finally the potential environmental transformation of ceria in the presence of phosphate was studied for the 10 K PVP capped ceria library NMs, as well as a commercially available uncapped ceria NM and a series of zirconium doped ceria NMs. Samples were transformed by being subjected to pH adjusted phosphatisation solutions made up of potassium phosphate, citric acid and ascorbic acid. Samples were analysed at

various time points by means of DLS – size and zeta potential, UV-VIS, TEM, FT-IR, Energy Dispersive X-ray Spectroscopy (EDX) and X-ray Diffraction Spectroscopy (XRD) so as to study the transformations occurring. Ceria and ceria-rich samples underwent transformation to larger particles growing into characteristic “sea urchin”/needle-like structures. Furthermore these samples underwent compositional transformation to phosphate-bearing phases, with the exception of the zirconia end member, which did not undergo phosphatisation. The transformations were dependent on time, ceria concentration and phosphate to ceria ratios, as well as the amount of zirconium within the doped samples; the latter did not inhibit these transformations, but neither did it transform to phosphate. Furthermore the commercially available ceria samples were exposed to a pH adjusted phosphatisation solution composed of a naturally occurring phospholipid. This underwent minimal physical and chemical changes, under these conditions. No characteristic phosphate ageing transformations were observed possibly due to too short an exposure time and/or the phospholipid molecule structure being unsuitable to induce this transformation.

To
My beloved mum and dad,
Hillary,
& Mario.

Acknowledgements

First and foremost I would like to thank my supervisor Professor Eugenia Valsami-Jones for all her help, guidance and support throughout the last three years. Her positive attitude has always helped to keep me going. Furthermore, I would also like to thank my co-supervisor Iseult Lynch.

I would like to acknowledge the financial support from FP7 funded projects: QualityNano (Grant Agreement no 262163, via a Transnational Access) for funding my visit to Karlsruhe Institute of Technology (KIT) in Germany for characterisation. I also received part-funding from NanoMILE (Grant Agreement no 310451) as well as the Malta Endeavour Scholarships Scheme (Group B).

In addition I would like to thank the following: all the doctoral researchers and staff of the Environmental Science Group at the University of Birmingham as well as the doctoral researchers based in room 325 in the Geography who have all been very obliging and supportive throughout the years; Christine Elgy, Isabella Römer and Anastasios Papadiamantis for their help in the lab; Richard Palmer, Dimitri Hapiuk and Jian Liu from the Nanoscale Physics Research Laboratory at the University of Birmingham for all their assistance in acquiring STEM data and its analysis; Paul Stanley and Theresa Morris from the Centre for Electron Microscopy at the University of Birmingham for their assistance with the TEM; Dennis Formosa, for his microscopy knowledge and support; Dr Zongbo Shi who so kindly allowed me to join him at Diamond Light Source and shared his beamtime; Diamond Light Source for access to beamline I18 (proposal no. SP12760) that contributed to the XAS results; Dr Konstantin Ignatyev for his assistance running the XAS analysis and his help and knowledge analysing data; Michael Bruns, Vanessa Trouillet and

the Surface and Interface Analysis group at KIT for their welcome during my stay and Vanessa for her knowledge and help with XPS analysis during and following my visit; the NEXUS team and Naoko Sano at the University of Newcastle for their efficient helpfulness with XPS analysis.

Last but certainly not least I would like to thank my family, especially my mother and my father for their continuous encouragement and support, both financially and emotionally, without which this work would have never been possible. I am also grateful to my sister, Hillary, whose energy and drive in her own field as well as her belief in me are truly an inspiration. Finally, Mario De Giovanni's assistance, encouragement, constant backing and advice throughout this project have been a great asset to me personally and to this work and are sincerely appreciated.

Table of Contents

Abstract.....	ii
Acknowledgements	vi
Table of Contents	viii
List of Figures.....	xix
List of Tables.....	xxxiv
List of Abbreviations	xxxvi
Chapter 1: Introduction.....	1
1.1 Scientific Rationale.....	1
1.2 Aims and Objectives of Research.....	3
1.2.1 Aim 1	4
1.2.2 Aim 2	5
1.2.3 Aim 3	5
1.4 Layout of Thesis	6
Chapter 2: Literature Review	8
2.1 Introduction	8
2.2 Nanomaterial Definitions	8
2.3 Nanomaterial classification	10
2.3.1 Structural	11
2.3.1.1 Dimensionality	11
2.3.1.2 Morphology	12
2.3.2 Chemistry	13
2.3.3 Origin.....	15

2.3.3.1 Natural Nano-objects	15
2.3.3.2 Incidental Nano-objects	15
2.3.3.3 Intentionally produced Nano-objects.....	16
2.3.3.3.1 Engineered or Manufactured nanomaterial synthesis routes	16
2.4 Nanomaterial Applications	18
2.4.1 Nanomaterials in consumer electronics, semiconductors, batteries and magnets	19
2.4.2 Nanomaterials in Food industry	19
2.4.3 Nanomaterials in textiles	20
2.4.4 Nanomaterials in cosmetics	20
2.4.5 Nanomaterials in paints and coatings	21
2.4.6 Nanomaterials used in medicine	21
2.5 Examples of nanomaterials and their properties.....	22
2.5.1 Cerium	22
2.5.2 Cerium Dioxide	23
2.5.2.1 Properties of Ceria	23
2.5.2.2 Fundamental properties of ceria	24
2.5.2.3 Synthesis methods of Ceria	26
2.5.2.4 Ceria Uses.....	26
2.5.3 Zirconium doped Ceria.....	27
2.5.3.1 Synthesis methods of Zirconium doped Ceria.....	28
2.5.3.2 Zirconium doped Ceria Uses	28
2.5.6 Zinc	28
2.5.7 Zinc Oxide	29
2.5.7.1 Properties of Zinc Oxide.....	29

2.5.7.2 Crystal structure.....	30
2.5.7.3 Zinc oxide synthesis	31
2.5.7.4 Zinc oxide uses	32
2.5.8 Copper	33
2.5.8.1 Copper Oxide.....	33
2.5.8.2 Copper Oxide synthesis	34
2.5.8.3 Copper oxide uses.....	34
2.6 Nanotechnology concerns.....	35
2.7 Exposure to nanomaterials	37
2.7.1 Environmental release of nanomaterials.....	37
2.7.2 Human exposure to nanomaterials	38
2.8 Toxicology.....	39
2.8.1 Ceria Toxicity	41
2.8.2 Zinc oxide Toxicity	43
2.8.3 Copper oxide Toxicity	44
2.9 Life cycle analysis	46
2.10 Fate in the environment	46
2.11 Properties influencing nanomaterial behaviour and interactions	47
2.11.1 Nanomaterial Size and Surface Area.....	48
2.11.2 Nanomaterial Shape.....	49
2.11.3 Nanomaterial Surface charge.....	50
2.11.4 Nanoparticle Stability	52
2.11.4.1 Nanomaterial Interactions	52
2.12 Stabilisation of Nanomaterials	55

2.13 Capping Agents	57
2.13.1 Polyvinylpyrrolidone (PVP)	58
2.14 Transformations.....	59
2.14.1 Types of Transformations.....	62
2.14.1.1 Chemical Transformations	63
2.14.1.2 Physical Transformations	67
2.14.1.2.1 Aggregation	68
2.14.1.2.2 Disaggregation.....	69
2.14.1.2.3 Adsorption	69
2.14.1.3 Biological Transformations	70
2.14.1.4 Interactions with Macromolecules.....	71
2.15 Ageing	73
2.15.1 Accelerated Ageing	74
2.15.2 Ageing studies	75
2.16 Understanding nanomaterial risks	78
2.17 Risk Analysis.....	79
2.18 Conclusion.....	80
Chapter 3: Methodology.....	82
3.1 Introduction	82
3.2 Dynamic Light Scattering.....	84
3.2.1 Technique	84
3.2.1.1 Size	84
3.2.1.2 Zeta Potential.....	87
3.2.2 Sample Preparation.....	88

3.2.3 Procedure	89
3.2.3.1 Size Analysis	89
3.2.3.1.1 Data Analysis.....	90
3.2.3.2 Zeta Potential Analysis	90
3.3 Ultra-Violet Visible Spectroscopy (UV-VIS)	91
3.3.1 Technique	91
3.3.2 Sample Preparation.....	94
3.3.3 Procedure	94
3.4 X-ray Photoelectron Spectroscopy (XPS)	94
3.4.1 Technique	94
3.4.2 Sample Preparation.....	97
3.4.3 Procedure	98
3.5 Fourier Transform Infra-Red Spectroscopy (FT-IR).....	99
3.5.1 Technique	99
3.5.2 Sample Preparation.....	100
3.5.3 Procedure	100
3.6 X-ray Diffraction (XRD).....	100
3.6.1 Technique	100
3.6.2 Sample Preparation.....	102
3.6.3 Procedure	102
3.7 Transmission Electron Microscopy (TEM).....	103
3.7.1 Technique	103
3.7.2 Sample Preparation.....	104
3.7.3 Procedure	105

3.8 Scanning Transmission Electron Microscopy-Electron Energy Loss Spectroscopy (STEM-EELS).....	105
3.8.1 Technique	105
3.8.1.1 STEM	105
3.8.1.2 Electron Energy Loss Spectroscopy (EELS).....	107
3.8.2 Sample Preparation.....	108
3.8.3 Procedure	108
3.9 Energy Dispersive X-ray Spectroscopy (EDX).....	109
3.9.1 Technique	109
3.9.2 Sample Preparation.....	111
3.9.3 Procedure	111
3.10 Extended X-ray Absorption Fine Spectroscopy (EXAFS).....	111
3.10.1 X-ray absorption spectroscopy (XAS) Technique.....	111
3.10.2 Standard Preparation.....	115
3.10.3 Sample Preparation.....	116
3.10.4 Procedure	117
3.11 Inductively Coupled Plasma – Optical Emission Spectroscopy (ICP-OES).....	117
3.11.1 Technique	117
3.11.2 Sample Preparation.....	120
3.11.3 Calibration Standard Sample Preparation.....	120
3.11.4 Procedure	121
Chapter 4: Development of nanomaterial libraries for nanosafety studies: Synthesis and Characterisation of Polyvinylpyrrolidone (PVP) Capped Metal Oxide Nanomaterials....	122
4.1 Introduction	122

4.2 Chemicals	124
4.3 Glassware	124
4.4 Synthesis of PVP capped metal oxide nanomaterials.....	125
4.4.1 Synthesis of PVP capped ceria nanomaterials.....	125
4.4.2 Synthesis of PVP capped zinc oxide nanomaterials.....	126
4.4.3 Synthesis of PVP capped copper oxide nanomaterials.....	127
4.4.4 Synthesis of PVP reference sample	127
4.4.5 Reaction Scale-up	127
4.5 Characterisation	128
4.6 Characterisation of Physical properties	129
4.6.1 Appearance	129
4.6.2 Size	130
4.6.2.1 Dynamic Light Scattering.....	131
4.6.2.2 Transmission Electron Microscopy	136
4.6.2.3 Scanning Transmission Electron Microscopy	145
4.6.3 Shape and Structure	147
4.6.3.1 Transmission Electron Microscopy	147
4.6.3.2 Scanning Transmission Electron Microscopy	148
4.7 Characterisation of chemical properties	149
4.7.1 Surface Charge	149
4.7.2 Chemical Composition	151
4.7.2.1 FT-IR	151
4.7.2.2 UV-VIS.....	154
4.7.2.3 X-ray Photoelectron Spectroscopy	160

4.7.2.4 Energy Electron Loss Spectroscopy	165
4.7.2.5 Energy Dispersive X-ray Spectroscopy.....	168
4.7.2.6 EXAFS	169
4.7.2.7 ICP-OES	175
4.8 Reaction Mechanism	179
4.9 Conclusions	181
Chapter 5: Thermal Transformations of Manufactured Nanomaterials (MNMs) as a Proxy for Ageing.....	184
5.1 Introduction	184
5.2 Samples selected for temperature ageing	186
5.3 Samples preparation	187
5.4 Procedure.....	187
5.5 Characterisation	188
5.6 Monitoring Physical Changes.....	188
5.6.1 Size & Physical features	188
5.7 Monitoring Chemical Changes	206
5.7.1 Surface Charge	206
5.7.2 Chemical Composition	212
5.7.2.1 X-ray Photoelectron Spectroscopy	212
5.7.2.2 UV-VIS.....	221
5.8 Conclusions	238
Chapter 6: Phosphate induced Transformations of Ceria based Nanomaterials	241
6.1 Introduction	241
6.2 Laboratory prepared phosphate solution	248

6.2.1 Samples selected for phosphate ageing using a laboratory prepared phosphate solution	248
6.2.2 Sample preparation	249
6.2.3 Laboratory prepared Phosphate solution preparation	249
6.2.4 Phosphate exposure method	250
6.2.4.1 10 K PVP Capped Ceria NMs phosphate pilot exposure	250
6.2.4.1.1 Characterisation	251
6.2.4.2 Zirconium doped ceria NMs phosphate exposure	251
6.2.4.2.1 Characterisation	252
6.3 Naturally occurring phospholipid exposure	253
6.3.1 Samples selected for phosphate ageing using a naturally occurring phospholipid ..	253
6.3.2 Samples preparation	253
6.3.3 Naturally occurring phospholipid solution preparation	253
6.5.2.2.3 Characterisation	254
6.4 Laboratory phosphate ageing of 10 K PVP capped ceria pilot study	254
6.4.1 Physical properties.....	255
6.4.1.1 Shape and Size.....	255
6.4.1.1.1 Dynamic Light Scattering.....	255
6.4.1.1.2 Transmission Electron Microscopy	258
6.4.2 Chemical properties.....	259
6.4.2.1 Surface Charge	259
6.4.2.2 Chemical Composition	261
6.4.2.2.1 UV-VIS.....	262
6.5 Laboratory phosphate ageing of zirconium doped ceria	264

6.5.1 Physical properties.....	265
6.5.1.1 Appearance	265
6.5.1.2 Shape and Size.....	267
6.5.1.2.1 Dynamic Light Scattering.....	267
6.5.1.2.2 Transmission Electron Microscopy	272
6.5.2 Chemical properties.....	277
6.5.2.1 Surface Charge	277
6.5.2.2 Chemical Composition	279
6.5.2.2.1 FT-IR	279
6.5.2.2.2 UV-VIS.....	282
6.5.2.2.3 XRD.....	286
6.5.2.2.4 EDX.....	289
6.6 Phosphate ageing of ceria nanomaterials using a naturally occurring phospholipid...293	
6.6.1 Physical properties.....	293
6.6.1.1 Appearance	293
6.6.1.2 Shape and Size.....	294
6.6.1.2.1 Dynamic Light Scattering.....	294
6.6.1.2.2 Transmission Electron Microscopy	295
6.6.2 Chemical properties.....	300
6.6.2.1 Surface Charge	300
6.6.2.2 Chemical Composition	301
6.6.2.2.1 XRD.....	301
6.7 Understanding the Phosphate Induced Transformations	303
6.8 Conclusions	304

6.8.1 Pilot phosphate ageing of 10 K PVP capped ceria NMs	304
6.8.2 Phosphate ageing of zirconium doped ceria	305
6.8.3 Phosphate ageing of ceria nanomaterials using a naturally occurring phospholipid	307
Chapter 7: Conclusions.....	309
Chapter 8: Future Work.....	316
Appendix 1	318
Appendix 2	320
Appendix 3	322
Appendix 4	328
Appendix 5	329
Appendix 6	333
Appendix 7	336
Appendix 8	337
Appendix 9	339
Appendix 10	341
Appendix 11	342
References	345

List of Figures

Figure 2.1 Nanometer scale comparing objects found in nature (Which Lab, 2015).....	10
Figure 2.2 Classification of nanomaterials according to dimensionality based on the concept of Siegel (Gusev, 2011).....	11
Figure 2.3 The relationships between 0-D, 1-D and 2-D nanomaterials in 3D space (MTX9100, 06/05/2014, Hussainova, 06/05/2014).	12
Figure 2.4 Classification according to morphology (Buzea et al., 2007).....	13
Figure 2.5 Additional nanomaterial classification composition (Buzea et al., 2007).	13
Figure 2.6 Uniformity and Agglomerated state of nanoparticles (Buzea et al., 2007).....	14
Figure 2.7 MNPs formation comparing the top-down and bottom-up approaches (Buzea et al., 2007).	18
Figure 2.8 Graphical illustration of the ceria oxygen vacancy formation. An oxygen atom moves away from its lattice position leaving behind two electrons which localise on two cerium atoms, turning Ce (4+) into Ce (3+) (Skorodumova et al., 2002).	25
Figure 2.9 Stick and Ball representation of ZnO crystal structures (a) rarely-observed rock-salt structure, (b) zinc blende and (c) wurzite, where the grey balls denote Zn ²⁺ ions whilst black balls represent O ²⁻ ions (Özgür et al., 2005).	31
Figure 2.10 The application of ZnO in the different sectors (Association, 2011).....	32
Figure 2.11 The annual production volumes of copper oxide nanomaterials (data are adapted from Piccinno et al. (2012)). The numbers next to each application category indicate the number of articles retrieved in 2013 from Thomson Reuters ISI Web of Science and their respective percentage share (Bondarenko et al., 2013).....	35

Figure 2.12 Nanomaterial lifecycle resulting with release into the environment (Mitrano et al., 2015).....	36
Figure 2.13 Pathways to exposure and fate of NMs in the environment (Oberdorster et al., 2005).....	38
Figure 2.14. Various physical and chemical characteristics that will have an influence on the NPs' behaviour (Hassellöv, 2009).....	48
Figure 2.15 Decrease in surface area to volume ratio for cuboctahedral nanoparticles (fraction of surface atoms given as %) (Sonstrom and Baumer, 2011).....	49
Figure 2.16 Library of nanoparticle shapes: TEM and SEM micrographs gold nanoparticles by Dr Željka Krpetić (CBNI, UCD) (CBNI, 2014).	50
Figure 2.17 Electric double layer (Kopeliovich, 2013).....	51
Figure 2.18 The two forces namely Van der Waals and electrostatic repulsion, on which the DLVO is based (Kopeliovich, 2013).....	53
Figure 2.19 Schematic of the main mechanisms that can be used for the stabilisation of NPs (assuming positively charged surfaces) (Bertrand et al., 2013).....	56
Figure 2.20 A 5 nm nanoparticle with different hydrophobic ligand molecules examples (left to right: trioctylphosphine oxide (TOPO), triphenylphosphine (TPP), dodecanethiol (DDT), tetraoctylammonium bromide (TOAB) and oleic acid (OA)) (Sperling and Parak, 2010).....	57
Figure 2.21 Structure of PVP monomer	58
Figure 2.22 Reaction of PVP and metal ions in the presence of water to form nanoparticles.	59
Figure 2.23 Key transformations that nanoparticles can undergo (Mitrano et al., 2014)....	62

Figure 2.24 The behaviour and effects of nanomaterials are dependent on the nanomaterial and critical interactions that occur (Lowry et al., 2012).....	63
Figure 2.25 Schematic illustration of various metal (Me) and metal oxide (MeOx) NP dissolution and ligation processes (Louie et al., 2014).....	66
Figure 2.26 Schematic of selected chemical transformations of silver nanoparticles in the environment. Important transformations include photo-induced aggregation, sulfidation, dissolution, and complexation with chloride (Louie et al., 2014).	67
Figure 2.27 Physical transformations of nanoparticles depicting homo and hetero aggregation (Lowry et al., 2012).	68
Figure 2.28 Biological transformation with specific reference to biological oxidation and biological degradation (Lowry et al., 2012).	71
Figure 2.29. Interaction of nanoparticles with macromolecules (Lowry et al., 2012).	72
Figure 3.1 Hydrodynamic diameter (D_h) measured in three different scenarios - capped particles, aggregates and non-spherical particles (Far, 2014).	84
Figure 3.2 Liquid layer around a particle is formed of the Stern Layer and diffuse layer (Ensol Instruments Ltd.).....	88
Figure 3.3 Schematic of MNM dispersion being filtered through a syringe filter into cuvette using a syringe.	89
Figure 3.4 Zeta potential cell used for the measurement analysis (The Hebrew University of Jerusalem, 2009).	91
Figure 3.5 Excitation of electrons by means of light (Deciedro, 2011).	92
Figure 3.6 UV-VIS Spectrophotometer set-up (Sheffield Hallam University, 2015).	93

Figure 3.7 XPS process where the sample is bombarded with incoming x-ray beams and photoelectrons, with unique information depending on the sample material, are emitted (Chavez, 2011).	96
Figure 3.8 Mounted samples on sample holder	98
Figure 3.9 Vibration, rotation, translation (Intermolecular Forces, 2014)	99
Figure 3.10 X-ray diffraction in crystalline material (Institute of Physics, 2015).	101
Figure 3.11 Side-view schematic of Transmission Electron Microscope (Foothill College, 2014).....	104
Figure 3.12 STEM Schematic (Tanaka, 1992)	107
Figure 3.13 EDX Principle (Hutchison, 2007)	110
Figure 3.14 Example indication of L- and K- edges as the energy coefficient decreases with increasing energy until an absorption edge is reached (Bauer and Bertagnolli, 2012).	113
Figure 3.15 X-ray absorption spectroscopy (XAS) spectrum indicating XANES and EXAFS section (Penner-Hahn, 2016).	114
Figure 3.16 Schematic of EXAFS experiment at synchrotron (Diamond Light Source, 2014).....	115
Figure 3.17 Standard discs of zinc oxide (top left), copper (I) oxide (top right) and copper (II) oxide (bottom right) mounted on Kapton Tape.....	116
Figure 3.18 Teflon cell sealed with Kapton tape loaded with PVP capped metal oxide nanomaterial dispersion.....	116
Figure 3.19 Diagram of Sample introduction to ICP-OES.....	118
Figure 3.20 Inductively coupled plasma.....	119
Figure 4.1 Reflux set-up	126

Figure 4.2 Photograph of 10 K PVP capped ceria from left to right: original, scale-up x3 and scale-up x6.	130
Figure 4.3 Size distribution graphs for a) PVP capped ceria, b) PVP capped zinc oxide, c) PVP capped copper oxide and d) PVP reference samples.....	134
Figure 4.4 Size distribution graphs for scaled-up PVP capped ceria as prepared, x3 and x6 for a) 10 K PVP, b) 40 K PVP and c) 360 K PVP	135
Figure 4.5 Size distribution graphs for scaled-up PVP capped zinc oxide as prepared, x3 and x6 for a) 10 K PVP, b) 40 K PVP and c) 360 K PVP.....	135
Figure 4.6 Size distribution graphs for scaled-up PVP capped copper oxide as prepared, x3 and x6 for a) 10 K PVP, b) 40 K PVP and c) 360 K PVP.....	136
Figure 4.7 Histogram depicting size (nm) versus frequency for 10 K PVP capped ceria.	138
Figure 4.8 TEM images of 10 K PVP capped ceria nanoparticles.	139
Figure 4.9 Histogram depicting size (nm) versus frequency for 40 K PVP capped ceria.	139
Figure 4.10 TEM images of 40 K PVP capped ceria nanoparticles.	139
Figure 4.11 Histogram depicting size (nm) versus frequency for 360 K PVP capped ceria.	140
Figure 4.12 TEM images of 360 K PVP capped ceria nanoparticles.	140
Figure 4.13 Histogram depicting size (nm) versus frequency for 10 K PVP capped zinc oxide.	141
Figure 4.14 TEM images of 10 K PVP capped zinc oxide nanoparticles.	141
Figure 4.15 Histogram depicting size (nm) versus frequency for 40 K PVP capped zinc oxide.	141
Figure 4.16 TEM images of 40 K PVP capped zinc oxide nanoparticles.	142

Figure 4.17 Histogram depicting size (nm) versus frequency for 360 K PVP capped zinc oxide.	142
Figure 4.18 TEM images of 360 K PVP capped zinc oxide nanoparticles.	142
Figure 4.19 Histogram depicting size (nm) versus frequency for 10 K PVP capped copper oxide.	143
Figure 4.20 TEM images of 10 K PVP capped copper oxide nanoparticles.	143
Figure 4.21 Histogram depicting size (nm) versus frequency for 40 K PVP capped copper oxide.	144
Figure 4.22 TEM images of 40 K PVP capped copper oxide nanoparticles.	144
Figure 4.23 Histogram depicting size (nm) versus frequency for 360 K PVP capped copper oxide.	144
Figure 4.24 TEM images of 360 K PVP capped copper oxide nanoparticles.	145
Figure 4.25 Size distribution of 10 K PVP capped ceria obtained by STEM.	146
Figure 4.26 Size distribution of 10 K PVP capped zinc oxide obtained by STEM.	146
Figure 4.27 Size distribution of 10 K PVP capped zinc oxide obtained by STEM.	147
Figure 4.28 STEM images of 10 K PVP capped ceria at magnification (a) x 1 M, (b) x 5 M and (c) x 10 M.	148
Figure 4.29 STEM images of 10 K PVP capped zinc oxide at magnification (a) x 2 M, (b) x 5 M and (c) x 5 M.	149
Figure 4.30 STEM images for 10 K PVP capped copper oxide at magnification (a) x 1 M, (b) x 2 M and (c) x 10 M.	149
Figure 4.31 FT-IR spectrum of 10 K PVP capped ceria.	153
Figure 4.32 FT-IR Spectra of 10 K PVP capped zinc oxide.	153
Figure 4.33 FT-IR Spectra of 10 K PVP capped copper oxide.	154

Figure 4.34 UV-VIS spectra for (a) PVP capped ceria, (b) PVP capped zinc oxide and (c) PVP capped copper oxide.....	159
Figure 4.35 UV-VIS spectra for as prepared 10 K, 40 K and 360 K PVP capped copper oxide.	160
Figure 4.36 XPS spectra of 10 K PVP capped ceria, 40 K PVP capped ceria and 360 K PVP capped ceria NMs from bottom to top respectively.	163
Figure 4.37 XPS spectrum for PVP capped zinc oxide representative of 10 K, 40 K and 360 K PVP capped zinc oxide.	164
Figure 4.38 XPS spectra for 10 K PVP capped copper oxide, 40 K PVP capped copper oxide and 360 K PVP capped copper oxide NMs from bottom to top respectively.....	165
Figure 4.39 (a) Reference EELS spectrum for CuO and Cu ₂ O and (b-d) EELS spectra for 10 K PVP capped copper oxide.....	166
Figure 4.40 (a) Reference EELS spectrum for Ce ³⁺ and Ce ⁴⁺ , (b-c) EELS spectra for 10 K PVP capped ceria and (d) Ce ⁴⁺ distribution.	168
Figure 4.41 EDX spectrum for 10 K PVP capped zinc oxide NMs.	169
Figure 4.42 EXAFs spectra of 10 K, 40 K and 360 K PVP capped zinc oxide and reference spectrum for zinc oxide.	171
Figure 4.43 EXAFs spectra for PVP capped copper oxide NMs.	173
Figure 4.44 EXAFs spectra for copper standards used for sample fittings.	174
Figure 4.45 ICP-OES values for scaled-up PVP capped ceria as prepared, x3 and x6 for (a) 10 K PVP, (b) 40 K PVP and (c) 360 K PVP.....	177
Figure 4.46 ICP-OES values for scaled-up PVP capped zinc oxide as prepared, x3 and x6 for (a) 10 K PVP, (b) 40 K PVP and (c) 360 K PVP.	177

Figure 4.47 ICP-OES values for scaled-up PVP capped copper oxide as prepared, x3 and x6 for (a) 10 K PVP, (b) 40 K PVP and (c) 360 K PVP.....	178
Figure 4.48. ICP-OES values for different PVP capped metal oxide NMs (a) ceria (b) zinc oxide and (c) copper oxide.	178
Figure 4.49 Hydrolysis of metal nitrates.	179
Figure 4.50 Mechanism for synthesis of PVP capped metal oxide nanoparticles.....	180
Figure 4.51 Mechanism reactions for syntheses of PVP capped metal oxide nanomaterials.	181
Figure 5.1 a) and b) Size distribution for 10 K PVP samples exposed to a) 25 °C and b) 45 °C as a function of time.	192
Figure 5.1 c) and d) Size distribution for 10 K PVP samples exposed to c) 65 °C and d) 80 °C as a function of time.	193
Figure 5.2 a) and b) Size distribution graphs (left) and TEM images (right) for 10 K PVP ceria samples exposed to a) 25 °C and b) 45 °C as a function of time.....	194
Figure 5.2 c) and d) Size distribution graphs (left) and TEM images (right) for 10 K PVP ceria samples exposed to c) 65 °C and d) 80 °C as a function of time.....	195
Figure 5.3 a) and b) Size distribution graphs (left) and TEM images (right) for 40 K PVP ceria samples exposed to a) 25 °C and b) 45 °C as a function of time.....	196
Figure 5.3 c) and d) Size distribution graphs (left) and TEM images (right) for 40 K PVP ceria samples exposed to c) 65 °C and d) 80 °C as a function of time.....	197
Figure 5.4 a) and b) Size distribution graphs (left) and TEM images (right) for 360 K PVP ceria samples exposed to a) 25 °C and b) 45 °C as a function of time.....	198
Figure 5.4 c) and d) Size distribution graphs (left) and TEM images (right) for 360 K PVP ceria samples exposed to c) 65 °C and d) 80 °C as a function of time.....	199

Figure 5.5 Size distribution graphs (left) and TEM images (right) for Commercial ceria samples exposed to a) 25 °C, b) 45 °C, c) 65 °C and d) 80 °C as a function of time.	200
Figure 5.5 Size distribution graphs (left) and TEM images (right) for Commercial ceria samples exposed to a) 25 °C, b) 45 °C, c) 65 °C and d) 80 °C as a function of time.	201
Figure 5.6 a) and b) Size distribution graphs (left) and TEM images (right) for 10 K PVP capped copper oxide samples exposed to a) 25 °C and b) 45 °C as a function of time. ...	202
Figure 5.6 c) and d) Size distribution graphs (left) and TEM images (right) for 10 K PVP capped copper oxide samples exposed to a) 25 °C, b) 45 °C, c) 65 °C and d) 80 °C as a function of time.	203
Figure 5.7 a) and b) Size distribution graphs (left) and TEM images (right) for 10 K PVP capped zinc oxide samples exposed to a) 25 °C and b) 45 °C as a function of time.....	204
Figure 5.7 c) and d) Size distribution graphs (left) and TEM images (right) for 10 K PVP capped zinc oxide samples exposed to c) 65 °C and d) 80 °C as a function of time.....	205
Figure 5.8 Change in average zeta potential (mV) as a function of time for 10 K PVP samples at 25, 45, 65 and 80 °C.	208
Figure 5.9 Change in average zeta potential (mV) as a function of time for 10 K PVP capped ceria samples at 25, 45, 65 and 80 °C.	209
Figure 5.10 Change in average zeta potential (mV) as a function of time for 40 K PVP capped ceria samples at 25, 45, 65 and 80 °C.	209
Figure 5.11 Change in average zeta potential (mV) as a function of time for 360 K PVP capped ceria samples at 25, 45, 65 and 80 °C.	210
Figure 5.12 Change in average zeta potential (mV) as a function of time for commercial ceria samples at 25, 45, 65 and 80 °C.....	210

Figure 5.13 Change in average zeta potential (mV) as a function of time for 10 K PVP capped copper oxide samples at 25, 45, 65 and 80 °C.	211
Figure 5.14 Change in average zeta potential (mV) as a function of time for 10 K PVP capped zinc oxide samples at 25, 45, 65 and 80 °C.	211
Figure 5.15 XPS Spectra for 10 K PVP capped ceria as prepared and after 28 days at T=25, 45, 65 and 80 °C (from bottom to top).	215
Figure 5.16 XPS Spectra for 40 K PVP capped ceria as prepared and after 28 days at T=25, 45, 65 and 80 °C (from bottom to top).	216
Figure 5.17 XPS Spectra for 360 K PVP capped ceria as prepared and after 28 days at T=25, 45, 65 and 80 °C (from bottom to top).	217
Figure 5.18 XPS Spectra for commercial ceria as prepared and after 28 days at T=25, 45, 65 and 80 °C (from bottom to top).	218
Figure 5.19 XPS Spectra for 10 K PVP capped zinc oxide as prepared and after 28 days at T=25, 45, 65 and 80 °C (from bottom to top).	219
Figure 5.20 XPS Spectra for 10 K PVP capped copper oxide as prepared and after 28 days at T=25, 45, 65 and 80 °C (from bottom to top).	220
Figure 5.21 a) and b) UV-VIS spectra for 10 K PVP samples exposed to a) 25 and b) 45 °C as a function of time.	224
Figure 5.21 c) and d) UV-VIS spectra for 10 K PVP samples exposed to c) 65 and d) 80 °C as a function of time.	225
Figure 5.22 a) and b) UV-VIS spectra for 10 K PVP capped ceria exposed to a) 25 and b) 45 °C as a function of time.	226
Figure 5.22 c) and d) UV-VIS spectra for 10 K PVP capped ceria exposed to c) 65 and d) 80 °C as a function of time.	227

Figure 5.23 a) and b) UV-VIS spectra for 40 K PVP capped ceria exposed to a) 25 and b) 45 °C as a function of time.	228
Figure 5.23 UV-VIS spectra for 40 K PVP capped ceria exposed to a) 25, b) 45, c) 65 and d) 80 °C as a function of time.	229
Figure 5.24 a) and b) UV-VIS spectra for 360 K PVP capped ceria exposed to a) 25 and b) 45 °C as a function of time.	230
Figure 5.24 c) and d) UV-VIS spectra for 360 K PVP capped ceria exposed to c) 65 and d) 80 °C as a function of time.	231
Figure 5.25 a) and b) UV-VIS spectra for Commercial ceria exposed to a) 25 and b) 45 °C as a function of time.	232
Figure 5.25 c) and d) UV-VIS spectra for Commercial ceria exposed to c) 65 and d) 80 °C as a function of time.	233
Figure 5.26 a) and b) UV-VIS spectra for 10 K PVP capped zinc oxide exposed to a) 25 and b) 45 °C as a function of time.	234
Figure 5.26 c) and d) UV-VIS spectra for 10 K PVP capped zinc oxide exposed to c) 65 and d) 80 °C as a function of time.	235
Figure 5.27 a) and b) UV-VIS spectra for 10 K PVP capped copper oxide exposed to a) 25 and b) 45 °C as a function of time.	236
Figure 5.27 c) and d) UV-VIS spectra for 10 K PVP capped copper oxide exposed to c) 65 and d) 80 °C as a function of time.	237
Figure 6.1 Possible Nanoparticle Transformations.	242
Figure 6.2 Phospholipid structure (Miko, 2014).	245
Figure 6.3 Chemical composition of bile. Percentages represent ratio to total solute concentration (mg/ml) (Farina, 2009)	247

Figure 6.4 DLS size histograms for 10 K PVP capped ceria NM sample exposed to 5 mM phosphate solution as a function of time a) 1 part NM solution, 1 part phosphate solution and 3 parts water, b) 4 parts NM solution and 1 part phosphate solution and c) 1 part NM solution and 4 parts phosphate solution.....	257
Figure 6.5 Zeta Potential for all 10 K PVP capped ceria phosphate exposed samples as a function of time.	261
Figure 6.6 UV-VIS spectra for sample from Scenario A (1 part NM + 4 parts phosphate) as a function of time.....	263
Figure 6.7 UV-VIS spectra for sample from Scenario B (4 parts NM + 1 part phosphate) as a function of time.....	263
Figure 6.8 UV-VIS spectra for sample from Scenario C (1 part NM + 1 part phosphate + 3 parts H ₂ O) as a function of time.	264
Figure 6.9 Samples A-G (left to right) after immediate addition of 4 mL of 5 mM phosphate solution to 1 mL of NM solution (Scenario A).	266
Figure 6.10 Samples A-G (left to right) after 21 days exposed to Scenario A.....	266
Figure 6.11 Samples A-G (left to right) after 7 days exposed to Scenario D.....	267
Figure 6.12 DLS size histograms for zirconium doped ceria samples A-G exposed to 1 mM phosphate solution (Scenario D) as a function of time.....	270
Figure 6.13 DLS size histograms for zirconium doped ceria samples A-G exposed to 5 mM phosphate solution (Scenario A) as a function of time.....	271
Figure 6.14 Zeta Potential of zirconium doped ceria samples A-G exposed to 1 mM phosphate solution as a function of time.	278
Figure 6.15 Zeta Potential of zirconium doped ceria samples A-G exposed to 5 mM phosphate solution as a function of time.	279

Figure 6.16 FT-IR spectra for pristine (left) and 21 day 5 mM phosphate exposed samples A-G (top to bottom).....	281
Figure 6.17 UV-VIS spectra for pristine, immediately exposed, 7 and 21 days exposed samples exposed to 1 mM phosphate solution.	284
Figure 6.18 UV-VIS spectra for pristine, immediately exposed, 7 and 21 days exposed samples exposed to 5 mM phosphate solution.	285
Figure 6.19 XRD patterns for the pristine (left) and 21 day 5 mM phosphate exposed samples A-G (bottom to top).....	288
Figure 6.20 TEM image and EDX spectra of sample B exposed to 5 mM phosphate solution for 21 days where (A) shows the core NM and (B) shows the edge spectrum. ..	290
Figure 6.21 TEM image and EDX spectra of sample B exposed to 5 mM phosphate solution for 21 days where (A) shows the needles and (B) shows the core NM spectrum.	291
Figure 6.22 TEM image and EDX spectrum of sample C exposed to 5 mM phosphate solution for 21 days.	291
Figure 6.23 TEM image and EDX spectrum of sample D exposed to 5 mM phosphate solution for 21 days.	292
Figure 6.24 TEM image and EDX spectrum of sample E exposed to 5 mM phosphate solution for 21 days.	292
Figure 6.25 TEM image and EDX spectrum of sample F exposed to 5 mM phosphate solution for 21 days.	292
Figure 6.26 TEM image and EDX spectrum of sample G exposed to 5 mM phosphate solution for 21 days.	293

Figure 6.27 DLS size histograms for commercial ceria NMs exposed to a) 3 mg/mL and b) 15 mg/mL phospholipid solution as a function of time.....	295
Figure 6.28 a) TEM image and b) Histogram depicting size (nm) versus frequency for Sample A.	297
Figure 6.29 a) TEM image and b) Histogram depicting size (nm) versus frequency for NMs exposed to 3 mg/mL phospholipid solution at time 0.	298
Figure 6.30 a) TEM images and b) Histogram depicting size (nm) versus frequency for NMs exposed to 3 mg/mL phospholipid solution after 96 hours.	298
Figure 6.31 a) TEM image and b) Histogram depicting size (nm) versus frequency for NMs exposed to 15 mg/mL phospholipid solution at time 0.	299
Figure 6.32 a) TEM images and b) Histogram depicting size (nm) versus frequency for NMs exposed to 15 mg/mL phospholipid solution after 96 hours.	299
Figure 6.33 Average zeta potential for commercial ceria NMs (Sample A) exposed to 3 mg/mL and 15 mg/mL phospholipid solution as a function of time.	301
Figure 6.34 XRD patterns of pristine commercial ceria NMs prior to exposure, NMs exposed to 3 mg/mL phospholipid solution for 96 hours and NMs exposed to 15 mg/mL phospholipid solution for 96 hours.	303
Figure 6.35 Transformation of ceria and ceria-rich nanoparticles in the presence of a mixture of organic acids and phosphate.	304
Figure A.2.1. UV-VIS spectra for scaled-up PVP capped ceria as prepared, x3 and x6 for a) 10 K PVP, b) 40 K PVP and c) 360 K PVP	320
Figure A.2.2. UV-VIS spectra for scaled-up PVP capped zinc oxide as prepared, x3 and x6 for a) 10 K PVP, b) 40 K PVP and c) 360 K PVP	320

Figure A.2.3. UV-VIS spectra for scaled-up PVP capped copper as prepared, x3 and x6 for a) 10 K PVP, b) 40 K PVP and c) 360 K PVP	321
Figure A.4.1 DLS size distribution graphs for 10 K PVP capped ceria NMs at room temperature over 6 months.	328
Figure A.8.1 FT-IR spectra for 7 day 5 mM phosphate exposed samples A-G (top to bottom).	337
Figure A.8.2 FT-IR spectra for 7 day (left) and 21 day (right) 1 mM phosphate exposed samples A-G (top to bottom).	338
Figure A.9.1 XRD pattern for the 21 day 1 mM phosphate exposed samples A-G (bottom to top).	339
Figure A.9.2 XRD pattern for the 7 day 5 mM phosphate exposed samples A-G (bottom to top).	340

List of Tables

Table 2.1 Properties of ceria.....	24
Table 2.2 Properties of zinc oxide	30
Table 3.1 Properties studied and techniques used in this project.	83
Table 4.1 Chemicals used in this study.	124
Table 4.2. Quantities and volumes used to synthesise PVP capped ceria NMs	125
Table 4.3. Scale-up experiment quantities used for PVP capped ceria synthesis.	128
Table 4.4 Size and PDI values for PVP capped NMs	133
Table 4.5 TEM data values obtained for PVP capped ceria NMs.....	138
Table 4.6 TEM data values obtained for PVP capped zinc oxide NMs	140
Table 4.7 TEM data values obtained for PVP capped copper oxide NMs.....	143
Table 4.8 The average zeta potential values for 10 K PVP capped samples.....	150
Table 4.9. Percentage amount of Ce ³⁺ and/or Ce ⁴⁺ in samples containing ceria.....	164
Table 4.10 Average concentration and standard deviation for NM dispersions synthesised.	176
Table 6.1. Quantities used to prepare a 1 mM and 5 mM phosphate solution	250
Table 6.2 Three different phosphate exposure scenarios prepared for 10 K PVP capped ceria NMs with varying volumes of NM dispersion, 5 mM phosphate solution and milliQ water.	251
Table 6.3 Volumes of NM dispersions and 1 or 5 mM phosphate solutions required to prepare each of the zirconium doped ceria phosphate exposure samples.	252
Table 6.4 Quantities used to prepare natural occurring phospholipid exposure.	254

Table 6.5. TEM images for the as prepared, 1 week and 3 week phosphate aged 10 K PVP capped ceria NMs.	259
Table 6.6 Z-Average (nm) values obtained for pristine and aged zirconium doped ceria samples.	269
Table 6.7 TEM images for (from left to right) Pristine, 7 day old 1 mM phosphate exposed samples, 21 day old 1 mM phosphate exposed samples, 7 day old 5 mM phosphate exposed samples and 21 day old 5 mM phosphate exposed samples A-G (from top to bottom).	274
Table 6.8 TEM size values obtained for commercial ceria samples and phospholipid exposed commercial ceria samples.	297
Table A.1.1 Average Zeta Potential Values for PVP capped metal oxide nanoparticle and scaled-up nanoparticle dispersions.	318
Table A.3.1 ICP-OES Concentration Values obtained for PVP capped metal oxide nanoparticle and scaled-up nanoparticle dispersions.....	322
Table A.5.1 STEM Characterisation data of commercial ceria NMs.....	329
Table A.5.2 DLS Characterisation data of commercial ceria NMs.....	331
Table A.5.3 Zeta Potential Characterisation data of commercial ceria NMs.....	332
Table A.5.4 UV-VIS Characterisation data of commercial ceria NMs.....	332
Table A.6.1 PCC statistical analysis data.	333
Table A.7.1 Average zeta potential values of the phosphate exposed 10 K PVP capped ceria NMs.	336
Table A.10.1 Average zeta potential values of the phospholipid exposed commercial ceria NMs.	341

List of Abbreviations

$(C_6H_9NO)_nMO_x$	Polyvinylpyrrolidone Capped Metal Oxide
$[M(H_2O)_n]^{x+}$ or $[M(H_2O)_n-1(OH)]^{(x-1)+}$	Metal Hydroxide Intermediate States
$\mu(E)$	Linear Absorption Coefficient
μL	Microlitre
μm	Micrometer ($1 \times 10^{-6} m$)
$^{\circ}$	Degrees
$^{\circ}C$	Degrees Celsius
0-D	Zero dimensional
1-D	One dimensional
$1s \rightarrow 3d$	Transition from the 1s orbital to the 3d orbital
$1s \rightarrow 4p$	Transition from the 1s orbital to a 4p orbital
$1s \rightarrow 4p_{xy}$	Transition from the 1s orbital to the $4p_{xy}$ orbital
$1s \rightarrow 4p_z$	Transition from the 1s orbital to the $4p_z$ orbital
2-D	Two dimensional
3-D	Three dimensional

10 K	10 000 Dalton
40 K	40 000 Dalton
360 K	360 000 Dalton
Å	Ångström
A-Ceria or Sample A	Cerium (IV) oxide nanoparticles
ADF	Annular Dark Field
Ag or Ag(0)	Silver
Ag ⁺	Silver ions
Al	Aluminium
Al K α	Aluminium x-ray source resulting in emission at 1486.6 eV
amu	Atomic Mass Unit
ATR	Attenuated Total Reflection
Au	Gold
<i>b</i>	Path length (Beer-Lambert's Law)
B	Constant used in the equation relating X-ray wavelength to atomic number. It is dependent on the specific shells.
B.C.	Before Christ

BE	Binding Energy			
Be	Beryllium			
BF	Bright Field			
B-Zirconium doped Ceria or Sample B	$Ce_{0.9}Zr_{0.1}O_2$ nanoparticles			
C	Carbon			
<i>c</i>	Concentration (Beer-Lambert's Law)			
C	Spot size			
C_{60}	Carbon 60 or Buckminsterfullerene			
CdS	Cadmium Sulfide			
CdSe	Cadmium Selenide			
Ce	Cerium			
Ce 10 K PVP	10,000	Polyvinylpyrrolidone	Capped	Ceria
	Nanoparticles			
Ce 360 K PVP	360,000	Polyvinylpyrrolidone	Capped	Ceria
	Nanoparticles			
Ce 40 K PVP	40,000	Polyvinylpyrrolidone	Capped	Ceria
	Nanoparticles			

Ce(III)NO ₃	Cerium (III) Nitrate
Ce(NO ₃) ₃ .6H ₂ O	Cerium nitrate hexahydrate
Ce ₂ O ₃	Cerium (III) oxide
Ce ³⁺ or Ce (III)	Trivalent cerium ions
Ce ⁴⁺ or Ce (IV)	Tetravalent cerium ions
CEH	Centre for Ecology & Hydrology
Ce-O	Cerium – Oxygen bond
CeO ₂	Cerium dioxide
CeO _x	Cerium (III) or Cerium (IV) oxide
CePO ₄	Cerium Phosphate
Ceria	Cerium oxide or cerium dioxide
cm	Centimetre
cm ²	Centimetre squared
CNTs	Carbon nanotubes
Co	Cobalt
Cu (I)	Copper (I) ions
Cu (II)	Copper (II) ions

Cu 10 K PVP or Cu10	10,000 Polyvinylpyrrolidone Capped Copper Oxide Nanoparticles
Cu 360 K PVP or Cu360	360,000 Polyvinylpyrrolidone Capped Copper Oxide Nanoparticles
Cu 40 K PVP or Cu40	40,000 Polyvinylpyrrolidone Capped Copper Oxide Nanoparticles
Cu or Cu(0)	Copper
Cu(NO ₃) ₂	Copper (III) nitrate
Cu(OH) ₂	Copper Hydroxide
Cu ₂ O	Copper (I) Oxide
CuO	Copper (II) Oxide
Cu-O	Copper – Oxygen bond
CuO _x	Copper (I) or Copper (II) oxide
CuZnFe ₂ O ₄	Copper Zinc Iron Oxide
C-Zirconium doped Ceria or Sample C	Ce _{0.75} Zr _{0.25} O ₂ nanoparticles
d	Distance / diameter
D	Diffusion co-efficient

DDT	Dodecanethiol
D_h	Hydrodynamic diameter
DLS	Dynamic Light Scattering
DLVO	Derjaguin-Landau-Verwey-Overbeek Theory
D-Zirconium doped Ceria or Sample D	$Ce_{0.48}Zr_{0.52}O_2$ nanoparticles
e^-	Electron
EDX	Energy Dispersive X-ray Spectroscopy
EELS	Electron Energy Loss Spectroscopy
EMRC	European Medical Research Councils
ENMs	Engineered Nanomaterials
ESCA	Electron Spectroscopy for Chemical Analysis
ESF	European Science Foundation
EU	European Union
eV	Electron Volt
EXAFS	Extended X-ray Absorption Fine Spectroscopy
E-Zirconium doped Ceria or Sample E	$Ce_{0.25}Zr_{0.75}O_2$ nanoparticles

FDA	Food and Drug Administration
Fe ₂ O ₃	Iron (III) oxide
Fe ₃ O ₄	Iron (II,III) oxide
FEG	Field Emission Gun
FT-IR	Fourier Transform Infra-red Spectroscopy
FWHM	Full width at half maximum
F-Zirconium doped Ceria or Sample F	Ce _{0.1} Zr _{0.9} O ₂ nanoparticles
g	Gram
gcm ⁻¹	Gram per centimetre
GPR	General Purpose Reagent
G-Zirconium oxide or Sample G	Zirconium (IV) oxide nanoparticles
H	Hydrogen
H ₂ O	Water
H ₂ O ₂	Hydrogen Peroxide
H ₃ O ⁺	Hydronium
HAADF	High-Angle Annular Dark Field
I(E)	Incident X-ray Intensity

$I_0(E)$	Transmitted X-ray Intensity
ICP-OES	Inductively Coupled Plasma Optical Emission Spectroscopy
IR	Infra-red
ISO	International Organization for Standardization
IUPAC	International Union of Pure and Applied Chemistry
K	Kilo (1000)
K	Potassium
k	Boltzmann constant
K orbital	First Electron Shell
KE	Kinetic Energy
K-edge	Edge associated with first electron shell
keV	Kilo Electron Volt
KH_2PO_4	Monopotassium Phosphate
KIT	Karlsruhe Institute for Technology (Germany)
K_{sp}	Solubility Product Constant
kV	Kilovolt
L	Litre

L orbital	Second Electron Shell
L-edge	Edge associated with second electron shell
Li	Lithium
LMM	L-inner level-M-inner level-M-inner level electron transition
M (magnification)	One million
M orbital	Third Electron Shell
M(NO ₃) _x	Metal nitrate
Me	Metal
M-edge	Edge associated with third electron shell
MeO _x or MO _x	Metal Oxide
mg	Milligram
Mg K α	Magnesium x-ray source resulting in emission at 1253.6 eV
mg/L	Milligram per litre
mg/mL	Milligram per millilitre
min	Minute
mL	Millilitre

mm	Millimetre
mM	Millimolar
MNMs	Manufactured Nanomaterials
MNPs	Manufactured nanoparticles
MOH _x	Metal Hydroxide
mrad	Milliradian
mV	Millivolt
MWCNT	Multiwall Carbon Nanotubes
M ^{x+}	Metal ions
MΩcm	Megaohm centimetre
N	Nitrogen
<i>n</i>	An integer determined by the order given used in Bragg's Law
NanoMILE	Engineered <u>nanomaterial</u> <u>mechanisms</u> of <u>interactions</u> with <u>living</u> systems and the <u>environment</u> : a universal framework for safe nanotechnology
NERC	Natural Environment Research Council
NiO	Nickel oxide

NM	Nanomaterials
nm	Nanometer (1×10^{-9} m)
NO_3^-	Nitrate ions
NOM	Natural Organic Matter
NPs	Nanoparticles
O	Oxygen
OA	Oleic Acid
O-H or -OH	Hydroxide
P value	Probability value
P=O	Phosphorus Oxygen double bond
PCC	Pearson's Product Moment Correlation Coefficient
PDI	Polydispersity Index
PEG	Polyethylene glycol
pH	Measure of acidity or basicity in an aqueous solution
P-O	Phosphorus Oxygen single bond
PO_4^{3-}	Phosphate ions
ppm	Parts per million

PVP	Polyvinylpyrrolidone
Q ₁₀	The factor by which the rate of a chemical reaction will increase following Arrhenius's equation.
r	Radius of the particle
Ref 10 K	10,000 polyvinylpyrrolidone reference sample
Ref 360 K	360,000 polyvinylpyrrolidone reference sample
Ref 40 K	40,000 polyvinylpyrrolidone reference sample
REO	Rare Earth Oxide
RF	Radio Frequency
R _H	Hydrodynamic Radius
ROS	Reactive oxygen species
rpm	Revolutions per minute
s	Seconds
SEM	Scanning Electron Microscopy
SiO ₂	Silicon dioxide
STEM	Scanning Transmission Electron Microscopy
STEM-EELS	Scanning Transmission Electron Microscopy – Electron Energy Loss Spectroscopy

T	Temperature
TEM	Transmission Electron Microscopy
TiO ₂	Titanium Dioxide
TOAB	Tetraoctylammonium bromide
TOPO	Trioctylphosphine oxide
TPP	Triphenylphosphine
U	Uranium
U.S.	United States
UK	United Kingdom
UV	Ultraviolet
UVA	Ultraviolet light type A (400-315 nm)
UV-VIS	Ultra-Violet visible spectroscopy
V _A	Van der Waals Attraction
V _R	Electrostatic Repulsion
V _T	Potential Energy of Particles
Wcm ⁻¹⁰ C ⁻¹	Watt per cm per degree Celcius
wt/wt	Weight/Weight

XANES	X-ray Absorption Near Edge Spectroscopy
XAS	X-ray Absorption Spectroscopy
XPS	X-ray Photoelectron Spectroscopy
XRD	X-ray Diffraction Spectroscopy
Z	Atomic Number
Zn (II)	Zinc (II) ions
Zn 10 K PVP or Zn10	10,000 polyvinylpyrrolidone capped zinc oxide nanoparticles
Zn 360 K PVP or Zn360	360,000 polyvinylpyrrolidone capped zinc oxide nanoparticles
Zn 40 K PVP or Zn40	40,000 polyvinylpyrrolidone capped zinc oxide nanoparticles
Zn or Zn (0)	Zinc
Zn(NO ₃) ₂	Zinc nitrate
Zn ₃ (PO ₄) ₂	Zinc Phosphate
ZnO	Zinc Oxide
Zn-O	Zinc – Oxygen bond
ZnS	Zinc Sulfide

ZrO_2	Zirconium Dioxide
ϵ	dielectric constant of the solvent
ϵ	Constant of proportionality called the <i>absorbivity</i> used in Beer-Lambert's Law
ϵ_0	the vacuum permittivity
ζ	Zeta Potential
η	Viscosity
θ	The angle between the incident ray and the scattering planes
λ	Wavelength
σ	Constant used in the equation relating X-ray wavelength to atomic number. It is dependent on the specific shells.

Chapter 1: Introduction

1.1 Scientific Rationale

‘Atoms on a small scale behave like *nothing* on a large scale’ (Feynman, 1959). In fact, nanomaterials, substances having at least one dimension between 1 and 100 nm (JRC, 2010, ISO, 2010a), have significantly distinct properties to those of their bulk counterpart. These include high surface-to-volume ratio and significantly distinct chemical, electronic, optical, magnetic & mechanical properties from those of their bulk counterpart (Ansari et al., 2010, Tejamaya et al., 2012, Nowack and Bucheli, 2007). These materials have drastically changed our daily life with their diverse uses in many everyday fields such as goods for children, appliances, food and beverages, electronics, automotive, home and garden and health and fitness including clothing, cosmetics and personal care (Vance et al., 2015).

Nanotechnology continues to grow rapidly. Between 2010 and 2013 a 24 % increase in consumer products containing nanomaterials had been recorded (Nanotechnologies, 2013). As of November 2015 there were more than 1,800 products listed in the Consumer Products Inventory (The Project on Emerging Nanotechnologies, 2015). The increased use of manufactured nanomaterials (MNMs) results in increased environmental release, hence concerns that exposure of humans and other organisms is inevitable. The potential environmental impact of MNMs is poorly understood, and the need to better understand MNM fate and transformations is particularly urgent. Furthermore, to date, no sufficient work has been done to establish the changes that nanomaterials undergo when incorporated into, and released from, products. As a result,

“nanotoxicity”, the study of the toxicity of nanomaterials, has become a major research objective in the EU and internationally (Aydın et al., 2012). Many aspects in the field of nanotoxicity remain poorly studied and challenging due to the difficulties in identifying, characterising and monitoring nanomaterials particularly after their release in the environment (Nowack and Bucheli, 2007, Valsami-Jones and Lynch, 2015b, Handy et al., 2008).

During their life time many nanomaterials undergo significant transformations such as biological transformations, interactions with macromolecules and physical and chemical transformation (Sarathy et al., 2008, Louie et al., 2014). Assessing the environmental and human health implications of nanomaterials requires an understanding of the potential exposure routes, transformations, behaviours and effects of the nanomaterials (Auffan, 2013, Lowry et al., 2012, Tso et al., 2010, Rickerby and Morrison, 2007, Nowack and Bucheli, 2007, Lynch et al., 2014). The transformations taking place vary depending on the nanomaterial. Some metals such as zinc oxide undergo dissolution, silver easily undergoes sulfidation and other metal oxides such as titanium dioxide may possibly remain largely unaffected (Louie et al., 2014, Mitrano et al., 2015, Lowry et al., 2012). Literature has shown that rare earth oxides (REOs) transform biologically on exposure to phosphate compounds at a low pH (Li et al., 2014), however this biotransformation of REOs has not always been seen or studied in depth. Thus there is notable uncertainty which needs to be mitigated, about the state of many nanomaterials once they have been released into the environment.

Ageing is an important part of a nanomaterial’s life cycle that can be considered as a transformation over time. One main reason why ageing is important for nanomaterials is the fact that this may apply a lot more to MNMs than their bulk counterparts as they are

more reactive and therefore more likely to transform. Unfortunately there is a lack of knowledge and literature when it comes to the ageing of nanomaterials. To date there are no standard testing methods for ageing or accelerated ageing of nanomaterials. Only on very few occasions has it been considered how aged nanomaterials will affect the environment and biological systems. Aged MNMs may no longer have the same characteristics of their pristine counterparts (Mitrano et al., 2014). Ageing related transformations are likely to be influenced by the duration of ageing as well as environmental factors such as temperature, MNM concentration and media properties.

1.2 Aims and Objectives of Research

The overall objective of this PhD work is to carry out a detailed study of MNM transformations in an environmental or biological context. More specifically, the research aims to investigate and quantify where possible, the chemical and structural alterations and transformations which may occur to different MNMs (including a purpose-made library containing MNMs showing systematic property changes) in different conditions. In order to achieve this overall objective a number of specific aims discussed below need to be firstly achieved. The results obtained by achieving these aims are extremely valuable for the developing field as well as future use or modification of the studied nanomaterials.

1.2.1 Aim 1

To synthesise a new nanomaterial library and characterise its components by means of a multi-method approach.

Firstly nanomaterial synthesis and thorough characterisation of the physical and chemical properties using various techniques were needed to obtain a library of comparable nanomaterials with a range of core chemistries, but the same capping. Polyvinylpyrrolidone (PVP) capped ceria nanomaterials were prepared according to Merrifield et al. (2013). The synthesis protocol was successfully modified to produce a range of PVP capped metal oxide MNMs where the metal oxides were cerium dioxide, copper oxide and zinc oxide. Characterisation was carried out by means of Dynamic Light Scattering (DLS) – size and zeta, Ultraviolet-visible light Spectroscopy (UV-VIS), Transmission Electron Microscopy (TEM), Scanning Transmission Electron Microscopy-Electron Energy Loss Spectroscopy (STEM-EELS), Fourier Transform-Infra-red (FT-IR), Inductively Coupled Plasma-Optical Emission Spectroscopy (ICP-OES), X-ray Photoelectron Spectroscopy (XPS), Energy Dispersive X-ray Spectroscopy (EDX) and Extended X-ray Absorption Fine Spectroscopy (EXAFS) so as to confirm the success of the synthesis and its modification. This library allows focussing on just one property (core metal composition) to be tested for its toxicological significance whilst other variables (size, capping...) are kept unchanged.

1.2.2 Aim 2

To study any chemical or physical alterations to nanomaterials, particularly the developed PVP capped nanomaterial library, resulting from temperature ageing studies.

Part of this work aims to study the thermal transformations of MNMs, where temperature serves as a proxy for ageing over time. Research into ageing techniques in this case temperature ageing in particular had to be carried out. The temperature ageing study performed needed to be developed and decided upon. Time and temperature dependent studies were carried out on a fully characterised library of laboratory synthesised comparable PVP capped metal oxide nanomaterials, where the metal oxides were cerium dioxide, copper oxide and zinc oxide, and commercially available uncoated cerium dioxide. The work aimed to study the physical and chemical changes occurring to the MNMs on exposure to various temperatures (25, 45, 65 and 80 °C) for a period of 4 weeks. Size, zeta potential, agglomeration/aggregation and valency state of the NMs were studied through DLS, zeta potential, UV-VIS, TEM and XPS, as a function of time.

1.2.3 Aim 3

To study any chemical or physical alterations to ceria and ceria containing nanomaterials, resulting from phosphate induced ageing studies.

This part of the work aimed to study phosphate induced biotransformations of different ceria nanomaterials (including those belonging to the MNM library). This is

environmentally relevant due to the extensive natural presence of phosphorus and its compounds (EPA, 2012). Initially research into phosphate ageing had to be carried out. The ageing study performed needed to be developed and decided upon. Time dependent studies were carried out on some of the fully characterised ceria MNMs from the library, commercially available uncoated cerium dioxide and commercially available zirconium doped ceria MNMs. All the MNMs were exposed to a pH adjusted potassium phosphate solution for a period of 3 weeks. The commercially available uncoated cerium dioxide MNMs were also exposed to a pH adjusted phospholipid solution for 96 hours. Physical and chemical properties were studied by means of a multi-method approach using XRD, DLS – size and zeta, UV-VIS and TEM.

1.4 Layout of Thesis

This thesis opens with an introduction to the research area and a detailed description of the aims and objectives of this project. The literature review is presented in Chapter 2 giving an introduction to nanotechnology and allowing for a better understanding of the concept and of nanomaterials. Particular reference is given to nanomaterials; their chemistry, fate, behaviour and risks. Importance is given to ageing and the changes nanomaterials undergo as a function of time. Literature relevant to ceria, zinc oxide and copper oxide will be considered as they are the MNMs synthesised and utilised in the work.

The methodology is then presented in Chapter 3. Details on the characterisation techniques and the methodology regarding these techniques is put across in this chapter.

The following three chapters explain the experimentation and discuss the results obtained. Chapter 4 deals with the PVP capped nanomaterial library synthesis and characterisation. Chapter 5 and 6 deal with the temperature ageing and phosphate ageing studies respectively. Furthermore each of these chapters offers conclusions on these results.

The thesis closes with Chapter 7 summarising the conclusions made and Chapter 8 offering recommendations for future work that could follow on from this work.

Chapter 2: Literature Review

2.1 Introduction

This chapter compiles a review on the literature relevant to the research idea of this thesis (Section 1.1). The chapter begins with an introduction to nanomaterials, their classification and uses. This leads to an overview on release, exposure and possible transformations of nanomaterials. An attempt is made to shed light on the concept of ageing of nanomaterials and highlight the limited number of studies that have taken place. Particular interest is given to ceria, zinc oxide and copper oxide as these are the nanomaterial synthesised and used for the research.

2.2 Nanomaterial Definitions

According to the British Standards Institution Vocabulary (BSI, 2011) a nanomaterial is a “material with any external dimension in the nanoscale or having internal structure or surface structure in the nanoscale”. This, however is a very generic definition and there have been numerous debates regarding nanotechnology nomenclature (Auffan et al., 2009). On 18 October 2011, the European Commission adopted the following definition of a nanomaterial:

“A natural, incidental or manufactured material containing particles, in an unbound state or as an aggregate or as an agglomerate and where, for 50 % or more of the particles in the number size distribution, one or more external dimensions is in the size range 1 nm – 100 nm.

In specific cases and where warranted by concerns for the environment, health, safety or competitiveness the number size distribution threshold of 50 % may be replaced by a threshold between 1 and 50 %.

By derogation from point 2, fullerenes, graphene flakes and single wall carbon nanotubes with one or more external dimensions below 1 nm should be considered as nanomaterials.”

(European commission, 2011).

A generally accepted and simpler definition for nanomaterials describes them as substances having at least one dimension between 1 and 100 nm in size (JRC, 2010). A nanometre (nm) is one thousand millionth of a meter, 10^{-9} m. To illustrate this, the size of a tennis ball is 1,000,000,000 nm wide and viruses are around 100 nm in diameter (Figure 2.1).

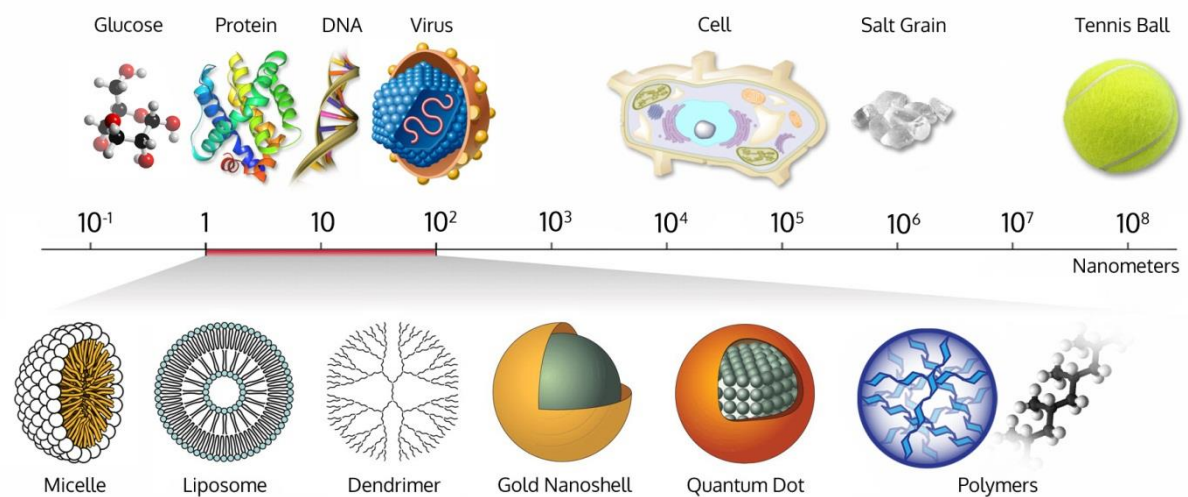


Figure 2.1 Nanometer scale comparing objects found in nature (Which Lab, 2015).

A nano-object has been defined as “a material with one, two or three external dimensions in the nanoscale” (ISO, 2008). One such example is a nanoparticle which is a “nano-object with all three external dimensions in the nanoscale” (ISO, 2008).

Materials with nano-scale (10^{-9} or one billionth of a meter) features have high surface-to-volume ratio and distinctive chemical, electronic, optical, magnetic & mechanical properties compared to those of the bulk material (Mansoori and Soelaiman, 2005, European commission, 2013, Tejamaya et al., 2012). This was first noted by Richard Feynman who stated that ‘Atoms on a small scale behave like *nothing* on a large scale’ (Feynman, 1959).

2.3 Nanomaterial classification

Nanomaterials can be grouped using a number of different classification methods. These methods which are discussed in further detail below are (Alagarsi, 2011):

- Structural – Dimensionality and Morphology
- Chemistry
- Origin

2.3.1 Structural

2.3.1.1 Dimensionality

According to Siegel (1994), nanomaterials can be classified into 4 groups based on their dimensionality as seen in Figure 2.2.

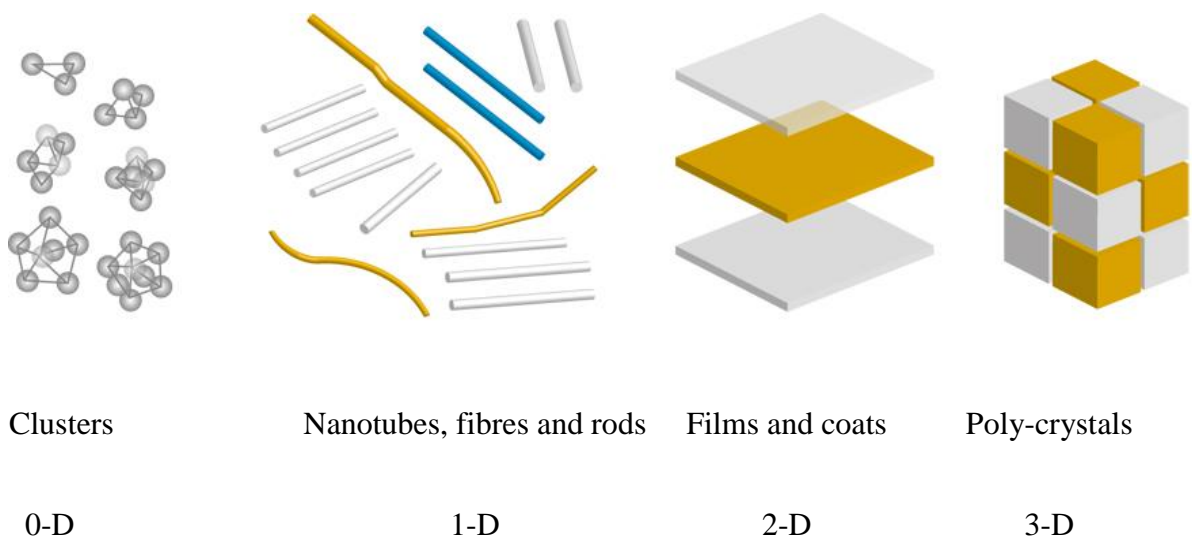


Figure 2.2 Classification of nanomaterials according to dimensionality based on the concept of Siegel (Gusev, 2011).

Zero dimensional (0-D) nanomaterials have all their dimensions (x,y,z) in the nanoscale and include spheres, clusters and quantum dots. One example is a gold

nanoparticle cluster. One dimensional (1-D) materials have two dimensions (x,y) in the nanometer scale and comprise of nanotubes such as carbon nanotubes, nanorods, wires and fibres. Two dimensional (2-D) nanomaterials have one dimension in the nanoscale and include surface coatings, thin films, plates and networks. Examples include graphene sheets and sol-gel layers. Finally three dimensional (3-D) nanomaterials are considered as the bulk material (R.W. Siegel, 1994, Gusev, 2011). An example is graphite. Figure 2.3 shows the relationships between 0-D, 1-D and 2-D nanomaterials in 3D space.

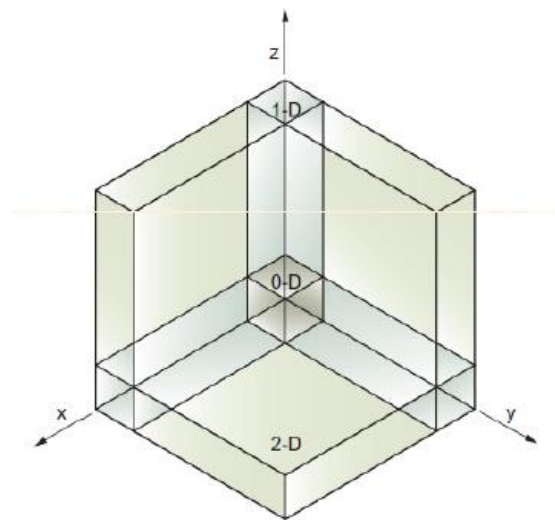


Figure 2.3 The relationships between 0-D, 1-D and 2-D nanomaterials in 3D space (MTX9100, 06/05/2014, Hussainova, 06/05/2014).

2.3.1.2 Morphology

Extending further into nanomaterial structure, nanomaterials may be classified according to their form and morphology. Characteristics of this classification include flatness, sphericity and aspect ratio. The latter can be sub-divided into high and low aspect ratio as seen in Figure 2.4 (Buzea et al., 2007).

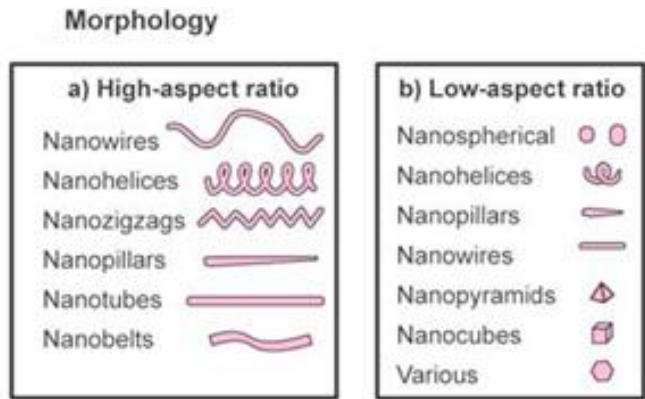


Figure 2.4 Classification according to morphology (Buzea et al., 2007).

2.3.2 Chemistry

Nanomaterials can also be classified based on their chemistry. Figure 2.5 shows that many may either be composed of a single material such as gold nanoparticles or a composite consisting of two or more materials as in the case of polymer capped/coated nanoparticles e.g. polyvinylpyrrolidone capped cerium dioxide (Buzea et al., 2007).

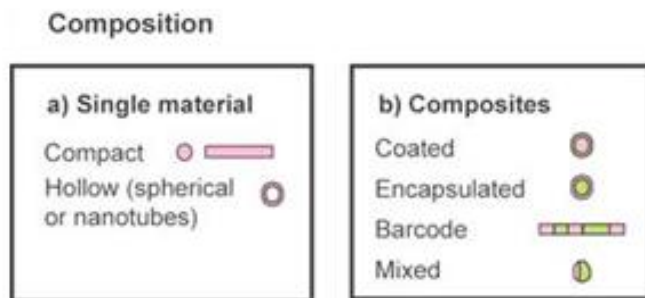


Figure 2.5 Additional nanomaterial classification composition (Buzea et al., 2007).

In the case of nanoparticles this can result in several categories, which include the following (Ray et al., 2009):

1. Metals, such as gold and silver nanoparticles
2. Metal oxides, such as cerium dioxide, titanium dioxide and zinc oxide
3. Carbon nanomaterials such as fullerenes, nanotubes and graphene
4. Quantum dots such as cadmium telluride and cadmium selenide
5. Organic such as polymeric nanoparticles like Poly(organophosphazene)
6. Core-shell, such as Platinum-Palladium and Rhodium-Palladium nanoparticles

Based on the chemistry, nanoparticles can exist as uniformly dispersed in a medium or in an agglomerated or aggregated state (Figure 2.6) (Buzea et al., 2007).

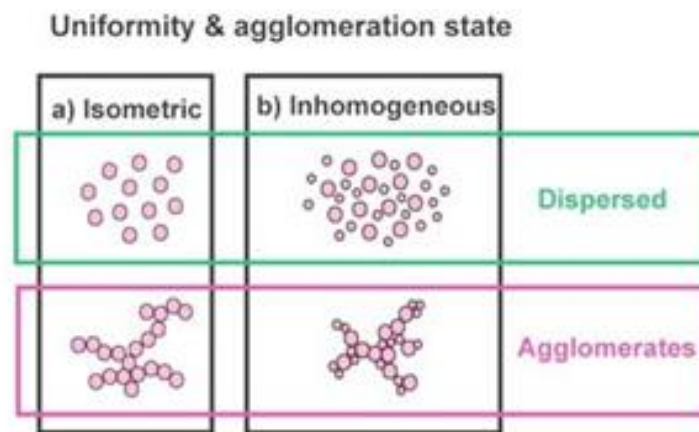


Figure 2.6 Uniformity and Agglomerated state of nanoparticles (Buzea et al., 2007).

Other classifications have also been put forward. For instance, Tomalia (2009) speaks about classifying nanomaterials, nanoparticles in particular, with respect to their

“softness” and/or “hardness”. In this case inorganic nanoparticles are referred to as hard and organic ones are referred to as soft.

2.3.3 Origin

Nano-objects may be one of three kinds: natural, incidental and intentionally produced (manufactured or engineered) (Farré et al., 2011, Oberdorster et al., 2005, Cole, 2011); all three types are defined below.

2.3.3.1 Natural Nano-objects

Natural nano-objects include those from naturally occurring environmental processes. Natural nano-objects can be found in waters, soils and sediments. They can result from natural occurrences such as biogeochemical processes, ash from volcanoes, sea salt and particles from weathering and erosion (Lowry et al., 2012, Cole, 2011, Oberdorster et al., 2005).

2.3.3.2 Incidental Nano-objects

Anthropogenic nanomaterials produced unintentionally are referred to as incidental nanomaterials. They are a result of the action of man and examples include incineration, combustion within chimneys and combustion engines (Lowry et al., 2012, Cole, 2011, Farré et al., 2011).

2.3.3.3 Intentionally produced Nano-objects

Intentionally produced nano-objects, are, in the strict sense, nanomaterials which are intentionally man-made in order to obtain specifically required physicochemical properties such as composition, shape, size and surface chemistry to be used for a specific application. These can be engineered or manufactured nanomaterials. According to the International Organization for Standardization (ISO) (2010b), a manufactured nanomaterial is a nanomaterial with specific properties or specific composition produced intentionally for commercial purposes (e.g., transparency) whilst an engineered nanomaterial is a nanomaterial designed so that it displays a special function (e.g., quantum dots). These nanomaterials can either be created by means of a ‘top-down’ or ‘bottom-up’ approach (Domènech et al., 2012). Intentionally produced nanomaterials are used in cosmetics, sunblock, semiconductors, polymers and drug delivery systems (Lowry et al., 2012, Cole, 2011, Oberdorster et al., 2005).

2.3.3.3.1 Engineered or Manufactured nanomaterial synthesis routes

As mentioned, engineered or manufactured nanomaterials can be made either by a top-down manufacturing method or a bottom-up synthesis method. These are depicted in Figure 2.7.

The top-down approach involves starting with a larger macroscopic sample and generating smaller pieces, by a breakdown of the original object. This can be achieved by using one of various techniques (Domènech et al., 2012), for example electroexplosion,

laser ablation, spluttering, milling, grinding or photolithography. The top-down approach delivers nanoscale object by the physical separation of an existing material structure. This technique is ideal for making surface imprints that need to be replicated (Balzani, 2008, Romer Roche, 2013). There are a number of disadvantages linked with this MNMs formation practice. These include the fact that bulky instrumentation is normally needed, single NP production is difficult due to surface structure imperfections, there is a high contamination probability, the NPs obtained are most likely to be polydisperse and it is difficult to prepare very small uniform particles (Balzani, 2008, Romer Roche, 2013).

The bottom-up approach involves building up of nanomaterials by combining atoms (Balzani, 2008). This method principally involves chemical processes to form the MNMs. Commonly used techniques include crystallisation/precipitation, sol-gel synthesis, chemical vapour deposition, gas-phase aggregation and self-assembly routes, such as wet chemistry synthesis (Hannink, 2006). An example of a wet chemistry synthesis is a reflux reaction. This involves heating a reaction mixture to the boiling point temperature of the reaction solvent. As the solution evaporates and starts to travel up the condenser, it is condensed back into the reaction flask. This method is one of the best synthesis methods as it involves a simple set up that ensures a constant reaction temperature is maintained and the solvent does not dry out (Chua, 2016).

The bottom-up approach has a number of advantages over the top-down approach. Firstly, it has the ability to form uniform particles of different shapes and structures (Balzani, 2008). The bottom-up approach is also a cleaner method and the NPs obtained are more homogeneous having fewer defects and being more monodisperse (Romer Roche, 2013).

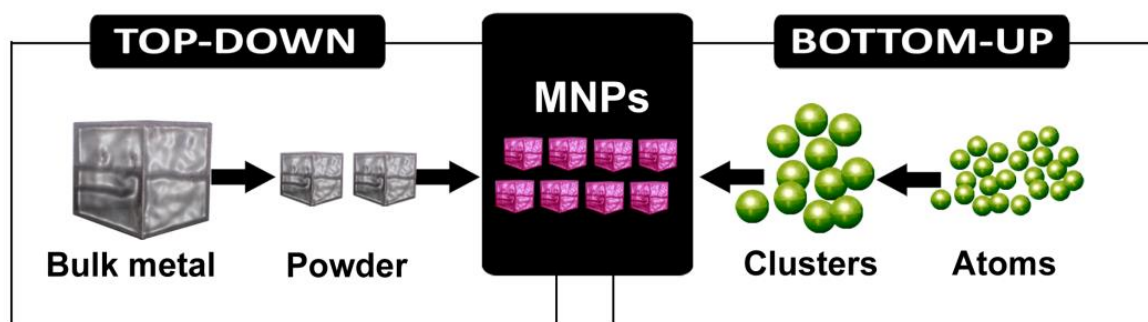


Figure 2.7 MNPs formation comparing the top-down and bottom-up approaches (Buzea et al., 2007).

2.4 Nanomaterial Applications

The nanotechnology field has drastically changed everyday life with its limitless uses as a result of the nanomaterials' distinctive properties (Tejamaya et al., 2012, Römer et al., 2013). The broad range of synthesis methods available result in nanomaterials with diverse physical and chemical properties (De Marzi et al., 2013). These materials are already extensively used in many commonplace fields such as those of the optical, energy and fuel, electronic, structural, automotive, clothing, food additives, beverage products, cosmetic, conservational, paints and pigments, medical and health care varieties (Aydın et al., 2012, Tejamaya et al., 2012, Thwala et al., 2013, Mitrano et al., 2014). Nanotechnology continues to grow rapidly due to the potential for the development of new products and applications with the advantages of increased economic feasibility for production, better functionality of nanomaterials and less environmental pollution (Mitrano et al., 2014). Between 2010 and 2013 a 24 % increase in the presence of consumer products containing nanomaterials had been recorded amounting to a total of 1,628 documented consumer products containing nanomaterials (Nanotechnologies, 2013). As of November 2015 there were more than 1,800 products listed in the Consumer

Products Inventory (The Project on Emerging Nanotechnologies, 2015). One estimate for the production of engineered nanomaterials was 2000 tonnes in 2004 and increasing to 58,000 tonnes by 2011-2020 (Nowack and Bucheli, 2007).

2.4.1 Nanomaterials in consumer electronics, semiconductors, batteries and magnets

A large number of nanomaterials are encountered in this field of applications. There is a long list of possible materials that can be used to improve this area, including ZnO, ZnS, Ag, TiO₂, SiO₂, CeO₂, Co, CdS and CdSe quantum dots and CNTs (Mitrano et al., 2014, Hong et al., 2009, El Naggar et al., 2015, Bruce et al., 2008).

2.4.2 Nanomaterials in Food industry

In the food industry nanomaterials may be used both in the food produced as well as for containers and packaging. With regards to the food production, nanomaterials may be used as additives and/or supplements, increasing the range of food textures, colours and tastes and in crop pesticides. Some examples of nanostructures used in this industry, which may have either been natural or manufactured, include proteins, lipids, silica and titania nanoparticles and nanostructured emulsions. The use of nanomaterials in food containers and packaging has several advantages. They can extend food life and improve food safety as well as enhance the packaging polymer properties (Mitrano et al., 2014, Cushen et al., 2012).

2.4.3 Nanomaterials in textiles

In the textile industry nanomaterials help to enhance and improve the performance and functionality, develop smart materials with novel functions, satisfy the need for hygienic clothing and allow for innovative textile processes (Ibrahim, 2015, Harifi and Montazer, 2012). Self-cleaning, water and/or dirt repellence, antimicrobial, conductive and antistatic (wrinkle-resistant), solvent-, UV-, and abrasion resistant, decreased flammability or increase the strength of dyes or colourants are some examples of such functionalities (Mitrano et al., 2014, Ibrahim, 2015). Examples of improved textile properties are enhanced self-cleaning, antibacterial and UV protection properties of nano titanium dioxide treated textiles (Montazer and Seifollahzadeh, 2011). Another commonly used nanomaterial for textiles is silver due to its antibacterial effect (Lee et al., 2003, Sotiriou and Pratsinis, 2010, Benn and Westerhoff, 2008)

2.4.4 Nanomaterials in cosmetics

Both metal and carbon based MNMs are used in the cosmetic and sunscreen industries because of their enhancement of properties such as colour, transparency and solubility (Raj et al., 2012). TiO₂ and ZnO are used specifically for their UV filtration and absorption properties. The nano version of these materials reduces the chalky appearance of traditional formulations obtained using micro sized particles (Mitrano et al., 2014). A new EU Regulation 1223/2009 (Cosmetics Regulation) has been in force since 11 July 2013. One significant change in this regulation is that the nanomaterials present in cosmetics must be labelled in the list of ingredients with the word “nano” in brackets

following the name of the substance, e.g. “titanium dioxide (nano)” (European commission, 2015).

2.4.5 Nanomaterials in paints and coatings

Nanomaterials are added to paints and coatings to obtain specific desirable properties including protection against deterioration, better surface appearance, good chemical resistance, decreased permeability, optical clarity, increased thermal stability, easy to clean surface and anti-reflective properties. Photoactive nanomaterials are sometimes added in the hope of keeping the paints and coatings clean.

A range of coatings involving the use of manufactured nanomaterials are being developed for various purposes. Some of these are fabric coatings for water and stain resistance, antimicrobial coatings for infection prevention, preservation coatings, conductive coatings for solar cells, scratch resistant coatings in the field of optics and anti-fouling coatings for marine applications (Mitrano et al., 2014).

2.4.6 Nanomaterials used in medicine

The European Science Foundation (ESF) defined nanomedicine as “the science and technology of diagnosing, treating, and preventing disease and traumatic injury, relieving pain, and preserving human health using molecular tools and molecular knowledge of the human body” (Foundation, E. E. S. 2004. Nanomedicine, An ESF–European Medical Research Councils (EMRC) forward look report. Strasbourg Cedex, France: ESF). Techniques in nanomedicine make it possible to deliver therapeutic agents into targeted

specific cells, cellular compartments, tissues, and organs by using nanoparticulate carriers (Zhao and Castranova, 2011). Examples of some applications of nanomaterials in medicine include fluorescent biological labelling (Wang et al., 2002, Chan and Nie, 1998, Bruchez et al., 1998), drug delivery (Malam et al., 2009, Faraji and Wipf, 2009, Yang et al., 2015, Goenka et al., 2014) and tissue engineering (Goenka et al., 2014, Zhang and Webster, 2009, Harrison and Atala, 2007).

2.5 Examples of nanomaterials and their properties

This section discusses examples of nanomaterials. Information about four different commonly used engineered nanomaterials, namely ceria, zirconium doped ceria, zinc oxide and copper oxide is given. The chemistry and properties of the metal and metal oxide, synthesis and uses of the metal oxide of each nanomaterial will be discussed below.

2.5.1 Cerium

Cerium was first discovered by Wilhelm Hisinger and Jöns Jacob Berzelius in 1803 in its oxide form and simultaneously isolated by Martin Klaproth (Royal Society of Chemistry, 2015a). Carl Gustav Mosander followed to successfully isolate this element in 1839 (Cole, 2011).

Cerium is used in the form of mischmetal for metallurgical purposes (Prospect, 2010). Mischmetal reacts with impurities in reducing the effect of these impurities on the properties of the metal.

The element cerium, having an atomic number of 58 forms part of the lanthanide series and is the most abundant rare earth element (US EPA, 2009, Prospect, 2010, Royal Society of Chemistry, 2015a). It is a very reactive iron-grey, ductile, malleable metal (Prospect, 2010, US EPA, 2009, Royal Society of Chemistry, 2015a) having a melting point of 798 °C, a boiling point of 3,443 °C and a density of 6.770 gcm⁻¹ (Prospect, 2010, US EPA, 2009, Royal Society of Chemistry, 2015a). Cerium is a strong oxidising agent that is stabilised by means of an oxygen ligand. When present in compounds, cerium can exist as cerous, that is in its trivalent state (Ce³⁺) or as ceric, that is in its tetravalent state (Ce⁴⁺) (Prospect, 2010).

In nature, it can be found along with other lanthanides however due to its tetravalent valency state stability it can be separated out from other rare-earth elements which can only exist in the trivalent state (US EPA, 2009).

2.5.2 Cerium Dioxide

Cerium dioxide, also referred to as cerium oxide or ceria, has the molecular formula CeO₂. Exposure to commercially used cerium compounds is most likely through exposure through cerium dioxide (US EPA, 2009).

2.5.2.1 Properties of Ceria

Table 2.1 shows some of the properties of ceria (Prospect, 2010).

Table 2.1 Properties of ceria

Property	Details
Molecular weight	172.11
Molecular Formula	CeO ₂
Form	Pale-yellow, heavy powder. White when pure.
Melting point	2400 °C
Density	7.65 g/cm ³
Water solubility	Insoluble
Other solubility	Insoluble in dilute acid

2.5.2.2 Fundamental properties of ceria

The ability for ceria to have such extensive uses is due to its properties (Chen and Chang, 2005). These properties include its semi-conductivity, high thermodynamic affinity for oxygen and sulphur and radical scavenging due to its cubic fluorite structure (Baer et al., 2013, Lin et al., 2006, Di Monte et al., 1998, Logothetidis et al., 2003, Campbell and Peden, 2005, Bamwenda and Arakawa, 2000, Kuchibhatla et al., 2012, Morris et al., 2013). Additionally ceria also has UV-blocking properties due to absorption below 400 nm caused by charge-transfer bands (Masui et al., 1997).

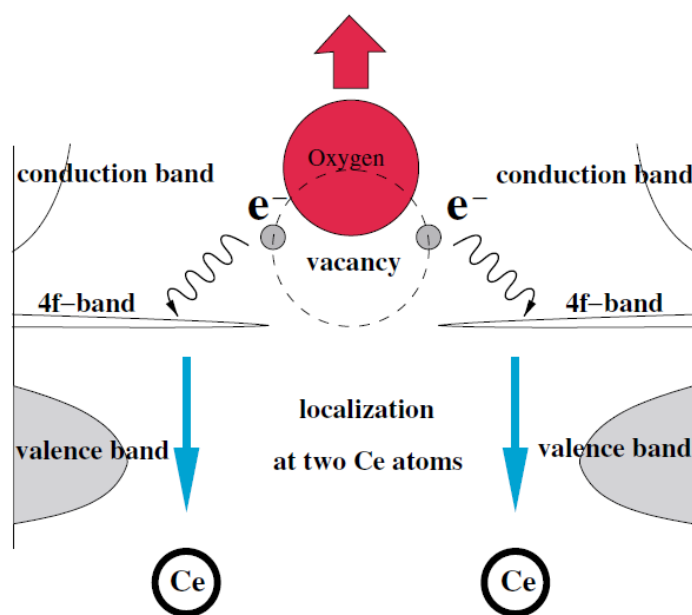


Figure 2.8 Graphical illustration of the ceria oxygen vacancy formation. An oxygen atom moves away from its lattice position leaving behind two electrons which localise on two cerium atoms, turning Ce (4+) into Ce (3+) (Skorodumova et al., 2002).

Most important is its redox ability to cycle between Ce^{3+} and Ce^{4+} (that has a characteristic yellow colour) (Paulenova et al., 2002, Kuchibhatla et al., 2011, Merrifield et al., 2013, Skorodumova et al., 2002). In ceria oxygen vacancy formation occurs by means of an oxygen atom moving away from its lattice position and hence leaving behind two electrons as seen in Figure 2.8. These two electrons localise on the 4f orbital of two neighbouring cerium atoms resulting in the change from Ce (4+) to Ce (3+) (Skorodumova et al., 2002). In an oxygen rich environment this process is reversed.

2.5.2.3 Synthesis methods of Ceria

There are various synthesis methods to produce ceria (Morris et al., 2013, Chen and Chang, 2005, Fu et al., 2003). Some of these are: sol-gel techniques, forced hydrolysis, sonochemical, pyrolysis (Mädler et al., 2002), microemulsion (Masui et al., 1997), precipitation (Morris et al., 2013, Chen and Chang, 2005), thermal hydrolysis (Hirano and Inagaki, 2000), hydrothermal and electrothermal.

2.5.2.4 Ceria Uses

Ceria was first commercially used in 1999 as catalytic agents in diesel particulate filters (De Marzi et al., 2013). Since then its use has increased and become more diverse. Nowadays it can be found in optical equipment, micro-electronics, solid oxide fuel cells, solar cells, catalysis applications, bio-medical applications, oxidation resistance, UV absorbents and filters, anti-reflective coatings, abrasives for chemical mechanical planarizations and metallurgical and glass/ceramic applications (Baer et al., 2012, Djuričić and Pickering, 1999, Lin et al., 2006, Matijević and Hsu, 1987, Logothetidis et al., 2003, Yin et al., 2002, Kuchibhatla et al., 2011, Chen and Chang, 2005, Bamwenda and Arakawa, 2000, Morris et al., 2013).

CeO₂ MNMs are used as a diesel additive directly into fuel to catalytically promote soot oxidation and degradation since the particle remains intact but Ce³⁺ on the surface is oxidised to Ce⁴⁺. Because most of the CeO₂ is likely to be captured by diesel filters or the catalytic converter (Ulrich and Wichser, 2003), its pathway to the landfill and/or to recycling is considered very important (Park et al., 2008). Little is known about how

MNM materials flow through recycling plants and so determining whether CeO₂ will make it back into the environment via this route is important. Likewise little is known of the fate and reactivity of nano CeO₂ once released into the atmosphere. CeO₂ NP can form secondary organic aerosols by the adsorption of organic molecules on their surface (Lee and Donahue, 2011). Because of its ability to adsorb oxygen on its surface defects (oxygen vacancies), it was shown to efficiently reduce H₂O₂, a common constituent in the atmosphere (Heckert et al., 2008) to decarboxylate & polymerise small organic molecules (Cervini-Silva et al., 2005), thus altering a number of other atmospheric species.

2.5.3 Zirconium doped Ceria

Nanomaterial doping is the deliberate introduction of one atom into the structure (or lattice) of another in order to manipulate the properties of the main structure to obtain specific properties. Doping nanomaterials provides a flexible way to tune to the properties of the materials while maintaining their high surface areas (Chen et al., 2005). Some examples of doping synthesis techniques include precipitation (Chen and Chang, 2012) and wet chemical synthesis (Meyssamy et al., 1999).

The CeO₂-ZrO₂ system is one of the most studied mixed-metal oxides in the literature due to its important role in the operation of automotive catalysts (Lukehart and Scott, 2013). The incorporation of zirconium into the cerium dioxide lattice has been shown to strongly affect the redox properties of ceria by increasing its oxygen storage (Ozawa et al., 1993, Fornasiero et al., 1995).

2.5.3.1 Synthesis methods of Zirconium doped Ceria

Examples of synthesis methods used to obtain zirconium doped ceria include precipitation (Chen and Chang, 2012), hydrothermal (Chen et al., 2009, Weng et al., 2009), gel route (Fornasiero et al., 1995) and inorganic sol-gel technique (Hartridge and Bhattacharya, 2002, Fornasiero et al., 1995, Liang et al., 2008).

2.5.3.2 Zirconium doped Ceria Uses

The main use of zirconium doped ceria is in catalytic science (Aneggi et al., 2006) with the aim of obtaining optimised catalytic properties for ceria (Zhang et al., 2006a). Zirconium doped ceria has been thoroughly investigated for the three-way catalyst (TWC) application due to the unique oxygen storage capacity and has gained more attention on the utilisation for diesel soot oxidation (Liang et al., 2008, Pisarello et al., 2002). Zirconium doped ceria particles have also been used as ion conductors (Hartridge and Bhattacharya, 2002) and resistive oxygen sensors (Chen and Chang, 2012).

2.5.6 Zinc

Zinc was discovered by Andreas Marggraf in 1746. Zinc, having atomic number 30, is a transition metal and mostly used to galvanise metals. It has a melting point of 419.527 °C and a boiling point of 907 °C (Royal Society of Chemistry, 2015c).

2.5.7 Zinc Oxide

Zinc oxide has the molecular formula ZnO and is naturally found as zincite, appearing red/orange due to manganese impurities. A single crystal of ZnO is colourless whilst pure microcrystalline ZnO is white turning yellow on heating and reverting to white on cooling (Association, 2011).

2.5.7.1 Properties of Zinc Oxide

ZnO has a wide band gap of 3.37 eV and large exciton binding energy making it suitable for optoelectronics in the blue/UV region (Anderson and Chris, 2009, Klingshirn, 2007b, Klingshirn, 2007a, Moezzi et al., 2012, Yan et al., 2004). It has piezoelectric and pyroelectric properties (Sunandan and Joydeep, 2009). Its surface conductivity is highly sensitive to different gaseous species adsorbed to the surface (Wöll, 2007, Anderson and Chris, 2009). ZnO also has high thermal conductivity and radiation hardness (Anderson and Chris, 2009). Other basic properties can be seen in Table 2.2 (Association, 2011).

Table 2.2 Properties of zinc oxide

Property	Details
Molecular mass	81.37 amu
Density	5.606 gcm ⁻³
Stable phase at 300 K	Wurtzite
Melting point	1975 °C
Sublimation temperature	1200 °C
Thermal conductivity	0.6, 1-1.2 Wcm ⁻¹⁰ C ⁻¹
Band gap (RT)	3.370 eV
Refractive index	2.008

2.5.7.2 Crystal structure

ZnO can have three structures namely hexagonal wurtzite, cubic zinc-blende structure and a rarely-observed cubic rock-salt structure as seen in Figure 2.9 (Özgür et al., 2005, Klingshirn, 2007a, Desgreniers, 1998). However, under ambient conditions crystalline ZnO has a wurtzite crystal structure.

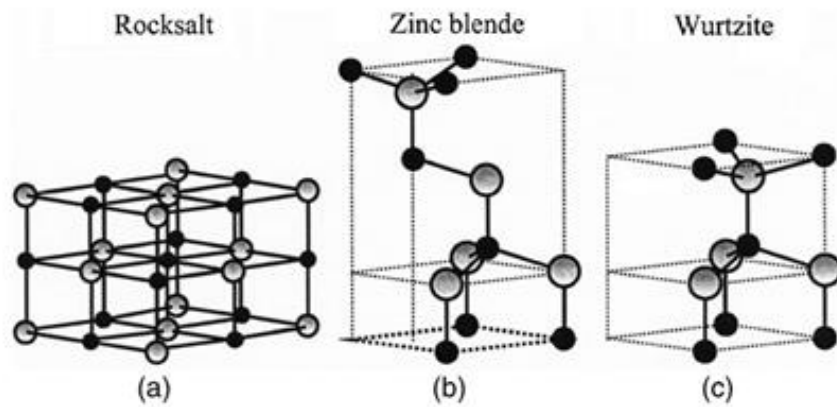


Figure 2.9 Stick and Ball representation of ZnO crystal structures (a) rarely-observed rock-salt structure, (b) zinc blende and (c) wurzite, where the grey balls denote Zn^{2+} ions whilst black balls represent O^{2-} ions (Özgür et al., 2005).

2.5.7.3 Zinc oxide synthesis

ZnO synthesis methods include the sol-gel method, the evaporation of solutions and suspensions, evaporative decomposition of solutions, conventional ceramic fabrication, and wet chemical synthesis (Guo et al., 2000). Other methods are those of microemulsion synthesis, mechanochemical processing, spray pyrolysis and drying, thermal decomposition of organic precursor, RF plasma synthesis, supercritical-water processing, self-assembling, hydrothermal processing, vapour transport process, sonochemical or microwave-assisted synthesis, direct precipitation and homogeneous precipitation (Kumar et al., 2013, Arora et al.).

2.5.7.4 Zinc oxide uses

The use of ZnO is first recorded in 2000 B.C. where it was used in medicinal skin cream (Frederickson et al., 2005). Throughout the years ZnO has been employed in other sectors although today its use in some of these has been replaced. One such example is paints. Nowadays 1.2 million tonnes of ZnO are produced annually with the main application being the rubber industry (Moezzi et al., 2012, Klingshirn, 2007a). Figure 2.10 shows the application of ZnO in different sectors. These include the rubber, ceramic, chemical, paint, agricultural, electronic and pharmaceutical industries.

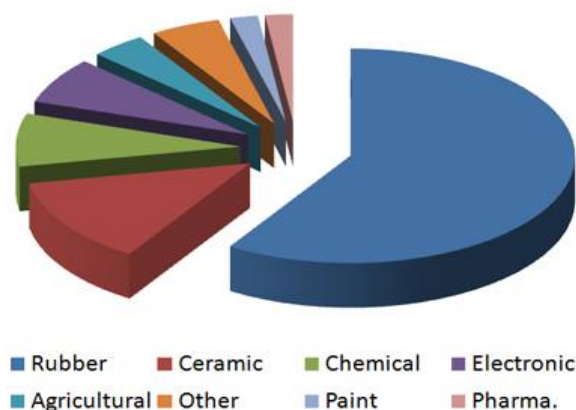


Figure 2.10 The application of ZnO in the different sectors (Association, 2011)

ZnO is used for preparing solar cell, gas sensors, chemical absorbent varistors, electrical and optical devices, electrostatic dissipative coating, catalysts for liquid phase hydrogenation, and catalysts for photo-catalytic degradation instead of titania nanoparticles (Hong et al., 2009). It is also an approved sunscreen ingredient in many countries around the world due to its sun protection properties. This is because it has been found that sunscreens containing physical blockers of UV light (such as zinc oxide

particles) are highly effective in protecting cells against UV-induced DNA damage (Cayrol et al., 1999). Pinnell et al. (2000) have shown that zinc oxide absorbs UV-radiation more effectively than titanium dioxide (TiO₂) over a broad range, particularly in the UVA region. This has resulted in zinc oxide sometimes being the sole active ingredient in some broad-spectrum sunscreens.

2.5.8 Copper

Copper, which is a reddish-gold metal, was discovered in prehistoric times. Copper has an atomic number of 29, a melting point of 1084.62 °C and a boiling point of 2560 °C. Copper metal does occur naturally but by far the greatest source is in minerals such as chalcopyrite and bornite. Copper is obtained from these ores and minerals by smelting, leaching and electrolysis. Its most common use is in electrical equipment including wiring and motors (Royal Society of Chemistry, 2015b).

2.5.8.1 Copper Oxide

Copper can form two oxides, copper (I) oxide and copper (II) oxide. Copper (I) oxide occurs in nature as the red or reddish brown mineral cuprite with a cubic or octahedral crystal morphology. Depending on the method of preparation and particle size, the synthetic material is yellow, orange, red, or purple. It has a melting point 1235 °C and decomposes above 1800 °C (Richardson, 2000).

Copper (II) oxide occurs in nature as the black minerals tenorite (triclinic crystals) and paramelaconite (tetrahedral, cubic crystals). It has a melting point 1330 °C and

decomposes above 1030 °C. Copper(II) oxide is used as a precursor to a number of copper(II) salts (Richardson, 2000).

2.5.8.2 Copper Oxide synthesis

This is achieved through various preparation methods including sonochemical, alcohothermal synthesis, direct thermal decomposition, electrochemical methods, colloid-thermal synthesis process and microwave radiation (Suleiman et al., 2013).

2.5.8.3 Copper oxide uses

Copper oxide nanomaterials are being used in catalysts, electronics and technology (semiconductors, electronic chips, heat transfer nanofluids, superconductors and electrode materials) (Mudunkotuwa et al., 2012, Bondarenko et al., 2013), gas sensors, solar cells and lithium batteries (Bondarenko et al., 2013). Other applications include wood preservation (Heinlaan et al., 2008). Copper oxide has also been used to fight the undesirable growth of bacteria, fungi and algae hence its use in face masks, wound dressings and socks to give these products biocidal properties (Bondarenko et al., 2013). Figure 2.11 shows the annual production volumes of copper oxide nanomaterials (Bondarenko et al., 2013).

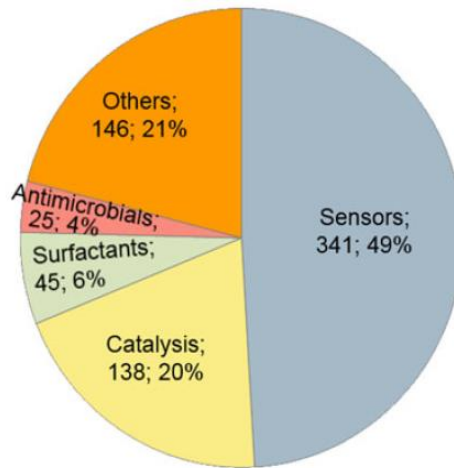


Figure 2.11 The annual production volumes of copper oxide nanomaterials (data are adapted from Piccinno et al. (2012)). The numbers next to each application category indicate the number of articles retrieved in 2013 from Thomson Reuters ISI Web of Science and their respective percentage share (Bondarenko et al., 2013).

2.6 Nanotechnology concerns

Despite nanotechnology's popularity there are related concerns due to the fact that the properties of nanomaterials may differ from those of the bulk material and this may also apply to their toxicity. In addition, their small size may enable them to interact with the cellular machinery in ways that are different to bulk materials and may be hazardous. One concern is the lack of legislative measures to ensure that nanomaterials are fully assessed for their safety and that manufacturers label their products as having nano-components.

The increased production and use of NMs also results in the release of such materials into the environment (Figure 2.12) (Nowack and Bucheli, 2007, Thwala et al., 2013, Tso et al., 2010) both intentionally and unintentionally (Nowack and Bucheli, 2007)

and hence the concerns of exposure of humans and other organisms have been increasing (Kim et al., 2010, Karakoti et al., 2012, Tso et al., 2010).

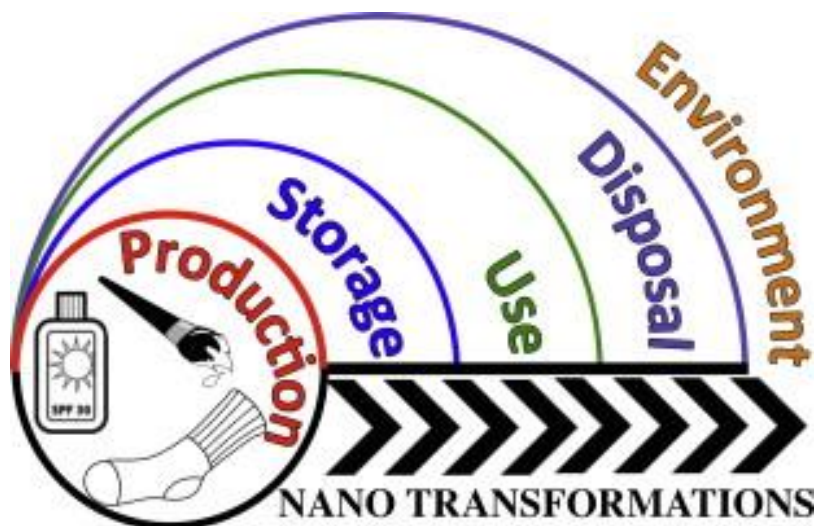


Figure 2.12 Nanomaterial lifecycle resulting with release into the environment (Mitrano et al., 2015).

The impact of nanomaterials on biota is poorly understood (Thwala et al., 2013, Rickerby and Morrison, 2007, Mudunkotuwa et al., 2012), partly due to the lack of data at environmentally realistic conditions (Cumberland and Lead, 2009). The U.S. Environmental Protection Agency have said that “Not enough is known to enable meaningful predictions on the biodegradation of nanomaterials in the environment and much further testing and research are needed” (Environmental Protection Agency, 2007). Furthermore, to date, few studies have tried to establish the changes that nanomaterials undergo when incorporated into, and released from, products.

2.7 Exposure to nanomaterials

The release of nanomaterials which may be from point sources or nonpoint sources. Point sources are locations of localised release, such as production facilities, landfills or treatment plants whilst nonpoint sources are diffuse and widespread release locations, following product use (Nowack and Bucheli, 2007). The release of these materials in turn leads to environmental and human exposure.

2.7.1 Environmental release of nanomaterials

Whether or not nanomaterials are released directly into the water, soil or atmosphere, they ultimately end up in one of these environmental compartments (Gottschalk et al., 2015, Maurer-Jones et al., 2013, Keller et al., 2013) . Environmental release varies on the basis of the prevailing conditions during the release. Some of these include the handling, the form of the MNM, its persistence and the source magnitude (Nowack and Bucheli, 2007). Once present in the environment there are a number of complicated ecological processes that nanomaterials can become involved in where they are affected by environmental factors such as light, oxidants or microorganisms (Larner et al., 2012, Nowack and Bucheli, 2007, Lowry et al., 2012, Louie et al., 2014). Figure 2.13 shows the pathways to exposure and the fate of NMs in the environment (Oberdorster et al., 2005).

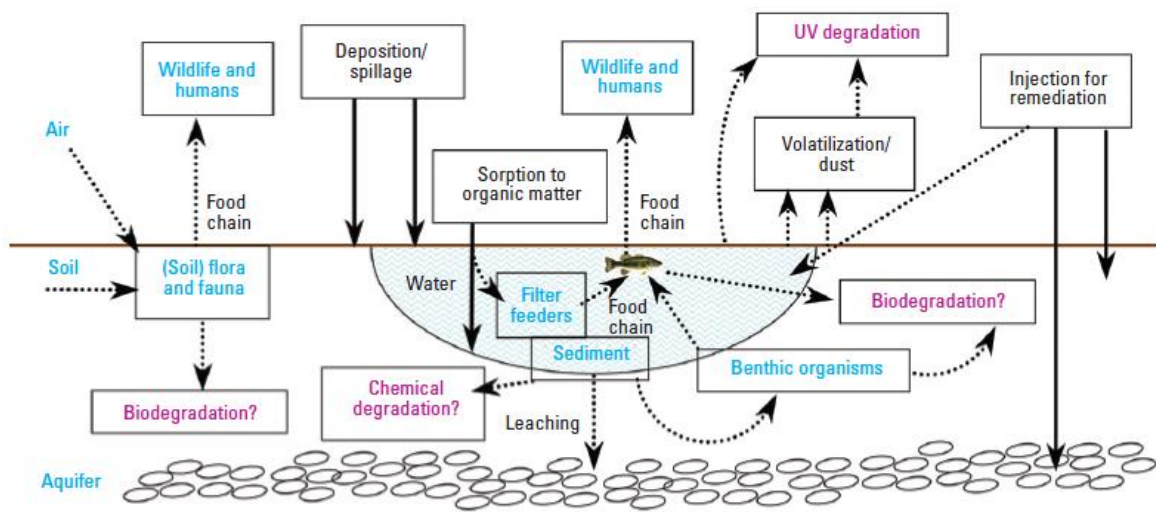


Figure 2.13 Pathways to exposure and fate of NMs in the environment (Oberdorster et al., 2005).

2.7.2 Human exposure to nanomaterials

There are a number of routes through which humans may be exposed to nanoscale objects. For example by inhaling combustion derivatives and other airborne nanoparticles, consuming nanomaterial containing food and drink and being exposed to medically administered nanoparticles (Rickerby and Morrison, 2007, Mitrano et al., 2015). The specific mechanisms via which humans are exposed to nanomaterials are inhalation, ingestion and skin exposure (Oberdörster et al., 2005). Exposure can be through direct contact with nanoscale objects in the air, soil or water or indirectly through consumption of plants or animals which have accumulated NMs (Nowack and Bucheli, 2007, Bergin and Witzmann, 2013). Nanomaterials used in the food sector have the possibility of being ingested and therefore induce exposure to humans (Mitrano et al., 2015, Bergin and Witzmann, 2013, Martirosyan and Schneider, 2014). Several studies have shown that ingested or inhaled NMs can cross biological barriers and migrate to various organs and

tissues where they can potentially cause organ damage (Phenrat et al., 2008, Martirosyan and Schneider, 2014, Feng et al., 2015, Bakand and Hayes, 2016).

2.8 Toxicology

As a result of toxicity concerns, “nanotoxicity”, the study of the toxicity of nanomaterials, has become a major research objective (Aydın et al., 2012). Traditionally toxicology was understood to be the study of the poisoning effects that chemicals have on humans, animals and the environment. Indeed The Society of Toxicology defines toxicology as “the study of the adverse effects of chemical, physical and biological agents on people, animals and the environment” (Anon, 2011). The discipline of toxicology was founded by Paracelsus (1493-1541) who was a German-Swiss physician and alchemist (Online, 2014). He is credited to have popularised the phrase 'the dose makes the poison'.

Typical chemical toxicity testing involves obtaining dose-response relationships between cells or organisms subjected to known doses of chemicals over a period of time. These results then allow for the determination of appropriate dosages for drugs and acceptable limits for exposure to pollutants (Anon, 2011). Similar studies are required for nanomaterials and some nano specific protocols already exist. However, nanotoxicology is more complex, not necessarily linearly related to dosage and dependent on properties not traditionally affecting toxicity. These include size, surface charge, concentration, coating and aggregation (Auffan et al., 2009). Thus, Cho et al. (2011) show that sedimentation of NPs can influence how many NPs are taken up by cells in an in vitro assay; this is not a variable that would have normally been considered in a toxicity assay.

According to Elsaessar et al. (2012) MNMs bring about new toxicology challenges that need to be overcome through further research. NMs have their own toxicity profile that may vary from that of the bulk material, although the precise mechanism of this variability still remains unclear (Thwala et al., 2013). Furthermore, twenty five years of research have confirmed that nanoscale materials can display unexpected and unusual toxicity with toxicological studies on the same nanomaterial and model system often reporting slightly different conclusions (Anon, 2011).

Most toxicology studies have been carried out with mammalian cells and results from such *in vitro* studies cannot be directly translated into potential effects in the environment (Nowack and Bucheli, 2007). The lack of data at environmentally realistic conditions is one of the major limitations in nano-ecotoxicology (Cumberland and Lead, 2009). Another challenge is the potential accumulation of NPs by organisms and the transfer throughout food chains (Auffan, 2013). The effects of environmental abiotic factors are often ignored and hence their toxicity effects are not well understood (Thwala et al., 2013).

Many aspects in the study of nanotoxicity remain poorly studied and challenging due to the difficulties in identifying, characterising and monitoring nanomaterials particularly after their release into the environment. Two important parameters to consider when it comes to toxicology are concentration and time (Auffan et al., 2009). In addition, the environmental effects such as light, oxidants or microorganisms (Nowack and Bucheli, 2007, Valsami-Jones and Lynch, 2015a, Handy et al., 2008) on NMs cannot be predicted from the known ecotoxicity of the bulk forms (Manier et al., 2012). Effective communication of nanotechnology risk can contribute to sustainable development and although nanotechnology risk media coverage has risen in the past years there is still a

need for more coverage and knowledge (Boström and Löfstedt, 2010). Additionally, to date, many studies do not consider realistically relevant doses and therefore there is the need to consider modifying and updating these studies in order to obtain more environmentally applicable results.

2.8.1 Ceria Toxicity

In the case of ceria oxidative stress could play an important role in toxicity. Oxidative stress results in macromolecular damage and is implicated in various disease states such as diabetes, cancer and neurodegeneration (Ray et al., 2012). Oxidative stress is common for metal-based nanoparticles (Aydın et al., 2012). This results in the release of reactive oxygen species (ROS). ROS are chemically reactive species that consist of radical and non-radical oxygen species formed by the partial reduction of oxygen (Ray et al., 2012). ROS could serve as signalling molecules or the cause of oxidative damage to the tissues. The role of ROS depends on the delicate equilibrium between ROS production, and their scavenging (Sharma et al., 2012). According to Knaapen et al. (2004), there are three main factors which cause ROS release. Firstly, active redox cycling on the surface of NPs, particularly the metal-based NPs, secondly, oxidative groups functionalised on NPs and, lastly, particle–cell interactions.

It has been suggested that one of the main factors causing this stress is active redox cycling on the surface of nanoparticles such as in the case of ceria, where cerium can cycle between Ce^{3+} or Ce^{4+} (Aydın et al., 2012) as discussed in Section 2.5.2.2.

To date a number of toxicity studies have been carried out on nano-ceria both *in vivo* and *in vitro*. These include, but are not limited to, the following examples. Van

Hoecke et al. (2009) studied the fate and effects of nano cerium oxide particles in aquatic toxicity tests and concluded that chronic toxicity increases as particle diameter decreases. In addition the toxicity is related to the surface area. Thill et al. (2006) studied the impact of a model water dispersion of 7 nm cerium oxide NPs on Gram-negative bacteria (*Escherichia coli*). The study concluded that in order for cytotoxicity to occur, direct contact had to be made between the cerium oxide NPs and the *E. coli*. Yang et al. (1999) studied the distribution and bioavailability of rare earth elements such as cerium in an aquatic microcosm concluding that most of the elements were adsorbed by the sediment. This could, however, lead to later re-release into the water if conditions change.

Morimoto et al. (2015) performed inhalation and intratracheal instillation studies of cerium dioxide (CeO₂) NPs to investigate the pulmonary toxicity. CeO₂ NPs induced both acute and chronic inflammation. Some studies (Yokel et al., 2013, Gaiser et al., 2012, Rotoli et al., 2012) reported a low toxicity of ceria towards eukaryotic cells, even though no protective effect was observed. Thus, Gaiser et al. (2012) showed that even though ceria NPs smaller than 25 nm or between 1 and 5 µm adhered to cell membrane and entered cells, they did not show any significant cytotoxicity. De Marzi et al. (2013) studied the one-day and ten-day effects of ceria exposure on different cell lines and found that the toxicity assays are greatly dependent on the systems being studied.

Furthermore, the combination of materials, for example the use of nanoceria with other particles such as those in diesel exhaust, may increase their toxicity (Ma et al., 2014a) and render the biosafety of nanoceria more challenging to determine.

2.8.2 Zinc oxide Toxicity

Zinc oxide commonly undergoes dissolution, an important process potentially affecting nanomaterial toxicity. Listed here are some examples (though not an exhaustive list) of a number of toxicity studies, which have been carried out with zinc oxide.

Since ZnO NPs are widely used in sunscreen, human skin exposure is one of the most important exposure routes. Cross et al. (2007) reported minimal dermal adsorption of ZnO NPs from a nanoparticulate zinc oxide sunscreen formulation using Franz-type diffusion cells exposed for 24 hours. Electron microscopy was used to verify the location of NPs in exposed membranes.

A study by Reddy et al. (2007) showed that the toxicity of ZnO is selective to different bacterial cells and human immune cells. This result could lead to biomedical and antibacterial applications.

In a different study Cory et al. (2008) investigated the response of normal human cells to ZnO NPs and compared them to the response of cancerous cells. The results showed ZnO to have a strong preferential ability to kill cancerous cells. This leads to the possibility that ZnO NPs may be used as anticancer agents possibly further enhancing their selectivity by linking tumour targeting ligands (Cory et al., 2008).

ZnO has been studied by Nair et al. (2009) in order to investigate the specific role of size, surface capping and aspect ratio of these particles on toxicity. This study was carried out on prokaryotic and eukaryotic cells. Wet chemical methods were used to synthesise the particles which were used to study cytotoxicity of mammalian cells by using a human osteoblast cancer cell line. Antibacterial activity was tested using Gram-negative bacteria (*Escherichia coli*) as well as Gram-positive bacteria (*Staphylococcus aureus*).

Results showed that, as the particle size decreased, the antibacterial activity increased. The results also suggested selective toxicity of the ZnO to cancer cells. Nair et al. (2009) noted that the toxicity of ZnO NPs is greatly affected by the surface capping agent.

Li et al. (2012a) investigated the toxicity of ZnO NPs to isolated rat liver mitochondria and found that the ZnO NPs resulted in collapse of mitochondrial membrane potential, swelling, depression of respiration, inner membrane permeability to hydrogen and potassium ions, alterations of ultrastructure, release of cytochrome, generation of ROS, and Zn^{2+} liberation from ZnO NPs.

Pasupuleti et al. (2012) studied the toxicity of zinc oxide NPs through the oral route by comparing acute oral toxicological potential of nano-sized zinc oxide (20 nm) with its micro-sized zinc oxide administered to rats in different concentrations. They concluded that nano-size zinc oxide exhibited toxicity at lower doses.

The toxic effect of ZnO NPs to the environment have also been studied and reported. Thus Lin and Xing (2008) measured plant root growth and seed germination following treatment with five types of metal and metal oxide NPs and found nano-Zn in the form of a Zn^{2+} solution and nano-ZnO in suspension form, to inhibit growth.

2.8.3 Copper oxide Toxicity

Copper is an essential element for organisms, required for maintaining homeostasis (Galhardi et al., 2005). Despite this, copper ions may cause toxicity once they exceed the physiological tolerance range *in vivo* (Zietz et al., 2003). This is the reason for the grave concern of public and scientific researchers regarding the possible health effects and toxicology of copper oxide nanomaterials.

Toxicity assessment studies have primarily focused on investigating the effects of different exposure routes, such as via the respiratory or gastrointestinal tracts. The toxicity of spark-generated CuO NPs was evaluated in human bronchial epithelial cells and lung adenocarcinoma cells (A549 cells) using an *in vitro* air–liquid interface exposure system (Jing et al., 2015). It was found that dose-dependent toxicity was consistent between *in vitro* and *in vivo* studies. Additionally, A549 cells were more susceptible to CuO NPs than primary bronchial epithelial cells.

Karlsson et al. (2008) investigated and compared different NPs and nanotubes regarding cytotoxicity and ability to cause DNA damage and oxidative stress. From the particles studied (CuO, TiO₂, ZnO, CuZnFe₂O₄, Fe₃O₄, Fe₂O₃), CuO NPs were most potent regarding cytotoxicity and DNA damage. The study highlighted the *in vitro* toxicity of CuO NPs and that this was not likely explained by Cu ions released to the cell medium. These particles also caused oxidative lesions and were the only particles that induced an almost significant increase in intracellular ROS (Karlsson et al., 2008).

Bulcke et al. (2014) studied the uptake and toxicity of copper oxide NPs in cultured primary brain astrocytes. The brain astrocytes were exposed to 5 nm laboratory synthesised dimercaptosuccinate-coated CuO NPs. Results showed that the NPs were taken up by the cultured astrocytes and the excess of internalised copper oxide NPs caused cell toxicity by accelerating the formation of ROS.

Environmental research into CuO NPs' toxicity has mostly focused on their effects on organisms, especially those in aqueous environments. One example is the study of Hu et al. (2012) who investigated the toxicity of copper oxide nanoparticles in the blue mussel (*Mytilus edulis*) by exposing the organisms to doses of copper oxide NPs. Toxicity was

evident at the biochemical, cellular and histological levels with the main site of nanoparticle accumulation being the gill.

2.9 Life cycle analysis

A very important consideration for assessing toxicity is life cycle analysis and understanding (Tso et al., 2010, Mitrano et al., 2015, Hirschier and Walser, 2012, Nowack et al., 2010, Nowack et al., 2012, Fransman et al., 2016). The potential hazard posed may change during the life cycle of the material from its time of manufacture through to its disposal, recycling or transformation into other forms (Osmond and McCall, 2010, Mitrano et al., 2015).

Assessing the environmental and human health implications of nanomaterials requires an understanding of the potential exposure routes, nanomaterial property effects on behaviour, possible transformations that the material can undergo and how these transformations may occur through time. In other words a full analysis of what may happen to a MNM through its life cycle (Mitrano et al., 2015).

2.10 Fate in the environment

Once released into the environment, nanomaterials including nanoparticles can interact with various chemical and biological species (Elsaesser and Howard, 2012, Louie et al., 2014, Lowry et al., 2012). Interaction with living species, both flora and fauna, may result in a change in properties of the MNMs. The interactions that take place are dependent on the materials' chemical and physical properties as well as the characteristics

of the receiving environment (Chen et al., 2008, Chen and Elimelech, 2008, Saleh et al., 2008). Upon entry into the environment, NMs may remain intact or undergo: dissolution; complexation (i.e. association with other ionic or molecular dissolved chemical substances); biological or chemical transformation into other chemicals; complete mineralization (to carbon dioxide and water, if C-based NMs or to sparingly-soluble mineral phases, if metal-based NMs); agglomeration/disagglomeration; settling or a combination of these (SCENIHR, 2009). These transformations taking place over time change the behaviour, properties and toxicity of the nanomaterials (Sarathy et al., 2008, Mitrano et al., 2015).

2.11 Properties influencing nanomaterial behaviour and interactions

Nanomaterials including nanoparticles can differ in both physical and chemical characteristics as seen in Figure 2.14. Characteristics include shape, size, size distribution, structure and crystallinity, composition, porosity and surface area, surface functionality, surface charge, surface speciation, agglomeration state and concentration (Hassellöv, 2009, Christian et al., 2008). All these will have an influence on the behaviour, stability and toxicity of the material.

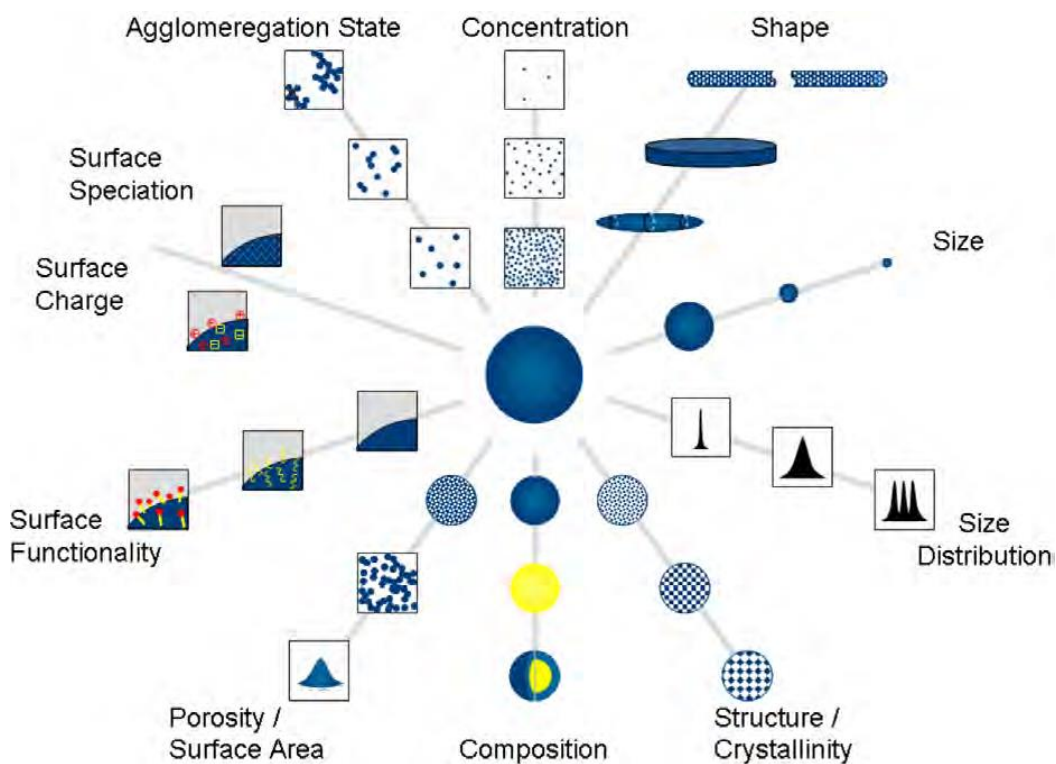


Figure 2.14. Various physical and chemical characteristics that will have an influence on the NPs' behaviour (Hassellöv, 2009).

2.11.1 Nanomaterial Size and Surface Area

According to Hoet et al. (2004) the properties of particles can change depending upon particle size. This is due to the number of atoms localised at the surface. Nanomaterials' small size gives rise to a high surface area to volume ratio, resulting in increased chemical reactivity (Elsaesser and Howard, 2012). Figure 2.15 shows a decrease in surface area to volume ratio for cubo-octahedral nanoparticles where the fraction of surface atoms is given as a percentage (Sonstrom and Baumer, 2011). This high surface area to volume ratio is often correlated with higher biological reactivity. Increased surface area may (Hansen et al., 2006) or may not (Hsiao and Huang, 2011) increase the cytotoxic mechanisms compared with the particle size. Particle size can affect bandgap energy,

melting point and reactivity (Romer Roche, 2013). Additionally, changes in characteristics based on size can result in increased toxicological effects (Aydin et al., 2012).

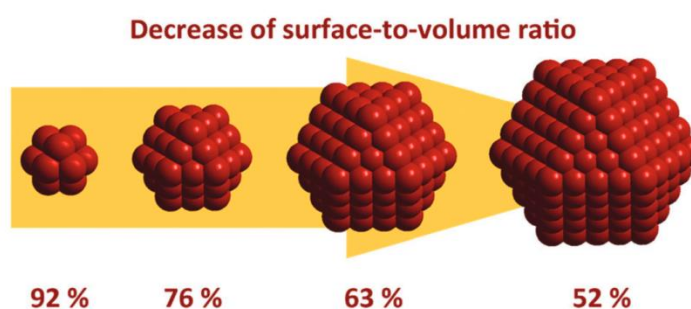


Figure 2.15 Decrease in surface area to volume ratio for cuboctahedral nanoparticles (fraction of surface atoms given as %) (Sonstrom and Baumer, 2011).

2.11.2 Nanomaterial Shape

Nanomaterials can exist in many different shapes including spheres, cubes, rods, prisms and stars. Figure 2.16 shows TEM and SEM images of various shapes of gold nanoparticles (CBNI, 2014). Due to quantum effects the shape of a nanoparticle can affect its stability and toxicity (Cole, 2011). Different NM shapes may increase interactions with organisms (Ispas et al., 2009) and organic materials.

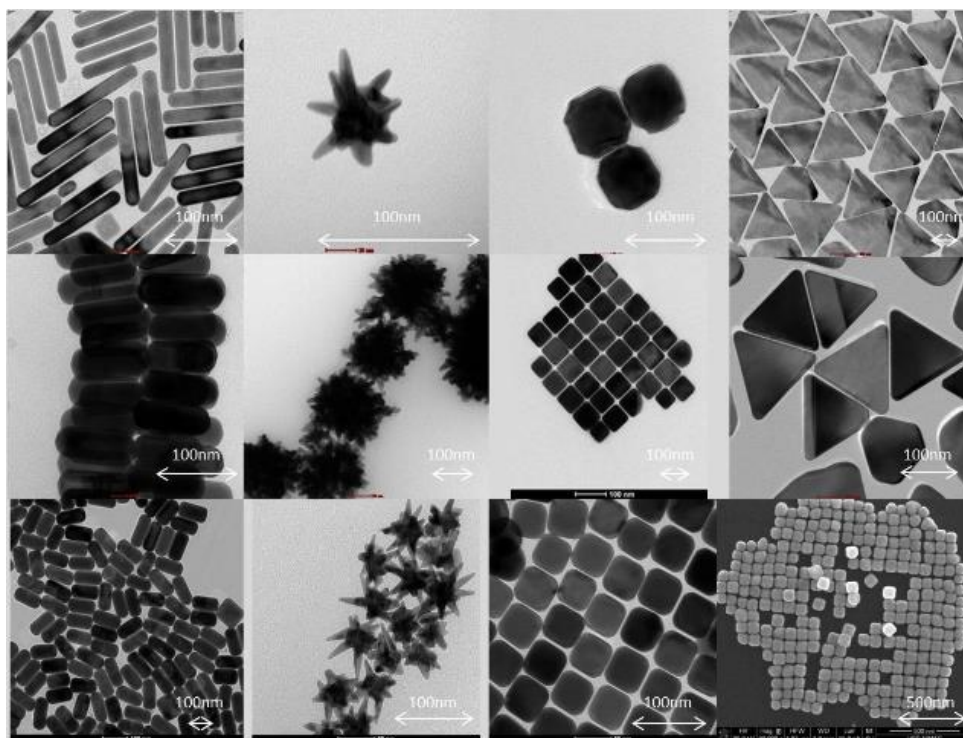


Figure 2.16 Library of nanoparticle shapes: TEM and SEM micrographs gold nanoparticles by Dr Željka Krpetić (CBNI, UCD) (CBNI, 2014).

2.11.3 Nanomaterial Surface charge

Nanomaterial surface charge density plays an important role in many applications, such as drug delivery and cellular uptake (Barisik et al., 2014). When a NP is immersed in an aqueous medium, it becomes charged due to protonation/deprotonation on the particle surface (Hunter, 1981). The resulting surface charge interacting with dissolved ions forms the electrical double layer surrounding the charged particle (Stojek, 2010) as seen in Figure 2.17. More counter-ions are accumulated, while co-ions are depleted within the electrical double layer.

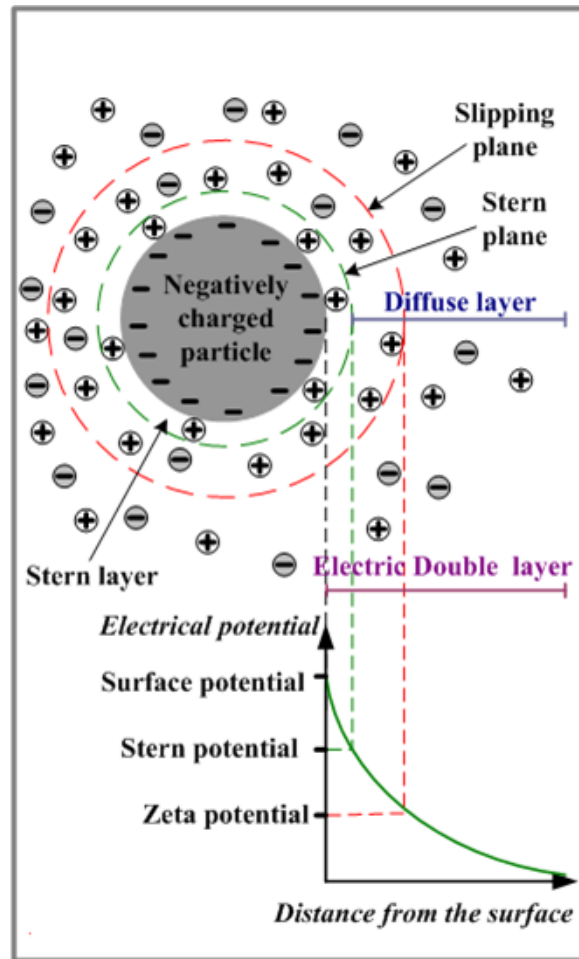


Figure 2.17 Electric double layer (Kopeliovich, 2013).

Transport of nanoparticles highly depends on the particle's surface charge properties. Thus the process of nanoparticle translocation through a nanopore depends on the surface charge densities of the pore and the particle (Ai et al., 2010). Due to the curvature effects, a particle's surface charge also depends on its size (Kobayashi et al., 2005, Behrens et al., 2000).

2.11.4 Nanoparticle Stability

The main concern when studying MNM toxicity is that they tend to agglomerate or self-aggregate due to their surface charge. This in turn causes the MNMs to precipitate due to their instability (Domènech et al., 2012). Stabilisation is in part determined by the conditions of synthesis and hence may introduce difficulties in their fabrication and subsequent application (Domènech et al., 2012). Although aggregation is determined by particle interactions based on surface charges, it is also dependent on the viscosity and polarisability of the suspension medium (Bertrand et al., 2013). Water hardness (effectively high ionic strength) has been found to worsen the agglomeration of engineered nanoparticles (Thwala et al., 2013). In order to determine the stability of a nanoparticle suspension, zeta potential (Figure 2.17) may be used as a proxy, and the background theory for this is explained below.

2.11.4.1 Nanomaterial Interactions

The stability of NMs in a suspension is determined by the net electrostatic surface interactions of the particles according to classic Derjaguin–Landau–Verwey–Overbeek (DLVO) theory (Stebounova et al., 2011). This theory was developed by B. Derjaguin and L. Landau and independently by E. Verwey and J.T.G. Overbeek. It gives an explanation of the stability of colloidal suspensions (Cole, 2011, Verwey, 1948, Derjaguin and Landau, 1993).

As seen in Figure 2.18, it describes the tendency of colloids to agglomerate or separate based on the balance between two forces, electrostatic repulsion (V_R) and van der

Waals attraction (V_A), assuming there is a balance between them as seen from Equation 2.1 (Kopeliovich, 2013).

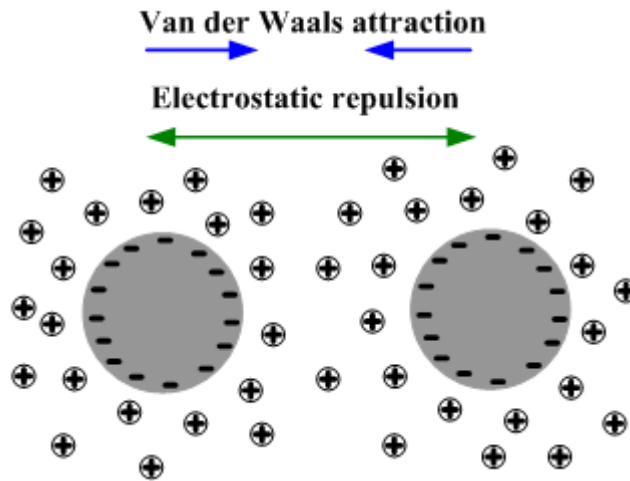


Figure 2.18 The two forces namely Van der Waals and electrostatic repulsion, on which the DLVO is based (Kopeliovich, 2013).

$$\text{Potential Energy of Particles } (V_T) = V_A + V_R$$

Equation 2.1

The interaction forces between nanoparticles determine the fate of individual and collective nanoparticles and in turn influence their behaviour. If the repulsive forces are greater than the attractive forces stability of the suspension will result; however if they are not this will result in coagulation (flocculation) (Bertrand et al., 2013).

The electrostatic repulsion is the repulsive interaction between the charges of the electric double layers on neighbouring particles. The electrostatic repulsion is dependent on the Stern constant and on the thickness of the double layer. It becomes significant when two colloids approach each other and their electrical double layers begin to interfere.

The electric repulsive potential energy can be calculated from equation 2.2 (Kopeliovich, 2013):

$$V_R = 2\pi\epsilon\epsilon_0 r\zeta^2 \epsilon^{-kx}$$

Equation 2.2

where ϵ is the dielectric constant of the solvent, ϵ_0 is the vacuum permittivity, ζ is the zeta potential, r is the radius of the particle and k is a function of the ionic concentration.

According to IUPAC, Van der Waals forces are ‘the attractive or repulsive forces between molecular entities (or between groups within the same molecular entity) other than those due to bond formation or to the electrostatic interaction of ions or of ionic groups with one another or with neutral molecules. The term includes: dipole–dipole, dipole-induced dipole and London (instantaneous induced dipole-induced dipole) forces. The term is sometimes used loosely for the totality of nonspecific attractive or repulsive intermolecular forces’ (IUPAC. Compendium of Chemical Terminology, 1997). The Van der Waals attractive potential energy can be calculated from equation 2.3 (Kopeliovich, 2013):

$$V_A = \frac{-Ar}{12x}$$

Equation 2.3

where A is the Hamaker constant, r is the radius of the particles and x is the distance between the surfaces.

Although the DLVO theory can be used to quantitatively estimate the energy of a colloidal system, it has some limitations with respect to NM dispersions. This theory is only applicable when there is no interference with diffusive or attractive forces (Kallay and Zalac, 2002). Also NMs generally do not show electrostatic stabilisation and on aggregating they may exhibit a complete overlap of the diffuse layers (Kallay and Zalac, 2002). Other limitations include that the theory cannot describe effects associated with particle properties such as shape as well as with dilute dispersions with low salt concentrations (Cole, 2011).

2.12 Stabilisation of Nanomaterials

When the NM surface is not protected by a molecule, interactions between NMs will occur to reduce their surface energy and this is what will lead to aggregation (Ju-Nam and Lead, 2008). Therefore an important feature in the production of the metal NMs is the ability to keep them physically isolated from each other to prevent this agglomeration and any possible further reactions (Thi My Dung Dang, 2013). The stabilisation of NMs is specifically required to:

- i. prevent their uncontrollable growth
- ii. prevent aggregation
- iii. control their final shape and size
- iv. allow particle dispersability in various solvents
- v. terminate the material growth reaction (Domènech et al., 2012).

Stabilisation occurs through colloidal forces. These colloidal forces can be classified in three main types: Van der Waals interactions (electrosteric), electrical double-layer interactions (electrostatic) discussed above as well as steric interactions as seen in Figure 2.19. Apart from these forces, hydrophobic and solvation forces also play a role in the stabilisation of NMs. The most popularly employed method is polymer-assisted fabrication. Stabilisation with polymers occurs by two simultaneous approaches which influence one another. Firstly the substantial increase in viscosity of the polymer matrix and secondly the decrease in the energy of particle-particle interactions (Domènech et al., 2012).

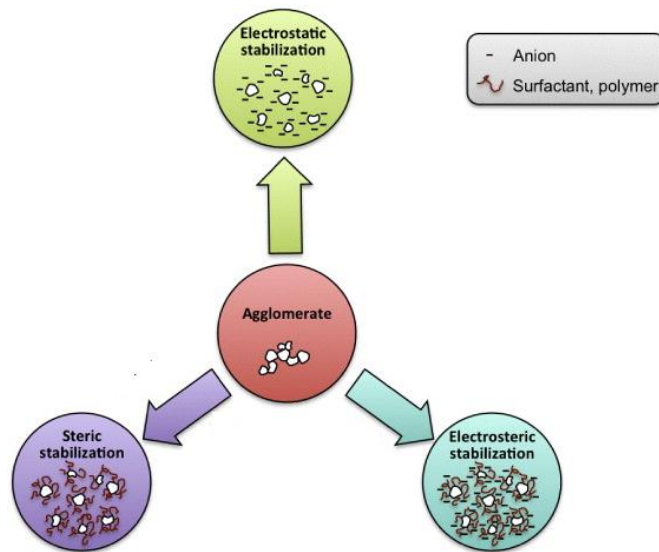


Figure 2.19 Schematic of the main mechanisms that can be used for the stabilisation of NPs (assuming positively charged surfaces) (Bertrand et al., 2013).

2.13 Capping Agents

Often nanoparticles are surface-modified or coated or capped with inorganic or organic matrices (Figure 2.20) in order to obtain specific properties (Nowack and Bucheli, 2007, Labille et al., 2010). These properties include inhibiting nanoparticle overgrowth and aggregation as well as precise control of the structural characteristics of the resultant nanoparticles (Niu and Li, 2013).

The ligand molecule has to first bind to the particle surface by some attractive interaction, either chemisorption, electrostatic attraction or hydrophobic interaction, most commonly provided by a head group of the ligand molecule (Sperling and Parak, 2010). As seen in Figure 2.19 the repulsive force between particles can then result from electrostatic, electrosteric or steric stabilisation depending on the particle system.

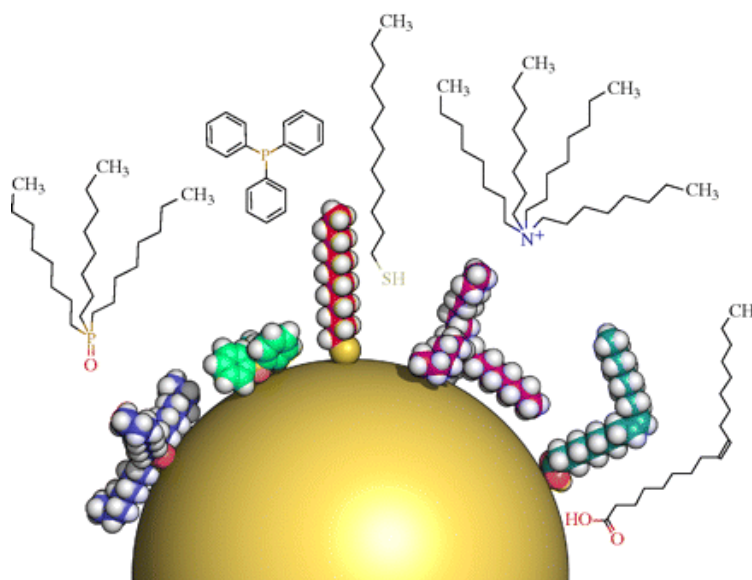


Figure 2.20 A 5 nm nanoparticle with different hydrophobic ligand molecules examples (left to right: trioctylphosphine oxide (TOPO), triphenylphosphine (TPP), dodecanethiol (DDT), tetraoctylammonium bromide (TOAB) and oleic acid (OA)) (Sperling and Parak, 2010).

It is important to note that this capping, besides resulting in the stabilisation of the nanoparticles (Yang and Rahaman, 1997) also affects the behaviour of the nanoparticles (Nowack and Bucheli, 2007). Just like the core of the nanoparticle, the shell can also undergo transformations (Talpin and Yin, 2011). These changes in behaviour need further study.

Examples of commonly used nanoparticle capping agents include citrate, polyethylene glycol (PEG) and polyvinylpyrrolidone (PVP). The latter example is discussed below.

2.13.1 Polyvinylpyrrolidone (PVP)

One of the most frequently used protective agents in metal NMs synthesis is poly(N-vinyl-2-pyrrolidone) (PVP) (Hoppe et al., 2006), the structure of which can be seen in Figure 2.21.

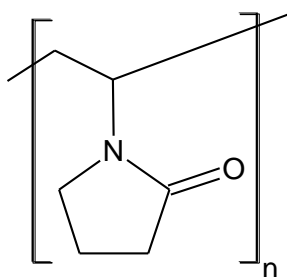


Figure 2.21 Structure of PVP monomer

PVP is a water-soluble polymer due to its hydrogen bonding capability. It has been extensively used as a protecting agent against agglomeration of metal colloids in the well-

known polyol process (Sun and Xia, 2002). In this synthetic procedure the PVP polymer is considered to act both as solvent and as reducing agent of the metal ions (Figure 2.22).

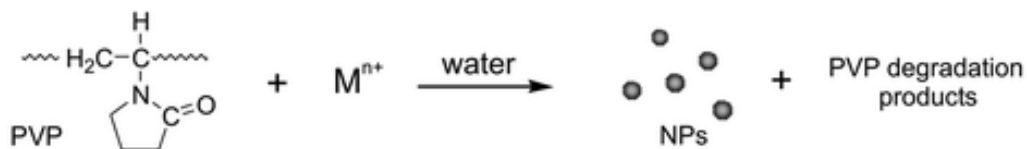


Figure 2.22 Reaction of PVP and metal ions in the presence of water to form nanoparticles.

Hoppe et al. (2006) have put forward two possible mechanisms to explain the reduction step. The reduction process can be due to direct abstraction of hydrogen atoms from the polymer by the metal ion and/or reduction of the metal precursor by organic macroradicals formed by degradation of PVP (Hoppe et al., 2006).

Due to PVP's ability to act as a reducing agent (Zhang et al., 1996) by varying the ratio of metal salt to PVP, the size and shape of the nanoparticle can be tuned.

2.14 Transformations

Once released into the environment, NMs undergo complex interactions and transformations that determine their fate, the exposure concentration and form, and the biota they may interact with (Baalousha et al., 2014, Mitrano et al., 2015).

Transformations are changes that occur to the nanomaterial or the nanomaterial coating or the conformation of a number of nanomaterials or all of these, changing their behaviour and properties over time (Sarathy et al., 2008, Mitrano et al., 2014, Louie et al., 2014). Just as the release of MNMs into the environment could occur at any time during the manufacturing, use or disposal of the nano-product, transformations can occur at any

point within the materials' life cycle (Mitrano et al., 2014). The time at which a nanomaterial transforms during its life cycle affects its fate, transport and behaviour.

The interactions and transformations of NMs in the environment depend on the physical and chemical characteristics of the NMs and the environmental compartment to which they are released (Baalousha et al., 2014, Louie et al., 2014).

Environmental factors, such as temperature and humidity among others, may play a role on these transformations (Thwala et al., 2013). These changes vary from one nanomaterial to another, depending on their physicochemical properties (Mitrano et al., 2015), e.g. the nanomaterial's size (Nowack and Bucheli, 2007, Rickerby and Morrison, 2007), shape/structure, surface area, charge, surface coating and chemical reactivity of the surface and its solubility (Kim et al., 2010, Aydın et al., 2012, Thwala et al., 2013, Karakoti et al., 2012, Labille et al., 2010).

The uniqueness of every nanomaterial's situation results in a great deal of complexity and the consequences of one slight change in one of the nanomaterial's parameters could be significant transformations of the nanomaterial.

Transformations have the possibility of increasing potential toxicity, as in the case of silver where silver ions are released, or decreasing reactivity, as in the case of adsorption of organic matter onto the surface of the nanoparticle. Therefore, understanding and determining these transformations could help to better recognise the benefits or risks of these materials (Mitrano et al., 2015).

Key transformations that nanomaterials can undergo include physical mechanisms, degradation and transformation and surface modification (Figure 2.23). These include biological transformations, interactions with macromolecules and physical and chemical transformation and could result in toxicology behaviours and effects, potential

accumulation in an organism and transfer through the food chain (Nowack and Bucheli, 2007, Tso et al., 2010, Rickerby and Morrison, 2007, Lowry et al., 2012, Auffan, 2013, Lynch et al., 2014). The physical state and chemical form of the NMs are of particular concern as they will determine the pathways of NMs within ecological systems and their toxicity to a particular organism (Larner et al., 2012). It is important to understand and characterise the changes as they occur over time (Karakoti et al., 2012). This is as yet not well understood (Mudunkotuwa et al., 2012). The transformations taking place are highly dependent on the nanomaterial. In addition, a whole range of other behavioural changes may also take place including photochemical modifications, dissolution, aggregation and surface adsorption which all directly affect the mobility and uptake of nanomaterials (Nowack and Bucheli, 2007, Karakoti et al., 2012, Mudunkotuwa et al., 2012).

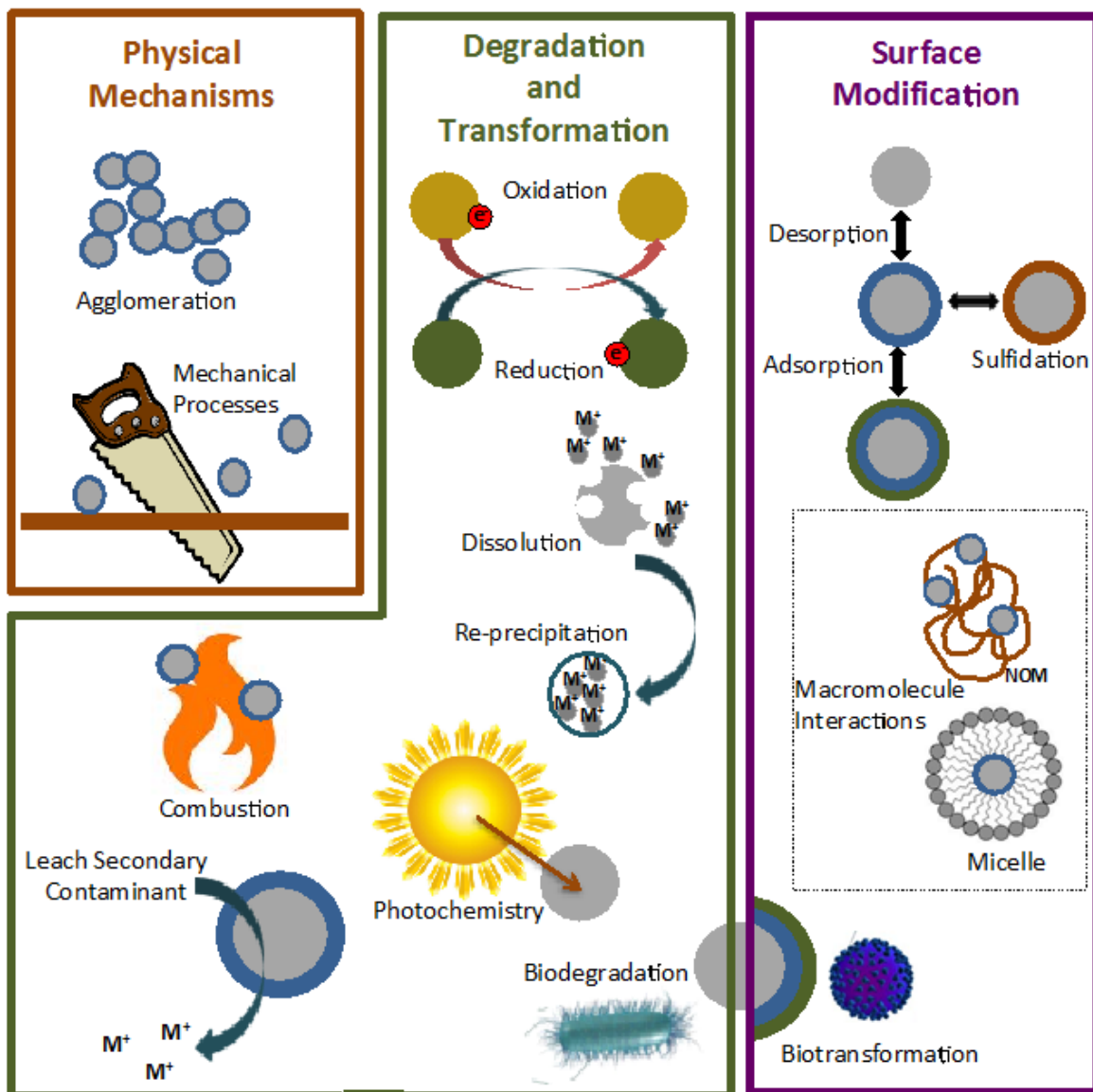


Figure 2.23 Key transformations that nanoparticles can undergo (Mitrano et al., 2014).

2.14.1 Types of Transformations

Due to the vast number of NMs and their numerous applications it is important to note that many different transformations exist (Mitrano et al., 2014, Lowry et al., 2012). NM core transformations can be related to a number of well-known molecular chemistry reactions. Transformations that NMs undergo can be grouped as chemical, physical,

biological or interaction with macromolecules and are discussed below (Lowry et al., 2012) (Figure 2.24).

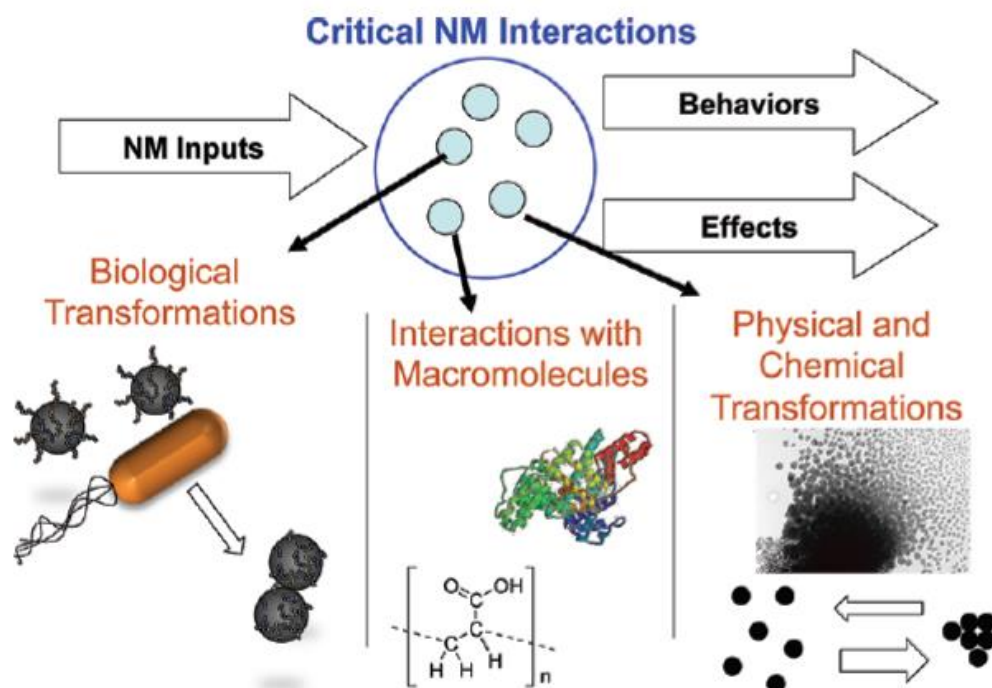


Figure 2.24 The behaviour and effects of nanomaterials are dependent on the nanomaterial and critical interactions that occur (Lowry et al., 2012).

2.14.1.1 Chemical Transformations

A chemical transformation is the conversion of a compound to one with a different structure, valency or composition. There are numerous chemical transformations that can occur due to various different factors. These can involve a change to the material surface, a change in the oxidation state, or a formation of a core-shell material by surface reactions (Mitrano et al., 2014).

An example of a chemical transformation is a redox reaction. A reduction, oxidation or both can take place changing the nanomaterial by the transfer of an electron to and from chemical moieties (Louie et al., 2014). Whether or not NMs are reduced or oxidised depends on the standard potential for the redox transformation and the availability of a suitable oxidant or reductant. This happens to many elemental nanomaterials such as silver, iron and cerium. Thus it has been demonstrated that Ag^+ ion can be reduced to form $\text{Ag}(0)$ NPs in the presence of organic matter (Hou and Jafvert, 2009) and ceria NPs have been shown to be redox labile under environmental conditions and in biological media (Karakoti et al., 2010).

Oxidation could result in the formation of an insoluble oxide surface coating, hinder further oxidation and affect the behaviour of the nanomaterial. Oxidation could also lead to dissolution (discussed below). Oxidation and reduction reactions are highly influenced by water chemistry. Oxidising zones can be found in natural waters and aerated soils whilst reduction areas can be groundwater and sediment. Redox cycling is very common in tidal zones due to the dynamic environment present within these areas (Mitrano et al., 2014, Lowry et al., 2012, Louie et al., 2014).

Another example of transformations is that due to light. Light may cause excitation of the nanomaterial, free radical formation and/or changes to the MNM surface/coating. Thus changes to the nanomaterial product can be due to incident light wavelength, the ability of light penetration to the outer layers of the material and photosensitivity or photo-degradation potential. There are certain nanomaterials that are specifically used for their photo-catalytic ability. Examples of these include titanium dioxide and zinc oxide, two nanomaterials that are commonly used in paints, self-cleaning materials and sunscreen due to this property (Mitrano et al., 2014). Sunlight-catalysed

redox reactions (photo-oxidation and photo-reduction) may prove to be a very important transformation process affecting NM coatings, oxidation state, generation of ROS, and persistence in the environment (Louie et al., 2014). Hence sunlight irradiation is thought to influence the toxicity of silver nanoparticles in the environment since these particles are UV light sensitive (Li et al., 2012b).

Combustion is another chemical transformation resulting in the oxidation of the NM or its surface coating. This type of transformation occurs frequently during waste incineration. In the case of ceria NPs it also occurs when petrol is burnt (Mitrano et al., 2014).

Many NMs may undergo dissolution or form complexes with strong ligands (Figure 2.25) (Louie et al., 2014). Dissolution is a reaction that involves the release of individual ions or molecules that are water-soluble. Sulfidation is a reaction with sulphur. These are chemical reactions that are especially common for soft metal cations such as silver, zinc and copper (Mitrano et al., 2014, Louie et al., 2014). These transformations can alter the surface charge and induce aggregation (Mitrano et al., 2014). Considering zinc oxide NPs in a wastewater treatment plant, both sulphide and phosphate are important ligands as zinc oxide is completely transformed to ZnS and $Zn_3(PO_4)_2$ particles due to the dissolution of zinc oxide followed by strong ligation as well as to Zn-ferrhydrite due to a dissolution-adsorption reaction (Lombi et al., 2013, Ma et al., 2014b, Louie et al., 2014).

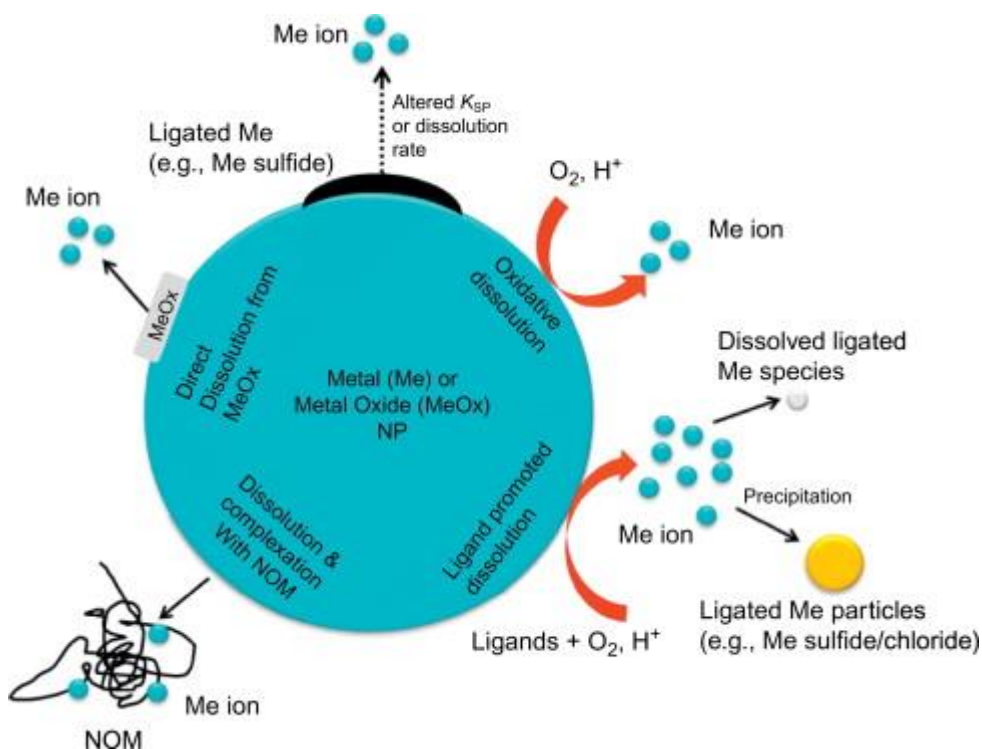


Figure 2.25 Schematic illustration of various metal (Me) and metal oxide (MeOx) NP dissolution and ligation processes (Louie et al., 2014).

Although a NM's chemical transformation is not necessarily restricted to one transformation process, it can nevertheless be the result of a single one. There is also the possibility that various or successive chemical transformations can take place. One example of such a nanoparticle is silver. Possible chemical transformations that may occur to silver can be seen in Figure 2.26.

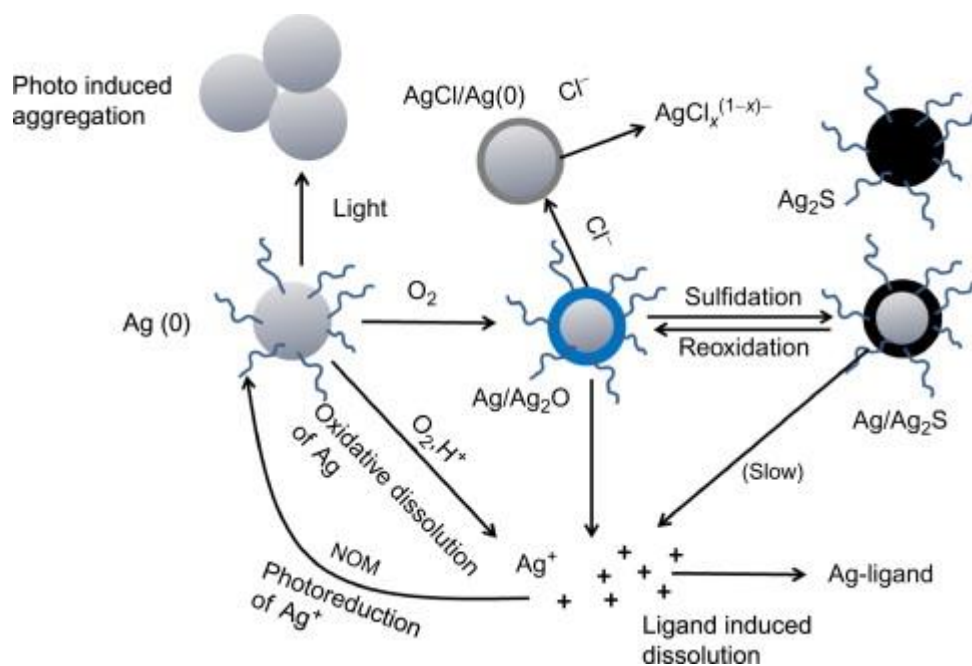


Figure 2.26 Schematic of selected chemical transformations of silver nanoparticles in the environment. Important transformations include photo-induced aggregation, sulfidation, dissolution, and complexation with chloride (Louie et al., 2014).

2.14.1.2 Physical Transformations

A variety of physical transformations may affect the fate and effects of NMs. These are changes that occur to the physical properties (e.g. size or shape) of the nanomaterial (Mitrano et al., 2014). These transformations include aggregation and disaggregation, and the adsorption of biomacromolecules. The latter can affect both aggregation and disaggregation (Louie et al., 2014).

2.14.1.2.1 Aggregation

One very important physical transformation that nanomaterials may undergo is known as aggregation (in the case of tightly bound materials) or agglomeration (in the case of loosely bound materials). This results in a change in the behaviour of the NMs and possibly a decrease in toxicity (Mitrano et al., 2014). The small size of NMs means that their transport is dominated by Brownian motion which is the random motion of particles suspended in a fluid and is enhanced by thermal energy. It also gives them a very high-surface area to volume ratio as mentioned in Section 2.2 and discussed in Section 2.11.1. These two conditions make NMs highly susceptible to collisions with and attachment to other surfaces (Louie et al., 2014). One of two types of agglomeration/aggregation may occur, namely homoagglomeration/homoaggregation which occurs between the same type of NM or heteroagglomeration/heteroaggregation which occurs between different types of NM (Lowry et al., 2012, Mitrano et al., 2014). Figure 2.27 shows homo and hetero aggregation for nanoparticles.

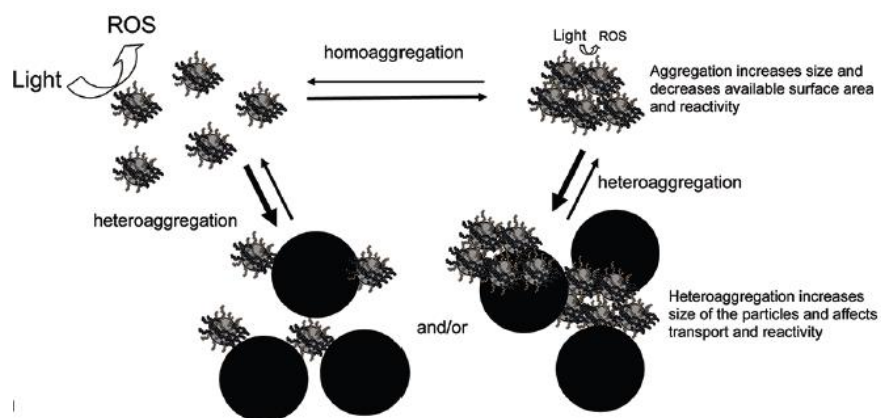


Figure 2.27 Physical transformations of nanoparticles depicting homo and hetero aggregation (Lowry et al., 2012).

Since in environmental systems the concentrations at which nanoparticle solutions will be found will be likely to be dilute, homoagglomeration/homoaggregation is unlikely and heteroagglomeration/heteroaggregation will tend to dominate. This may result in changes in transport, dissolution, reactivity and bio-uptake as have been recorded for NPs including silver (Bae et al., 2013, Louie et al., 2014) and zinc oxide (Ma et al., 2014b, Louie et al., 2014, Lin and Xing, 2008).

2.14.1.2.2 Disaggregation

Disaggregation, or aggregate breakup, may also affects NM behaviour; however this transformation is less well understood than aggregation. There are a number of factors that can affect the strength of attraction between aggregated NMs and therefore the potential for disaggregation includes the presence of surface coatings on the NM or organic macromolecules in solution, pH, ionic strength, time, and flow conditions (Louie et al., 2014).

2.14.1.2.3 Adsorption

Adsorption occurs when a mono-layer of organic and inorganic ligands forms on the surface of the nanoparticle by means of Van der Waals attractions or electrostatic interactions or chemical bonding. Adsorption may affect a NM's dissolution, charge and stability against aggregation. Adsorption can also take place with macromolecules and is discussed below in Section 2.14.1.3.

2.14.1.3 Biological Transformations

These are changes that occur to the nanomaterial and are related to living organisms or tissue (intercellular or extracellular) and environmental media (e.g. soils) (Louie et al., 2014, Lowry et al., 2012). Biological interactions, in the same way as physical ones, can affect surface charge, aggregation state and reactivity. These could occur to the core or the coating and possibly change the NMs' transport, bioavailability and toxicity (Lowry et al., 2012) by affecting surface charge, aggregation and reactivity (Mitrano et al., 2014). A significant biotransformation is the adsorption of biomacromolecules. Redox reactions are also fundamental to growth in all biological systems and can take place between the nanoparticles and the cytoplasm, cell wall, cell membrane or extracellularly *via* redox-labile enzymes and cytochromes or through ancillary intracellular ROS production such as hydroxyl radicals or H₂O₂ (Louie et al., 2014, Lowry et al., 2012).

An example of biological oxidation and biological degradation are shown in Figure 2.28. These transformations are dependent on the availability of biomolecules and can occur in the presence of microbes, enzymes or during ingestion.

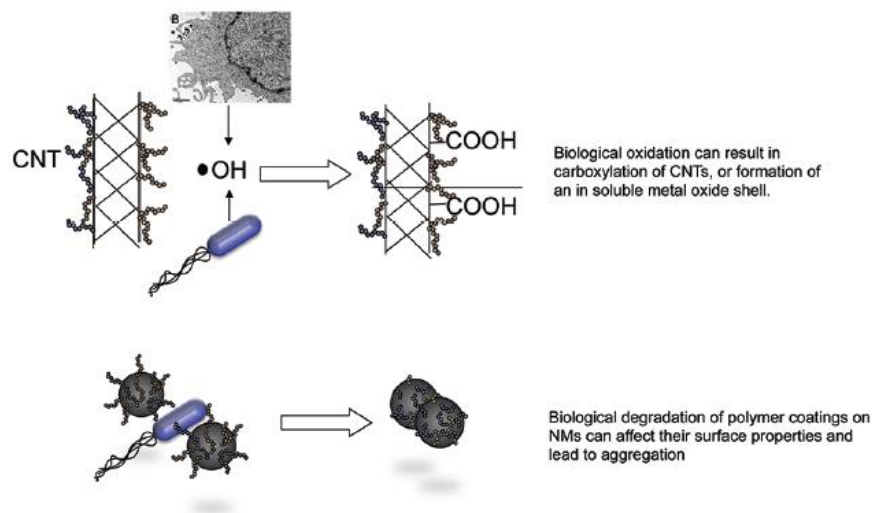


Figure 2.28 Biological transformation with specific reference to biological oxidation and biological degradation (Lowry et al., 2012).

Biological transformation studies have primarily been conducted *in vivo/vitro* for a variety of cell lines and organisms, bacteria and fungi, and plants. Montes et al. (2012) carried out an *in vivo* study using mussels which showed that in the study media ceria NPs remained unchanged however zinc oxide NPs dissolved. Zhang et al. demonstrated uptake and transformation of ceria NPs to cerium phosphate and cerium carboxylates in cucumber plants (Zhang et al., 2012).

2.14.1.4 Interactions with Macromolecules

Nanomaterials have the potential to interact with macromolecules. Macromolecules are molecules containing a very large number of atoms. There is a nearly endless number of biomacromolecules in living cells and in the environment. Examples include proteins and polysaccharides (Louie et al., 2014, Lowry et al., 2012).

Proteins interact with NPs in living cells and the latter interact with NPs in the environment (Lowry et al., 2012). One way in which these interactions can take place is by means of adsorption whereby a mono-layer of macromolecules forms on the surface of the NP. Adsorption of biomacromolecules on nanomaterial surfaces can occur in all environments and can significantly affect their surface chemistry and resulting behaviour in biological and environmental systems (Louie et al., 2014). These interactions that cause transformations as seen in Figure 2.29, may result in the fate, transport and behaviour of the nanomaterials in the environment to be varied.

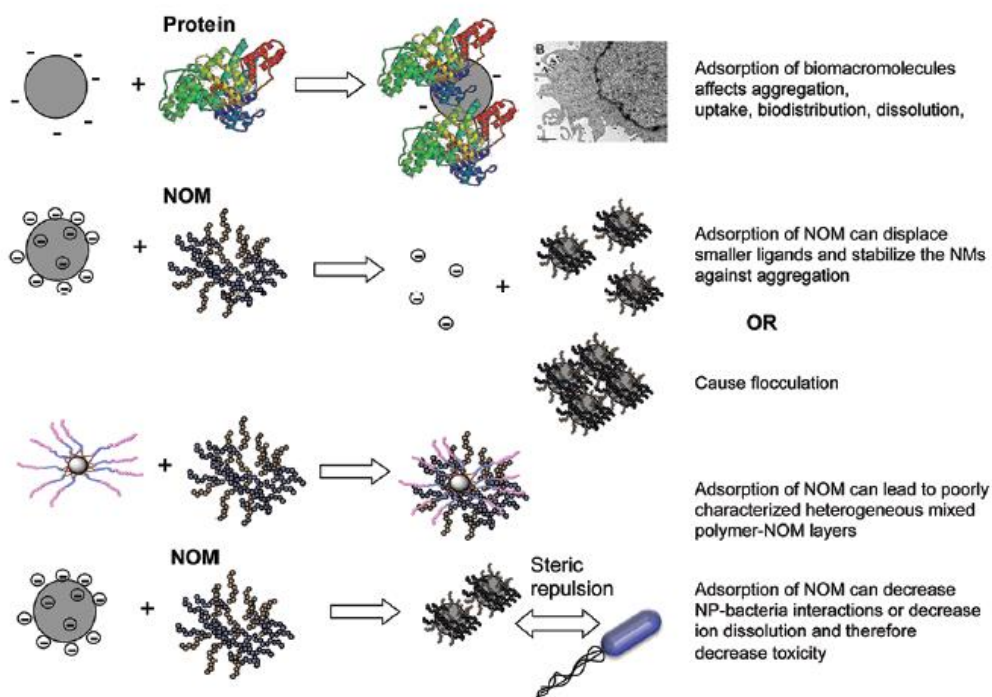


Figure 2.29. Interaction of nanoparticles with macromolecules (Lowry et al., 2012).

2.15 Ageing

An important aspect of life cycle analysis is to understand how transformations (Section 2.14) are effected by time. Therefore, ageing is an important part of a nanomaterial's life cycle as it can be considered as a transformation over time from their formation.

Most NMs react in ways that change their behaviour and properties over time (Sarathy et al., 2008). Aged NMs no longer have the same characteristics of their pristine counterparts (Mitrano et al., 2014).

From the literature it can be noted that there is a lack of long term studies taking place. Baer et al. (2013) state that changes that NPs undergo over time and in different environments are not well studied or documented. Labille et al. (2010) point out that the exotoxicological tests of the original material only are not enough and it is of great importance that ecotoxicological studies of the by-products formed by ageing are carried out too.

Predominantly the focus on research to date has been on pristine materials due to the complexity associated with exposure reactions in real-life environments. Nowack et al. (2012) concluded that by only studying the pristine material the fate of the material cannot be determined. Thwala et al. (2013) suggest that one needs to take into account future implications on nanoparticles because changes in the physicochemical environment can result in engineered nanoparticles that are more (or less) hazardous than the original ones. Aged or released NMs can provide more realistic information. Hence the importance of carrying out ageing studies in order to understand the transformation mechanism taking

place during ageing and to carry out studies on aged samples in order to understand the fate and behaviour of the nanomaterial.

To date there are no standard testing methods for ageing or accelerated ageing of NMs. Only on very few occasions has the effect of aged NMs on the environment and biological systems been considered. This distinct lack of information is what spurs the need for investigating ageing of NMs and any results obtained will hopefully help to fill some of the numerous gaps that exist in knowledge.

2.15.1 Accelerated Ageing

Accelerated ageing can be defined as a procedure that seeks to speed-up the ageing process of a material to obtain in a short time the results that would occur in ageing under normal conditions (Hemmerich 1998). This is achieved by subjecting the product to more severe stresses than normal environmental conditions for a much shorter time. Accelerated ageing tests are carried out for three main reasons, namely:

1. To establish in short time the chemical stability or physical durability of a material
2. To estimate or “predict” potential long-term serviceability of material systems under expected conditions of use
3. To better understand the possible chemical reactions involved and the physical consequences of ageing a material (Feller, 1995).

Any stress factor that can affect the properties over time should be included in the accelerated ageing. The results of these accelerated stress conditions are then correlated to

those at normal operating or storage conditions using physically appropriate statistical models (Hemmerich 1998).

2.15.2 Ageing studies

Unfortunately, there is a lack of knowledge and published material related to the ageing of NMs. This section offers a literature review with a compilation of examples of ageing studies.

Sarathy et al. (2008) studied the ageing of iron core/oxide-shell NPs in water focusing on changes in composition, structure and reactivity. The results showed that the iron NPs became more reactive in the first 2 days of water exposure and then gradually lost reactivity over the next few hundred days. In addition the NPs aged for longer than 3 days acquired properties that are relatively stable over weeks or months.

Auffan et al. (2010) aged titanium dioxide NPs, which are used in cosmetics, coated with an outer polydimethylsiloxane organic and an aluminium hydroxide inorganic layer. Suspensions were magnetically stirred for 6, 24 or 48 hours in the dark or under artificial daylight and results showed that 90 % of the total Si of the organic layer was desorbed while the remaining fraction was surface oxidised. The inorganic layer was affected to a lower extent and continued to protect against photocatalytic superoxide formation.

Botta et al. (2011) investigated the physical and chemical evolution during artificial ageing of four commercial sunscreens containing titanium dioxide NPs. Artificial ageing was carried out in the dark or under light for 48 hours at 30 °C. Results showed a significant release of colloidal residues containing titanium dioxide NPs from commercial

sunscreens into aquatic environment after artificial ageing. These results raised (eco)toxicity concerns for aquatic environments. Additionally, they highlighted the need for complete nanotechnology risk assessments to evaluate the potential fate and indirect exposure of nanomaterials not only during their manufacturing or use, but also throughout their entire life cycle.

Pereira et al. (2011) studied the ecotoxicity and genotoxicity of soils contaminated with organic and inorganic NPs as a function of time. Soil samples were contaminated with aqueous suspensions of two organic and five inorganic NPs. These were then tested after 2 hours and after 30 days. In general it was found that the toxicity after 2 hours was higher possibly due to the NPs not having enough time to stabilise within the soil. They found that ageing may have either contributed to the establishment of strong interactions of NPs with the soil or have promoted the degradation of the organic shells with the release of the core elements and an increased toxicity.

Kuchibhatla et al. (2011) studied the influence of ageing on the properties of cerium oxide NPs. Ceria was synthesised and the oxidation states were measured as a function of time by means of UV-Visible spectroscopy. The results showed that on ageing a ceria solution, the concentration of Ce^{4+} initially increases imparting the characteristic yellow colour with a maximum in intensity after 1-day of ageing. This intense yellow colour fades on ageing for 1 week showing a decrease in the amount of Ce^{4+} in the solution. After 3 weeks of ageing, the solution appears pale yellow in colour indicating the further reduction of Ce^{4+} and regeneration of Ce^{3+} . They proposed that the UV absorption band edge in ceria NPs can be chemistry driven and may not always be due to pure quantum confinement effects driven by particle size changes.

Roro et al. (2012) simulated a 25 year ageing pattern for thermal absorbers made of MWCNT/NiO composites by exposing them for 200 hours at 250 °C. This induced a slight decrease in reflectance correlated with decreases of C/Ni and of particle size.

Mudunkotuwa et al.'s (2012) studies provided some insights into the impacts of nanoparticle ageing and how the physicochemical characteristics and reactivity of nanomaterials can change upon ageing. Mudunkotuwa et al. (2012) studied the effect of ageing on copper by characterising and comparing fresh copper NPs, aged Cu NPs, and CuO NPs that differ in the level of oxidation. The Cu(aged) NPs were allowed to sit in a laboratory environment for several years under ambient conditions. Analysis took place as a function of pH and in the presence and absence of citric and oxalic acid. The ageing of the copper NPs was found to increase the average particle size and change the composition when compared to Cu(new) NPs and CuO NPs.

Thwala et al. (2013) studied the toxicity effects of silver and zinc oxide engineered NPs on duckweed. The experiments carried out were run for a period of 4 days and 14 days with the water medium used renewed on day seven. The results showed that the potential risks to aquatic plants of the NPs tested were highly dependent on environmental abiotic parameters. In addition, both particulates and dissolved ionic species account for the toxicity of nAg and nZnO. Based on the evaluation of the results Thwala et al. also suggest that one should not only consider present fate and biological effects, but should also take account future implications because changes in the physicochemical environment can result in engineered nanoparticles that are more hazardous. It was concluded that the toxicity of nAg and nZnO was driven both by particulates as well as the dissolved ionic species, and was directly influenced by environmental conditions such as pH and organic matter.

Rossano et al. (2014) studied the effects of ageing on the structure and stability of titanium dioxide NPs containing oil-in-water emulsions. Following the development of formulations incorporating different cosmetic grade TiO₂ NPs, ageing was performed under classical conditions at room temperature or under accelerated conditions at 50 °C, with or without TiO₂. The changes in the emulsion stability and the aggregation state of NPs were followed over time and results showed destabilisation under accelerated ageing conditions. Additionally, the NPs strongly affected the particle–droplets interactions and thus modified the emulsion microstructure with a coating-dependent effect.

C₆₀ fullerene nanoparticle suspensions were aged in the presence of microbes (Chae et al., 2014). Fullerene C₆₀ aggregates were observed to decrease in size while hydroxylation and photosensitised reactivity increased in the presence of microbes for 24 months. Stable-isotope-labelling C₆₀ aggregates aged in the presence of microbes for 203 days did not produce significant labelled carbon dioxide. The results show that while microbes may play an active role in ageing fullerene nanomaterials the rate of biodegradation of these particles is too slow to quantify or the biologically-enhanced transformation of these particles does not occur through microbial biodegradation to carbon dioxide.

2.16 Understanding nanomaterial risks

Although there is concern regarding the toxicity of NMs both to humans and the environment, it is important to keep in mind that not all NMs are toxic. Toxicity depends on a number of determining factors including chemical composition, shape, size and NM ageing. It is vital to enhance our understanding of toxicology through various studies in

order to obtain accurate information to establish well informed policy and regulatory processes.

In order to understand whether the NMs present in the environment pose a risk to the environment or to humanity a number of different questions have to be asked. These include:

- Are MNMs toxic in their present form? How much?
- Will MNMs transform in the environment into more toxic forms?
- How do MNMs move through the environment?
- What are the pathways for exposure?
- What populations are likely to be exposed?
- What is the frequency and duration of exposure?

Information gained from answering these questions will result in a better understanding of the NM and, subsequently, if it could be beneficial or pose a risk.

Botta et al. (2011) concluded their work by highlighting the vital need for a complete risk assessment in order to assess the potential fate and exposure of complex nanocomposite-based products during their lifetime.

2.17 Risk Analysis

Risk assessment studies for NMs have to take into account the toxicological hazard, the probability of exposure and the environmental and biological fate, transport, persistence, transformation into the finished product and recycling (Rickerby and

Morrison, 2007, Nowack and Bucheli, 2007). For nanomaterials to pose a risk there must be both a potential for exposure and a hazard that results after exposure as seen in the classical paradigm equation below (Nowack and Bucheli, 2007, Prospect, 2010):

$$\text{Risk} = \text{Hazard} \times \text{Exposure}$$

One without the other does not result in a risk. According to Hassellöv et al. (2009) the environmental risk assessment requires thorough characterisation of the NMs in question. Additionally it highlights the advantage of combining various complementing methods together in order to obtain more valuable information for understanding nanomaterial risks.

2.18 Conclusion

This chapter has given an overview and brought together the relevant literature that precedes the work presented here. An introduction to what nano is was presented. The extensive uses of nanomaterials in applications related to electronics, the food industry, textiles, cosmetics, paints and coatings and medicine were reviewed and particular attention was given to ceria, zinc oxide and copper dioxide as these are the nanomaterial synthesised and used for the research.

Despite the widespread and valuable uses of nanomaterials there are concerns associated with their widespread use before they have been fully assessed for their safety. Evidence in support of such concerns was described above.

In conclusion this review has highlighted two gaps in the knowledge which will be addressed in this work. These are the need for a comparable library of NMs for toxicity studies and a better understanding of how ageing influences the properties and behaviour of nanomaterials. Therefore the following chapters aim to tackle the synthesis and characterisation of a new nanomaterial library, study any chemical or physical alterations to a predetermined nanomaterial set resulting from temperature ageing studies and finally to study any chemical or physical alterations to a predetermined nanomaterial set resulting from phosphate induced ageing studies.

Chapter 3: Methodology

3.1 Introduction

This chapter gives a detailed description of the characterisation techniques and methods used throughout this work. Following MNM synthesis and ageing, samples were analysed and a comparative study was carried out. Samples were characterised by means of various physical and chemical analysis techniques. The properties studied and the methods used are summarised in Table 3.1. Each technique is discussed in more detail below. Following this details on the sample preparation and procedure for each technique are given as they were used in this work.

Table 3.1 Properties studied and techniques used in this project.

Property Studied	Techniques used
Appearance – Shape and size of NMs	Transmission Electron Microscopy Scanning Transmission Electron Microscopy
Surface charge – Charge at double electric layer	Dynamic Light Scattering (Zeta Potential)
Size – NM Diameter	Dynamic Light Scattering Transmission Electron Microscopy Scanning Transmission Electron Microscopy
NM composition – NM metal oxide core chemical composition and structure	Ultra-Violet/Visible Light Spectroscopy X-ray Photoelectron Spectroscopy Electron Energy Loss Spectroscopy Fourier Transform Infra-red X-ray Diffraction Spectroscopy Inductively Coupled Plasma – Optical Emission Spectroscopy Energy-dispersive X-ray Spectroscopy Extended X-ray absorption fine structure
NM dispersion metal oxide concentration	Inductively Coupled Plasma – Optical Emission Spectroscopy

3.2 Dynamic Light Scattering

3.2.1 Technique

3.2.1.1 Size

There are a number of techniques that can be used to measure particle size; however, few of these have the ability to determine particle size less than 10 nm (Particle Sciences, 2009). One of these is Dynamic Light Scattering (DLS). This method, also known as Photon Correlation Spectroscopy or Quasi-Elastic Light Scattering, is a rapid method capable of measuring the size of particles in solution without the need for elaborate sample preparation (Malvern, 2013a, Malvern, 2015b). The size value obtained is the hydrodynamic radius. This is defined as "the size of a hypothetical hard sphere that diffuses in the same fashion as that of the particle being measured" (Malvern, 2015a). Figure 3.1 shows the hydrodynamic diameter (D_h) measured in three different scenarios, namely capped particles, aggregates and non-spherical particles. In the case of non-spherical particles the resulting diameter calculated is indicative of the apparent size of the dynamic hydrated/solvated particle.

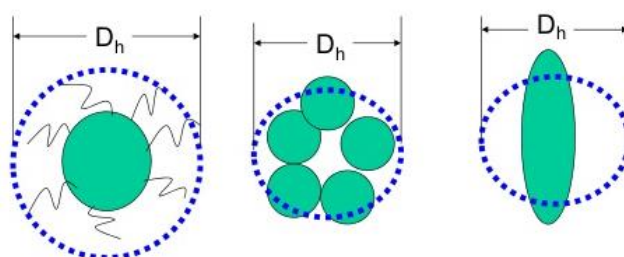


Figure 3.1 Hydrodynamic diameter (D_h) measured in three different scenarios - capped particles, aggregates and non-spherical particles (Far, 2014).

DLS works by using a coherent and monochromatic light, such as a laser, that allows for the observation of time-dependent fluctuations. These are due to the Brownian motion of the small particles, which in turn gives rise to constructive and destructive interference (Berne and Pecora, 1976, Vajtai, 2013, Kaszuba et al., 2008). This occurs as the light passes through the solution and on contact with the particles, is made to scatter (Peters, 2000). In comparison with the wavelength, the intensity of the scattered light is uniform for small particles (Malvern, 2015b). For larger particles the intensity is angle dependent. This intensity is then detected by means of a photomultiplier.

The analysis of the time-dependent fluctuations, which normally occur by means of a digital correlator, gives the diffusion co-efficient of the particles which may then be used along with the medium viscosity and the Stokes Einstein equation, to calculate the particle diameter (Malvern, 2013a, Malvern, 2015b). The Stokes Einstein equation is shown in Equation 3.1 where D is the diffusion co-efficient, k is the Boltzmann constant, T is the temperature, η is the viscosity and R_H is the hydrodynamic radius (Atkins, 2006, Malvern, 2015b).

$$D = \frac{kT}{6\pi\eta R_H}$$

Equation 3.1

Following this analysis of the particle size distribution, which may be done by using a standard log-normal assumption or, without an assumption, is done by fitting the data on assumed distributions. A monodispersed solution would give rise to a single exponential whilst a polydispersed one gives rise to a series of these (Malvern, 2013a).

The polydispersity index (PDI) is a measure of the distribution of the molecular mass in a sample (Atkins, 2006). The PDI is calculated by dividing the weight average molecular weight by the number average molecular weight as shown in Equation 3.2.

$$PDI = \frac{\textit{Weight average molecular weight}}{\textit{Number average molecular weight}}$$

Equation 3.2

The PDI is a dimensionless value. Values greater than 0.7 indicate that the sample has a very broad size distribution and that they are probably not suitable for analysis by means of this characterisation technique. Anything below this value is acceptable although ideally the lower the PDI the better (Malvern Personal Communication, 2012).

Another important value obtained is the Y-Intercept which evaluates the signal-to-noise ratio from a measured sample. It is often used to judge data quality and ideally a value of 1 is obtained although a good system will give intercepts greater than 0.6 and these results are considered acceptable (Malvern Personal Communication, 2012).

Disadvantages of this technique include the significant error in size measurements obtained for non-spherical particles. Furthermore many factors may affect the results. These include polydispersivity, aggregation and contamination (Baalousha et al., 2012). At times better size measurements may be obtained by filtering samples. The benefit of filtering samples is that of the removal of contaminating particles such as dust which may be present in the solvent (Malvern Personal Communication, 2012).

3.2.1.2 Zeta Potential

Owing to the fact that NMs may tend to self-aggregate due to their surface charge (Domènech et al., 2012), stability is an important parameter that needs to be considered when studying materials. The interface between particle and solution is formed of two regions as is seen in Figure 3.2. These are an inner region known as the Stern layer where ions are strongly bound and an outer region where ions are less strongly bound. This results in the presence of an electric double layer around each particle. As a particle moves the ions within the boundary or slipping plane move with it while those beyond do not. The potential at this boundary is known as the zeta potential. The zeta potential value gives an indication of the stability of the system. Particles with zeta potentials more positive than +30 mV or more negative than -30 mV are normally considered stable. When the zeta potential is 0 this is the isoelectric point, the point where no net electrical charge is carried and there is minimal repulsion. Therefore it is the point where the colloidal system is least stable (Malvern, 2013a).

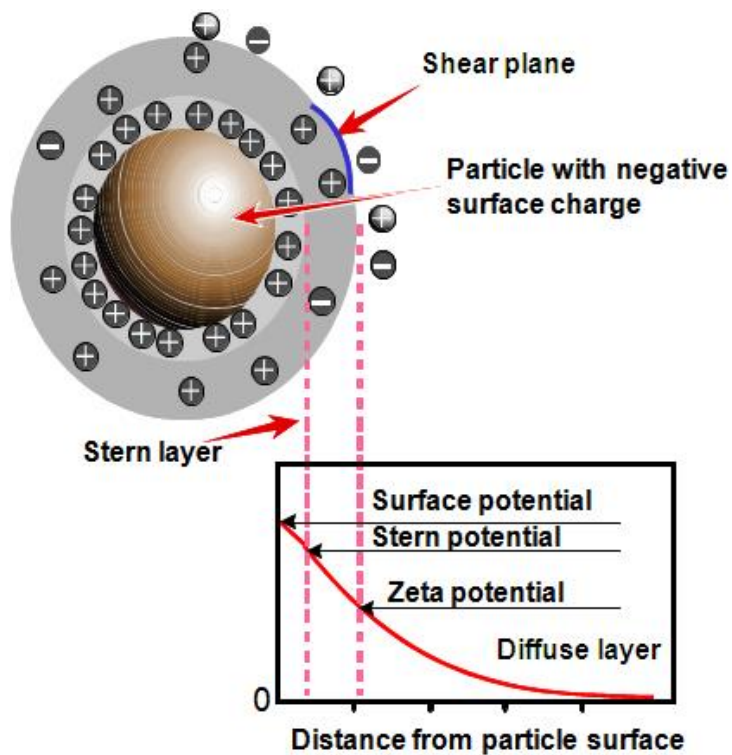


Figure 3.2 Liquid layer around a particle is formed of the Stern Later and diffuse layer (Ensol Instruments Ltd.)

3.2.2 Sample Preparation

Freshly prepared MNM solutions were first filtered through a 0.1 μm filter as shown in Figure 3.3 so as to remove any large particles that might result from solvent impurities or dust and that could interfere with the results. Scale-up samples were more viscous and therefore had to be filtered through a 0.2 μm filter rather than a 0.1 μm filter.

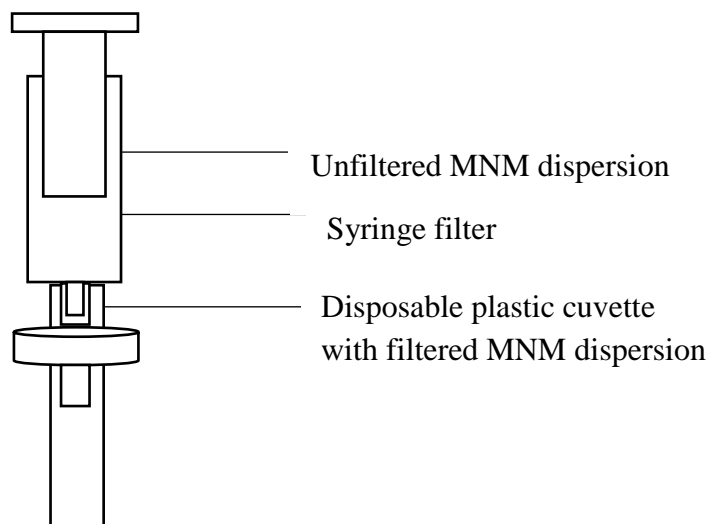


Figure 3.3 Schematic of MNM dispersion being filtered through a syringe filter into cuvette using a syringe.

3.2.3 Procedure

3.2.3.1 Size Analysis

Particle size analysis was carried out on a Malvern Zetasizer (nano ZS) using Zetasizer Software Version 7.10 (Malvern Instruments Ltd, 2014). A polystyrene cuvette was filled with about 1 cm of the filtered MNMs dispersed in water to be analysed. This was then placed in the sample holder of the particle size analysis apparatus. A standard operating procedure was set up for each material and involved inputting the refractive index and absorption values of the material and the dispersant. Once the parameters were set using the software, measurement was begun. A minimum of five consecutive measurements were collected to ensure repeatability and averaged to calculate a Z-Average size. The results were obtained at 20 °C with samples equilibrated for 2 minutes before measurements were started. The Stokes–Einstein algorithm (Equation 3.1) was

used to calculate the hydrodynamic diameter of analysed particles. The results obtained for three repeat samples were averaged.

3.2.3.1.1 Data Analysis

To add confidence and robustness the DLS data obtained from the temperature ageing study was analysed using a statistical method since observed changes were often subtle. The Pearson's product moment correlation coefficient (PCC) was calculated. This is a measure of the linear correlation and dependence between two variables. The coefficient is given as a value between +1 and -1 inclusive, where 1 is total positive correlation, 0 is no correlation and -1 is total negative correlation (Crawford, 2006). When the PCC analysis was successful, Excel stated the following, "The pair(s) of variables with positive correlation coefficients and P values below 0.050 tend to increase together. For the pairs with negative correlation coefficients and P values below 0.050, one variable tends to decrease while the other increases. For pairs with P values greater than 0.050, there is no significant relationship between the two variables."

3.2.3.2 Zeta Potential Analysis

Zeta potential analysis was carried out on a Malvern Zetasizer (nano ZS) using Zetasizer Software Version 7.10 (Malvern Instruments Ltd, 2014). A zeta potential cuvette (Figure 3.4) was injected with about 1 mL of the NMs dispersed in deionised water to be analysed and was then placed in the sample holder of the apparatus. A standard operating procedure was once again set up for each material and involved inputting the refractive index and absorption values of the material and the dispersant. Once the

parameters were set using the software, the measurement was begun. A minimum of three consecutive measurements were collected to ensure repeatability and averaged to calculate the Average Zeta Potential. The results were taken at 20 °C with samples equilibrated for 2 min before measurements were started. The results obtained for three repeat samples were averaged.

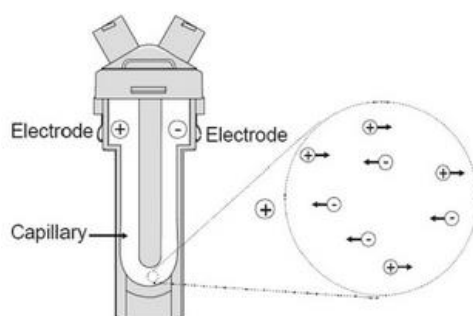


Figure 3.4 Zeta potential cell used for the measurement analysis (The Hebrew University of Jerusalem, 2009).

3.3 Ultra-Violet Visible Spectroscopy (UV-VIS)

3.3.1 Technique

Many molecules are able to absorb ultraviolet or visible light. When light is absorbed by outer valence electrons of an atom the electrons shift from the ground state to an excited higher orbital energy state as seen in Figure 3.5.

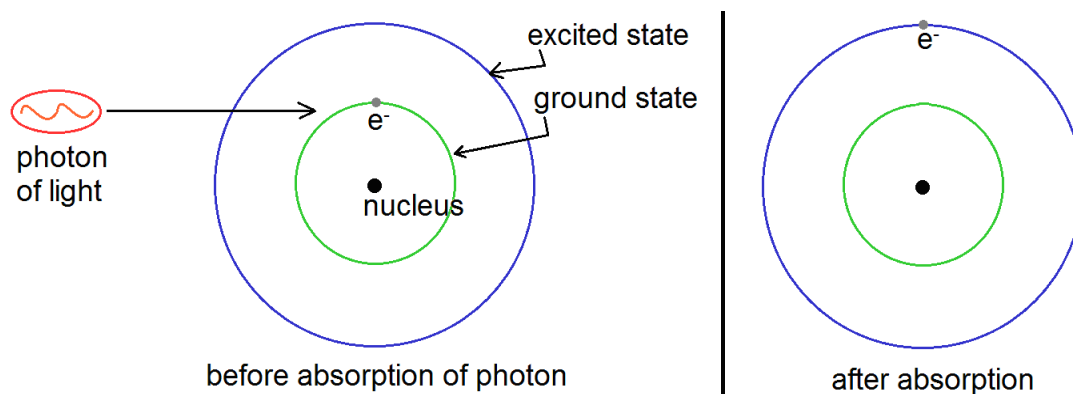


Figure 3.5 Excitation of electrons by means of light (Deciedro, 2011).

Every molecular species is capable of absorbing a characteristic frequency. This absorption attenuates the beam meaning it decreases the energy per unit area of beam radiation according to the absorption law. This law is also known as Beer-Lambert's law (Christian, 2004).

This law is a quantitative method to obtain the amount of attenuation. According to Beer-Lambert's law absorbance is directly proportional to the path length, b , and the concentration, c , of the absorbing species as seen in Equation 3.3 below. ϵ is a constant of proportionality called the *absorbivity*.

$$A = \epsilon bc$$

Equation 3.3

It is important to note that, Beer-Lambert's law is a limiting law in that it only describes absorption behaviour of dilute solutions (Christian, 2004).

This absorption property is exploited as a means of characterisation. Spectroscopists use the interactions of radiation with matter to obtain information about samples via a technique known as ultra-violet visible spectroscopy (UV-VIS). This

technique works by exciting the electrons by means of radiation and recording the attenuated light resulting in a plotted graph of absorbance versus wavelength. Figure 3.6 shows the internal equipment set-up.

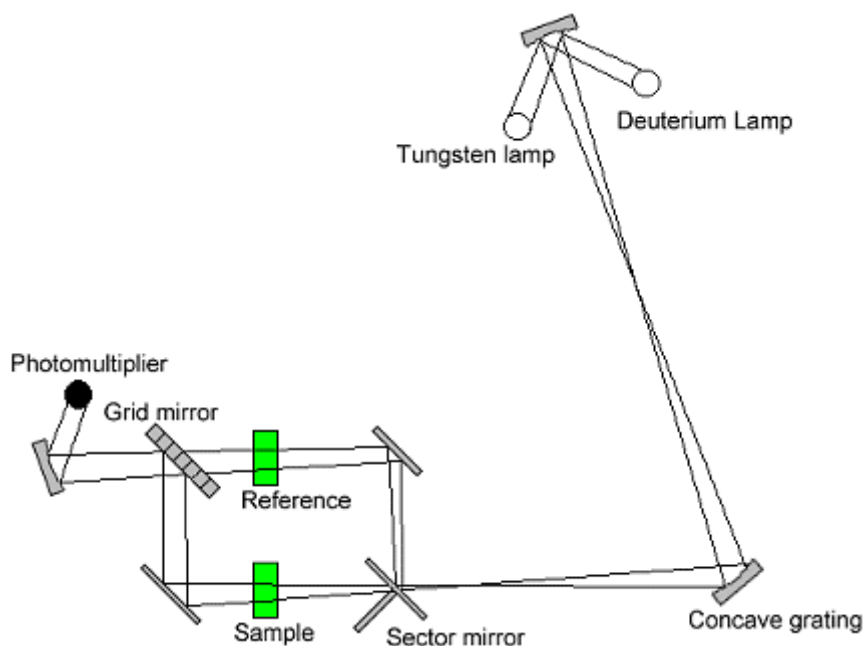


Figure 3.6 UV-VIS Spectrophotometer set-up (Sheffield Hallam University, 2015).

Absorption spectroscopy measures the amount of light absorbed as a function of wavelength resulting in a plot of intensity against wavelength. Like any other technique UV-VIS spectrometry has its advantages and disadvantages.

The UV-VIS is relatively easy to use, involves a rapid analysis and little sample preparation is required. A blank run can help to eliminate reflection scattering and absorption which may be due to the solvent. Errors, however, can arise due to nonlinear behaviour of the sample, the use of the wrong cuvette and solutions which are too concentrated.

3.3.2 Sample Preparation

Samples were diluted as necessary prior to UV absorption measurements. Unless stated otherwise when presenting the UV-VIS results obtained, the dilution involved adding 50 μL of the MNM dispersion to 5000 μL of deionised water.

3.3.3 Procedure

UV-VIS absorption spectra were obtained by means of a Jenway 6800 UV-VIS spectrophotometer. For analysis scans ranging below 300 nm quartz cuvettes (10 cm long) were used. If the scans commenced from 300 nm polystyrene cuvettes were used. A background spectrum was first obtained using ultrapure water. Following this spectrum scans of the MNM sample alongside a reference sample were run from 200 nm or 300 nm to 800 nm. Three readings were obtained to ensure reproducibility of the measurement and the average value was plotted. Where multiple repeat samples were used the average of the averaged UV-VIS results were plotted.

3.4 X-ray Photoelectron Spectroscopy (XPS)

3.4.1 Technique

X-ray photoelectron spectroscopy (XPS), also known as ESCA (electron spectroscopy for chemical analysis), was developed in the mid-1960s by Kai Siegbahn and his research group at the University of Uppsala in Sweden (Kratos Analytical Ltd., 2015, Engelhard, 2015, Materials Evaluation and Engineering Inc., 2009, King et al., 1995). The

technique is able to provide both elemental and chemical state information about the surface of solid material samples with virtually no restriction on the type of material which can be analysed (Kratos Analytical Ltd., 2015, Engelhard, 2015, Materials Evaluation and Engineering Inc., 2009).

A survey scan is carried out to obtain energy peaks that can be used for the identification of the elemental composition of the uppermost 20 to 50 Å of the analysed surface. All elements, except hydrogen and helium, can be detected (Materials Evaluation and Engineering Inc., 2009).

The sample is placed in an ultrahigh vacuum and is illuminated with low-energy x-rays (monochromatic or unfiltered Al K α or Mg K α). In modern spectrometers the x-rays are energy filtered or monochromatised using a quartz crystal to give x-rays with very little energy spread (Engelhard, 2015). The incident x-rays cause photoelectrons to be emitted from the surface as shown in Figure 3.7. The kinetic energy of these emitted electrons is characteristic of the element from which the photoelectron originated. Shake-up satellites may occur when the outgoing photoelectron simultaneously interacts with a valence e⁻ and excites it (shakes it up) to a higher energy level; the energy of the core e⁻ is then reduced slightly giving a satellite structure a few eV below (but above on a BE scale) the core level position.

The energy of this transition is balanced by the emission of an Auger electron or a characteristic x-ray. The analysis of Auger electrons can be used in XPS, in addition to emitted photoelectrons. The photoelectrons and Auger electrons emitted from the sample are detected by an electron energy analyser and their energy is determined as a function of their velocity entering the detector. By counting the number of photoelectrons and Auger electrons as a function of their energy, a spectrum representing the surface composition is

obtained. The position and intensity of the peaks in an energy spectrum provide the desired chemical state and quantitative information which is the primary data used for XPS (King et al., 1995).

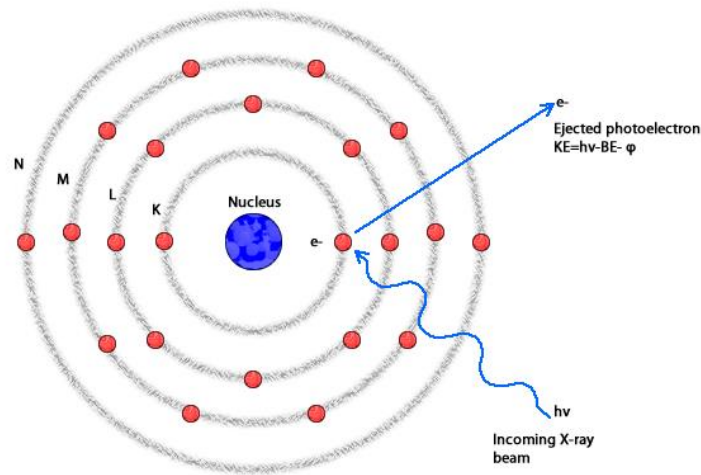


Figure 3.7 XPS process where the sample is bombarded with incoming x-ray beams and photoelectrons, with unique information depending on the sample material, are emitted (Chavez, 2011).

The desired chemical state and quantitative information are unique to a sample due to the fact that the chemical state of an atom alters the binding energy (BE) of a photoelectron which results in a change in the measured kinetic energy (KE). The BE is related to the measured photoelectron KE by means of Equation 3.4 where $h\nu$ is the photon (x-ray) energy (Kratos Analytical Ltd., 2015).

$$BE = h\nu - KE$$

Equation 3.4

The area under a peak in the spectrum is a measure of the relative amount of the element represented by that peak.

XPS is a surface sensitive technique because only those electrons generated near the surface escape and are detected. The photoelectrons of interest have relatively low kinetic energy. Due to inelastic collisions within the sample's atomic structure photoelectrons originating more than 20 to 50 Å below the surface cannot escape with sufficient energy to be detected.

For XPS analysis to take place the samples must not exceed 25 mm in any direction. Additionally the height should not exceed 12 mm and the samples must be compatible with an ultra-high vacuum environment (Materials Evaluation and Engineering Inc., 2009).

XPS is commonly used for the analysis of thin film contaminations, the evaluation of adhesion failures, the measurement of elemental composition of insulating materials (e.g., polymers, glasses), the identification of the chemical state of surface films (e.g., metal or oxide) and the quantitative elemental depth profiling of insulators. Furthermore, depth profiling and mapping are other analysis methods that can be carried out in order to obtain more information about the samples (Materials Evaluation and Engineering Inc., 2009).

3.4.2 Sample Preparation

A drop of the MNM dispersion was placed on the surface of a silicon wafer and allowed to air-dry overnight. It was ensured that the layer formed was thin and free from

air bubbles and cracks by spreading the drop placed on the wafer. The samples were then mounted on the sample holder as seen in Figure 3.8.

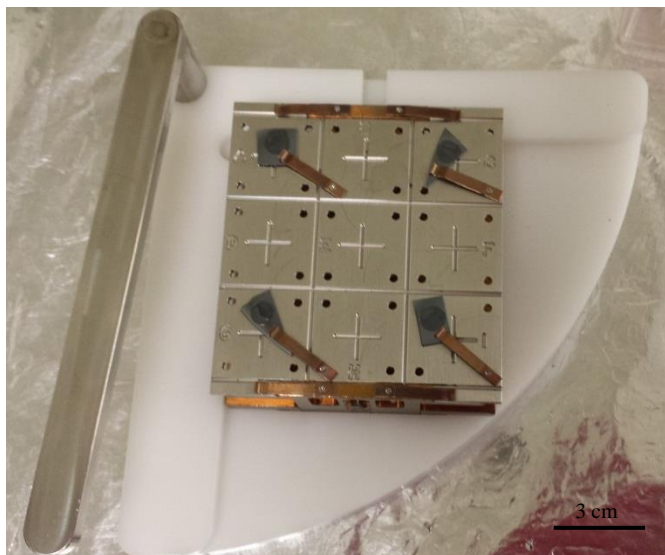


Figure 3.8 Mounted samples on sample holder

3.4.3 Procedure

XPS characterisation was carried out at Karlsruhe Institute for Technology (KIT) in Germany by Dip.-Ing. Vanessa Trouillet. XPS measurements were taken using a K-Alpha XPS spectrometer (ThermoFisher Scientific, East Grinstead, UK). All samples were analyzed using a microfocused, monochromated Al $K\alpha$ X-ray source (400 μm spot size). Two random points were analysed for each of the samples. The K-Alpha charge compensation system was employed during analysis, using electrons of 8 eV energy and low-energy argon ions to prevent any localized charge build-up. The spectra were fitted with one or more Voigt profiles (BE uncertainty: $\pm 0.2\text{eV}$) and Schofield sensitivity factors were applied for quantification. All spectra were referenced to the C1s peak (C-C, C-H) at

285.0 eV binding energy controlled by means of the known photoelectron peaks of metallic Cu, Ag, and Au, respectively.

3.5 Fourier Transform Infra-Red Spectroscopy (FT-IR)

3.5.1 Technique

Infra-red (IR) spectroscopy is a characterisation technique which allows for the structural identification of organic and inorganic molecules. The sample is irradiated with IR electromagnetic radiation ($\lambda = 0.7 \mu\text{m}$ to c. 1 mm) which causes vibrations, rotations and translations of the bonds within the molecule. These can be seen represented in Figure 3.9 for the ball and stick molecule shown. These vibrations, rotations and translations are unique for specific bonds. However, only vibrations which result in a rhythmical change in dipole moment of the molecule are observed in the IR spectrum obtained (Chapple, 2003, Silverstein, 2005).

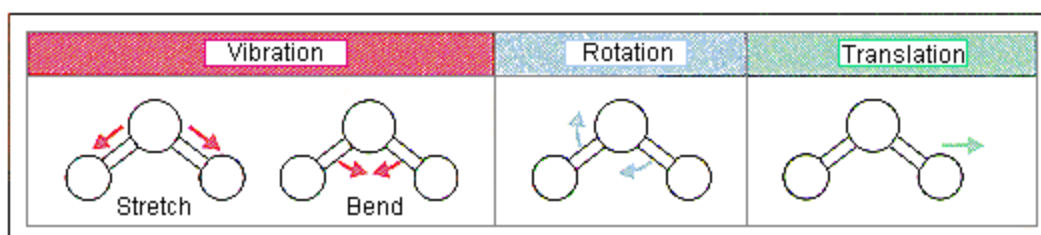


Figure 3.9 Vibration, rotation, translation (Intermolecular Forces, 2014)

Fourier Transform Infra-red spectroscopy involves splitting all the IR radiation into two beams, one of which is constant while the other is variable. Varying the distance between these two beams will result in the formation of constructive and destructive

interference. Repetitive variation gives rise to the entire radiation range passing through the samples (Silverstein, 2005).

3.5.2 Sample Preparation

Samples for FT-IR analysis were prepared in two ways. The first method involved freeze-drying the samples by leaving them to dry in covered vials for at least 24 hours. Dried samples were then crushed to obtain a powder to be used for analysis. The second method involved drying samples in a Gallenkamp hot box oven with a fan for three days.

3.5.3 Procedure

This characterisation technique was carried out using a Varian 660-IR FT-IR Spectrophotometer at the Chemistry Department of the University of Birmingham. ‘Agilent resolutions pro’ software (Agilent Technologies, 2012) was used to run the spectrometer. At the start background scans were carried out. Subsequently powdered samples were placed on the Attenuated Total Reflectance (ATR) attachment seen in and sample spectra were obtained between 400 and 4000 nm.

3.6 X-ray Diffraction (XRD)

3.6.1 Technique

X-ray diffraction (XRD) is a characterisation technique that allows for chemical composition determination and the analysis of a material’s structure. It is a technique that

makes use of X-rays in order to measure the inter-particle spacing resulting from interference between waves reflecting from different crystal planes (Hassellöv *et al.*, 2008) as seen in Figure 3.10.

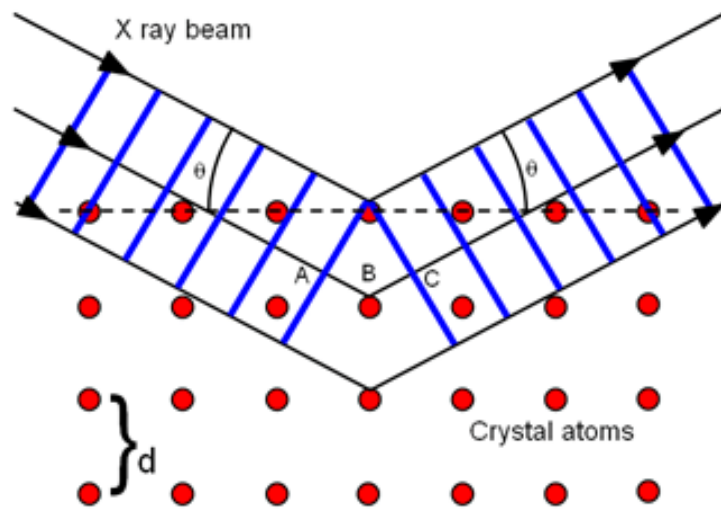


Figure 3.10 X-ray diffraction in crystalline material (Institute of Physics, 2015).

When x-rays are incident on an atom the beam may be absorbed and eject electrons (Warren, 1989) that oscillate with the same frequency as the incident beam. When x-rays are scattered from a crystal lattice peaks of scattered intensity may be observed. The conditions for maximum intensity contained in Bragg's law are shown in Equation 3.5 where d is the distance between crystal planes, θ is the angle between the incident ray and the scattering planes, λ is the wavelength and n is an integer determined by the order given (Bragg and Bragg, 1913).

$$2d\sin\theta = n\lambda$$

Equation 3.5

Due to the fact that emitted intensities are dependent on the atoms present and their location within the unit cell they are unique to a material (Suryanarayana and Norton, 2013, Hammond, 2015, Brundle et al., 1992). Therefore both elemental composition and average crystal structures can be determined (Suryanarayana and Norton, 2013, Hammond, 2015, Brundle et al., 1992). The technique is also suitable for evaluating microstructure by analysing width and shape of peaks.

XRD analysis is relatively easy with analysis possible in various atmospheres and simple sample preparation. A drawback is that samples need to be solid and adequately dried as the presence of water effects the pattern obtained. Additionally the sensitivity of XRD is lower than other elemental techniques. Despite this elemental composition and lattice structure can still be obtained (Suryanarayana and Norton, 2013, Hammond, 2015, Brundle et al., 1992).

3.6.2 Sample Preparation

Samples were dried at 60 °C in a Gallenkamp hot box oven with a fan for three days to ensure complete drying. Dried samples were then crushed to obtain the powder to be used for analysis.

3.6.3 Procedure

XRD analysis was carried out in the Department of Chemistry at the University of Birmingham using a Bruker D8 Advance diffractometer. Powdered samples were loaded into a 1 cm² disk holder using scotch tape and loaded into the diffractometer. Diffraction patterns were obtained by scanning with CuK α radiation over a range of Bragg angles (20⁰

to 80°) at room temperature over a period of 28 minutes. The resultant patterns were depicted as obtained and then analysed by comparing them to reference spectra using Eva software (Bruker, 2016).

3.7 Transmission Electron Microscopy (TEM)

3.7.1 Technique

The Transmission Electron Microscope (TEM), the first of which was built by Knoll and Ruska in 1931 (Romer Roche, 2013, Knoll and Ruska, 1932), is an indispensable tool for the analysis of nanomaterials. This is due to its ability to provide structural and chemical information over a range of length scales down to the level of atomic dimensions.

Figure 3.11 shows a side-view schematic of a TEM. It operates by generating high energy electrons with an accelerating voltage up to 300 kV by means of the electron gun (a field emission gun (FEG)) found at the top of the microscopic column. The gun typically uses a lanthanum hexaboride or tungsten thermionic emission source (Wang, 2000).

The electrons produced by a FEG are accelerated and then focused on the sample by a system of electromagnetic lenses (Kuntsche et al., 2011). The electron beam is emitted through the sample where they are scattered (changed in direction) by interaction with atoms of the solid. The scattered electrons then form a focused visual image of the sample on the fluorescent screen. The focusing of the image occurs by means of the different lenses (Goodwin, 2004). Although only a small amount of sample is needed for analysis this is the only amount analysed and therefore reduces the representative analysis.

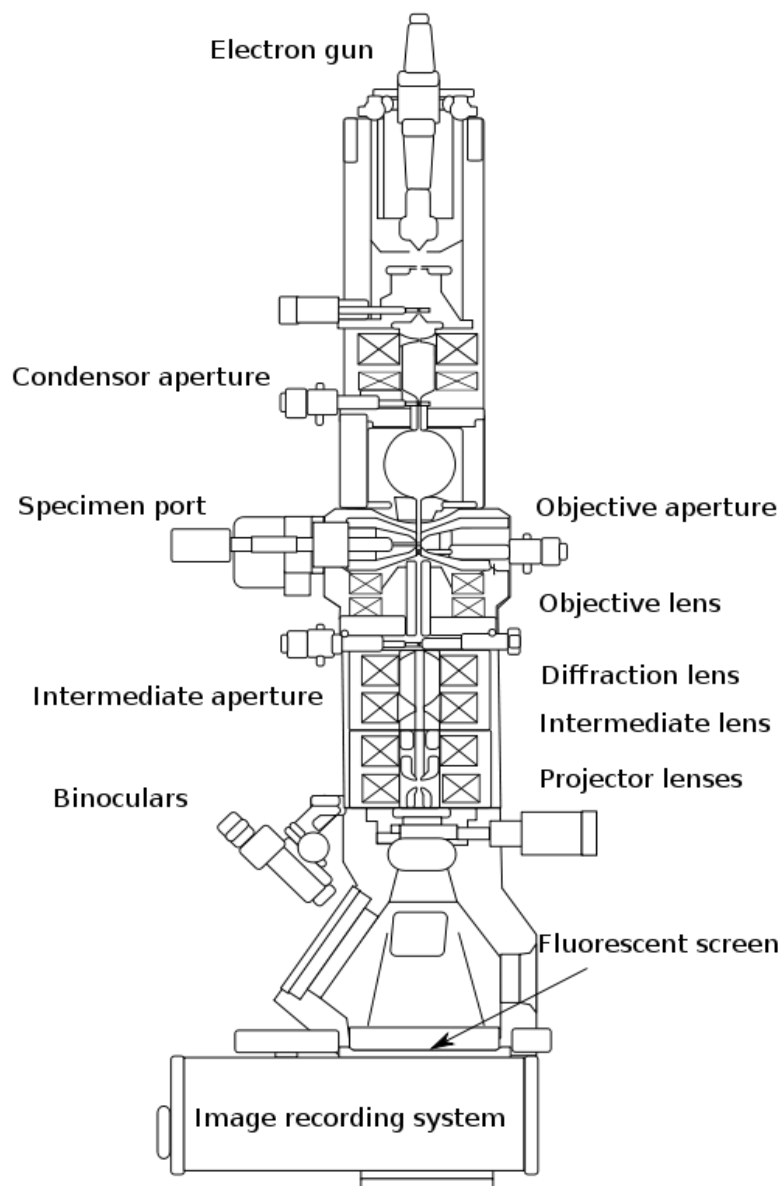


Figure 3.11 Side-view schematic of Transmission Electron Microscope (Foothill College, 2014)

3.7.2 Sample Preparation

Samples for TEM analysis were prepared on copper grids coated with a thin film of holey carbon (Carbon film on 300 mesh Copper grids 3.05 mm) using the drop method. This involves placing a drop of sample on the surface of the grid which was held stationary and suspended by means of TEM tweezers. The drop was allowed to stand on the grid for

a period of half an hour to an hour to allow the nanomaterials to adhere to the surface of the grid. Following this the grids were gently dipped repeatedly in ultrapure water to remove any loose material and excess salts from the grid. Any excess water that remained was carefully removed with a tissue. The grids were allowed to air-dry and kept covered to prevent any contamination from taking place. The sample preparation is simple. However, despite this, the drop method preparation may cause artefacts and change the structure of the materials imaged (Domingos et al., 2009).

3.7.3 Procedure

Imaging was carried out by means of a JEOL 1200EX TEM (accelerating voltage 80 kV). Image J was used to analyse the data (Rasband, 2015). In order to obtain a size distribution plotted as a histogram, at least 100 particles of each sample had to be analysed using this software.

3.8 Scanning Transmission Electron Microscopy-Electron Energy Loss Spectroscopy (STEM-EELS)

3.8.1 Technique

3.8.1.1 STEM

The Scanning transmission electron microscope (STEM), the first of which was built in 1938 by von Ardenne (Bogner et al., 2007), is a valuable tool for the

characterisation of nanomaterials. It offers a range of different imaging modes to provide information about elemental composition and electronic structure at the ultimate sensitivity, that of a single atom (Pennycook et al., 2007). The instrument works by combining principles of both the transmission electron microscope (TEM) and the scanning electron microscope (SEM) (Tanaka, 1992, FEI, 2015). Like TEM, STEM use requires very thin samples and looks primarily at beam electrons transmitted by the sample (Pennycook et al., 2007, FEI, 2015). STEM, a schematic of which can be seen in Figure 3.12, works like SEM, by forming a focused beam of electrons that is scanned over the sample from the upper-left to lower-right pixels of a specimen while some desired signal is collected to form an image (Tanaka, 1992, Pennycook et al., 2007, FEI, 2015). Electrons are accelerated from a source and focused to a point on the specimen by a set of condenser lenses and an objective lens. An objective aperture limits the maximum angle of illumination included in the incident probe which is scanned across the sample by a set of scan coils. The output of a variety of possible detectors can then be used to form an image (Pennycook et al., 2007). The usual detectors include a bright field (BF) detector that intercepts the transmitted beam and an annular dark field (ADF) detector that surrounds the transmitted beam to collect scattered electrons (Pennycook et al., 2007). The inner angle of this detector can be changed with post-specimen lenses from just outside the incident beam cone which gives maximum efficiency for collecting scattered electrons. This enhances the atomic number (Z) dependence of the image contrast and this configuration is often referred to as a Z -contrast or high-angle ADF (HAADF) image (Pennycook et al., 2007).

One of its principal advantages over the TEM is that it allows for the use of other signals such as secondary electrons, scattered beam electrons, characteristic X-rays and

electron energy loss that cannot be spatially correlated in the TEM (FEI, 2015). Its primary advantage over conventional SEM imaging is the improvement in spatial resolution (FEI, 2015). Other advantages include the ability to detect single atoms in annular dark-field STEM (ADF-STEM) where images are formed using large-angle scattered electrons (Tanaka, 1992). These images are straightforward to interpret and of higher resolution than those obtained in TEM studies for a lens with the same aberration coefficient (Tanaka, 1992).

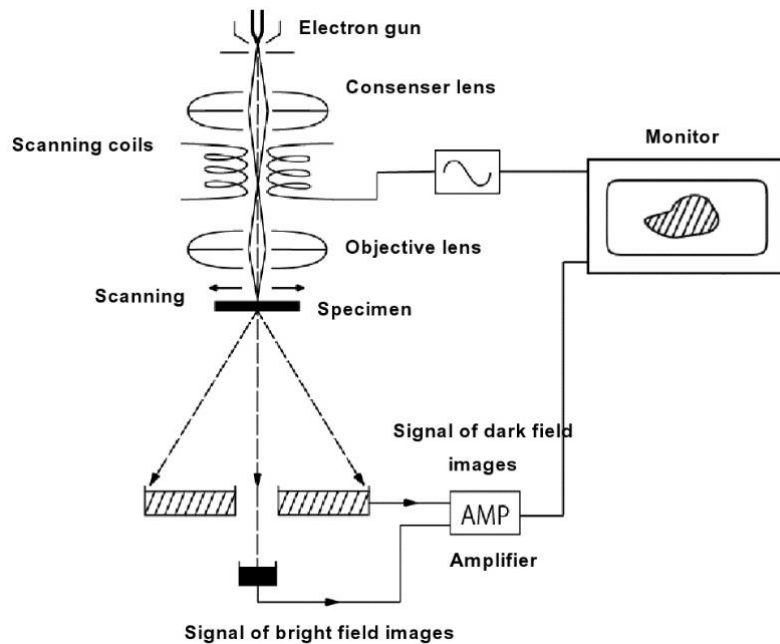


Figure 3.12 STEM Schematic (Tanaka, 1992)

3.8.1.2 Electron Energy Loss Spectroscopy (EELS)

Electron energy loss spectroscopy (EELS) involves measuring energy loss dispersion of inelastically scattered high-energy electrons transmitted through a thin sample (Browning and Pennycook, 2000, Hutchison, 2007). Inelastic scattering involves

the kinetic energy of incident particles not conserved and therefore when high-energy electrons interact with electrons in a solid they lose a certain amount of energy characteristic to the material and in turn transfer momentum to the solid (Browning and Pennycook, 2000). Inelastic scattering can be due to a range of processes: inter and intra band transitions, photon excitations, inner shell ionisations, plasmon excitations and Cherenkov radiation (Hutchison, 2007).

After the electron beam passes through the sample the electrons are split into their relative energies and collected by a detector. The amount of electrons collected for each energy value were recorded and plotted. Undetected electrons that have the same energy as the original electron beam make up the zero loss peak. Detected electrons which have interacted with inner shell atom electrons and vary in their energy content form the spectral peaks (Hutchison, 2007). Spectral peaks are characteristic to the material and can therefore be used for elemental analysis.

3.8.2 Sample Preparation

Samples for STEM analysis were prepared by means of the drop method as those for TEM investigation described in Section 3.7.2.

3.8.3 Procedure

STEM imaging and STEM-EELS analysis were carried out at the Physics Department of the University of Birmingham by Dimitri Hapiuk and Jian Liu. The HAADF (High-angle annular dark field)-STEM imaging was performed in a 200 kV

JEM2100F STEM (JEOL) with a spherical aberration corrector. HAADF images were acquired with inner and outer angles of 62 and 164 mrad at a probe convergence semi-angle of 19 mrad and camera length of 10 cm. The EELS spectra were recorded with an Enfina detector attached to a JEM2100F STEM (JEOL) operated at 200 kV. The collection semi-angle was 57.8 mrad, the camera length was 2 cm and the aperture size was 5 mm. The FWHM value at the zero-loss peak was 4 eV with a dispersion of 0.5 eV/channel and a 5 s acquisition time for CeO_x and 10 s for CuO_x, respectively. Reference spectra for each nanomaterial were obtained using commercially obtained nanomaterials. The EELS data was processed with DigitalMicrograph software (version 2.11).

3.9 Energy Dispersive X-ray Spectroscopy (EDX)

3.9.1 Technique

Energy dispersive X-ray spectroscopy (EDX) is a characterisation technique used to detect the chemical composition of a sample. When a sample is irradiated with a high energy beam an electron from the inner shell is emitted, thus ionising the atom. The atom quickly returns to a stable state by filling the vacancy with one of the outer electrons which will drop down into the vacant inner shell (Brydson and Hondow, 2011, Leng, 2008, Hutchison, 2007). The de-excitation process and hence the energy difference between the outer and inner shell electrons emits X-rays which are characteristic to the atom involved and can therefore be used for elemental analysis (Brydson and Hondow, 2011, Williams, 1996). Alternatively, another electron can be emitted, known as an Auger electron, which

can also be used for elemental analysis in other techniques (Leng, 2008). The principle for EDX can be seen in Figure 3.13 (Hutchison, 2007).

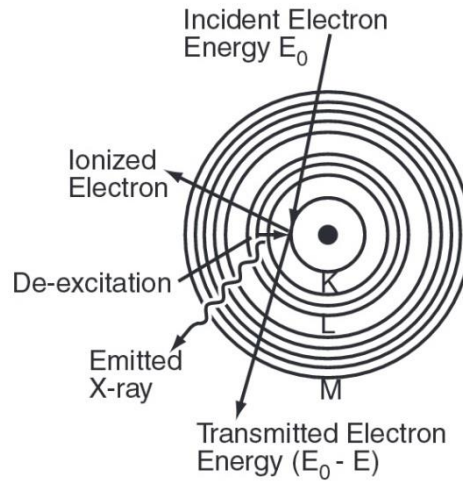


Figure 3.13 EDX Principle (Hutchison, 2007)

Moseley (1913) defined the relationship between the characteristic X-ray wavelengths (λ) and the atomic number (Z) as seen in Equation 3.6, where B and σ are constants that depend on the specific shells.

$$\lambda = \frac{B}{(Z - \sigma)^2}$$

Equation 3.6

Elements are able to generate more than one characteristic x-ray energy depending on the electron transition taking place. These are known as the K, L and M series, where a K series relates to the transition which takes place to fill a vacancy in the K orbital. The disadvantage of such a system is that it cannot detect light elements (up to Be) due to very few detectable X-rays being generated (Leng, 2008).

3.9.2 Sample Preparation

Samples were prepared as for TEM by means of the drop method as explained in Section 3.7.2.

3.9.3 Procedure

EDX was carried out by Jian Liu and Dimitri Hapiuk at the Nanoscale Physics Research Laboratory at the University of Birmingham on a JEM2100F STEM coupled with a Bruker XFlash 4030 EDX detector. The electron beam energy was 200 keV and spot size was 5C when recording the EDX spectra. Further imaging and EDX spectroscopy were carried out by Theresa Morris at the School of Metallurgy and Materials at the University of Birmingham. Samples were analysed by means of a JEOL 2100 TEM (accelerating voltage 200 keV). Inca was used in order to analyse the spectra obtained.

3.10 Extended X-ray Absorption Fine Spectroscopy (EXAFS)

3.10.1 X-ray absorption spectroscopy (XAS) Technique

X-ray absorption spectroscopy (XAS) is a widely used technique for determining the local geometric and/or electronic structure of matter. X-rays are ionising radiation that have sufficient energy to eject a core electron from an atom. Each core shell has a distinct

binding energy from which valuable structural and elemental information can be obtained (Penner-Hahn, 2001).

The technique involves a monochromatic energy beam of X-rays passing through a homogeneous sample, being absorbed and resulting in the excitation of an electron. The electron will be ejected when the photon energy is larger than the binding energy of the electron. In accordance with Beer-Lambert's law (already discussed in Section 3.3.1) this attenuation can be described by Equation 3.7 (Bauer and Bertagnolli, 2012, Antonio, 1992).

$$I(E) = I_0(E) \exp(-\mu(E) \cdot d)$$

Equation 3.7

Where $I(E)$ and $I_0(E)$ are the incident and transmitted x-ray intensities, $\mu(E)$ is the linear absorption coefficient and d is the sample thickness (Bauer and Bertagnolli, 2012, Antonio, 1992). The absorption coefficient decreases as the energy of the incident photon increases until a critical wavelength is achieved where the absorption coefficient increases abruptly (Figure 3.14). This rise indicates the ejection of a core electron of an atom and is called the absorption edge. Following this the absorption coefficient decreases monotonically with increasing energy until the next absorption edge is reached (Figure 3.14) (Bauer and Bertagnolli, 2012).

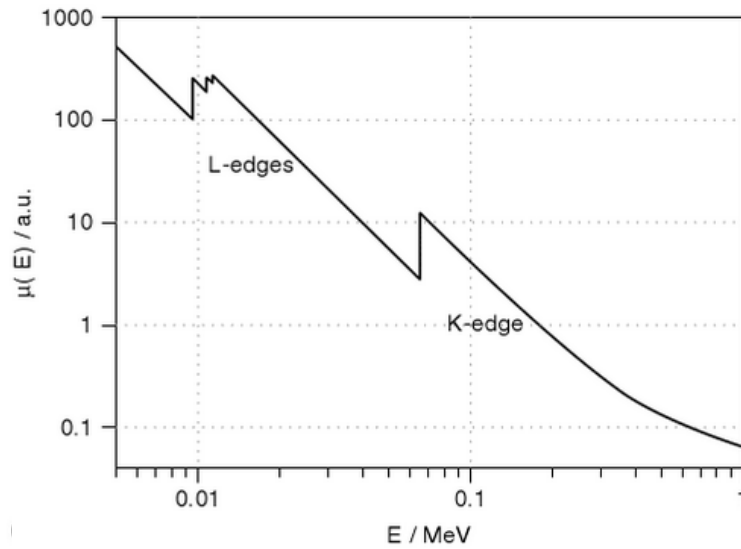


Figure 3.14 Example indication of L- and K- edges as the energy coefficient decreases with increasing energy until an absorption edge is reached (Bauer and Bertagnolli, 2012).

This behaviour only occurs with isolated atoms as the outgoing wave is spherical and results in X-ray absorption near edge spectroscopy (XANES) (Bauer and Bertagnolli, 2012, Glatzel and Juhin, 2013). For atoms in a molecule or in a condensed phase the absorption coefficient above the absorption edge displays a fine structure termed EXAFS, an acronym for extended X-ray absorption fine structure (Bauer and Bertagnolli, 2012, Antonio, 1992).

Therefore in an X-ray absorption spectroscopy (XAS) spectrum there are two parts, namely the XANES and the EXAFS as seen in Figure 3.15. The EXAFS spectrum results from constructive and destructive interference between the outgoing and the incoming photoelectron waves at the absorbing atom (Antonio, 1992).

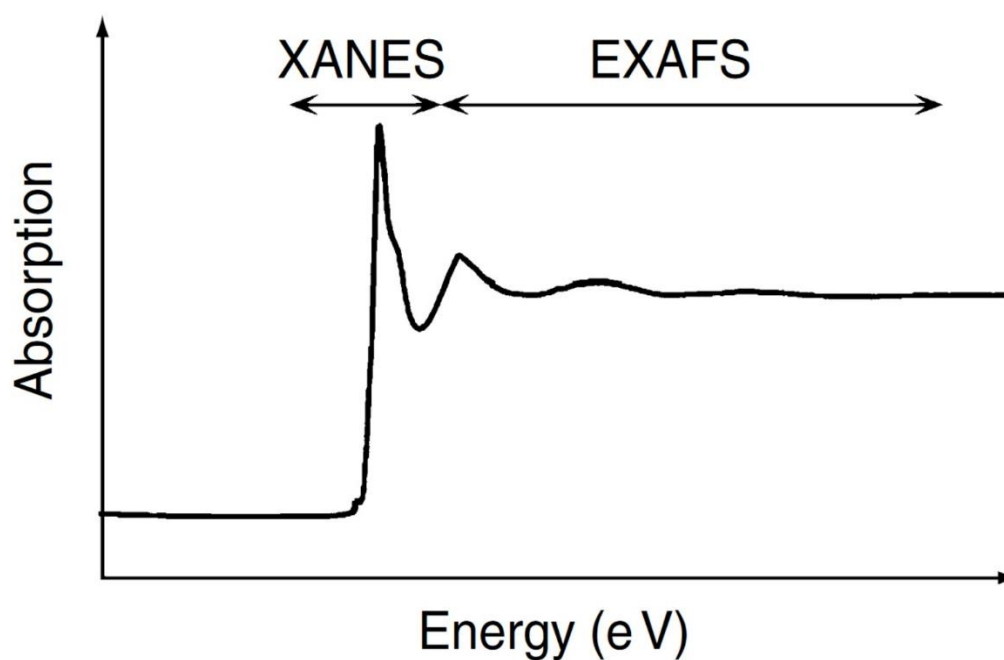


Figure 3.15 X-ray absorption spectroscopy (XAS) spectrum indicating XANES and EXAFS section (Penner-Hahn, 2016).

The EXAFS phenomenon was first detected in 1920 by Fricke and Hertz but the information contained was not fully recognised until the 1970s (Bauer and Bertagnolli, 2012, Antonio, 1992). The non-destructive technique which requires synchrotron radiation (Figure 3.16) provides element specific chemical bonding information. This includes information about the type and the number of neighbouring atoms and their distances from a central atom, that is, the absorbing atom and hence makes the technique widely applicable (Bauer and Bertagnolli, 2012, Antonio, 1992). Furthermore EXAFS is advantageous because the method is independent of the state of the matter and very sensitive up to a concentration of 1 % (Bauer and Bertagnolli, 2012, Antonio, 1992).

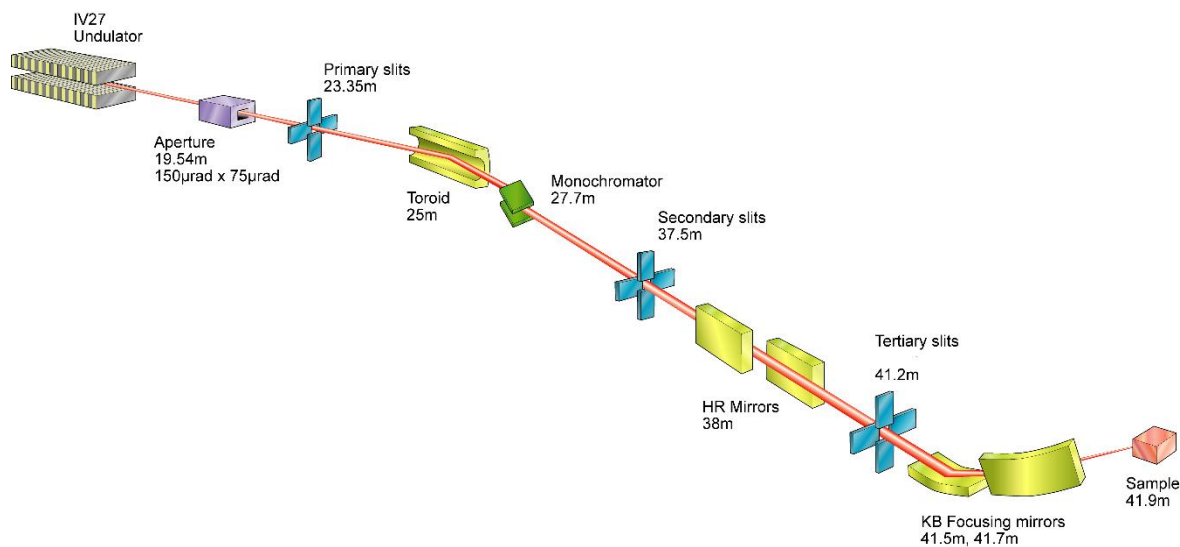


Figure 3.16 Schematic of EXAFS experiment at synchrotron (Diamond Light Source, 2014).

3.10.2 Standard Preparation

Prior to analysis solid powder standard discs had to be prepared for comparative purposes. Standard (copper (I) oxide, copper (II) oxide and zinc oxide) discs were prepared using 4 % wt/wt metal content in a 110 mg disc. The remainder of the weight was constituted of cellulose. The well-ground and mixed metal and cellulose were loaded into a dye and press and loaded with 3 tonnes of pressure. Following this the disc was carefully removed and placed on sticky Kapton tape on the sample holder as seen in Figure 3.17.

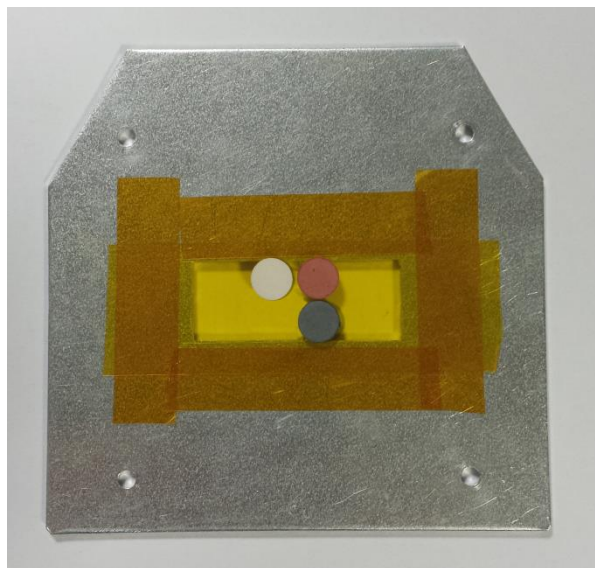


Figure 3.17 Standard discs of zinc oxide (top left), copper (I) oxide (top right) and copper (II) oxide (bottom right) mounted on Kapton Tape.

3.10.3 Sample Preparation

Liquid MNM dispersions were injected into Teflon cells sealed with Kapton tape (Figure 3.18). Samples were then attached to a sample holder using Kapton tape and loaded onto the beamline sample holder.



Figure 3.18 Teflon cell sealed with Kapton tape loaded with PVP capped metal oxide nanomaterial dispersion.

3.10.4 Procedure

Experiments were carried out at beamline I18 of Diamond Light Source in Didcot, UK. Spectra for both the reference samples and nanomaterial samples were obtained. The synchrotron radiation was monochromatised by a double crystal Si (111) monochromator. The measurements were conducted in air at room temperature. Data was processed and normalised in Athena (Ravel, 2015) and sample data was qualitatively compared with that of the reference samples.

3.11 Inductively Coupled Plasma – Optical Emission Spectroscopy (ICP-OES)

3.11.1 Technique

Atomic spectroscopy is the technique for determining the elemental composition of an analyte by its electromagnetic or mass spectrum. One such procedure is Inductively Coupled Plasma Optical Emission Spectroscopy (ICP-OES) seen in Figure 3.19. This method measures the light emitted by excited atoms when they return to their ground state (Chemiasoft, 2014). Each element in the periodic table has its own distinct set of emission wavelengths (EAG, 2014). By comparing the intensity of the emitted light obtained from a sample with that from standards of known concentration the elemental concentrations in the unknown sample are obtained. The ICP-OES method is able to analyse the elements from Li to U, except atmospheric species (C, H, O, N) and noble gases (EAG, 2014). ICP-

OES has many advantages including excellent sample throughput, a very wide analytical range, easy use and is highly automated (Perkin-Elmer Corporation, 2013).

Prior to sample introduction the instrument detector is calibrated using a series of standard reference solutions of known concentration for the analyte(s) of interest. Calibration curves are derived and then verified using standard reference solutions from a source independent of the calibration solutions wavelengths (EAG, 2014).

Although sample types can be liquids, metals, alloys, plastics, polymers or others, the sample is usually introduced in liquid form (Chemiasoft, 2014, EAG, 2014). Solid materials therefore have to be dissolved in an aqueous solution or solvent prior to analysis (Chemiasoft, 2014, EAG, 2014). Depending on the nature and concentration of the liquid samples they may need to be digested or diluted prior to introduction (EAG, 2014).

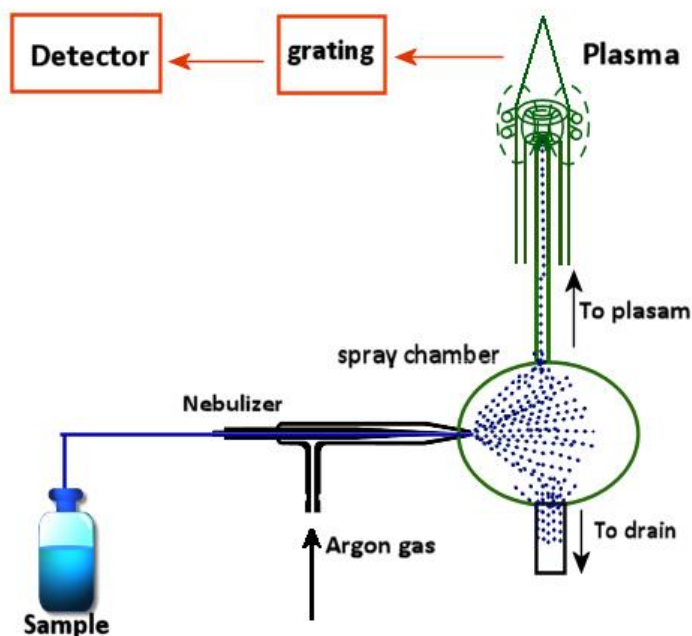


Figure 3.19 Diagram of Sample introduction to ICP-OES.

The liquid goes through different steps when injected to the ICP. It is converted to an aerosol using a nebulizer and then sprayed into the centre of the plasma (Chemiasoft, 2014, EAG, 2014). The next step involves the separation of aerosol within the spray chamber where more than 99 % of the injected sample goes to drain and less than 1 % carried out to the plasma (Chemiasoft, 2014).

The ICP source consists of a quartz torch inside a radio frequency (RF) coil as seen in Figure 3.20. Argon is passed through the torch and RF energy is applied to the coil. When a spark from a Tesla coil is added to the highly energised argon atoms electrons are stripped from the argon and the plasma is formed (Chemiasoft, 2014, EAG, 2014). The argon is present to maintain the plasma (Perkin-Elmer Corporation, 2013). The argon ions and free electrons are further agitated by the RF field causing the temperatures within the plasma to reach approximately 8000-10,000 Kelvin and cause the complete atomisation of the elements present within the sample (Chemiasoft, 2014, EAG, 2014, Perkin-Elmer Corporation, 2013). Adding mechanical energy to the electrons/ions by the use of the induced field within the heart of the plasma is called “Inductively Coupling” (Chemiasoft, 2014).

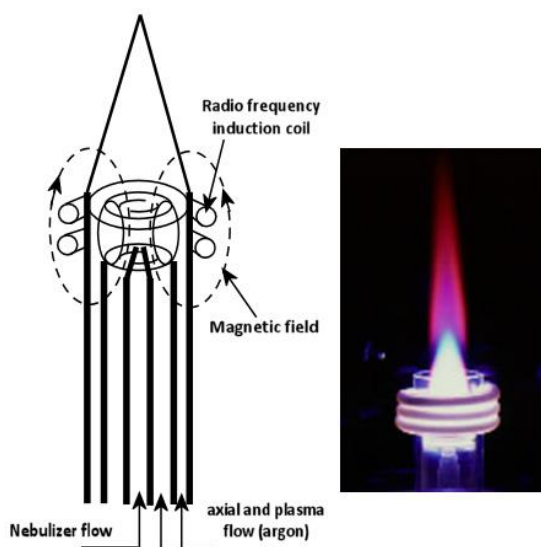


Figure 3.20 Inductively coupled plasma

The plasma excites atoms leading to photon emission and ionisation. The emitted radiation from the plasma is then used for analysis (Chemiasoft, 2014). The light is separated into its component wavelengths using a diffraction grating (EAG, 2014).

Detectors are used to quantify the amount of light at a given wavelength (Chemiasoft, 2014, EAG, 2014). There are two methods by which emitted light can be viewed, radially and axially. Radial viewing involves observing the light emitted by the sample by looking down the centre torch and results in the highest upper linear ranges. Axial viewing involves observation of the continuum background from the ICP itself which is reduced and the sample path is maximised providing better detection limits than those obtained via radial viewing. Finally the quantified light is compared to that of the calibration standards so as to obtain a final elemental concentration analysis of the sample.

3.11.2 Sample Preparation

0.5 μL of the MNM dispersion samples were first digested overnight in 20 % nitric acid. Following this the samples were diluted to 2 % nitric acid. Three batches for each sample type were analysed. Furthermore, for each batch of the different sample type, three repeat samples were measured.

3.11.3 Calibration Standard Sample Preparation

Calibration standards were needed as comparative references for the analysis. 1 ppm, 10 ppm, 50 ppm and 100 ppm calibration standards were prepared using TraceCERT[®] copper, zinc and cerium standards obtained from Sigma-Aldrich. This was

done using commercially obtained zinc, copper and cerium standards diluted to the desired concentration using 2 % nitric acid.

3.11.4 Procedure

ICP-OES analysis was carried out using an Optima 8000 spectrometer. The concentration of the samples was measured by comparison to the concentration of the standards. Methods for the analysis of zinc, copper and ceria were set up and utilised accordingly. Analysis took place using radial detection and a 70 second delay time. The final result was the average of three replicate readings that were obtained for each sample analysed.

Chapter 4: Development of nanomaterial libraries for nanosafety studies: Synthesis and Characterisation of Polyvinylpyrrolidone (PVP) Capped Metal Oxide Nanomaterials

4.1 Introduction

The increased use of manufactured nanomaterials (MNMs) results in increased environmental release, hence concerns that exposure of humans and other organisms is inevitable. The potential environmental impact of MNMs is poorly understood and the need to better understand MNM fate and transformations is particularly urgent. However, in order to do so there is first the need for well-developed and well characterised nanomaterial libraries with systematically varied properties that can be correlated to ecotoxicity studies.

This chapter focuses on the development of a polyvinylpyrrolidone (PVP) nanomaterial library aimed at the development of a set of particles with systematically varying properties. The library involves similarly capped nanoparticles where the core may be one of three commonly used nanomaterials, namely ceria, zinc oxide and copper oxide. The known uses of these nanomaterials have already been discussed in Chapter 2.

The capping chosen was PVP since it successfully stabilises the NMs by attaching to the hydroxyls on the surface of the NMs. Further detail is expounded in Section 4.8 where the reaction mechanism is discussed. Furthermore PVP is generally considered non-toxic. Indeed the U.S. Food and Drug Administration (FDA) has approved this

chemical for many uses (FDA, 2010).

The synthesis method used throughout was the same regardless of the NM core. This consisted of reflux reactions carried out using an identical protocol with the only difference being that equimolar quantities of varied metal nitrates were used.

The NM library prepared using the same method aims to minimise the number of variables between the different NMs. A library of systematically varied NM properties may have a range of applications; in this work they were specifically created to enable observations of the effect of a controlled variation of a single NM physicochemical property to toxicity.

A further development presented in this chapter was the study of a scale-up of the reaction of the NM synthesis. This was achieved by increasing the concentration of the starting reagents by a factor of three and six yet keeping the suspension volume unchanged. The aim of the scale-up was to improve the NMs' yield whilst keeping the process method and reaction duration the same. This fulfilled concentration requirements for samples to be sent to other laboratories for toxicity testing.

This chapter therefore focuses on the synthesis methodology giving a detailed description about the materials, methods and techniques used for the PVP capped metal oxide nanomaterials library synthesis and development. Following the synthesis extensive multi-method characterisation was required to fully describe the materials and their behaviour. This information is vital for the library materials to be used for reference purposes. Furthermore, characterisation results will help to explain future toxicity results. Details on the characterisation techniques implemented have already been discussed in Chapter 3. A manuscript based on the content of this chapter has recently been published (Briffa et al., 2017).

4.2 Chemicals

Chemicals were used as received from the supplier without the need for further purification. Table 4.1 shows the chemicals used together with their brand name and grade.

Table 4.1 Chemicals used in this study.

Chemical Name	Grade	Brand
Copper nitrate trihydrate	GPR	Sigma-Aldrich
Zinc nitrate	GPR	Sigma-Aldrich
Cerium nitrate	GPR	Sigma-Aldrich
Acetone	GPR	Sigma-Aldrich
PVP (10,000)	GPR	Sigma-Aldrich
PVP (40,000)	GPR	Sigma-Aldrich
PVP (360,000)	GPR	Sigma-Aldrich

4.3 Glassware

All glassware was cleaned in 10 % nitric acid solution in order to remove any residue metal ions. Prior to use, the glassware was washed with ultrapure water (18.2 M Ω cm at 25 °C).

4.4 Synthesis of PVP capped metal oxide nanomaterials

4.4.1 Synthesis of PVP capped ceria nanomaterials

PVP capped ceria nanoparticles were synthesised according to Merrifield et al. (2013). The method was chosen as it appeared versatile enough to allow systematic manipulation of material properties.

The synthesis involved dissolving 130 mg of cerium nitrate (Ce(III)NO_3) in a dispersion of 10 K, 40 K or 360 K PVP in deionised water. Varying the molar mass of the PVP had been reported to result in differently sized NMs (Merrifield et al., 2013, Zhou et al., 2007). Quantities and volumes used can be found in Table 4.2.

Table 4.2. Quantities and volumes used to synthesise PVP capped ceria NMs

PVP chain length	Amount of PVP used (g)	Volume of water (mL)	Mass of cerium nitrate used (mg)
10 K	2	60	130
40 K	1	60	130
360 K	0.155	60	130

The mixture was then heated under reflux (Figure 4.1) for 3 hours at around 105 °C following which it was quenched by running the flask under cold water. Once cooled enough acetone was added so that the mixture just turned milky. The acetone/water cosolvent system resulted in the PVP chains aggregating out due to the solubility of PVP in the cosolvent. Although acetone and water are miscible, the cosolvent becomes a poor

solvent for PVP chains, leading to the formation of aggregated globules (Atta et al., 2011). It is these aggregated globules that turn the solution milky.

The solution was then centrifuged at room temperature (24 °C) at 4000 rpm for 10 minutes. The pellet obtained was retained and washed with acetone. 5 mL of ultrapure water were added to the pellet to bring the NMs into suspension. The excess acetone present was allowed to evaporate off by being left to stir overnight in a fume hood.

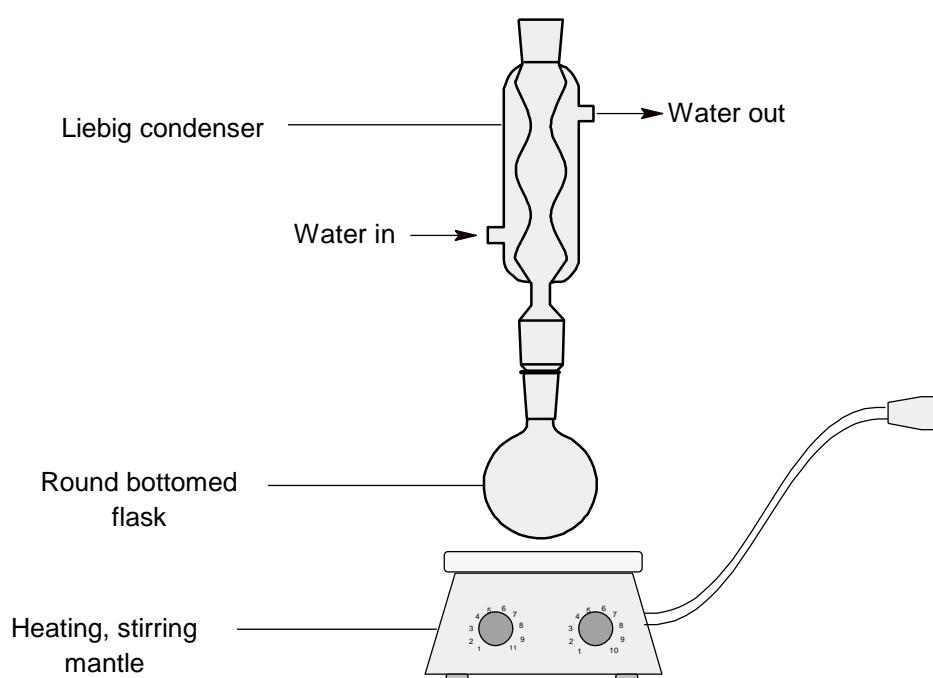


Figure 4.1 Reflux set-up

4.4.2 Synthesis of PVP capped zinc oxide nanomaterials

PVP capped zinc oxide NMs were synthesised by modifying the method used to synthesise PVP capped ceria NMs discussed in Section 4.4.1 above. However, instead of 130 mg of cerium nitrate, 89 mg of zinc nitrate were used as the starting reagent. This meant that an equimolar amount of zinc nitrate was used.

4.4.3 Synthesis of PVP capped copper oxide nanomaterials

PVP capped copper oxide NMs were synthesised using the same method used to synthesise PVP capped ceria NMs discussed in Section 4.4.1 above. However, instead of 130 mg of cerium nitrate, 73 mg of copper nitrate were used as the starting reagent. This meant that an equimolar amount of copper nitrate was used.

4.4.4 Synthesis of PVP reference sample

PVP control samples were synthesised to act as reference samples. The method used was the same as that to synthesise PVP capped ceria NMs discussed in Section 4.4.1 above. However, the metal-bearing nitrate starting reagent was omitted.

4.4.5 Reaction Scale-up

PVP capped NM dispersions were synthesised as explained above. The reaction was scaled-up to three and six times by increasing the amount of starting reagents by a factor of 3 and 6 yet keeping the volume of water used in the reaction constant. Table 4.3 shows the scaled-up quantities used.

Table 4.3. Scale-up experiment quantities used for PVP capped ceria synthesis.

Scale-up factor	10 K	40 K	360 K	Cerium	Zinc	Copper	Volume
	PVP	PVP	PVP	nitrate	nitrate	nitrate	of water
	(g)	(g)	(g)	(mg)	(mg)	(mg)	(mL)
x1	2	1	0.155	130	89	73	60
x3	6	3	0.465	390	267	219	60
x6	12	6	0.930	780	534	438	60

4.5 Characterisation

PVP capped metal oxide NM samples synthesised as described in Sections 4.4.1-4.4.3 and PVP reference samples prepared as explained in Section 4.4.4 were extensively characterised using various physical and chemical techniques. These included DLS – sizing and zeta potential (Section 3.2), UV-VIS (Section 3.3), XPS (Section 3.4), FT-IR (Section 3.5), ICP-OES (Section 3.11), TEM (Section 3.7) and STEM (Section 3.8). 10 K PVP capped ceria and copper oxide NMs were further characterised by means of EELS (Section 3.8) whilst 10 K PVP capped zinc oxide NMs were characterised by means of EDX (Section 3.9). EELS was the desired analysis technique over EDX due to the ability to "fingerprint" different forms of the same element. Despite this, the Zn L edge was not observed for the PVP capped zinc oxide NMs. This is most likely due to the small size of the particles. This is the reason for carrying out EDX on the 10 K PVP capped zinc oxide NMs. In spite of this, since zinc only has one oxidation state, the necessary information was still obtained. PVP capped zinc oxide and PVP capped copper oxide NMs were also characterised by means of EXAFS (Section 3.10). The ceria samples were not able to

have been characterised by EXAFS due to the limited beamline access time. Scaled-up samples (Section 4.4.5) were characterised by means of DLS – sizing and zeta potential, UV-VIS and ICP-OES. Details of all analytical techniques and their procedures can be found in Chapter 3.

4.6 Characterisation of Physical properties

4.6.1 Appearance

The colour of the PVP capped metal oxide NM dispersions is dependent on the type and amount of PVP.

10 K PVP capped metal oxide NM samples are yellow in colour. The solution colour lessens to colourless for 360 K PVP as the PVP chain length increases. According to the product specifications in solution 10 K PVP has a faint yellow to light yellow colour, 40 K PVP is colourless to light yellow and 360 K PVP is colourless to faint yellow (Sigma-Aldrich, 2016c, Sigma-Aldrich, 2016a, Sigma-Aldrich, 2016b). Furthermore the reduction in colour with longer PVP chain may also be influenced by the longer PVP chains better shielding the colour from the NM core.

Additionally the colour intensity increases as the scale-up factor increases due to more PVP and NMs within the solution (Figure 4.2). Furthermore, scaled-up PVP capped copper oxide samples have a green/blue tinge probably due to the presence of copper (II) ions in solution.

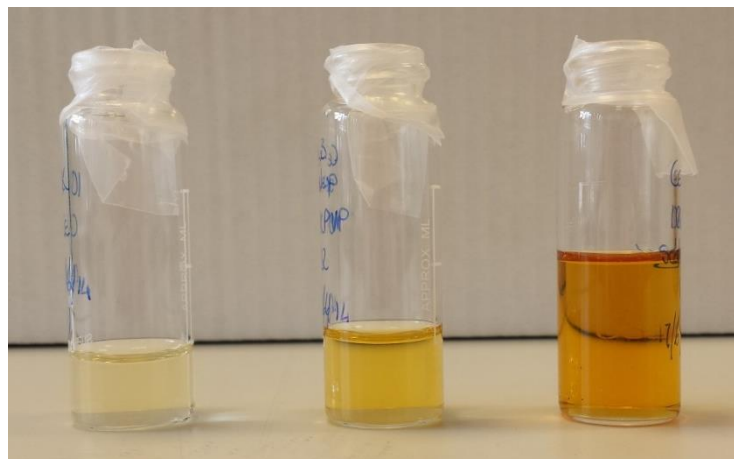


Figure 4.2 Photograph of 10 K PVP capped ceria from left to right: original, scale-up x3 and scale-up x6.

4.6.2 Size

Size characterisation was important to confirm that the particles produced were in fact of nanoscale size, i.e. one or more of their external dimensions was in the range 1 nm – 100 nm. Furthermore, as highlighted in Chapter 2, properties of nanomaterials may differ to those of the bulk material. Therefore, size characterisation reveals information which can then be linked to behavioural and toxicological profiles.

Size measurements were obtained by means of a multi-method approach. The three techniques used were DLS, TEM and STEM. More details on these techniques have been discussed in Chapter 3.

Each technique used measures size slightly differently. Specifically, DLS uses Brownian motion to measure the hydrodynamic diameter, which is the size of the hypothetical hard sphere that diffuses in the same way as the particle being measured. In this case the PVP capping is included in the measurement. TEM and STEM allow for imaging of the NMs by virtue of their electron density, with the latter having a higher resolution and therefore providing a more precise size measurement, especially for the

smaller particles. Due to its low electron density, PVP is invisible to both these techniques therefore it is the actual NM core size being measured.

4.6.2.1 Dynamic Light Scattering

As explained previously in Section 3.2.1.1, DLS was used to measure size, by means of the hydrodynamic diameter of the NMs. Table 4.4 shows the size and PDI values obtained for all the NM dispersions and scaled-up dispersions. Figure 4.3 shows the size distribution graphs for 10 K, 40 K and 360 K PVP reference samples and PVP capped ceria, zinc oxide and copper oxide samples. Figures 4.4-4.6 show the scale-up size distribution graphs for PVP capped ceria, zinc oxide and copper oxide samples respectively.

Results show that for the original x1 samples the size obtained was comparable regardless of the NM core and dependent on the type and amount of PVP used during the synthesis. The longer the PVP chain the greater the NM size obtained. This can clearly be seen in Figure 4.3. 10 K PVP capped NMs were measured to be c. 5-6 nm, 40 K PVP capped NMs measured c. 7-8 nm and 360 K PVP capped NMs measured c. 19-20 nm. Zhou et al. (2007) controlled the size of as-obtained CeO₂ spherical crystallites by varying synthetic parameters such as the molar ratio of PVP (repeating units) to Ce(NO₃)₃.6H₂O. This is the reason why changing the PVP type, which also constituted a change in molar ratio due to the different quantities used, resulted in a change in size.

The scale-up results show changes in size due to the modifications of the protocol to increase yield (Table 4.4 and Figures 4.4-4.6). The metal nitrate and PVP molar ratio remain constant yet the concentration of the reagents is increased since the reaction

volume is kept constant. This could be the reason for the change in size. In fact, Zhou et al. (2007) also reported a change in $\text{Ce}(\text{NO}_3)_3 \cdot 6\text{H}_2\text{O}$ to have an effect on the particle size obtained. The most significant changes in size are noticed for the scaling up of 360 K capped metal oxide NMs as the sizes decrease significantly. In the case of ceria the size decreases from 19.30 ± 0.136 nm to 4.778 ± 0.963 nm (x3) to 4.183 ± 0.758 (x6). The NM size for PVP capped zinc oxide decreases from 19.41 ± 1.272 to 9.296 ± 0.086 (x3) to 6.364 ± 0.178 (x6). Finally the size of the copper oxide sample decreases from 19.44 ± 0.183 to 9.545 ± 0.147 (x3) to 8.119 ± 0.167 (x6). Changes in size for the 10 K and 40 K PVP capped NM sizes are within the range of values of 3 nm and no noticeable trend can be seen in the results.

The PDI values obtained are all less than 0.7 except for the 10 K PVP capped ceria scaled-up by a factor of 3 indicating that the samples do not have a very broad size distribution and that they are suitable for analysis by means of this characterisation technique.

Table 4.4 Size and PDI values for PVP capped NMs

Sample	As prepared		Scale-up x3		Scale-up x6	
	Size	PDI	Size	PDI	Size	PDI
10 K PVP capped ceria	6.282 ± 0.047	0.190 ± 0.006	4.816 ± 0.090	0.344 ± 0.031	4.185 ± 0.212	0.213 ± 0.022
40 K PVP capped ceria	7.347 ± 0.091	0.195 ± 0.013	7.188 ± 0.175	0.195 ± 0.035	8.132 ± 0.249	0.420 ± 0.065
360 K PVP capped ceria	19.30 ± 0.136	0.385 ± 0.008	4.778 ± 0.963	0.387 ± 0.110	4.183 ± 0.758	0.780 ± 0.306
10 K PVP capped zinc oxide	5.291 ± 0.103	0.225 ± 0.016	7.040 ± 0.389	0.293 ± 0.3887	4.229 ± 0.805	0.362 ± 0.188
40 K PVP capped zinc oxide	8.075 ± 0.376	0.267 ± 0.024	8.282 ± 0.272	0.229 ± 0.028	6.250 ± 0.3083	0.275 ± 0.085
360 K PVP capped zinc oxide	19.41 ± 1.272	0.354 ± 0.040	9.296 ± 0.086	0.275 ± 0.018	6.364 ± 0.178	0.225 ± 0.020
10 K PVP capped copper oxide	4.999 ± 0.126	0.219 ± 0.039	3.838 ± 0.033	0.791 ± 0.250	6.550 ± 0.072	0.296 ± 0.014
40 K PVP capped copper oxide	7.303 ± 0.099	0.198 ± 0.020	4.765 ± 0.033	0.169 ± 0.019	4.375 ± 0.138	0.476 ± 0.060
360 K PVP capped copper oxide	19.44 ± 0.183	0.222 ± 0.002	9.545 ± 0.147	0.187 ± 0.030	8.119 ± 0.167	0.406 ± 0.039

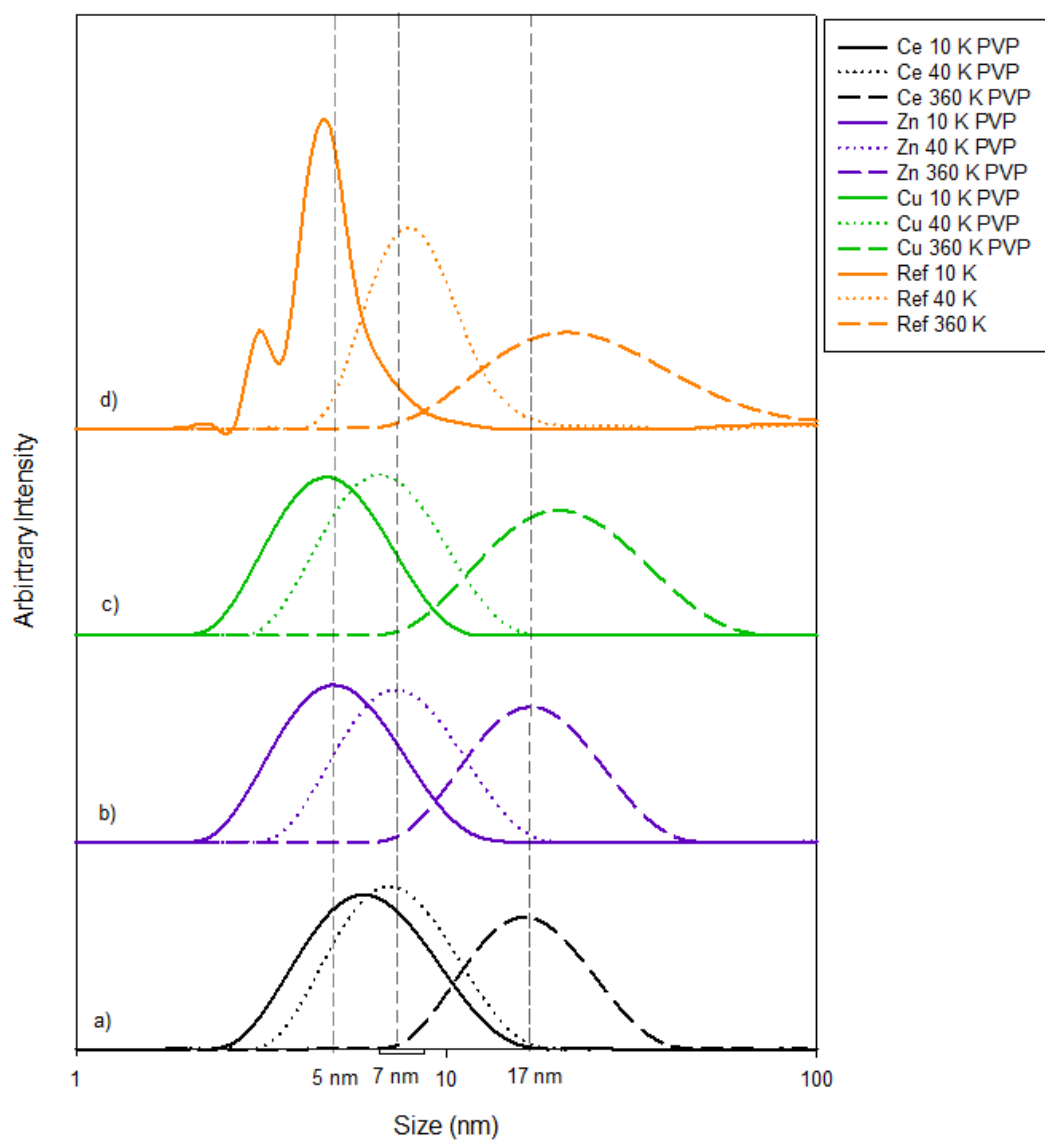


Figure 4.3 Size distribution graphs for a) PVP capped ceria, b) PVP capped zinc oxide, c) PVP capped copper oxide and d) PVP reference samples.

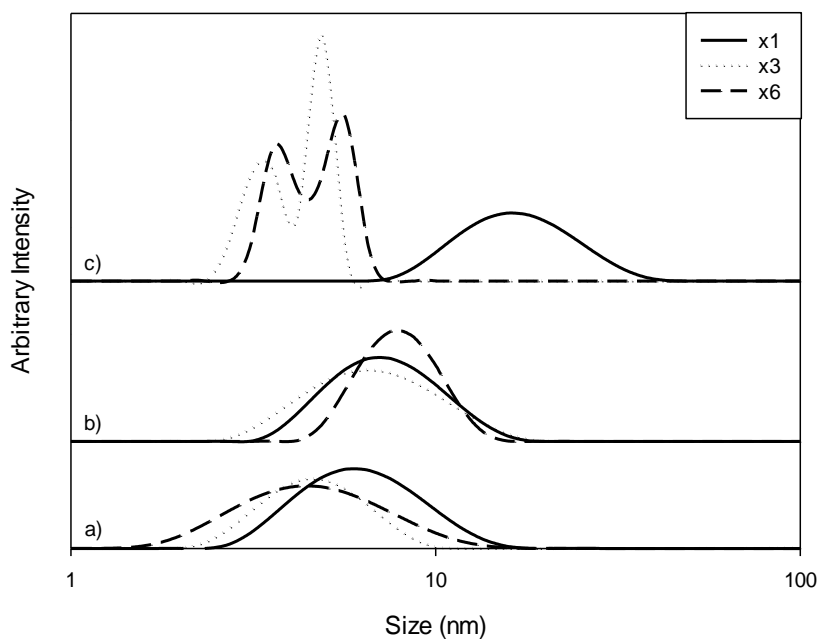


Figure 4.4 Size distribution graphs for scaled-up PVP capped ceria as prepared, x3 and x6 for a) 10 K PVP, b) 40 K PVP and c) 360 K PVP

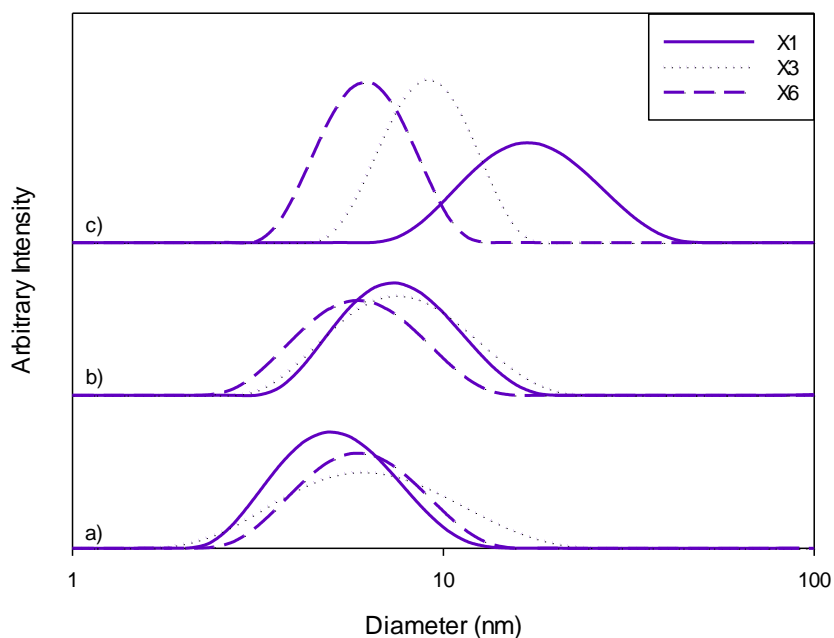


Figure 4.5 Size distribution graphs for scaled-up PVP capped zinc oxide as prepared, x3 and x6 for a) 10 K PVP, b) 40 K PVP and c) 360 K PVP

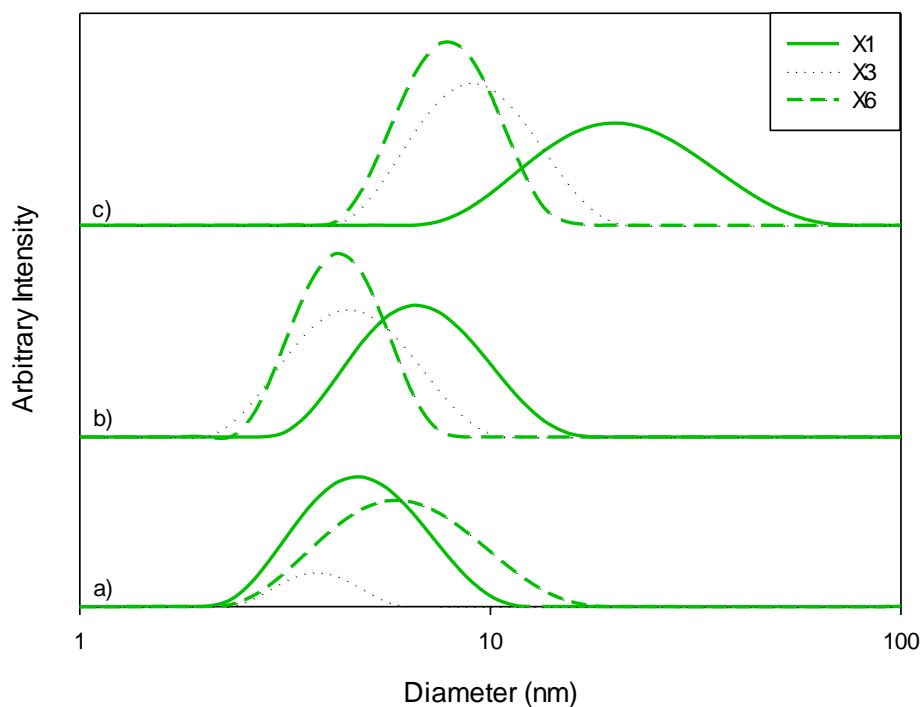


Figure 4.6 Size distribution graphs for scaled-up PVP capped copper oxide as prepared, x3 and x6 for a) 10 K PVP, b) 40 K PVP and c) 360 K PVP

4.6.2.2 Transmission Electron Microscopy

Size distribution was also examined by means of TEM. For each sample imaged, for which three different images obtained per sample are shown below, 100 particles were analysed in order to obtain a size and size distribution. These results are shown in Table 4.5-4.7 for PVP capped ceria, zinc oxide and copper oxide respectively. The size distribution results for each sample are also represented as histograms.

A similar trend to that noted from the DLS size results (Section 4.6.2.1) can be seen here. As the PVP chain length increases so does the NM core size. This is due to the molar weight of the PVP and the ratio of the PVP polymer repeating units to the nitrate.

The TEM sizes obtained are comparable amongst the different NMs when considering particles capped with the same type of PVP. It should however be noted that differences in the ionic radius of the core metal can influence lattice dimensions and hence size. This can be seen when comparing Ce and the other two smaller ions, Cu and Zn, and is reflected in the particle size measurements, with ceria producing particles nearly 2 nm larger in the case of the smallest 10 K PVP capped NMs. However, no significant effect is observed at larger sizes. Even for the 10 K PVP capped NMs, the difference is small enough to give overlapping size range for the three different metal oxides.

The 10 K PVP capped NMs have a size of c. 5-7 nm, the 40 K PVP capped NMs are c. 8-9 nm and the 360 K PVP capped NMs are c. 12-13 nm.

The trends for the DLS and TEM sizes are similar. However, the degree of change varies amongst the results of the two techniques. Size increases by DLS are higher than those measured by TEM. The reason for this is that DLS measures the hydrodynamic diameter and includes the PVP size changes within its measurements. The influence of this is stronger as the length of the polymer chain increases.

Out of the three size measurement techniques DLS (Section 4.6.2.1), TEM and STEM (Section 4.6.2.3), TEM looks to be associated with the largest error. TEM probably has a larger error than DLS due to human error during measuring of the diameter using ImageJ since far less particles were averaged. Additionally, TEM has a larger error than STEM because of the lower resolution of the TEM when compared with the STEM making the NMs harder to measure.

The histograms show the size distribution for each of the samples analysed. It can be noted that the histogram size ranges are broader for the 360 K PVP capped NMs than

for the 10 K and 40 K capped materials. The longer the PVP chain the wider the size distribution obtained.

Additionally the modality of the different histograms varies from one peak to three peaks. The modality represents the number of size fractions present within the sample. This depends on how similar the mean (size) and mode are. The greater the difference between the two values the greater the number of peaks observed.

Table 4.5 TEM data values obtained for PVP capped ceria NMs

Sample	Size (nm)	Standard deviation	Median	Mode
10 K PVP capped ceria	7.625	2.595	7.668	8.098
40 K PVP capped ceria	8.992	2.116	8.895	9.798
360 K PVP capped ceria	12.976	5.870	11.309	10.988

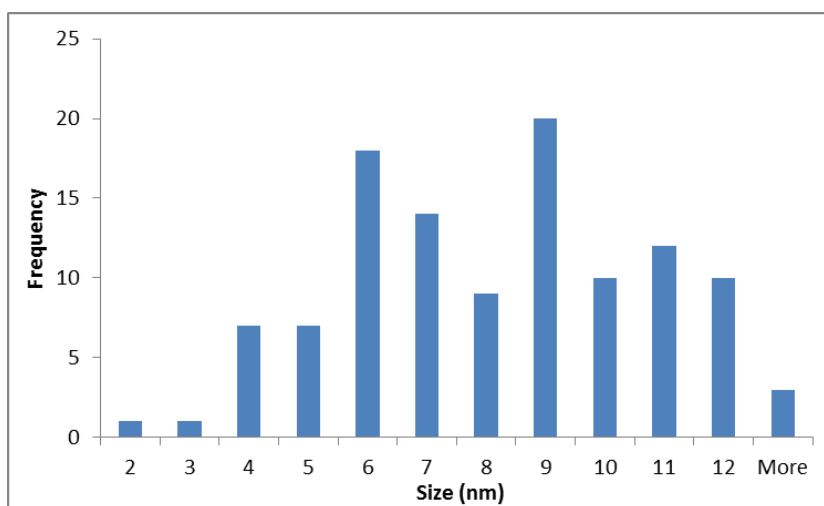


Figure 4.7 Histogram depicting size (nm) versus frequency for 10 K PVP capped ceria.

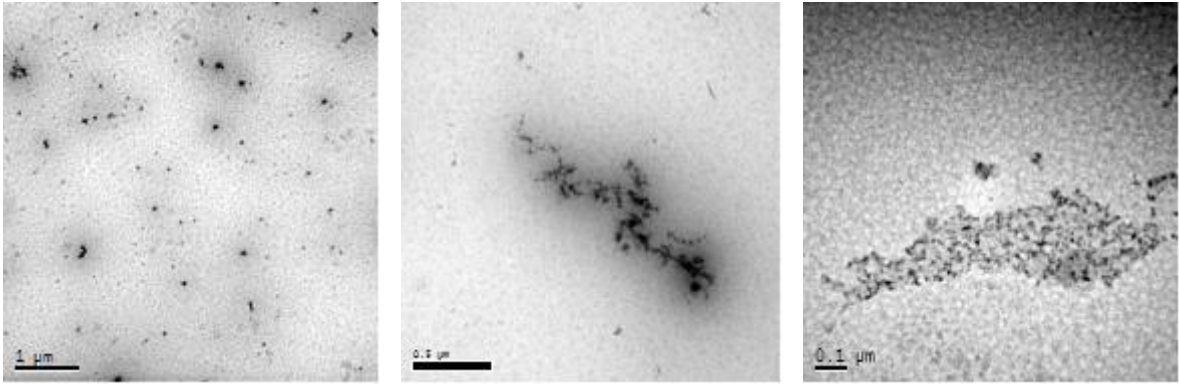


Figure 4.8 TEM images of 10 K PVP capped ceria nanoparticles.

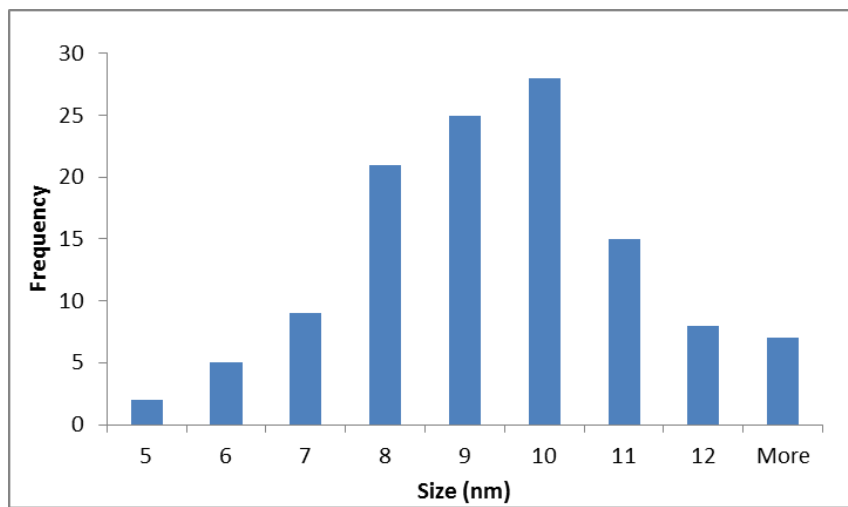


Figure 4.9 Histogram depicting size (nm) versus frequency for 40 K PVP capped ceria.

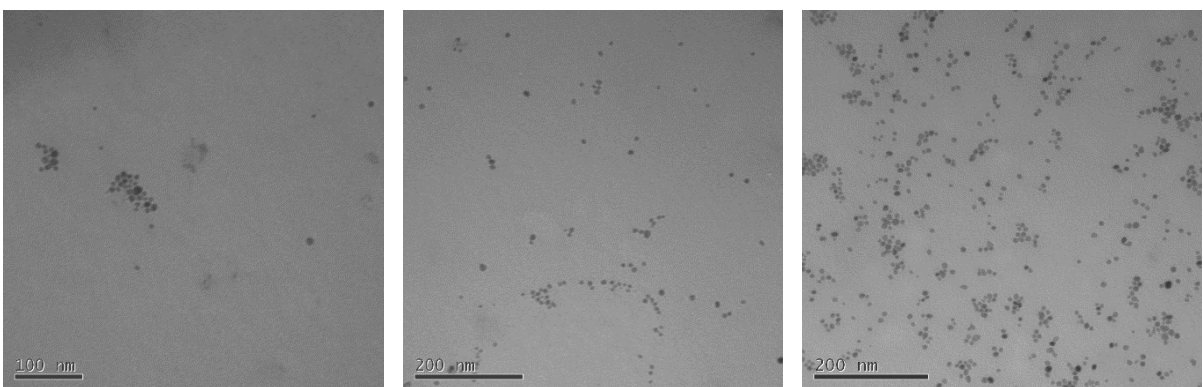


Figure 4.10 TEM images of 40 K PVP capped ceria nanoparticles.

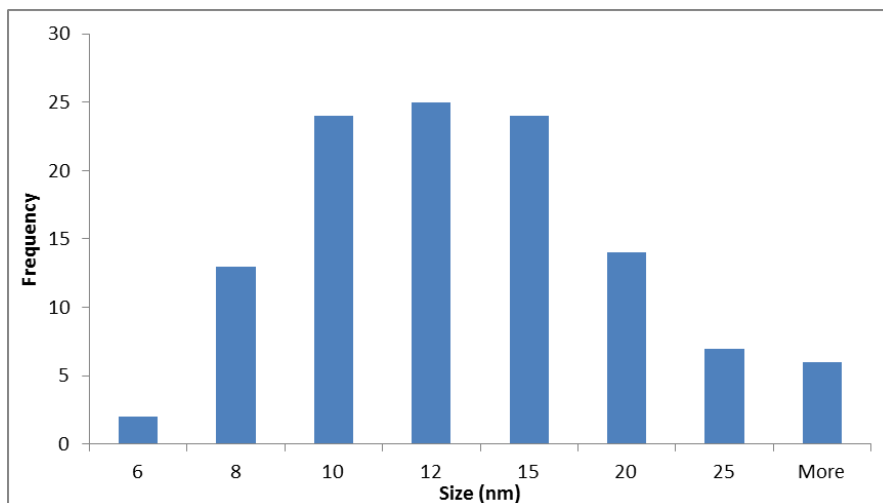


Figure 4.11 Histogram depicting size (nm) versus frequency for 360 K PVP capped ceria.

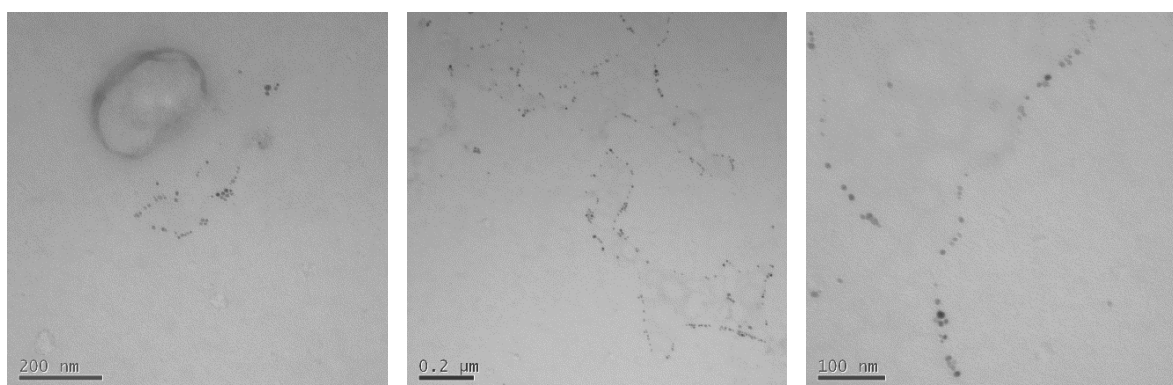


Figure 4.12 TEM images of 360 K PVP capped ceria nanoparticles.

Table 4.6 TEM data values obtained for PVP capped zinc oxide NMs

Sample	Size (nm)	Standard deviation	Median	Mode
10 K PVP capped zinc oxide	5.778	2.247	5.521	4.000
40 K PVP capped zinc oxide	9.336	3.329	8.454	11.978
360 K PVP capped zinc oxide	13.664	5.219	12.612	18.018

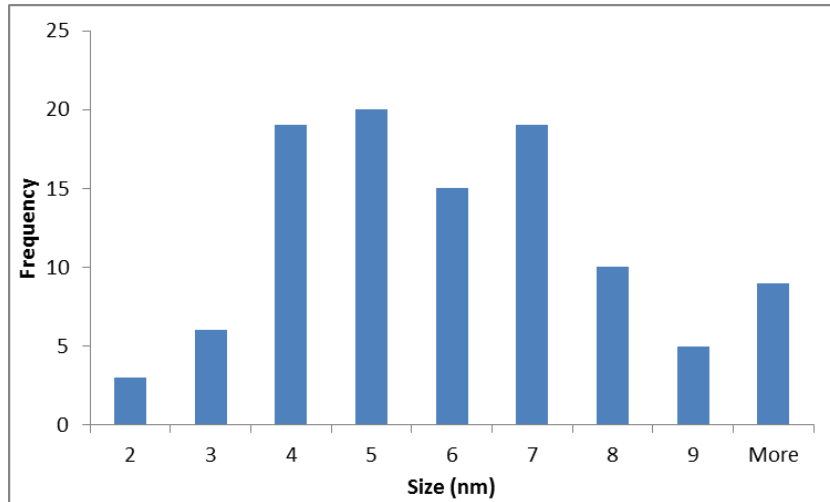


Figure 4.13 Histogram depicting size (nm) versus frequency for 10 K PVP capped zinc oxide.

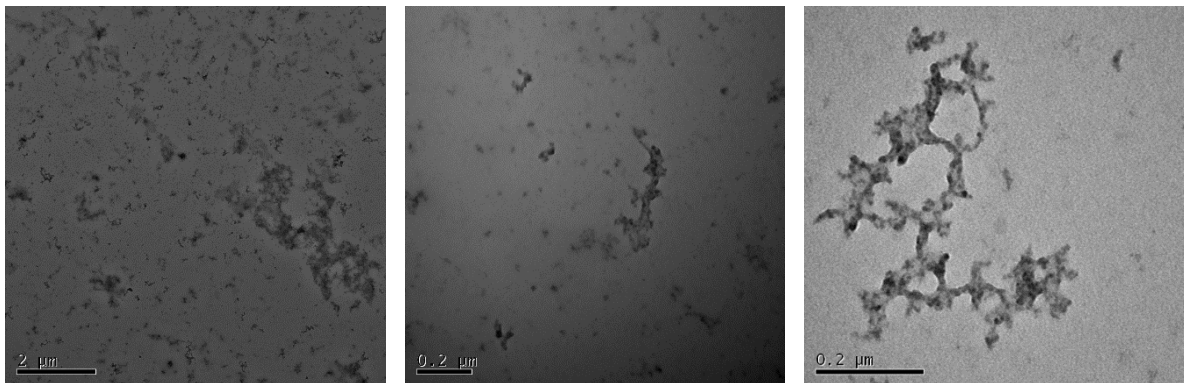


Figure 4.14 TEM images of 10 K PVP capped zinc oxide nanoparticles.

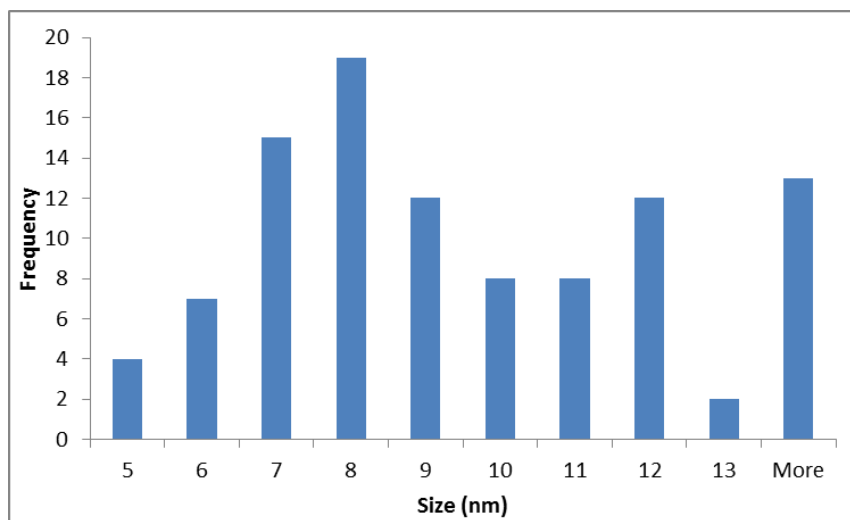


Figure 4.15 Histogram depicting size (nm) versus frequency for 40 K PVP capped zinc oxide.

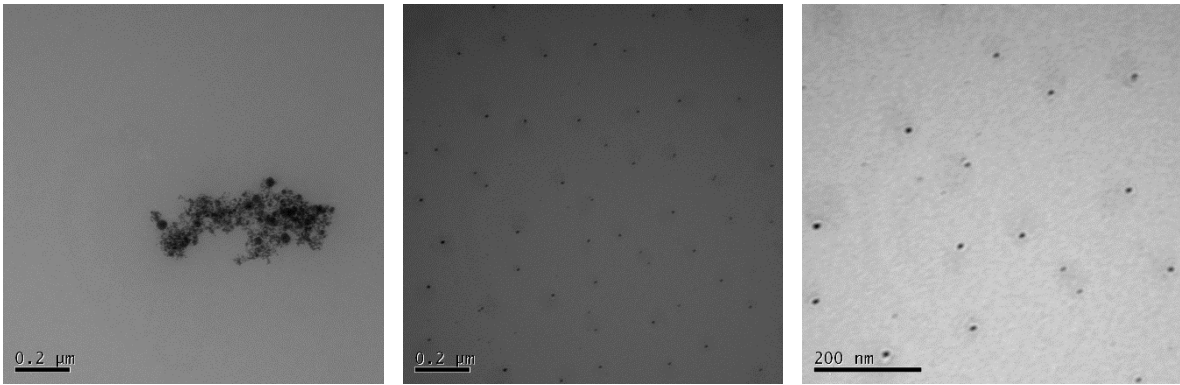


Figure 4.16 TEM images of 40 K PVP capped zinc oxide nanoparticles.

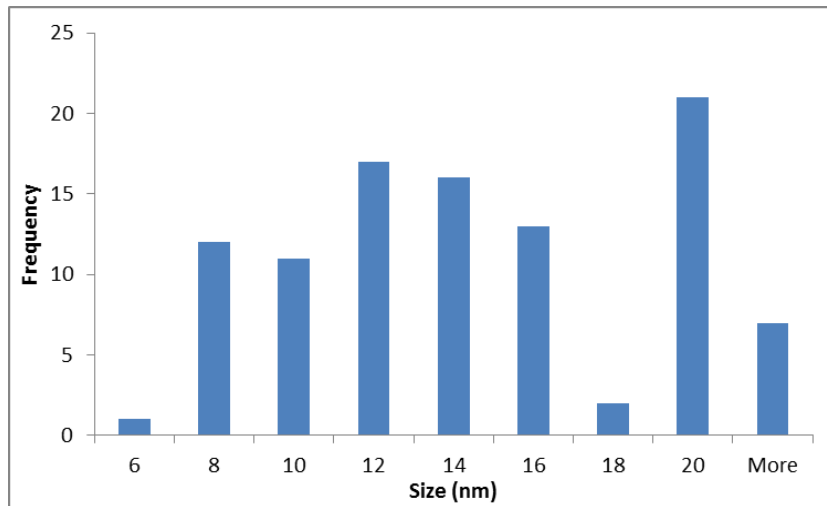


Figure 4.17 Histogram depicting size (nm) versus frequency for 360 K PVP capped zinc oxide.

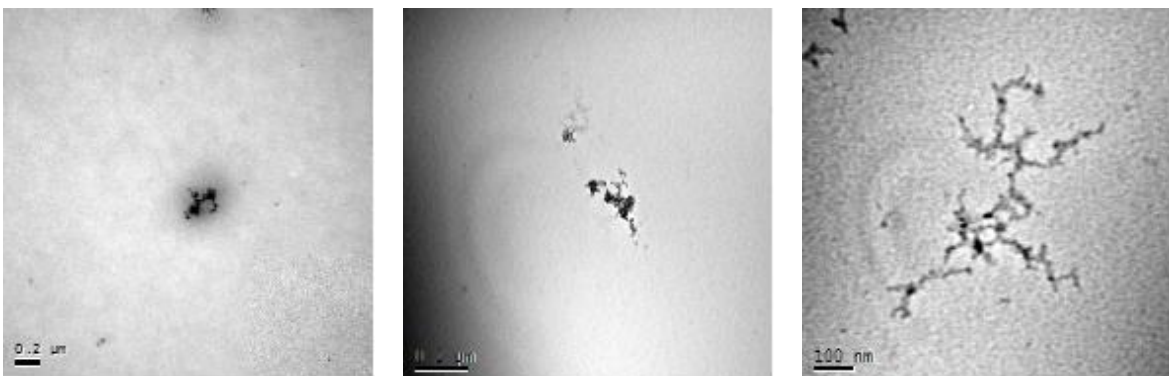


Figure 4.18 TEM images of 360 K PVP capped zinc oxide nanoparticles.

Table 4.7 TEM data values obtained for PVP capped copper oxide NMs

Sample	Size (nm)	Standard deviation	Median	Mode
10 K PVP capped copper oxide	5.950	2.069	5.556	4.491
40 K PVP capped copper oxide	9.320	2.670	9.292	9.292
360 K PVP capped copper oxide	12.144	3.63	11.626	8.035

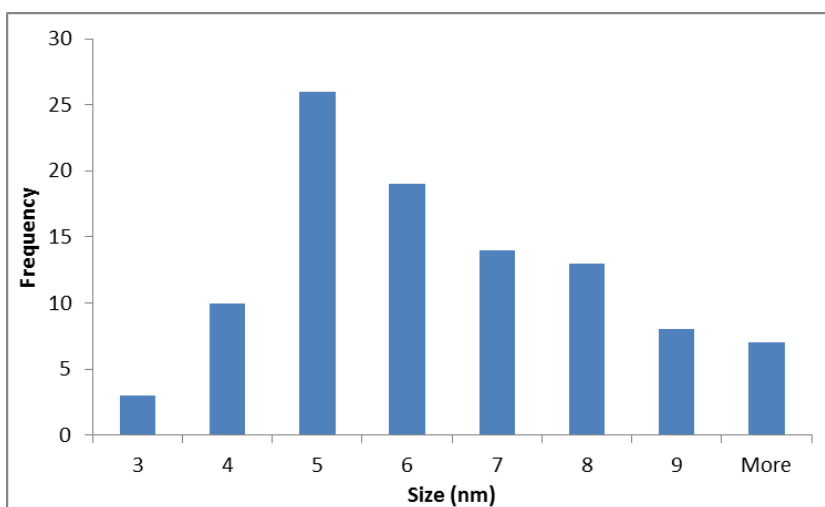


Figure 4.19 Histogram depicting size (nm) versus frequency for 10 K PVP capped copper oxide.



Figure 4.20 TEM images of 10 K PVP capped copper oxide nanoparticles.

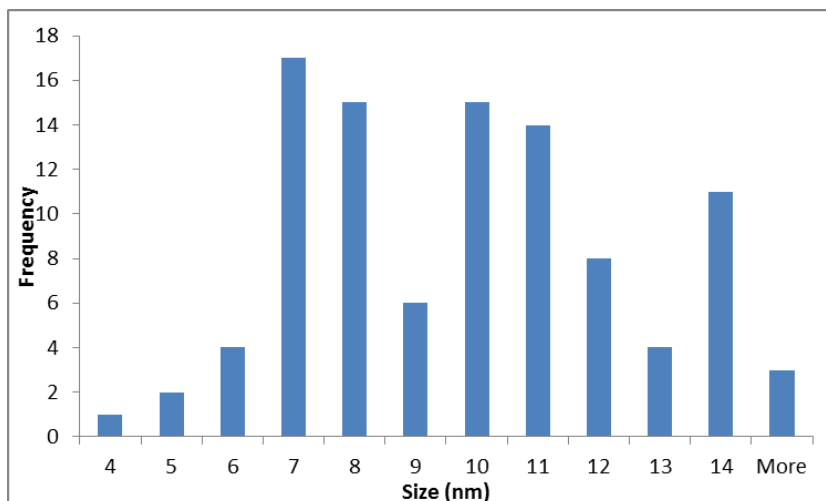


Figure 4.21 Histogram depicting size (nm) versus frequency for 40 K PVP capped copper oxide.

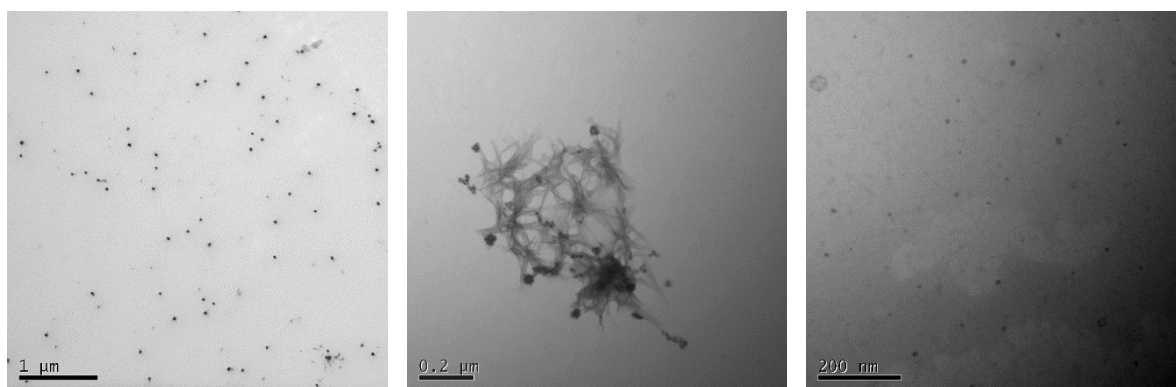


Figure 4.22 TEM images of 40 K PVP capped copper oxide nanoparticles.

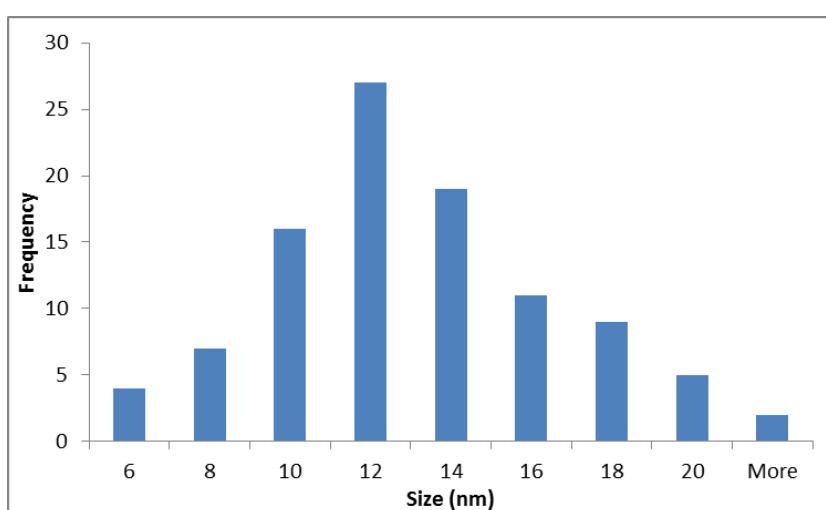


Figure 4.23 Histogram depicting size (nm) versus frequency for 360 K PVP capped copper oxide.

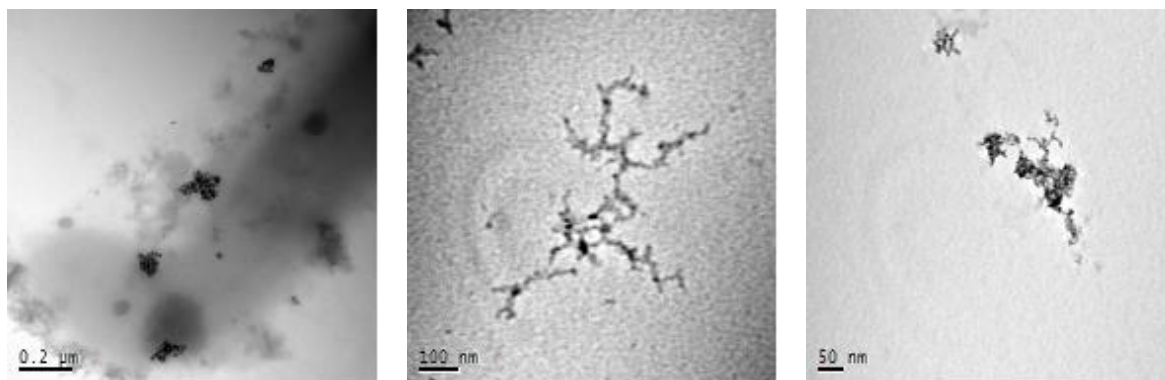


Figure 4.24 TEM images of 360 K PVP capped copper oxide nanoparticles.

4.6.2.3 Scanning Transmission Electron Microscopy

Size analysis was also carried out by means of STEM. Out of the three size analysis techniques implemented STEM technique provided smallest error values probably due to the resolution of the instrument. Figures 4.25-4.27 show the size distribution graphs for 10 K PVP capped ceria, zinc oxide and copper oxide respectively. 10 K PVP capped ceria NMs had an average diameter of 3.3 ± 0.8 nm, 10 K PVP capped zinc oxide NMs had an average diameter of 4.4 ± 0.9 nm and 10 K PVP capped copper oxide NMs had an average diameter of 3.8 ± 0.9 nm. As seen from the DLS and TEM results, regardless of the core material, the size of the NMs is comparable.

The sizes obtained by means of STEM are smaller than both those obtained by means of DLS (c. 5 nm) and TEM (c. 5-7 nm \pm c. 2). These results have already been discussed in Sections 4.6.2.1 and 4.6.2.2 for DLS and TEM respectively. The reasons for this have already been discussed in Section 4.6.2.2.

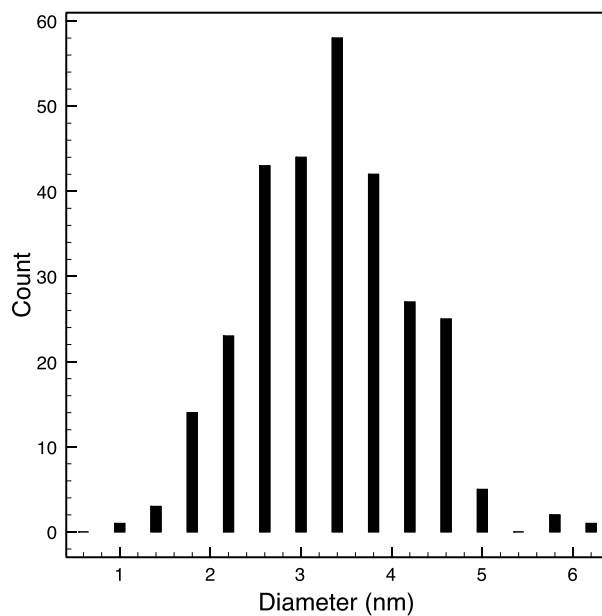


Figure 4.25 Size distribution of 10 K PVP capped ceria obtained by STEM.

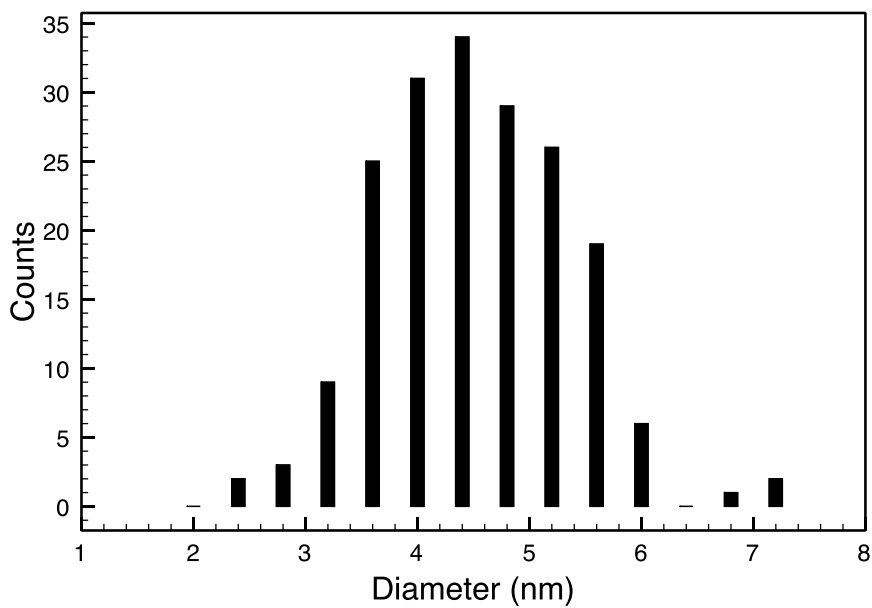


Figure 4.26 Size distribution of 10 K PVP capped zinc oxide obtained by STEM.

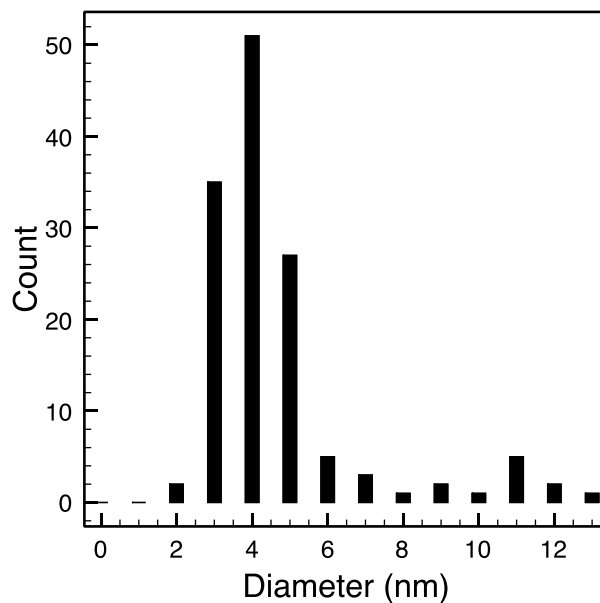


Figure 4.27 Size distribution of 10 K PVP capped zinc oxide obtained by STEM.

4.6.3 Shape and Structure

The shape and structure of the synthesised NMs could be determined from images obtained by means of the TEM or STEM.

4.6.3.1 Transmission Electron Microscopy

The TEM images can be seen in Section 4.6.2.2. All the images show small, spherical well-defined nanoparticles regardless of the core material or PVP capping chain length. On occasions these particles can be seen to cluster together as seen in Figure 4.20 (right) for 10 K PVP capped copper oxide. At times these clusters or particles look to be attached to one another with strands possibly composed of organic material as seen in Figure 4.14 (right) for 10 K PVP capped zinc oxide and Figure 4.22 (centre) for 40 K PVP capped copper oxide amongst others.

4.6.3.2 Scanning Transmission Electron Microscopy

STEM analysis was carried out by Jian Liu and Dimitri Haipuk (School of Physics, University of Birmingham) on the 10 K PVP capped metal oxide NM samples. Figures 4.28-4.30 show the STEM images for 10 K PVP capped ceria, zinc oxide and copper oxide respectively. On occasions aggregation was noted. This could have occurred during sample preparation as the samples were left to air dry on grids. STEM imaging allowed for the determination of the shape of the NMs. It was found that the ceria NMs were faceted as seen in Figure 4.28 (c). The copper oxide and zinc oxide NMs were spherical. The latter aggregated to be disc shaped and the sizes of these disc aggregations ranged from ~20 nm to a few hundred nm.

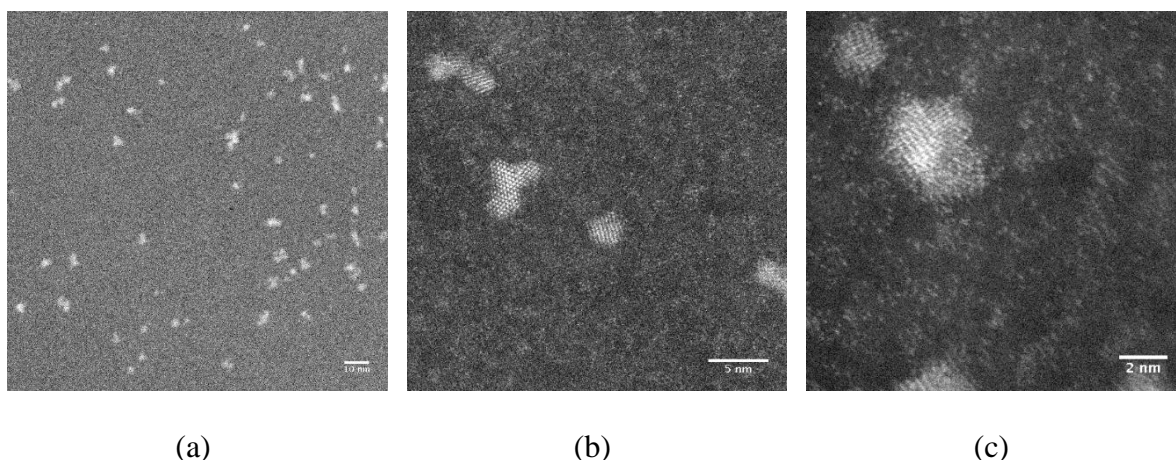


Figure 4.28 STEM images of 10 K PVP capped ceria at magnification (a) x 1 M, (b) x 5 M and (c) x 10 M.

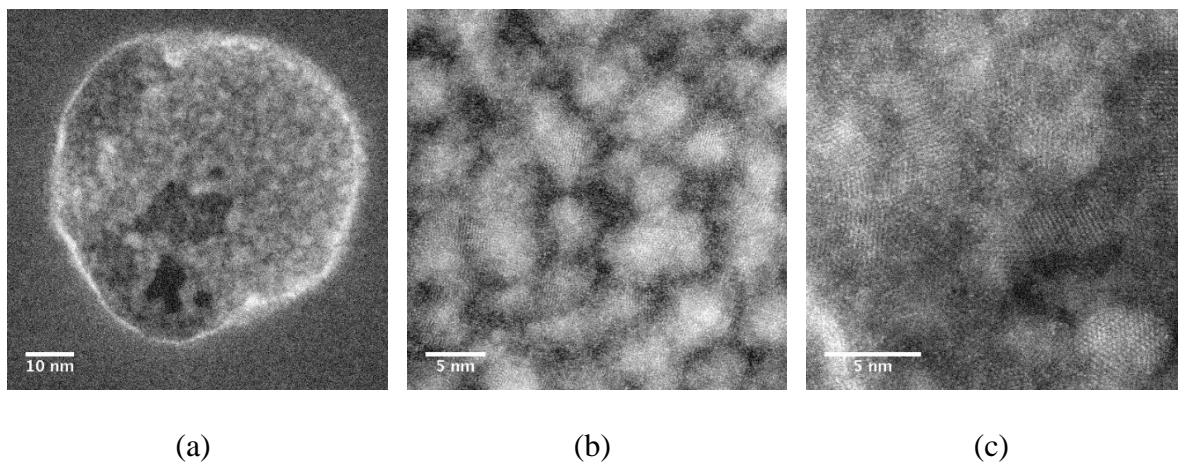


Figure 4.29 STEM images of 10 K PVP capped zinc oxide at magnification (a) x 2 M, (b) x 5 M and (c) x 5 M.

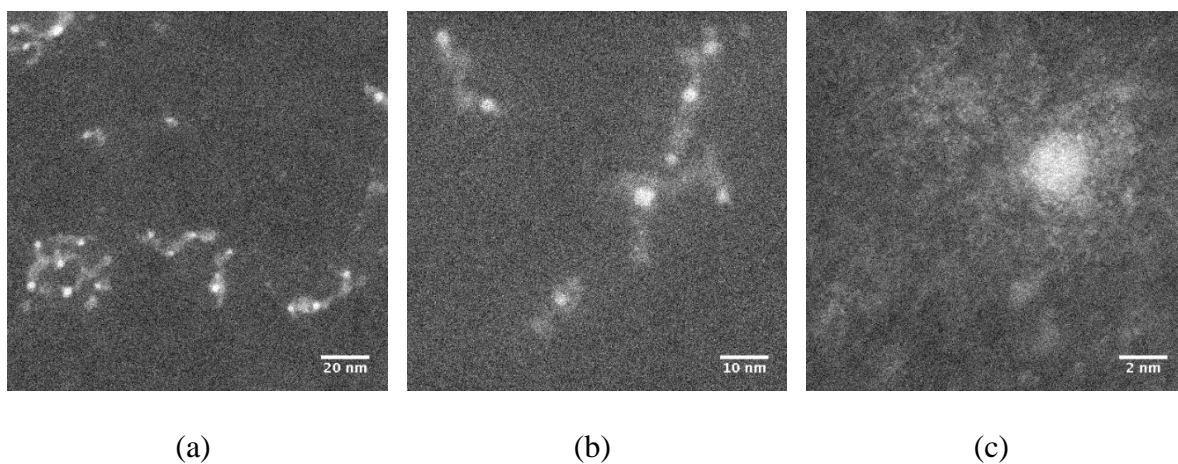


Figure 4.30 STEM images for 10 K PVP capped copper oxide at magnification (a) x 1 M, (b) x 2 M and (c) x 10 M.

4.7 Characterisation of chemical properties

4.7.1 Surface Charge

Zeta potential analysis was used to determine the surface charge of the synthesised NM library samples and scaled-up samples. Details on the technique and procedure can be

found in Chapter 3 (Section 3.2). Table 4.8 shows the average zeta potential values for 10 K PVP capped samples obtained at the pH of the NM dispersions in deionised water which was pH 6. A full table of all the average zeta potential values can be found in Appendix 1.

Table 4.8 The average zeta potential values for 10 K PVP capped samples.

Sample	Average Zeta Potential (mV)
10 K PVP reference sample	-1.81 ± 0.199
10 K PVP capped ceria	1.74 ± 0.136
10 K PVP capped zinc oxide	-0.892 ± 0.224
10 K PVP capped copper oxide	-0.292 ± 0.265

The Average Zeta Potential values obtained for all PVP capped samples regardless of the NM core, capping agent chain length or scale-up factor were very close to 0, the isoelectric point, the point where the colloidal system is least stable.

Despite this the NM dispersions are stable due to steric stabilisation. Steric stabilisation is a generic term used to refer to all aspects of the stabilisation of colloidal particles by nonionic macromolecules (Napper, 1977). With reference to this work it is achieved by polymer molecules such as PVP attaching to the surface of the NMs and forming a coating preventing the NMs from getting too close and aggregating (Napper, 1977, Heller and Pugh, 1960, Lourenco et al., 1996, Geddes, 2016).

4.7.2 Chemical Composition

The chemical composition of the NM library was characterised by a multi-method approach. FT-IR was implemented to confirm the presence of the metal – oxide bond. UV-VIS, XPS, EELS, EDX and EXAFS were carried out to determine and confirm the valency state of the metal forming the metal oxide core and confirm the presence of the metal oxide NMs.

4.7.2.1 FT-IR

FT-IR was used as a confirmatory characterisation technique in order to prove the presence of metal oxide NM core by observing the peak obtained as a result of the metal – oxygen bond stretching. Metal oxides generally result in absorption bands below 1000 cm^{-1} that arise from interatomic vibrations. Each metal – oxygen bond has a characteristic absorption frequency and observing these allows for the confirmation of the presence of the metal oxide NM core (Topnani et al., 2010). In the case of the PVP capped metal oxide NMs the most important region of the spectra is the region 400-600 cm^{-1} . This is the region where the characteristic inorganic stretching peaks should be seen. The two peaks found between 500-550 cm^{-1} and seen in every spectral figure are most likely due to the PVP capping.

Figure 4.31 shows the FT-IR spectrum of 10 K PVP capped ceria. Ce-O stretching is observed at c. 550 cm^{-1} as mentioned in the literature (Muruganatham Chelliah, 2012, Ansari et al., 2009). The peak just above 550 cm^{-1} is probably also due to Ce-O stretching.

Figure 4.32 shows the FT-IR spectrum for 10 K PVP capped zinc oxide. It can be deduced that the medium intensity peaks at just below 600 cm^{-1} and that at 517 cm^{-1} can be

attributed to Zn-O stretching. Literature has also shown the characteristic peak of Zn-O to be found below 500 cm^{-1} (Zhijian et al., 2003, Pholnak et al., 2014) yet no peaks were obtained in this region. Despite this Ismail (1991) reported peaks at $\nu = 670$ and 555 cm^{-1} related to the stretching vibrations of Zn-O bonds. The presence of the PVP capping could have caused the peaks to shift to the location that they are found in the spectrum obtained (Saravanan et al., 2011, Soltani et al., 2012).

Figure 4.33 shows the IR spectrum obtained for 10 K PVP capped copper oxide. The characteristic features seen for Cu-O stretching are a very small peak at 538 cm^{-1} , a slightly larger peak above 550 cm^{-1} at 557 cm^{-1} and a smaller peak at c. 570 cm^{-1} . According to Topnani et al. (2010) the asymmetric frequency of Cu_2O was found at 532 cm^{-1} and the Cu-O vibrational stretching of CuO NPs are found at 593 and 527 cm^{-1} . Therefore the peaks at 538 cm^{-1} , 550 cm^{-1} and 570 cm^{-1} seen in Figure 4.33 could be attributed to the same three stretching vibrations noted by Topnani et al. (2010) respectively yet shifted due to interactions of the NMs with the PVP capping (Saravanan et al., 2011, Soltani et al., 2012).

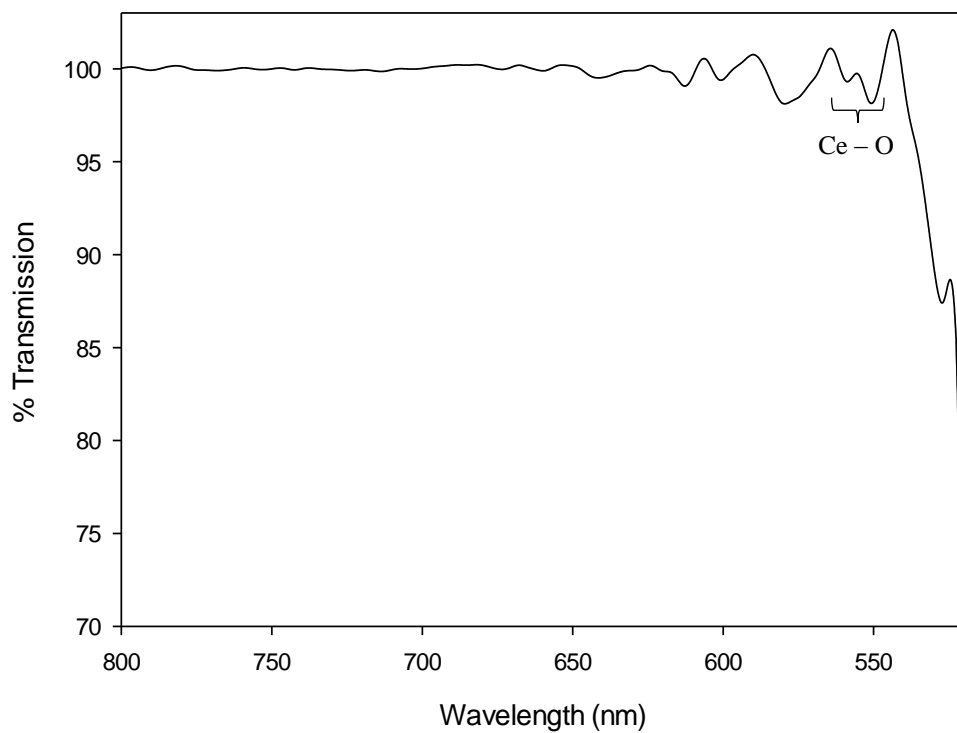


Figure 4.31 FT-IR spectrum of 10 K PVP capped ceria.

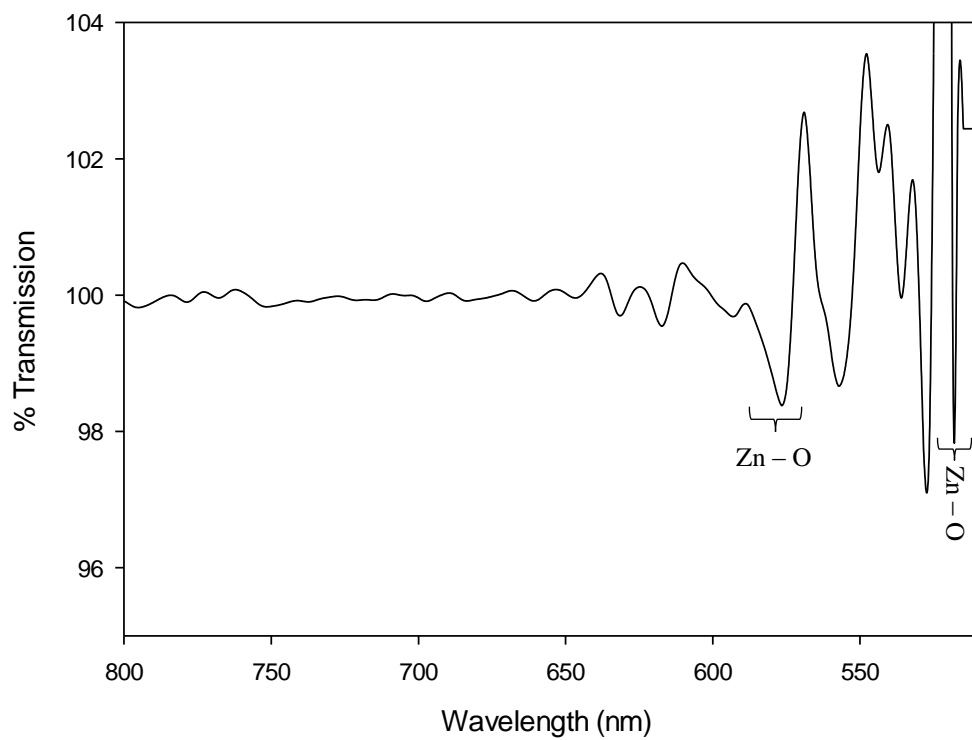


Figure 4.32 FT-IR Spectra of 10 K PVP capped zinc oxide.

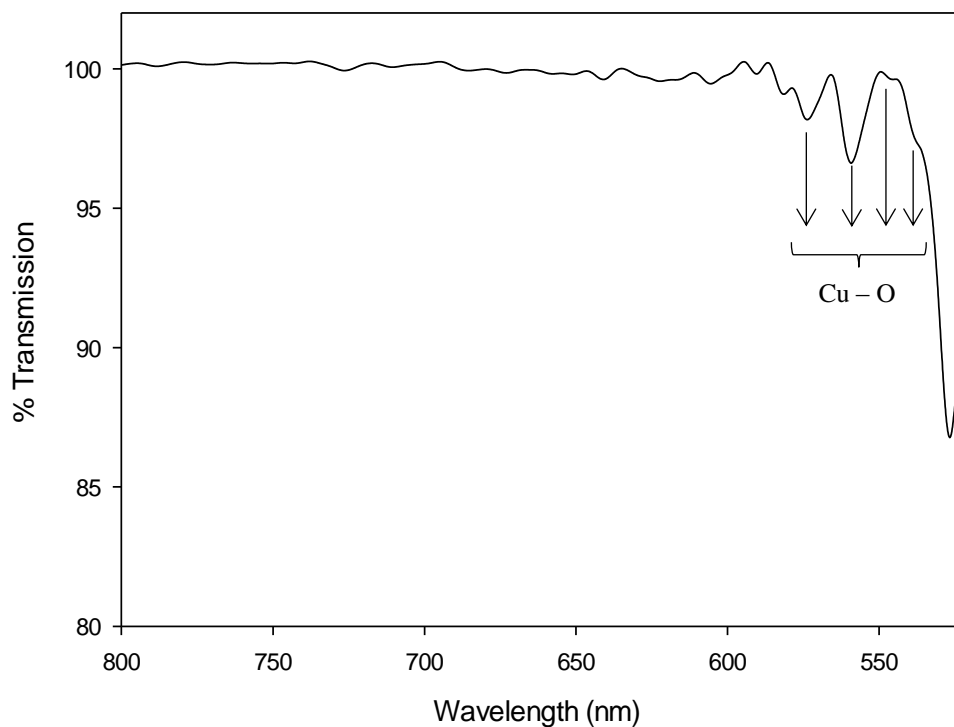


Figure 4.33 FT-IR Spectra of 10 K PVP capped copper oxide.

4.7.2.2 UV-VIS

UV-VIS spectroscopy is routinely used for the determination of analytes due to the characteristic absorbing frequency that every molecular species is capable of. Further details on this technique can be found in Chapter 3 in Section 3.3. UV-VIS allowed for the chemical characterisation of the different PVP capped metal oxides. In this work it was used to confirm the composition of the metal oxide NM core and attempt to determine the valency state of the metal core component. Figure 4.34 shows the UV-VIS spectra for 10 K, 40 K and 360 K PVP capped metal oxide NMs.

Primarily it should be noted that the absorption peak of PVP was found to be at c. 250 nm. This peak can be noted in all the spectra and could possibly be shadowing some

peaks of interest which are expected to be present in this region such as that of Ce_2O_3 , ZnO and CuO.

The UV absorption of cerium oxide is due to the charge-transfer transition between O $2p$ and Ce $4f$ bands (Tsunekawa et al., 2000). Both oxidation states of cerium strongly absorb ultraviolet light. They have two characteristic spectrophotometric absorbance peaks. The first peak is in the range between 230 and 260 nm and corresponds to cerium (III) absorbance. The second peak absorbance occurs in the 300 to 400 nm range and corresponds to cerium (IV) absorbance (Herrling, 2013).

The ceria spectra shown in black in Figure 4.34 show the presence of three peaks. These can be found at c. 254 nm, c. 300 nm and c. 250 nm. The latter is due to the presence of PVP whilst the other two peaks are due to ceria. The peak at c. 254 nm corresponds to the cerium (III) absorbance and is the same as the characteristic peak seen by Merrifield et al. (2013) for PVP capped ceria. The peak at 300 nm, which is less intense than that at 254 nm, is due to cerium (IV) absorbance (Herrling, 2013). Therefore it can be said that the ceria samples contain ceria in a mixed valency state composed of both cerium (III) and cerium (IV). It is important to note that UV light influences the peak intensity of the Ce^{3+} and Ce^{4+} peaks. UV causes the Ce^{3+} concentration to decrease and that of Ce^{4+} to increase suggesting that the Ce^{3+} loses an electron under the action of the radiation and is converted to Ce^{4+} (Burke, 1966). Other chemical analyses, including XPS, which do not cause any influence on the sample support this observation and are discussed further below.

The purple spectra in Figure 4.34 are representative of zinc oxide. Zinc is known to have one stable valency state, namely +2 (Chambers and Holliday, 2013) and studies have shown that the absorption edge for PVP capped ZnO NPs has a value of 296.95 nm

(Malvija et al., 2013). 10 K PVP capped zinc oxide tends to show two peaks, one at c. 300 nm and a much larger more intense peak at c. 250 nm. The latter corresponds to PVP and the former corresponds to zinc oxide. 40 K and 360 K PVP capped zinc oxide are also shown by the presence of these two peaks however that of zinc oxide is more intense and is found below 300 nm. It is likely that the PVP chain length shifts zinc wavelength to slightly lower values. These results indicate that as expected the core of the PVP capped zinc oxide NMs is in fact zinc oxide.

Finally the green spectra in Figure 4.34 show those belonging to the PVP capped copper oxide NMs. The absorption peak for CuO_2 is just below 600 nm (Thi My Dung Dang, 2011). This peak however was not noticeable in any of the copper oxide spectra. Chen et al. (2012) found that the peak for CuO at c. 280 nm. The smaller peak observed just above 300 nm could be a representative peak for CuO shifted slightly due to the interference of the PVP peak.

A further copper species can be seen represented by a clear peak at 440 nm which is characteristic of Cu_2O ; Zhang et al. (2006b) have demonstrated that a peak for Cu_2O can be found in this region. Additionally, Figure 4.35 shows the UV-VIS spectra for PVP capped copper oxide NMs as prepared without further dilution. Since this sample was not diluted the quartz cuvettes could not be used as the signal obtained would have been too strong due to the path length that would have travelled through the sample. Therefore this analysis was carried out using polystyrene cuvettes and therefore the analysis range could not scan down to 200 nm due to the absorption of the polystyrene. These spectra show the presence of a peak at 800 nm, which was not picked up when the samples were diluted and analysed using the quartz cuvettes. According to Lenglet et al. (1991) this absorption peak is due to the presence of cupric oxide (CuO). Therefore, like the ceria samples, the

copper oxide samples look to contain Cu in two oxidation states. Other analyses technique results, such as XPS, are discussed later.

An interesting feature in the copper oxide spectra is as in the case of zinc oxide, the peaks seems to shift to lower wavelength with longer PVP chain length. One reason for this could be the change in NM size discussed in Section 4.6.2 which is due to the type of PVP used. It has been noted that size influences optical properties. In fact surface plasmon resonance is influenced by many factors including nanoparticle size, morphology, composition, surface chemistry and surrounding environment (Kelly et al., 2002, Kreibig, 1995). Kelly et al. (2002) discussed the influence of size, shape and dielectric environment on the optical properties of metal nanoparticles. It has been noted in a number of cases, including zinc oxide quantum dots (Lin et al., 2005), gold (Fleger and Rosenbluh, 2009) and silver (Fleger and Rosenbluh, 2009, Mogensen and Kneipp, 2014) nanoparticles that a decrease in size causes a blue shift in absorption meaning a peak shift to a lower wavelength. Yet in this case the data shows a blue shift with increasing size or a red shift with decreasing size. Peng et al. (2010) state that as size decreases from $d \approx 20$ nm it blue-shifts but then turns over near $d \approx 12$ nm and strongly red-shifts. This could therefore explain why a red shift is seen in the spectral data since the size results discussed in Section 4.6.2 the NM sizes for 40 K and 10 K capped NM samples range from c. 3 nm – 11 nm.

Another noticeable feature of the spectra is the change in peak intensity. In the case of ceria and copper oxide the trend is a decrease in intensity as the PVP chain length increases. This could be attributed to the decrease in concentration with increasing polymer chain length. This is further discussed below in Section 4.7.2.7 where the ICP results are presented and explained. In the case of zinc oxide this trend does not look to be

so obvious possibly because the change in concentration for the different PVP capped zinc oxide samples (Section 4.7.2.7) is not as significant.

The UV absorption spectra of scaled up samples were obtained so as to confirm that the peaks noted for the as prepared samples were also noted for these samples. Results revealed the peaks to be found in the same location regardless of the scale-up factor. The scaled-up samples resulted in the need for more dilution prior to analysis as in the case for PVP capped ceria and PVP capped zinc oxide, or in the increase in peak intensity as in the case of copper oxide. These spectra can be found in Appendix 2.

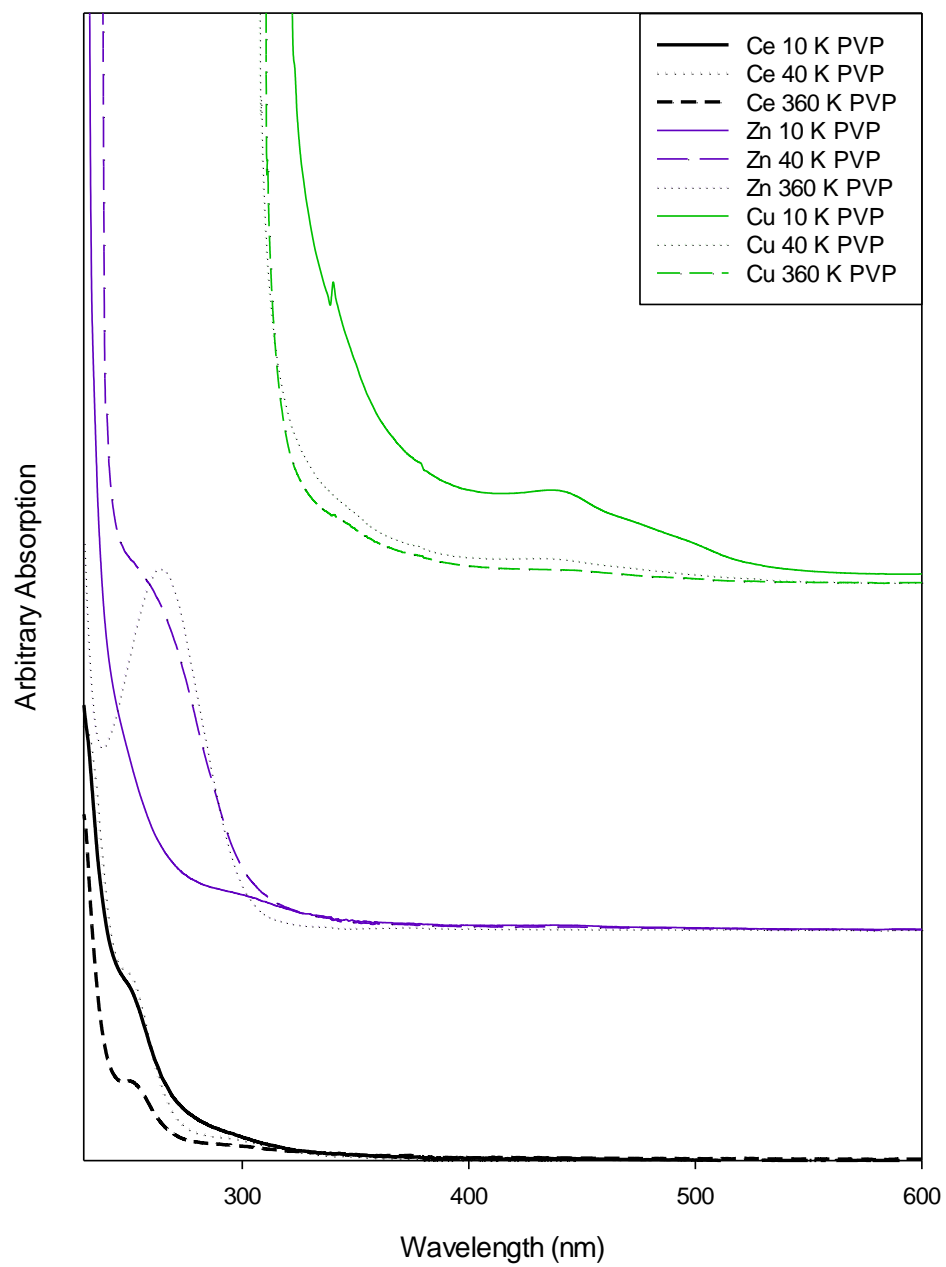


Figure 4.34 UV-VIS spectra for (a) PVP capped ceria, (b) PVP capped zinc oxide and (c) PVP capped copper oxide.

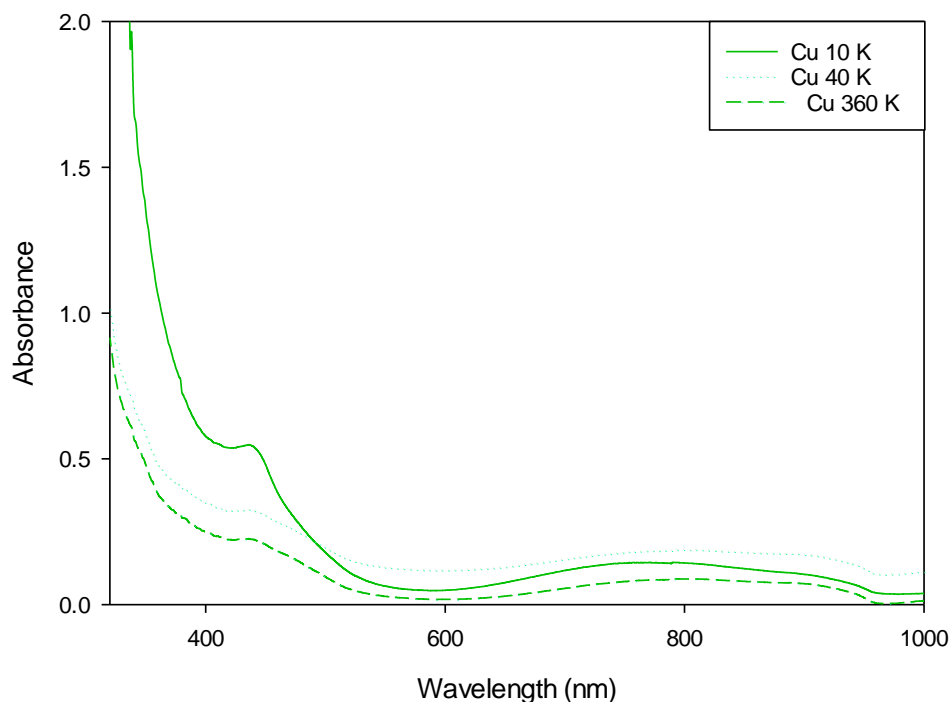


Figure 4.35 UV-VIS spectra for as prepared 10 K, 40 K and 360 K PVP capped copper oxide.

4.7.2.3 X-ray Photoelectron Spectroscopy

XPS was carried out as a chemical characterisation technique to determine the valency state of the metal forming the metal oxide NM cores. On analysing the samples charging was noted and the electronegativity of the polymer capping caused the shifting of peaks. Due to this and prior to peak analysis it was important to note that all spectra were referenced to the C1s peak (C-C, C-H) at 285.0 eV binding energy controlled by means of the well-known photoelectron peaks of metallic Cu, Ag, and Au, respectively.

As expected the PVP reference samples showed no presence of metal components and was therefore not recorded as a separate graph. The spectra simply showed the presence of carbon, nitrogen and oxygen which are the species present in PVP molecule ((C₆H₉NO)_n).

Kim et al. (2012) report Ce^{3+} having XPS peaks at 885.0 and 903.5 eV, whilst Ce^{4+} has peaks at 882.1, 888.1, 898.0, 900.9, 906.4, and 916.4 eV. Peaks between 875 to 895 eV belong to the Ce $3d_{5/2}$ while peaks between 895–910 eV correspond to the Ce $3d_{3/2}$ levels. A peak at 916 eV is a characteristic satellite peak indicating the presence of cerium (IV) (Heckert et al., 2008). Figure 4.36 shows the XPS spectra of the PVP capped ceria NMs. At the outset it can be noted that Ce 40 K is composed solely of Ce^{3+} due to the lack of the Ce (IV) distinguishing peak found at 917 eV. The other two ceria NMs are mixed valency samples, composed of both Ce^{3+} and Ce^{4+} . Calculated according to DeCaluwe (2009) and as seen in Table 4.9 it was determined that the 10 K Ce sample contained a mixed valency of 39 % cerium (III) oxide and 61 % cerium (IV) oxide whilst the 360 K Ce sample contained a mixed valency of 81.3 % cerium (III) oxide and 18.7 % cerium (IV) oxide. Between these two samples it could be seen that the longer the PVP chain the greater the percentage of cerium (III) oxide present. Merrified et al. (2013) stated that as the PVP chain length increases the overall particle size increases as seen from the size results in Section 4.6.2 but particles made of smaller individual particles and that smaller particle more likely to be Ce (III). However, when including the 40 K Ce sample, no trend could be noted. One possible reason for this could be that XPS is a surface characterisation technique and does not take into account the bulk of the material. The XPS results of 10 K and 360 K PVP capped ceria NMs are consistent with the UV-VIS results yet those of 40 K PVP capped ceria NMs are not in full agreement as they only show the presence of one cerium valency state. One reason for this discrepancy between XPS and UV-VIS could be that the amount of Ce (IV) could be too small to be picked up and XPS analyses represent a sample region of 400 μm which is therefore larger than individual nanoparticles. Another reason could be the fact that UV light causes Ce^{3+}

concentration to decrease whilst the Ce^{4+} absorption to increase (Burke, 1966) and therefore when picked up by UV-VIS it results from the technique explained in Section 4.7.2.2.

The binding energies of Zn (0) and Zn (II) are very similar with the former having a value of 1021.7eV and the latter a value of 1022 eV (Thermo Fisher Scientific Inc., 2013b). Due to this, and in order to decipher between the two, the kinetic energy needed to be analysed and the Auger peaks allow for this differentiation. In the case of the PVP capped zinc oxide samples only one spectrum is shown in Figure 4.37 since all the spectra obtained were the same. The LMM Auger line for the kinetic energy is found at about 988 eV implying that the samples were composed of Zn (II) rather than Zn (0) which would have resulted in a kinetic energy at 992 eV (Walker and Morton, 2001). These results are consistent with those obtained by UV showing that the sample is in fact composed of zinc oxide NMs.

The binding energy of copper metal is identical to that of copper (I) oxide having a value of 933 eV. The binding energy of copper (II) oxide is also very similar, with a value of 933.5 eV (Thermo Fisher Scientific Inc., 2013a). Since it is not possible to distinguish between Cu (I) and Cu (0) on the basis of the Cu 2p peak alone, the Auger line was also measured. This was detected at about 916 eV kinetic energy and indicates the presence of Cu (I) and excludes Cu (0). The different Cu (I) and Cu (II) species can be determined from the presence and intensity of the satellite peaks (explained in Section 3.4). Cu (II) has observable satellite features at 943 eV whilst Cu (I) oxide only has very weak satellites at 945 eV. Additionally the $\text{Cu}2p_{3/2}$ peak in Cu (II) oxide is shifted and is much broader compared to Cu (I) oxide (Thermo Fisher Scientific Inc., 2013a). Figure 4.38 shows the XPS spectra for all the PVP capped copper oxide NM samples. The spectra are similar in

all cases and show the presence of peaks at 940.0 and 944.0 eV that are satellites typical for the presence of Cu(II).

Therefore, it can be concluded that CuO or Cu(OH)₂ or both are present. The copper hydroxide may result from an incomplete synthesis as it is one of the intermediate species formed during the reaction procedure. Besides the satellite peaks the spectra also show 2 peaks at above and around 935 eV indicating that both copper (II) and copper (I) species are present within the samples as also noted from UV-VIS results.

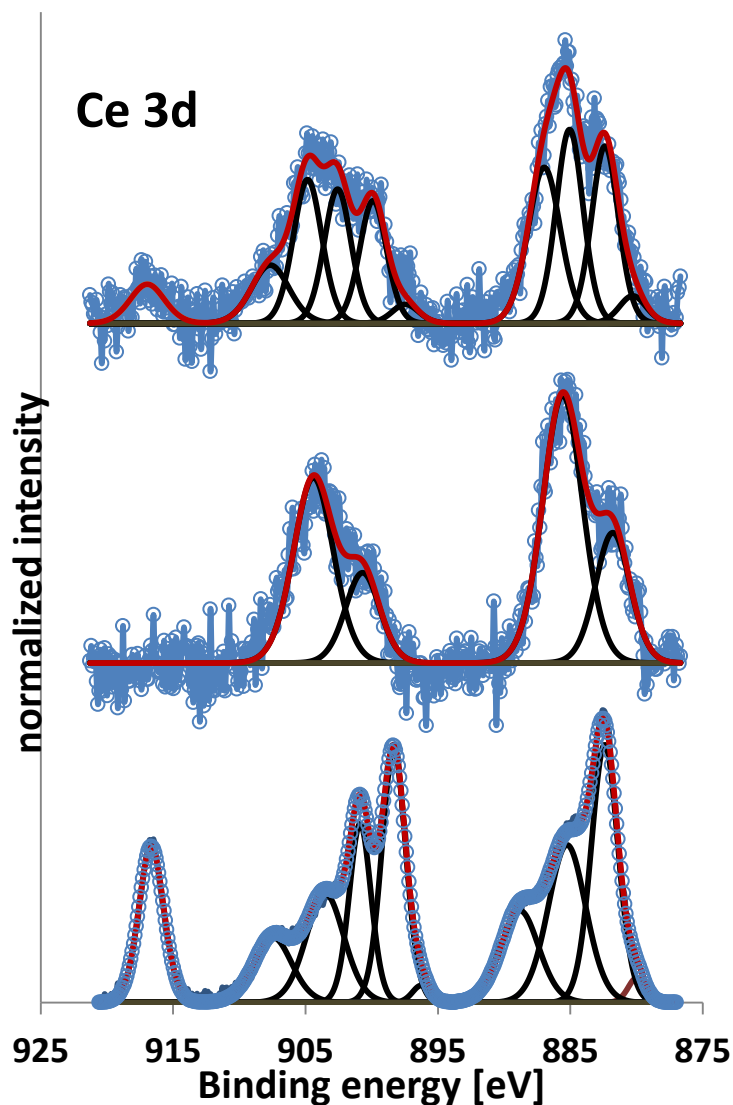


Figure 4.36 XPS spectra of 10 K PVP capped ceria, 40 K PVP capped ceria and 360 K PVP capped ceria NMs from bottom to top respectively.

Table 4.9. Percentage amount of Ce³⁺ and/or Ce⁴⁺ in samples containing ceria

Sample	Percentage Ce ³⁺ (%)	Percentage Ce ⁴⁺ (%)
10 K PVP capped ceria	39	61
40 K PVP capped ceria	100	0
360 K PVP capped ceria	81.3	18.7

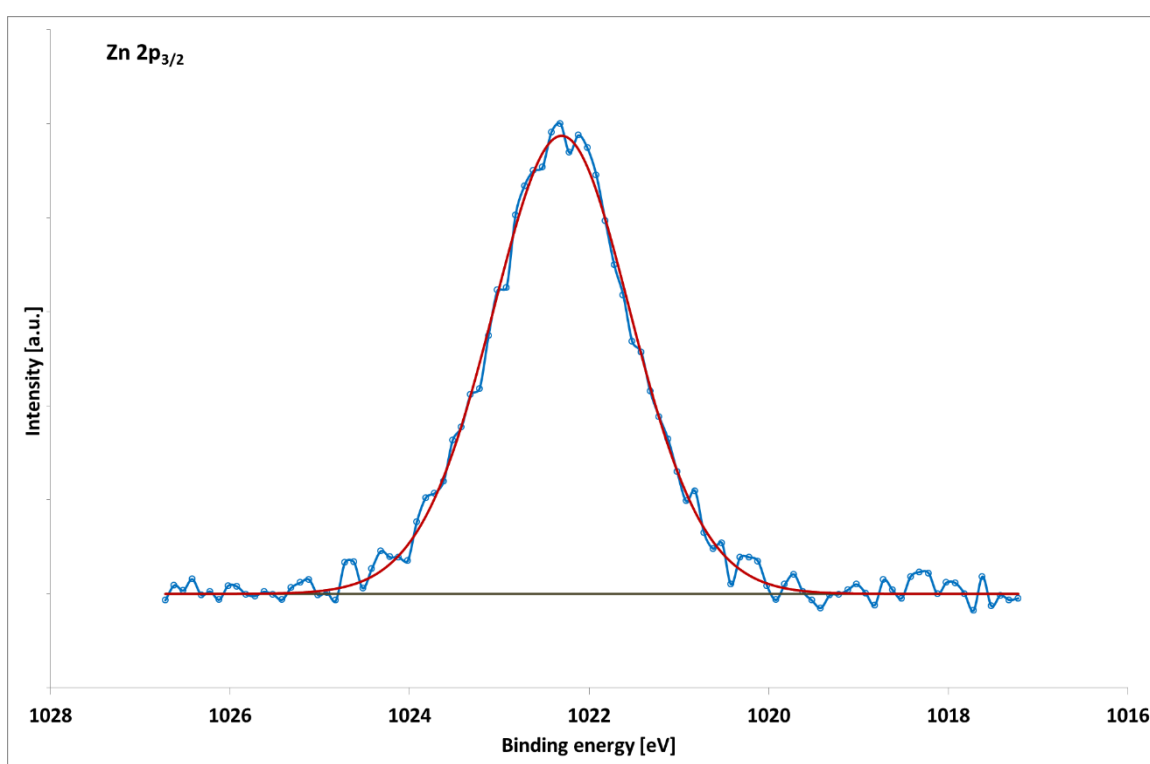


Figure 4.37 XPS spectrum for PVP capped zinc oxide representative of 10 K, 40 K and 360 K PVP capped zinc oxide.

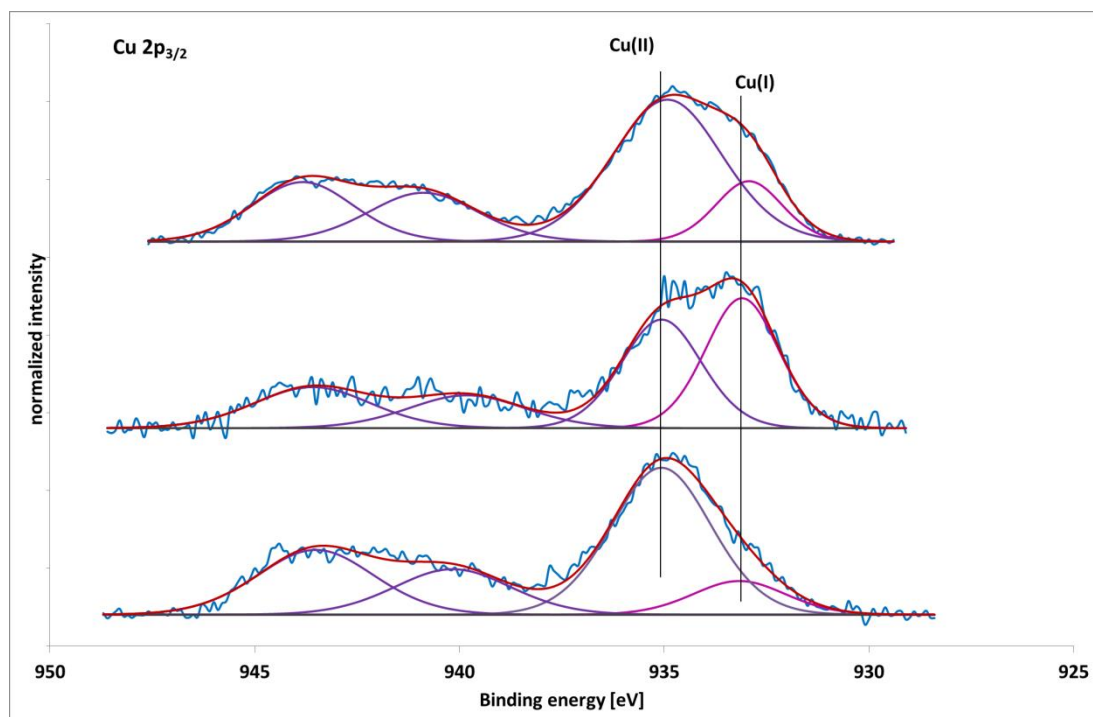


Figure 4.38 XPS spectra for 10 K PVP capped copper oxide, 40 K PVP capped copper oxide and 360 K PVP capped copper oxide NMs from bottom to top respectively.

4.7.2.4 Energy Electron Loss Spectroscopy

10 K PVP capped ceria and 10 K PVP capped copper oxide NMs were characterised by Jian Liu (School of Physics, University of Birmingham) by means of EELS.

Cu oxide

Figure 4.39 shows the reference and sample spectra for the copper oxide samples. Figure 4.39 (a) shows the reference O K-edge of CuO (blue) and Cu₂O (red). The O K-edge of the CuO and Cu₂O have different onsets and energy-loss near edge structure (ELNES) and can therefore be used to determine the oxidation state of Cu_xO (Potapov and Schryvers, 2004). Figures 4.39 (b-d) show the spectra for 10 K PVP capped copper oxide NMs. The spectra show some similarities to the O K-edge of the Cu₂O. The spectra show

similar onsets and shape at energy range from about 530 to 545 eV. However, after 545 eV the structure differs significantly. This could be caused by the oxygen in the PVP shell or by the absorbed oxygen on the surface. Additionally the Cu L-edge of Cu_xO is very weak probably due to the very small size of the particles (explained in Section 4.6.2) and cannot be used to characterise the sample.

Cu_2O was picked up by both XPS and UV-VIS. However, the CuO also picked up by these techniques is not seen by means of STEM-EELS. The probable reason for this is the small size of the particles proving difficult for the Cu L-edge to be used for the results analysis and interpretation. Therefore this does not necessarily mean that CuO is not present.

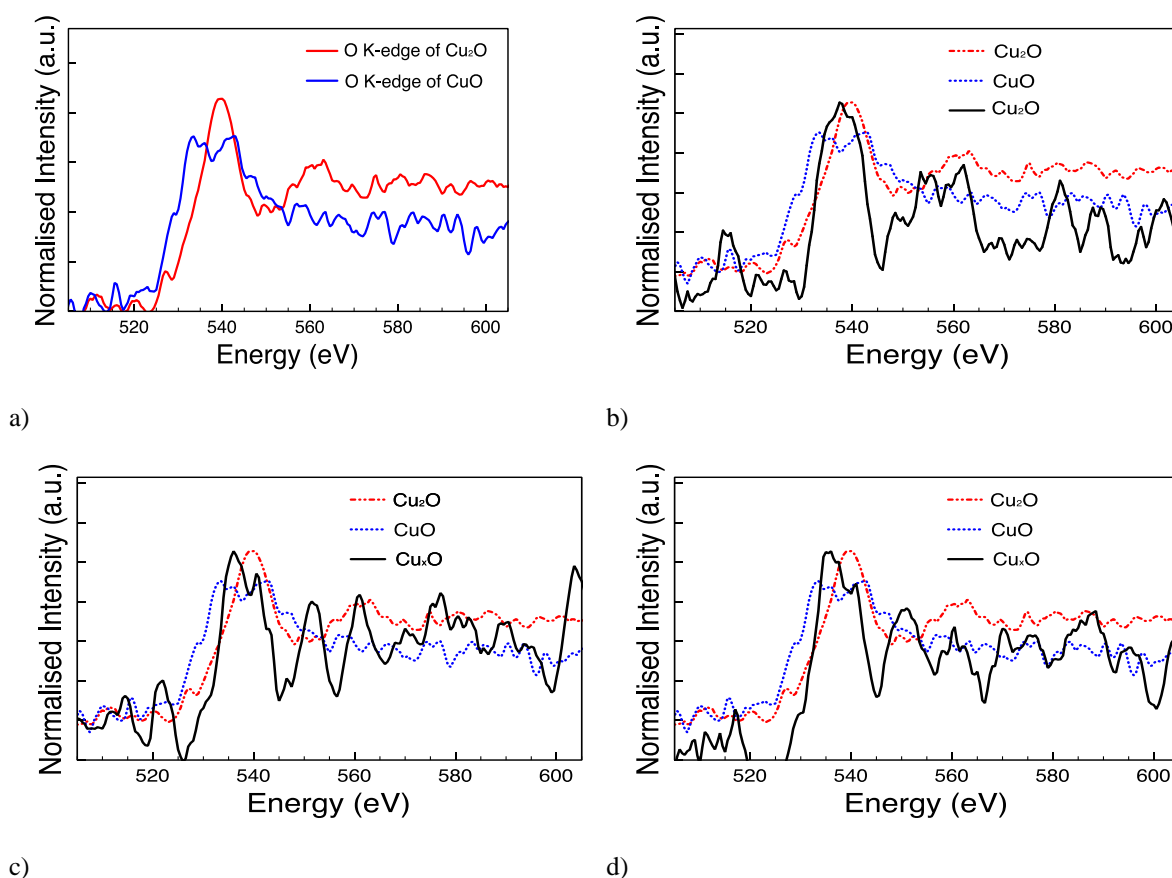


Figure 4.39 (a) Reference EELS spectrum for CuO and Cu_2O and (b-d) EELS spectra for 10 K PVP capped copper oxide.

Ce oxide

In general the oxidation states of cerium can be identified by the energy loss signal in EELS where white lines, which are sharp peaks appearing as white areas when an x-ray absorption spectrum is recorded, relating to the M-edge region of the spectra are observed. The EELS spectra of cerium is characterised by two sharp peaks at 901 and 883 eV forming due to the transition of a core electron to an unbound state. The first peak at 901 eV is due to the $3d_{3/2} \rightarrow 4f_{5/2}$ transition, denoted as M4, and the other at 883 eV is due to $3d_{5/2} \rightarrow 4f_{7/2}$ transition, denoted as M5 (Merrifield et al., 2013, Manoubi et al., 1990, Garvie and Buseck, 1999, Gatan Corporate, 2016).

Figure 4.40 shows the reference EELS spectrum for Ce^{3+} and Ce^{4+} , EELS spectra for 10 K PVP capped ceria and the Ce^{4+} distribution. The spectra (Figure 4.40 (b) and (c)) show the presence of both Ce^{3+} and Ce^{4+} . This correlates with the results obtained from both UV-VIS and XPS. From the spectra obtained multiple linear least-square fittings (MLLS) were performed to calculate the percentage of Ce^{4+} in the CeO_x clusters (Garvie and Buseck, 1999). The oxidation state varies for the different CeO_x clusters. The average percentage of Ce^{4+} in the CeO_x clusters is seen in the distribution in Figure 4.40 (d) and was found to be $35.9 \% \pm 13.1 \%$. The large associated error may be due to two reasons. In the first place the large noise signal obtained in the EELS of the CeO_x clusters due to the very small size of the particles (explained in Section 4.6.2) requires a short acquisition time and long exposure time that may affect the oxidation state. Secondly the possible shift of the zero-loss peak during analysis results in calibration discrepancies.

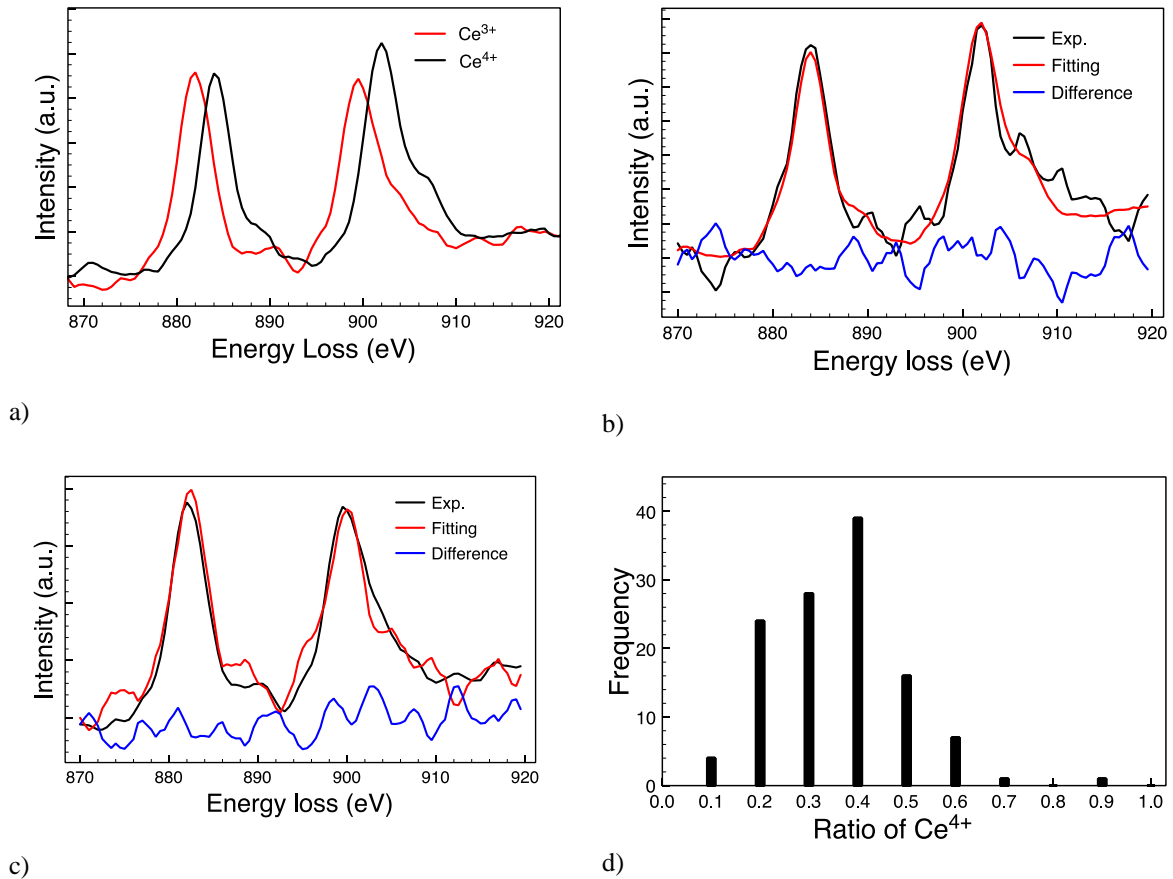


Figure 4.40 (a) Reference EELS spectrum for Ce^{3+} and Ce^{4+} , (b-c) EELS spectra for 10 K PVP capped ceria and (d) Ce^{4+} distribution.

4.7.2.5 Energy Dispersive X-ray Spectroscopy

The 10 K PVP capped zinc oxide NMs were characterised by Jian Liu by means of EDX. The spectrum obtained can be seen in Figure 4.41. The results show the presence of Zn, O, Cu and K. Zn and O are due to the presence of zinc oxide NMs and the Zn and O ratio is about 2:3. The Cu signal is obtained due to the use of the copper grids. The reason for the presence of potassium is unknown. It could be an impurity from the media used during the synthesis and dispersion.

The results from this technique therefore further support those obtained by means of UV-VIS and XPS, discussed in Section 4.7.2.2 and 4.7.2.3 respectively, and confirm the presence of zinc oxide NMs.

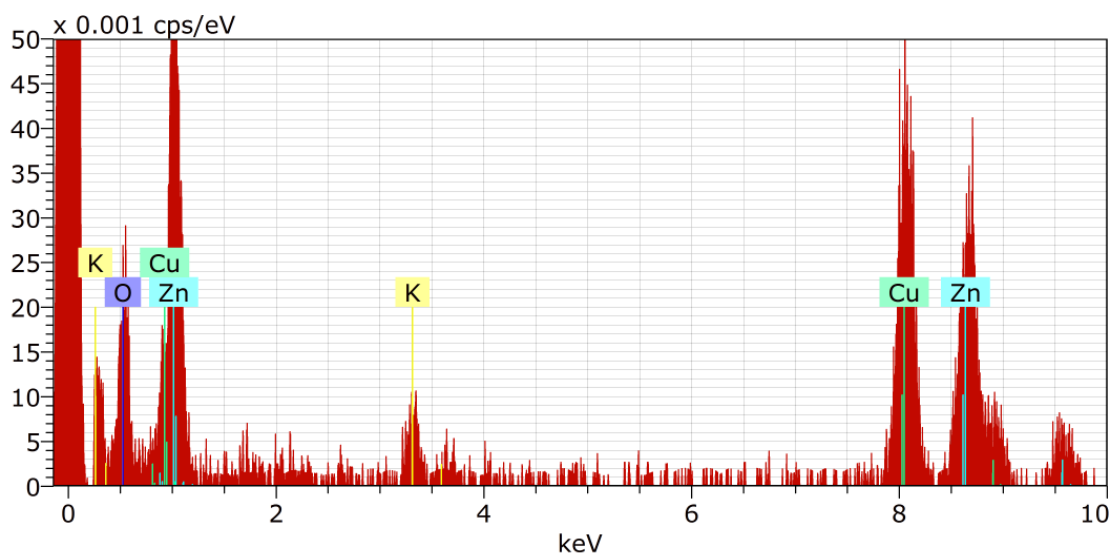


Figure 4.41 EDX spectrum for 10 K PVP capped zinc oxide NMs.

4.7.2.6 EXAFS

EXAFS analysis for PVP capped zinc oxide and copper oxide NM dispersions was carried out at the UK's national synchrotron science facility, Diamond Light Source, in Oxfordshire. In order to analyse the ceria NM samples, modifications to the set-up to allow for a higher energy scan were needed. Time constraints did not allow for the modifications to be made within the beam time available. Thus future work would be needed in order to obtain this data. Data were obtained for the zinc oxide and copper oxide NM and were normalised using Athena software; they can be seen plotted in Figures 4.42-4.43.

Figure 4.42 shows the spectra obtained for the zinc oxide standard and PVP capped zinc oxide NMs. The spectra look to be similar in all cases regardless of the PVP chain length yet they do not resemble the spectrum obtained for the zinc oxide standard. Pereshtein et al. (2013) suggested that the shape and position of the 1s–4p absorption peak maximum in ZnO NPs strongly depend on the particle size. They demonstrated this in their work where the XANES data of the 300 nm ZnO (purchased from Sigma-Aldrich) and 2.1 nm ZnO (purchased from GFS Chemicals) differ. Hence, it is likely that particle size is the reason for the spectra of the reference and samples not matching as bulk ZnO was used as the reference. Despite this, the major peaks are found in the same region for both the reference and the samples confirming, along with the knowledge obtained from various other characterisation techniques, that the samples are in fact zinc oxide. Furthermore, the spectrum Pereshtein et al. (2013) obtained for their 2.1 nm particles resembles that obtained for the PVP capped zinc oxide nanoparticles which range in size from c. 3 nm – 20 nm as discussed in Section 4.6.2.

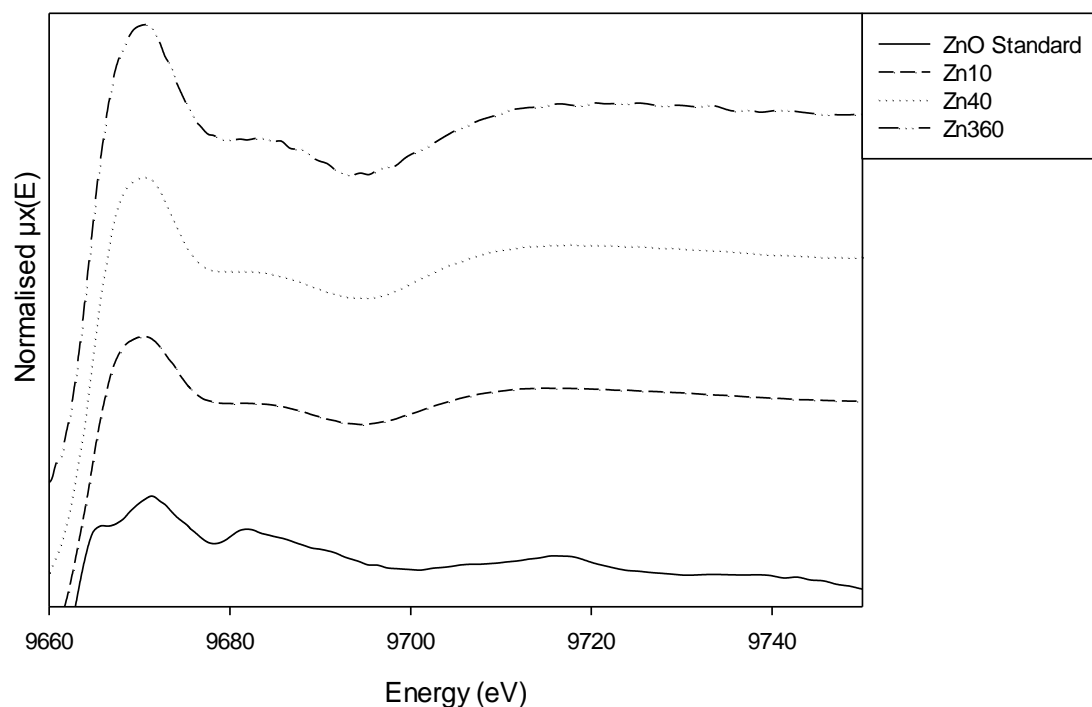


Figure 4.42 EXAFS spectra of 10 K, 40 K and 360 K PVP capped zinc oxide and reference spectrum for zinc oxide.

In the case of copper samples the Cu K-edge is present due to the $1s \rightarrow 4p$ transition. The Cu 4p orbitals of copper (I) compounds split into $4p_{xy}$ and $4p_z$ orbitals due to ligand field splitting. As a result two peaks may be seen in the EXAFS data, namely those labelled B and D in the figures below. The former is due to the $1s \rightarrow 4p_{xy}$ transition whilst the latter is due to the $1s \rightarrow 4p_z$ transition. In copper (I) oxide each copper atom forms two collinear bonds with oxygen atoms. The antibonding copper $4p_z$ molecular orbitals have higher energy than $4p_{xy}$ orbitals due to the repulsive interaction between electrons along z axis. The covalent ligand orbital overlaps along the z axis and reduces the intensity of the $1s \rightarrow 4p_z$ transition. Consequently peak B is intense and appears at lower energy than peak D (Gaur and Shrivastava, 2011).

Copper (II) compounds have a d_9 configuration and the possibility of a $1s \rightarrow 3d$ transition. This transition is not possible for Cu (0) and Cu (I) compounds since there is no hole in the 3d orbital. Due to this transition a weak characteristic pre-edge peak representing this transition occurs for most copper (II) compounds. This can be seen labelled A in the figures below. The features between peaks C and E are due to transitions to Cu 4p-like final states which split into $4p_{xy}$ and $4p_z$. Peak C is attributed to transitions to the $4p_{xy}$ state. Peak E is attributed to the $1s \rightarrow 4p_z$ transition (Gaur and Shrivastava, 2011).

Figure 4.43 shows the EXAFS spectra obtained for the PVP capped copper oxide NM samples. Peaks A, C and E marked in purple correspond to copper (II) components whilst peaks B and D marked in green correspond to copper (I) components. It can be clearly noted that the spectrum obtained for 360 K PVP copper oxide is similar to that of metallic copper seen in Figure 4.44. This was most likely caused by the reduction of the NMs by the beam during the analysis since the filter size had to be changed to a larger size due to the lower concentration when compared to the 10 K and 40 K samples (as explained in Section 4.7.2.7). The 10 K and 40 K PVP capped copper oxide NM samples show features pertaining to both Cu (II) and Cu (I) compounds. Therefore the samples are formed of mixed valency copper. This correlates with the results obtained from the other chemical characterisation techniques namely, FT-IR, UV-VIS and XPS. The copper (I) features look to be more prominent than those belonging to copper (II). This could be the reason why EELS simply picked up Cu_2O and not CuO and that diluting the samples prior to UV-VIS lost the CuO peak at 800 nm. Furthermore the intensity of peak A is greater for 10 K PVP capped samples rather than for 40 K PVP capped samples possibly implying that the amount of copper (II) components decreases as the PVP chain length increases. In

fact the XPS spectra in Figure 4.38 show more Cu (I) present for 40 K PVP capped copper oxide NM samples than the 10 K samples.

Figure 4.44 shows the spectra for a number of copper standards measured and obtained from Dr Ryo Sekine (NERC Centre for Ecology & Hydrology (CEH)). Attempts were made to fit the sample spectra using copper nitrate, copper hydroxide, copper (I) oxide, copper (II) oxide and copper metal spectra. This was done in order to analyse the samples' speciation quantitatively. Despite this, no adequate fitting was achieved. This seems to indicate the presence of a more complex oxidation state of copper oxide. It is hoped that future beam time will shed light on the samples' quantitative speciation.

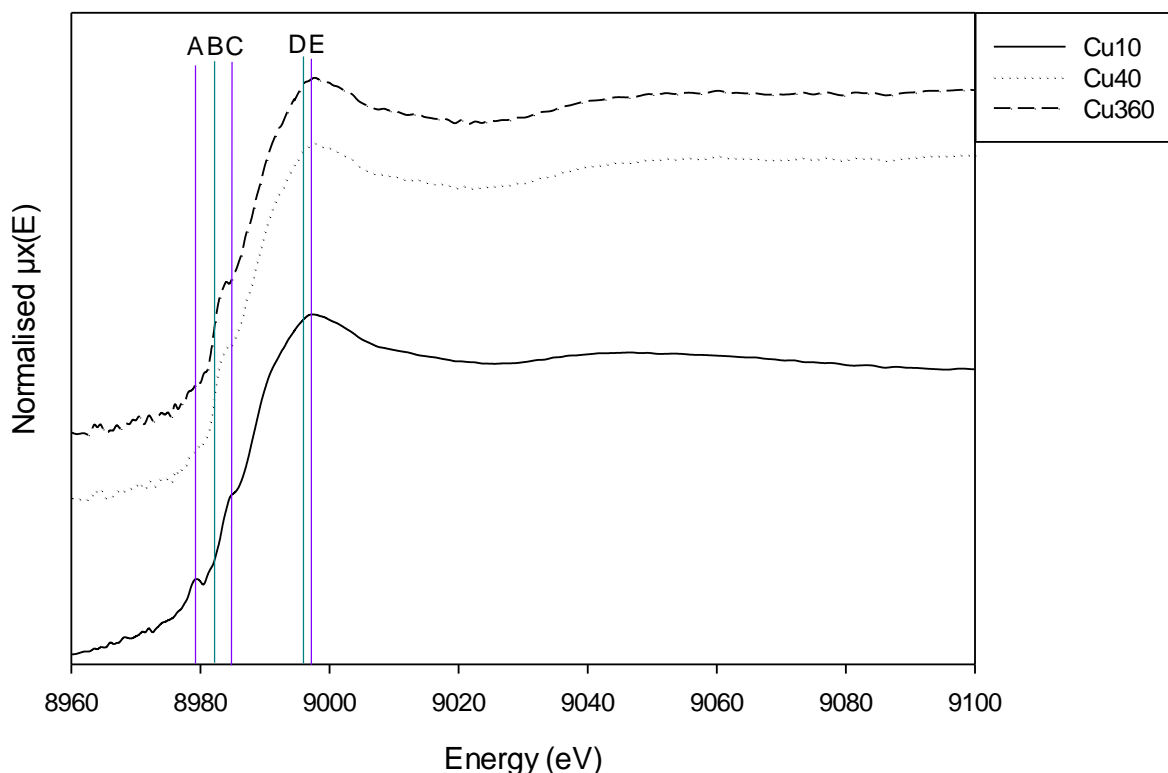


Figure 4.43 EXAFs spectra for PVP capped copper oxide NMs.

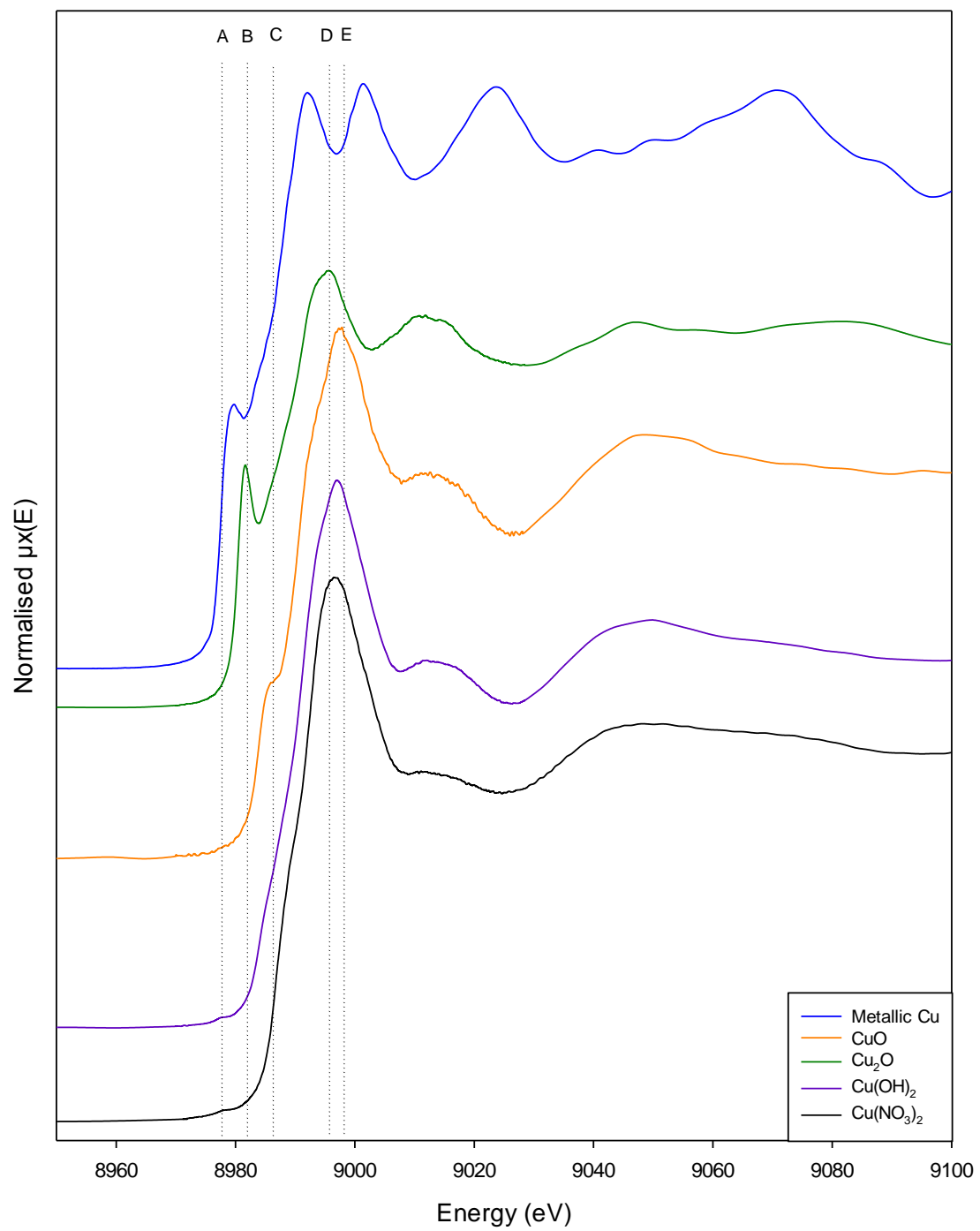


Figure 4.44 EXAFs spectra for copper standards used for sample fittings.

4.7.2.7 ICP-OES

In order to determine the concentration of the synthesised NM dispersions by comparison with a range of freshly prepared standards of varying concentration ICP-OES was carried out. All the concentration results are shown in Appendix 3. Table 4.10 shows the average concentration and the standard deviation for each sample type and scale-up factor. The data can be visualised in Figures 4.45-4.48.

On analysing the data obtained, (Table 4.10) and Figures (4.45-4.48), it can be seen that the sample concentration increases as the scale-up factor increases. The synthesis method (Section 4.4) ensured that unreacted material was removed as only the PVP capped metal oxide NM pellet was retained. This increase in yield proves the success of the reaction scale-up. The reason for the increase in yield is most probably due to the shift of the reaction equilibrium. This is in accordance with Le Chatelier's principle which states that 'if a dynamic equilibrium is disturbed by changing the conditions, the position of equilibrium moves to counteract the change' (Le Chatelier, 1884). Hence the increased amount of starting reagents in the same volume of water results in the equilibrium shift and a greater yield. Despite the increase in final concentration the increase factor is not simply directly related to the increase in starting reagents. One reason for this could be that the reaction time was kept the same and therefore the greater amount of reagents did not have enough time to react fully. Another reason for this reduction in reaction efficiency could be due to the steric hindrance of the PVP polymer. Additionally, as the scale-up factor became greater, the error associated with the concentration results also increased.

Furthermore, as the PVP chain length increases irrespective of the NM core, the final concentration obtained decreases despite the initial amount of nitrate used was kept

constant regardless of the PVP chain length used. This is probably due to the different amounts of PVP used depending on the type of PVP together with the longer the chain the greater the percentage of loops and tails and hence the more difficult for the NMs to reach the binding site.

Finally, apart from 10 K PVP capped copper oxide, there is no significant difference in molar concentration based on the type of metal oxide core as seen in Figure 4.48. Despite this the concentration values are so small that the 10 K PVP capped copper oxide value can still be considered comparable to the other 10 K PVP capped metal oxide NMs. The PVP has no preferential affinity to the different metal oxide NM cores and the initial and final molar quantities between the different metal oxide NMs are similar and comparable for a specific type of PVP. The concentration is however dependent on the type of PVP used as previously mentioned.

Table 4.10 Average concentration and standard deviation for NM dispersions synthesised.

Sample	x1 (mg/L)	x3 (mg/L)	x6 (mg/L)
Ce 10 K PVP	2.030 ± 0.480	11.378 ± 2.123	15.631 ± 4.268
Ce 40 K PVP	1.595 ± 0.370	8.216 ± 2.121	15.561 ± 6.114
Ce 360 K PVP	0.236 ± 0.039	3.246 ± 0.929	5.178 ± 2.936
Zn 10 K PVP	0.906 ± 0.137	3.246 ± 0.728	7.353 ± 2.848
Zn 40 K PVP	0.856 ± 0.126	2.421 ± 0.718	6.563 ± 1.951
Zn 360 K PVP	0.154 ± 0.084	0.619 ± 0.139	1.818 ± 1.006
Cu 10 K PVP	1.440 ± 0.231	3.364 ± 0.980	4.273 ± 0.814
Cu 40 K PVP	0.779 ± 0.212	1.915 ± 0.266	6.261 ± 1.935
Cu 360 K PVP	0.228 ± 0.057	0.617 ± 0.347	1.972 ± 0.990

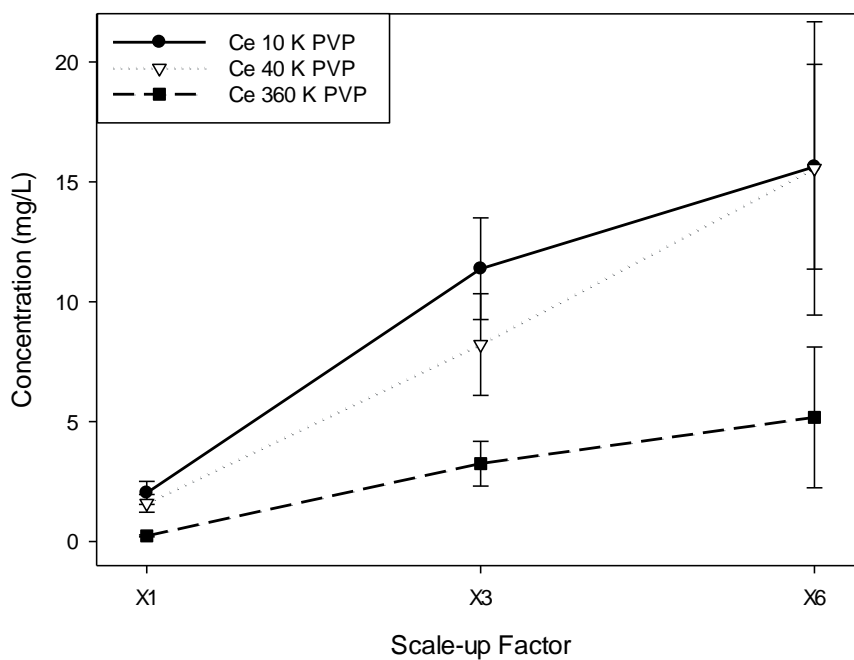


Figure 4.45 ICP-OES values for scaled-up PVP capped ceria as prepared, x3 and x6 for (a) 10 K PVP, (b) 40 K PVP and (c) 360 K PVP.

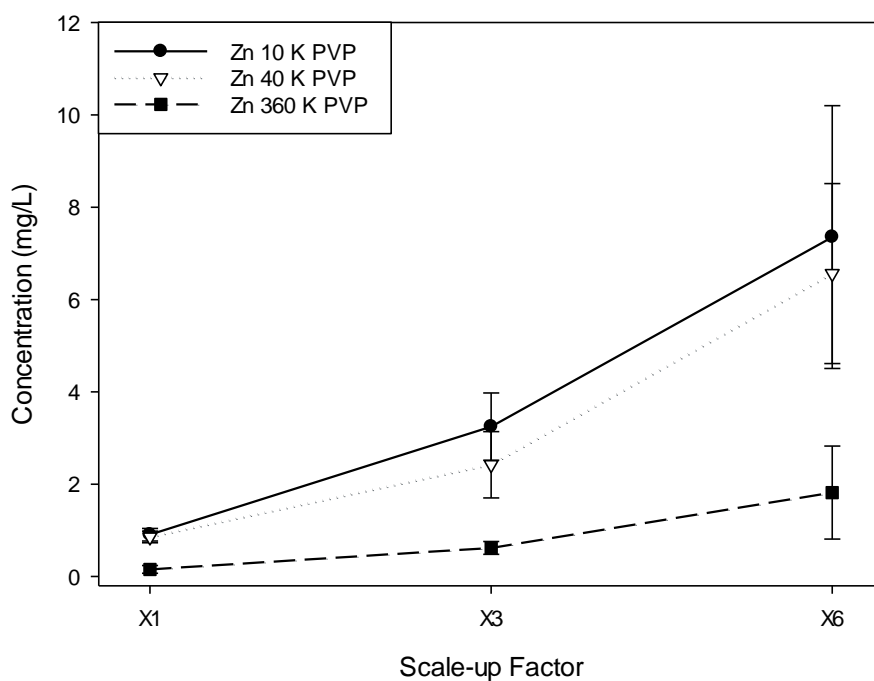


Figure 4.46 ICP-OES values for scaled-up PVP capped zinc oxide as prepared, x3 and x6 for (a) 10 K PVP, (b) 40 K PVP and (c) 360 K PVP.

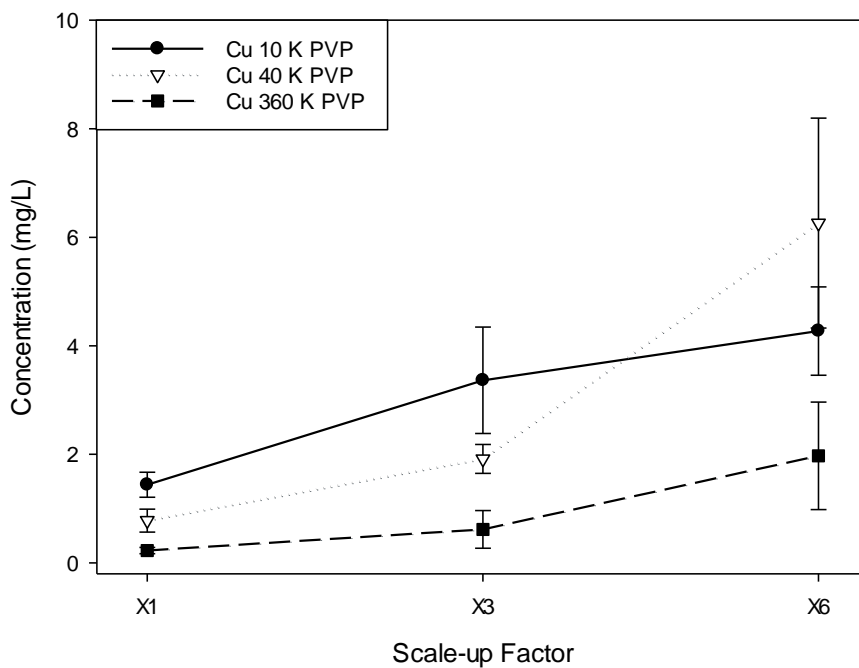


Figure 4.47 ICP-OES values for scaled-up PVP capped copper oxide as prepared, x3 and x6 for (a) 10 K PVP, (b) 40 K PVP and (c) 360 K PVP.

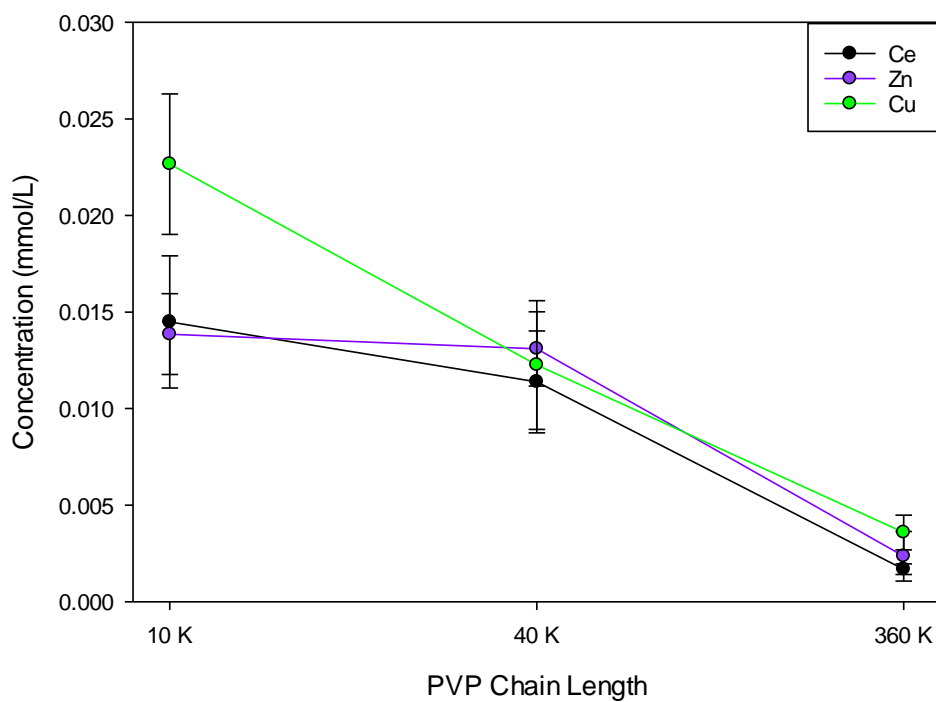


Figure 4.48. ICP-OES values for different PVP capped metal oxide NMs (a) ceria (b) zinc oxide and (c) copper oxide.

4.8 Reaction Mechanism

It is understood that the mechanism of NM formation is the same in all cases suggesting that the protocol is very robust and has the potential to generate a wide range of comparable manufactured NMs. Furthermore it is believed that the mechanism is as that described by Merrifield et al. (2013) for PVP capped ceria NPs.

All metal nitrates are soluble in water (Ramsden, 2000). Therefore the metal nitrate in solution results in the formation of M^{x+} ions. Hydrolysis involves further chemical reaction of hydrated ions with the water. Metal ions in aqueous solution behave as Lewis acids meaning that they accept a lone pair of electrons from a Lewis base such as OH^- as depicted in Figure 4.49. The positive charge on the metal ion draws electron density from the O-H bond in the water. This increases the bond's polarity making it easier to break. When the O-H bond breaks an aqueous proton is released producing an acidic solution.

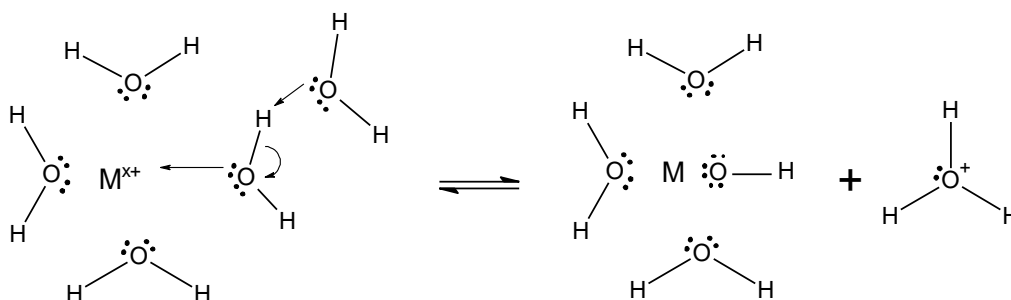


Figure 4.49 Hydrolysis of metal nitrates.

The PVP chains attach to the nanoparticles by means of the carbonyl groups of the PVP attaching to the hydroxyls on the surface of the nanoparticles. The attachment of the

PVP results in a strong stabilisation of the metal oxide nanoparticles. The longer the PVP chain the greater the number of adsorption sites and the stronger the adsorption. Therefore more nanoparticle cores are able to attach along the polymer chain once they are able to come into contact with these sites. This results in larger particle size obtained as the PVP polymer chain length increases for two reasons. Firstly the longer chain contributes to a larger hydrodynamic diameter. Secondly, a longer chain allows for a greater number of nanoparticles to nucleate along a single PVP chain and therefore the particles are likely to coalesce and form larger clusters along the chain.

Steric stabilisation ensures colloidal stability of the NM solution. An overall schematic of the reaction mechanism can be seen in Figure 4.50 and Figure 4.51 depicts the mechanism reaction for the syntheses.

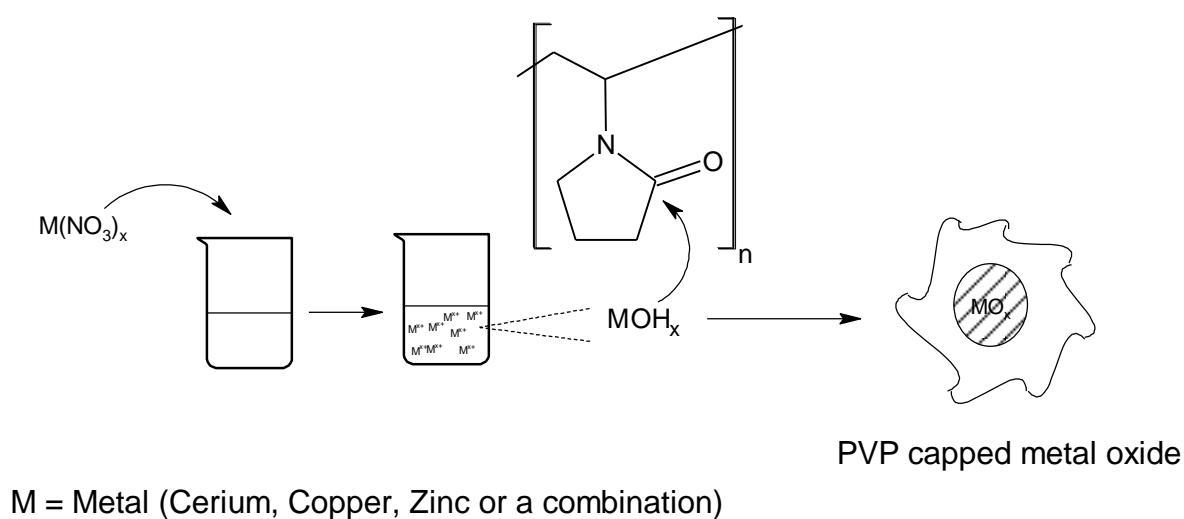


Figure 4.50 Mechanism for synthesis of PVP capped metal oxide nanoparticles.

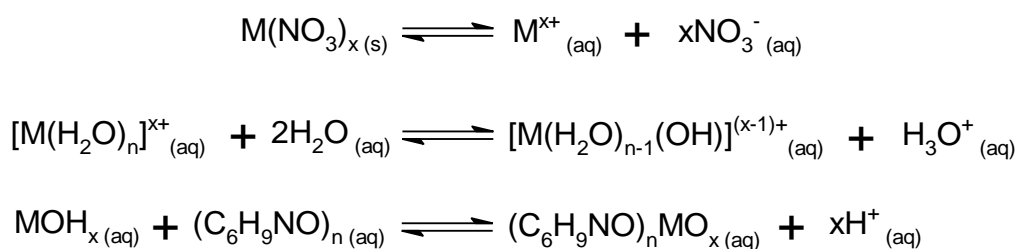


Figure 4.51 Mechanism reactions for syntheses of PVP capped metal oxide nanomaterials.

4.9 Conclusions

The PVP hydrothermal synthesis implemented by Merrifield et al. (2013) to synthesise and characterise PVP capped ceria NMs has successfully been used to synthesise PVP capped ceria. The procedure was further extended to produce a range of different size core/capping NMs. The synthesis was also modified in order to obtain PVP capped zinc oxide and copper oxide NMs. Furthermore the synthesis was scaled-up by a factor of three and a factor of six.

A multi-method characterisation approach was taken in order to determine as much information as possible about the NM samples. Characterisation has shown that the modifications were successful and the synthesis is easily adaptable.

The NM sizes obtained were found to be dependent on the PVP capping, and independent of the metal oxide core. As the PVP chain length increased so did the NM size. Size measurements were obtained by means of a multi-method approach, namely DLS, TEM and STEM. DLS showed the 10 K PVP capped NMs to be c. 5-6 nm, 40 K PVP capped NMs to be c. 7-8 nm and 360 K PVP capped NMs to be c. 19-20 nm. TEM showed comparable values to those obtained for 10 K and 40 K PVP capped NMs with the former having a size of c. 5-7 nm and the latter c. 8-9 nm. The size results for the 360 K

capped metal oxide NMs obtained by means of TEM are smaller than those obtained by DLS and were c. 12-13 nm. STEM sizes values were obtained for 10 K PVP capped NMs and showed the core NP size to be c. 3-4 nm.

The zeta potential of all samples and scaled-up samples was found to be close to zero regardless of the NM core but rather due to steric stabilisation brought about by the PVP capping.

FT-IR was implemented to confirm the presence of the metal – oxide bond. UV-VIS, XPS, EELS, EDX and EXAFS were carried out to determine and confirm the valency state of the metal forming the metal oxide core. Results confirmed the presence of the metal oxide NMs. The NMs were found to be present as mixed oxides when the metal present could occur more than one valency state, specifically in the case of copper and ceria. Whereas in the case of zinc, only pure zinc oxide was formed.

The scale-up was confirmed by means of ICP-OES, which was used to determine the concentration of the samples. Moreover it was noted that as the PVP chain length increased the NM concentration decreased regardless of the NM core and the molar concentration of the different NMs was comparable amongst the different PVP types.

PVP has been found to play a significant role in the synthesis of the NMs. Additionally results have shown it to play a role in determining both the materials' physical properties, including appearance and size, as well as the materials' chemical properties including surface charge, concentration and oxidation state composition.

This work provided the development of a NM library which can provide comparable NMs for toxicology or behavioural studies as variables are systematically altered. Examples of behavioural studies include temperature ageing and phosphate ageing studies explored in Chapters 5 and 6 respectively.

With respect to further work on the NM library this could ideally include studying the oxide speciation forming the nanomaterial core by means of EXAFS. Additionally attempts could be made to extend the nanomaterial library further by changing the initial metal nitrate reagent.

Chapter 5: Thermal Transformations of Manufactured Nanomaterials (MNM)s as a Proxy for Ageing

5.1 Introduction

Ageing is an important part of a nanomaterial's life cycle and can be considered as a transformation over time. It is very relevant to nanomaterials because they are more reactive than their bulk counterparts due to their larger surface area to volume ratio. Most NMs react in ways that change their behaviour and properties over time (Sarathy et al., 2008). Aged NMs no longer have the same characteristics of their pristine counterparts (Mitrano et al., 2015). During ageing several structural and chemical changes occur that are affected by time, temperature and nanoparticle physicochemical properties, particularly composition and concentration. Changes in temperature have been found to affect various nanoparticle properties including size, aggregation and shape as well as the rate of the reaction (Auffan et al., 2009, Karakoti et al., 2012).

Varying properties such as temperature, humidity and oxidation, speed up the normal ageing processes of materials and thus offering more information on the long-term effects within a shorter time. Elevated temperature studies is one way of studying accelerated ageing.

Consequently thermal treatments could possibly be used as a proxy for ageing over time. To date this has been used in a diversity of fields including those of materials such as composites, polymers and metal behaviour testing, conservation and environmental

aspects such as organism mortality (Demir et al., 2004, Lazzari and Chiantore, 2000, Favaro et al., 2006, Omastová et al., 2003, Zhang et al., 2016, Song et al., 1995). Despite these many applications of this approach, temperature ageing has not been implemented in the field of nanotechnology for the understanding of nanomaterial physical and chemical behaviour in prolonged environmental exposure scenarios.

This Chapter deals with the temperature ageing scenario of samples from the PVP NM library described in Chapter 4, as well as commercially available ceria NMs as a proxy for ageing over time. It discusses the samples selected to undergo temperature ageing, the ageing procedure and the characterisation analysis. The work aims to study the physical and chemical changes occurring to the NMs on exposure to various temperatures for a period of 4 weeks. This duration was chosen to represent a longer ageing period than that currently extant in the literature. Furthermore, it was recognised as a long enough period within the project time duration to determine the influence of temperature, as the PVP capped metal oxide NMs were found to be stable at room temperature, when measured by DLS, for a minimum of six months. This can be seen for 10 K PVP capped ceria in Figure A.4.1 in Appendix 4.

The temperature ageing study was carried out at 25, 45, 65 and 80 °C. The first temperature is often used as reference room temperature. The final temperature chosen is lower than the boiling point of water to avoid the physical impact of boiling. Though 80 °C is not environmentally relevant, it was selected as the highest acceleration temperature following the 10 degree rule. The other chosen temperatures fall within the range of 25-80 °C in order to effectively cover the chosen range.

5.2 Samples selected for temperature ageing

The following samples were used for the temperature ageing studies:

- 10 K PVP (for reference)
- 10 K PVP capped ceria
- 40 K PVP capped ceria
- 360 K PVP capped ceria
- 10 K PVP capped zinc oxide
- 10 K PVP capped copper oxide
- Commercial cerium (IV) oxide NPs (Sample A)

The first six samples listed are taken from the NM library developed and discussed in Chapter 4 whilst the seventh sample is a commercially available cerium (IV) oxide sample obtained from Promethean Particles Ltd. (Nottingham). The first is a PVP reference sample included to study the influence of temperature simply on the capping. The Promethean particles are uncapped ceria nanoparticles synthesised through a continuous hydrothermal synthesis. They have a hydrodynamic diameter of 172.1 ± 1.705 nm. Further characterisation of these NMs can be found in Appendix 5. The reason for selecting these samples was to compare:

1. The reference 10 K PVP sample with the PVP capped metal oxide nanoparticle samples. Only one PVP chain length was chosen due to time constraints as well as to limit

the number of samples and rather include more NM containing samples. Therefore the most commonly used PVP chain length amongst the samples was chosen.

2. The differing PVP chain length capped NMs were included to compare differently sized but similar composition NMs.

3. The 10 K PVP capped metal oxide NMs were all selected from the library in order to compare NM samples with different metal oxide cores yet keeping the same size and the same capping agent.

4. Commercial cerium (IV) oxide was included to compare capped and uncapped ceria samples.

5.3 Samples preparation

The 10 K PVP capped ceria, zinc oxide and copper oxide nanoparticle samples and 10 K PVP reference sample were prepared as explained in Section 4.4 and used as prepared. The commercial cerium (IV) oxide NMs (Sample A) were obtained from Promethean Particles Ltd. (Nottingham) as dispersions in deionised water. The commercial samples were then prepared by mixing 100 μL of the NM dispersions having an initial concentration of ~ 2 wt% in water with 4900 μL of milliQ water.

5.4 Procedure

Three replicates of each of the selected samples mentioned in Section 5.2 were placed in closed vials on a shaker set at 80 rpm in a Raven 2 incubator. Three replicates were used to ensure repeatability and reproducibility. The temperature was set and the

ageing was carried out for 28 days. The temperature ageing study was carried out at 25, 45, 65 and 80 °C.

5.5 Characterisation

Sample characterisation by means of DLS took place at various time points (t=0, 4, 12, 24, 48, 72, 120, 168, 336, 504, 672 hours), both for sizing purposes and also to measure zeta potential (Section 3.2) and UV/VIS (Section 3.3). TEM (Section 3.7) imaging and XPS analysis (Section 3.4) took place at t=0 and at the end of the 28 days.

5.6 Monitoring Physical Changes

5.6.1 Size & Physical features

The size and physical conformation of the NM dispersions exposed to elevated temperatures for a period of 28 days were monitored by means of DLS and TEM. The results can be seen in Figures 5.1-5.7.

The general trend for all samples seen from the DLS results is a decrease in the primary size of the NMs and the development of a second peak at a larger size. The decrease in primary size could indicate the dissolution of the NMs or the loss of the PVP whilst the development of the second peak indicates aggregation of the NMs. This aggregation is seen from the TEM images. As the exposure temperature increases the rate of change of size also increases. The TEM images initially show uniform, spherical, well or relatively well-dispersed particles aggregating more significantly as the temperature is

elevated. Despite a similar trend noted for all samples, significant differences in how the trend is influenced can be noted between the reference, capped and uncapped samples.

Figure 5.1 represents the data obtained for the 10 K PVP sample with the general trend being a decrease in the intensity of primary size peak and development of a second peak at a larger size. This is relatively unaffected until the 80 °C temperature showing minimal changes in size up until this temperature. Comparing the PVP capped ceria NM dispersions in Figures 5.2-5.5 it can be seen that, besides the general trend, as the PVP chain length increases the development of the second peak, the aggregation peak, is found over a more contained region of the graph. This implies that the size of the aggregated particles becomes more uniform. The commercial ceria NMs are significantly affected at 80 °C. The results, shown in Figure 5.6, seem to indicate that a threshold temperature has been exceeded and the NMs are significantly physically transformed. Such drastic transformations are not observed for the PVP capped NMs indicating that the PVP influences the behaviour and protects the NMs. In addition, the rate of size changes looks to vary for the different NM cores (Figures 5.2, 5.7 and 5.8) with the 10 K PVP capped ceria NMs indicating the greatest variations followed by the 10 K PVP capped copper oxide NMs and then the 10 K PVP capped zinc oxide NMs. This reveals that the core composition also plays a role in influencing the rate of aggregation.

Since the observed changes were often subtle statistical manipulations were used to add confidence and robustness to the interpretations. The Pearson product-moment correlation coefficient (PCC) (Section 3.2.3.1.1) was calculated for the temperature, size, primary peak intensity and time of the different samples. The results of this analysis can be found in Appendix 6.

Initially the analysis was carried out on all the data obtained for all dispersions with a total of 44 data samples analysed. The results (Appendix 6) show that, for the commercial ceria NMs, there were no significant relationships between any pair of variables (size, peak intensity, temperature and time) in the correlation table since the value of P is greater than 0.050. As explained in Section 3.2.3.1.1 a P value greater than 0.050 implies no significant correlation. The analysis was then run again for the commercial ceria samples not including the data at 80 °C. This meant analysing 33 data samples rather than 44 and some correlation scenarios were obtained. This further implies that the 80 °C temperature seems to have exceeded a threshold temperature for the thermally induced transformations of the samples.

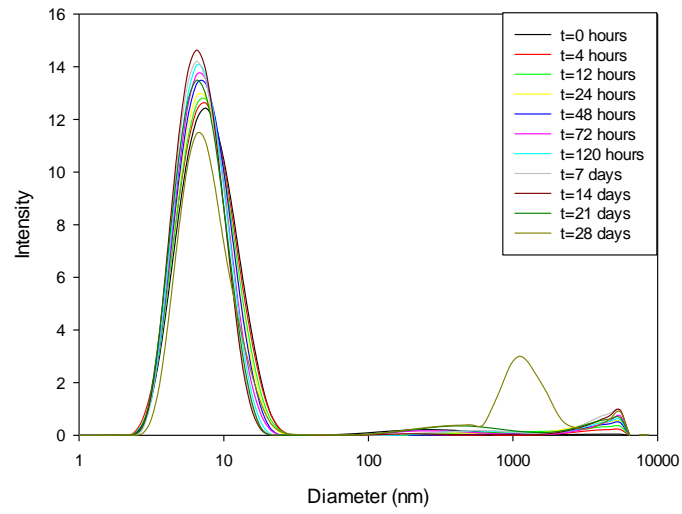
The statistical results show P to equal 1 and the correlation co-efficient to be equal to 0 for the relationship between temperature and time in all situations. This is due to the fact that the parameters are independent from one another.

Although some similarities can be drawn from the statistics no trends running throughout can be noted. This shows the complexity of the ageing scenario that the NMs undergo and further strengthens the importance of a thorough understanding of each nanomaterial in the various environment scenarios that it may be found.

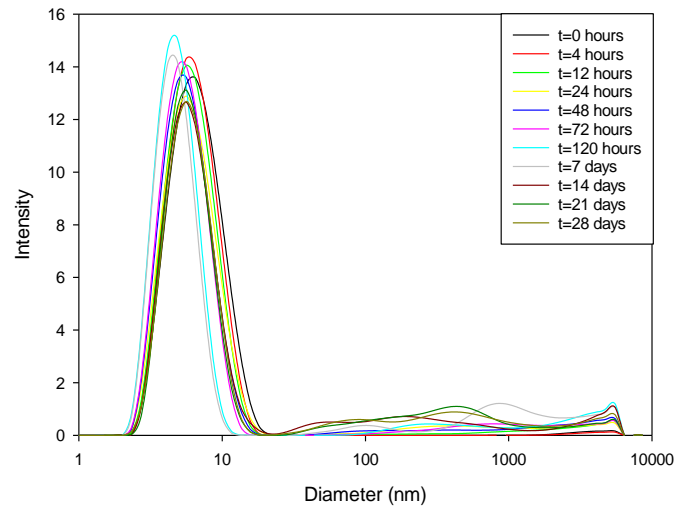
Size and temperature show a significant relationship in the case of 10 K, 40 K and 360 K PVP capped ceria and 10 K PVP capped zinc whilst in the case of all other samples there is no significant relationship between the two. This implies that core and capping interactions as well as the core composition are both influential properties to the NM behaviour. Size and time only show a significant correlation in the case of 40 K PVP capped ceria which could be due to the behaviour of the 40 K PVP. Size and peak intensity are significantly correlated in all cases except for 40 K PVP capped ceria,

commercial ceria and 10 K PVP capped copper oxide. This is dependent on the aggregation rate and process.

The relationship between peak intensity and time revealed a correlation coefficient with a negative sign in all cases except for the commercial sample data analysis when including the data at $T=80$ °C. The negative sign associated with the correlation coefficient implies that as time increases, the primary peak intensity does in fact decrease. This was clearly seen in the DLS size graphs and is discussed above. Despite this not all of these values are in fact significant according to the PCC statistical analysis. The commercial ceria and 40 K PVP capped ceria show the relationship not to be significant. Lastly, the relationship between intensity and temperature is significant in all cases except for the commercial ceria and the 10 K PVP capped zinc oxide NMs. When significant, the correlation is negative, except for 360 K PVP capped ceria meaning that as temperature increases intensity decreases. This can also be seen from the DLS graphs.

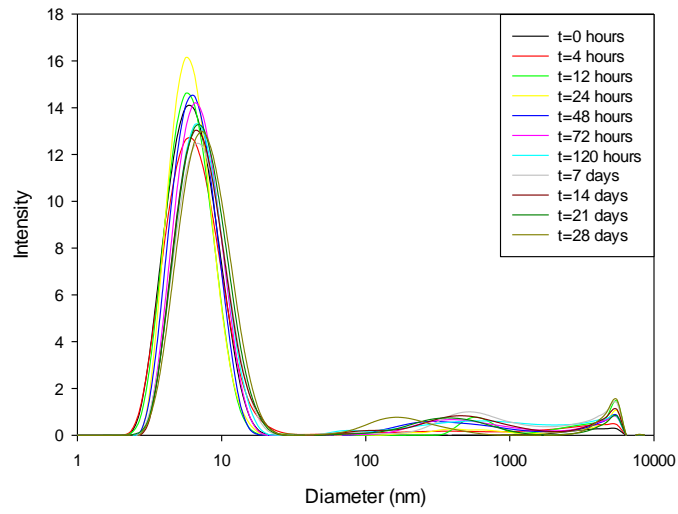


a)

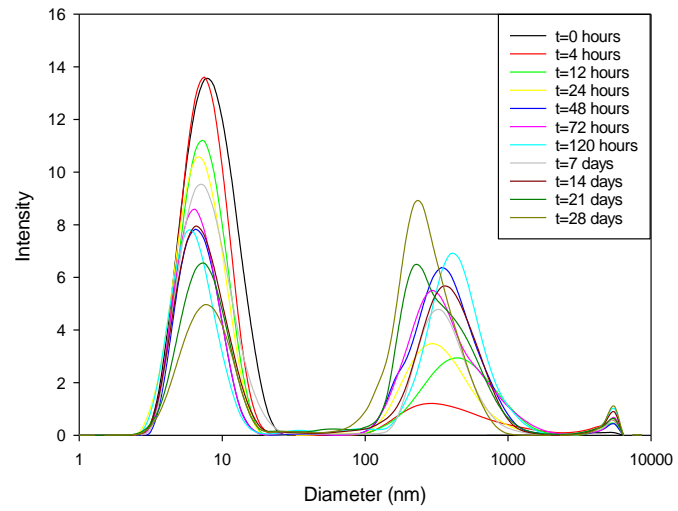


b)

Figure 5.1 a) and b) Size distribution for 10 K PVP samples exposed to a) 25 °C and b) 45 °C as a function of time.

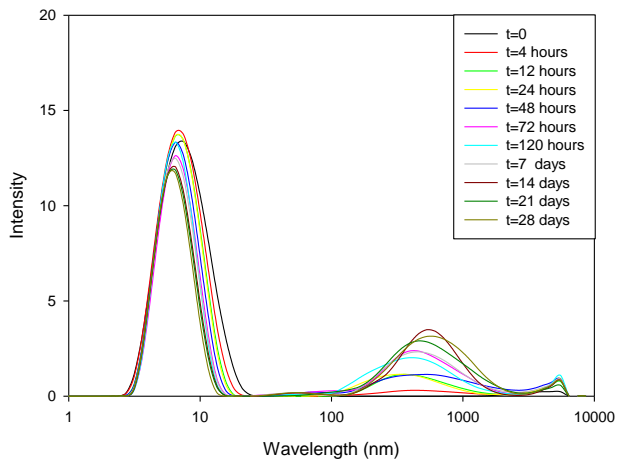


c)

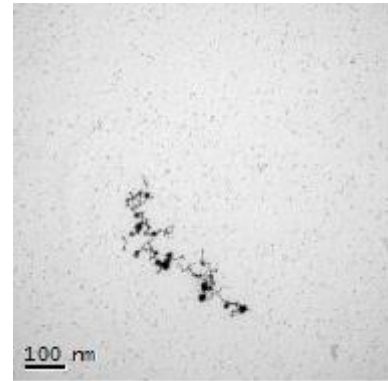


d)

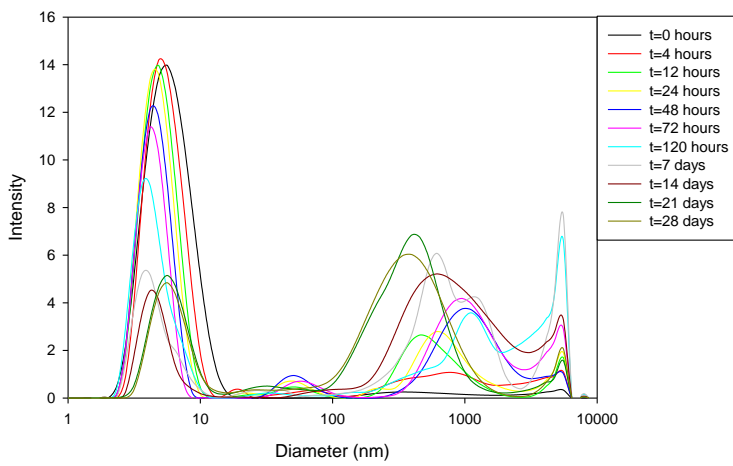
Figure 5.1 c) and d) Size distribution for 10 K PVP samples exposed to c) 65 °C and d) 80 °C as a function of time.



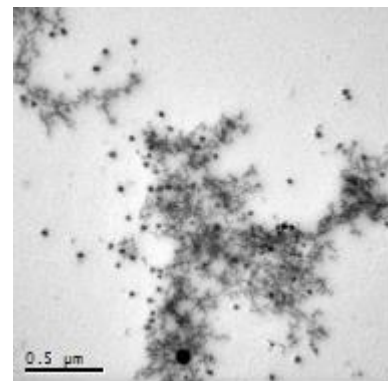
a)



a)

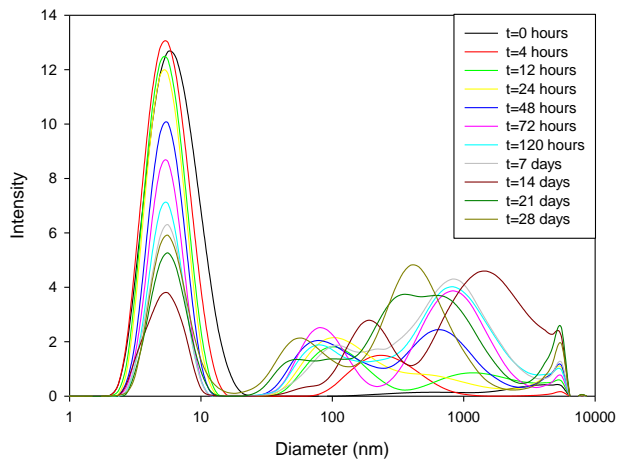


b)

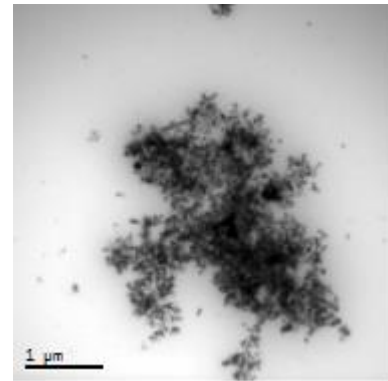


b)

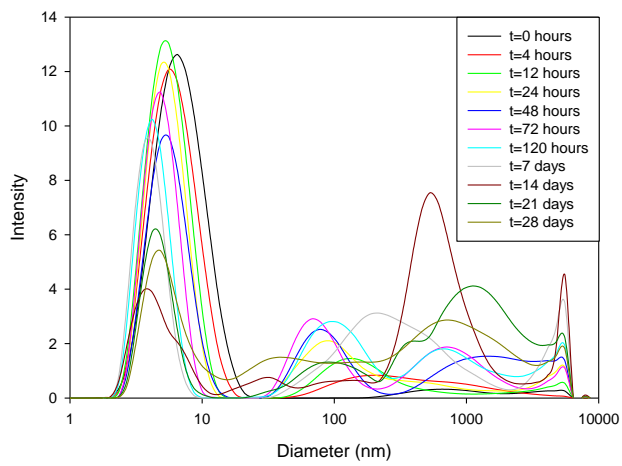
Figure 5.2 a) and b) Size distribution graphs (left) and TEM images (right) for 10 K PVP ceria samples exposed to a) 25 °C and b) 45 °C as a function of time



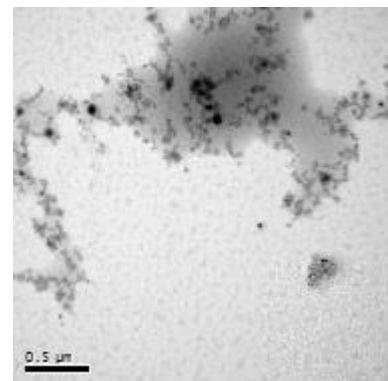
c)



c)

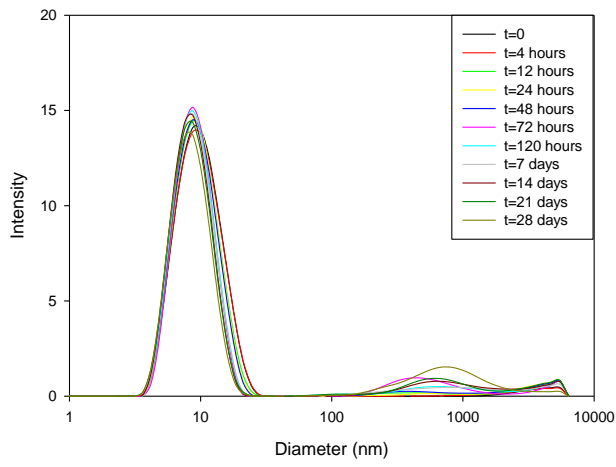


d)

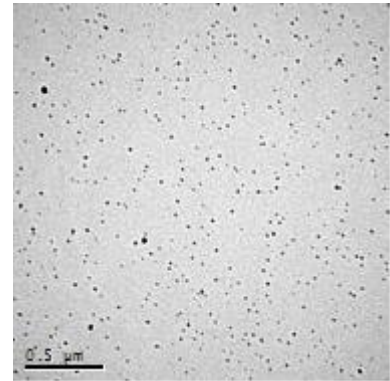


d)

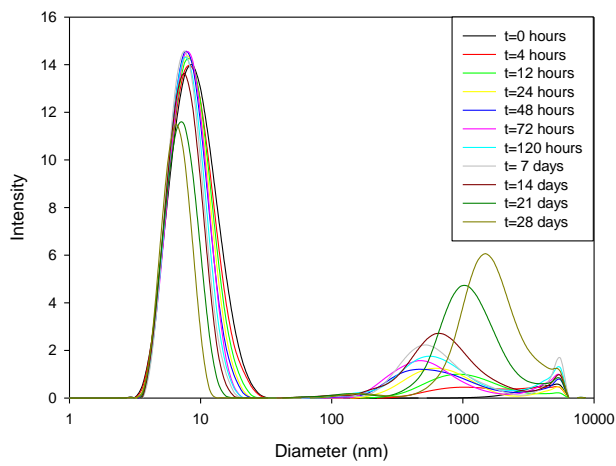
Figure 5.2 c) and d) Size distribution graphs (left) and TEM images (right) for 10 K PVP ceria samples exposed to c) 65 °C and d) 80 °C as a function of time



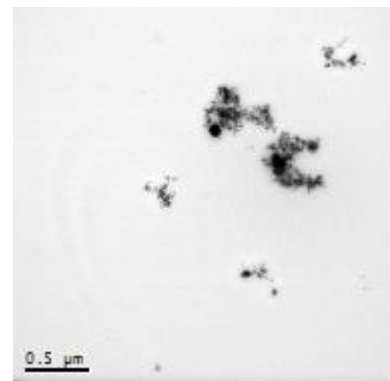
a)



a)

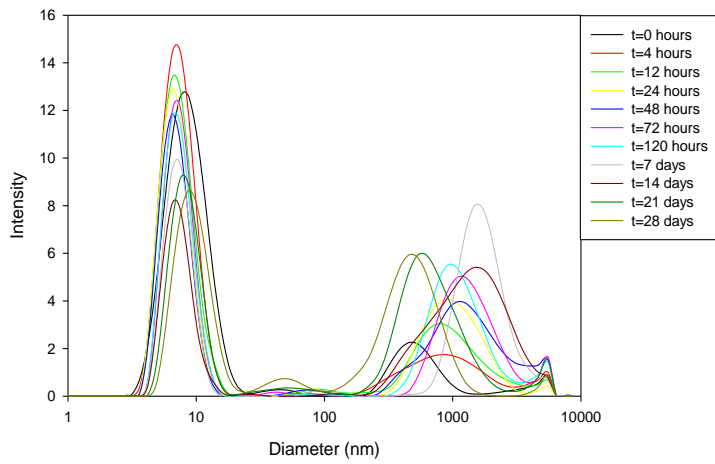


b)

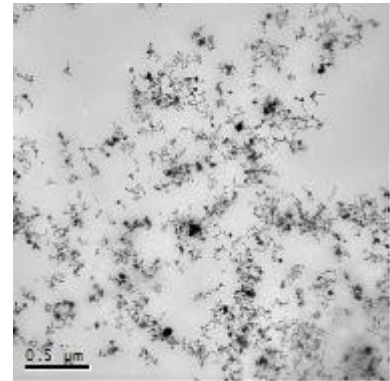


b)

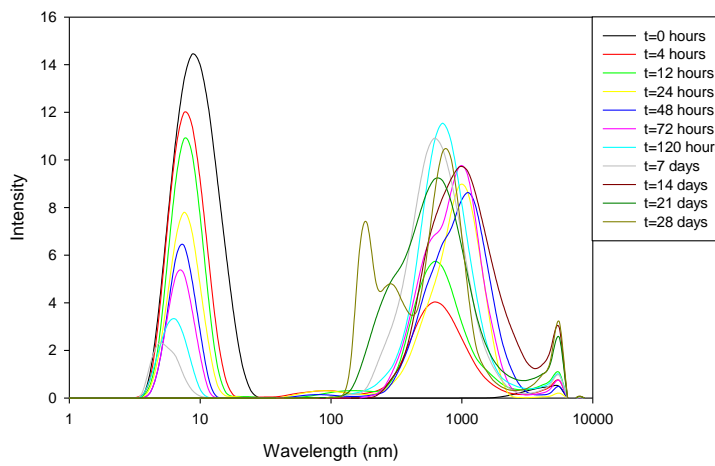
Figure 5.3 a) and b) Size distribution graphs (left) and TEM images (right) for 40 K PVP ceria samples exposed to a) 25 °C and b) 45 °C as a function of time.



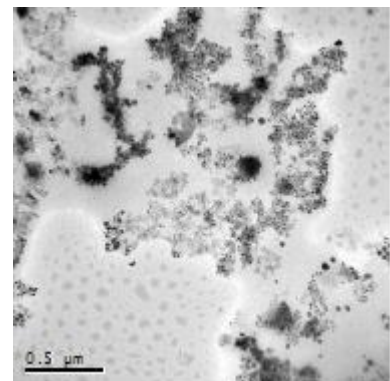
c)



c)

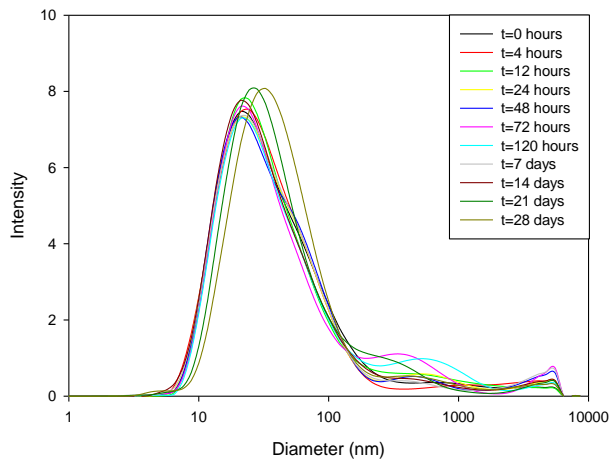


d)

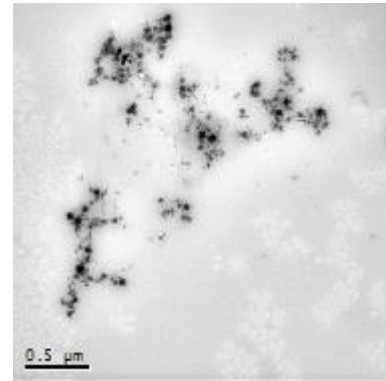


d)

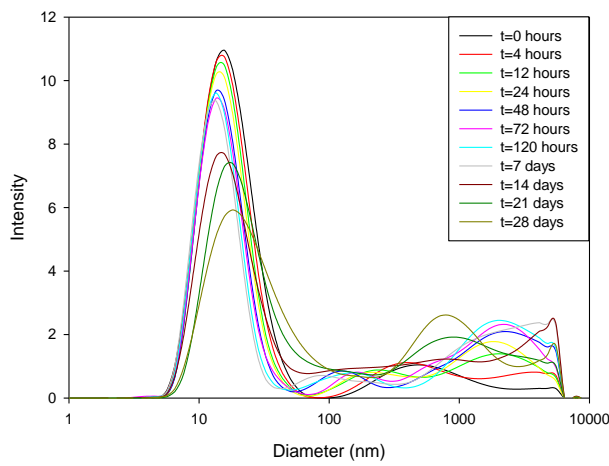
Figure 5.3 c) and d) Size distribution graphs (left) and TEM images (right) for 40 K PVP ceria samples exposed to c) 65 °C and d) 80 °C as a function of time.



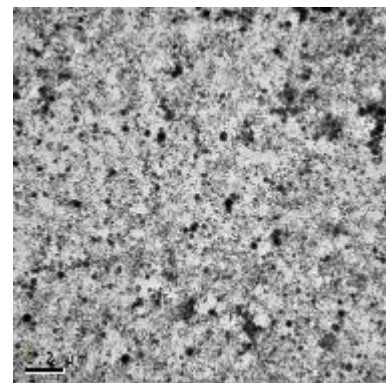
a)



a)

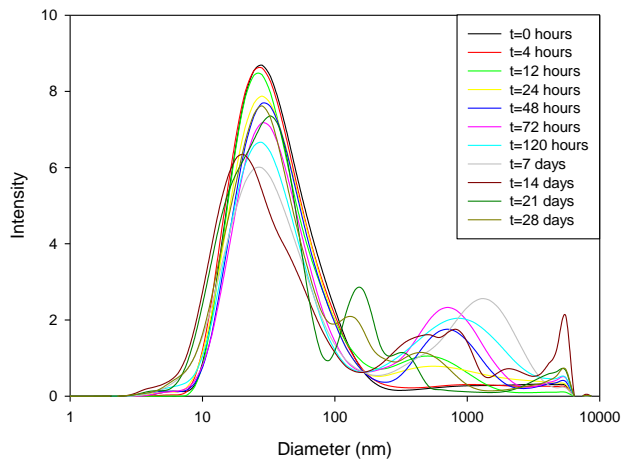


b)

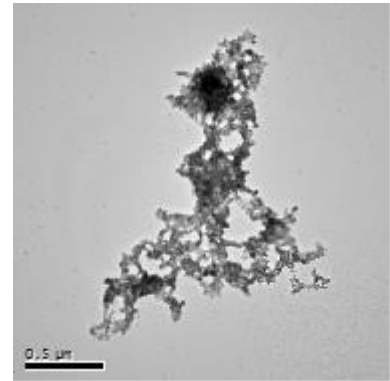


b)

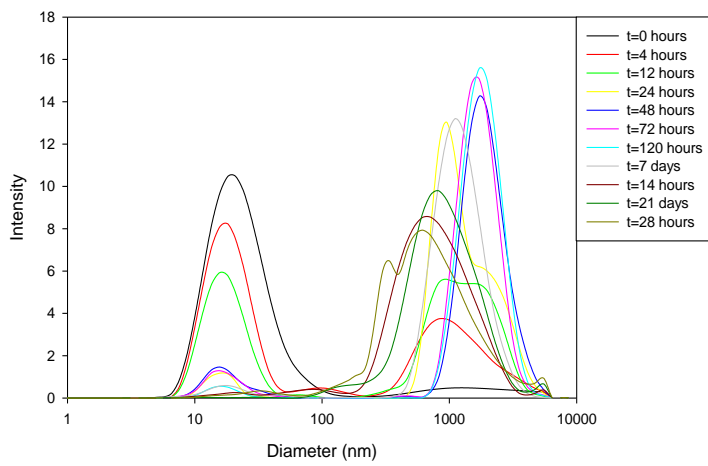
Figure 5.4 a) and b) Size distribution graphs (left) and TEM images (right) for 360 K PVP ceria samples exposed to a) 25 °C and b) 45 °C as a function of time.



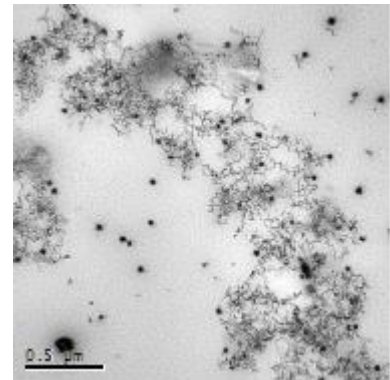
c)



c)

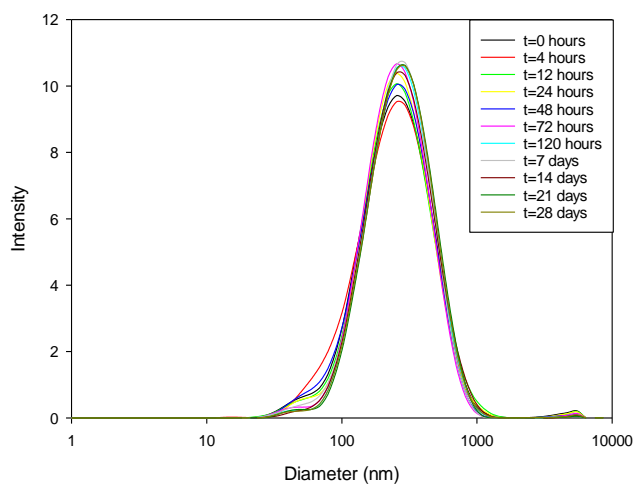


d)

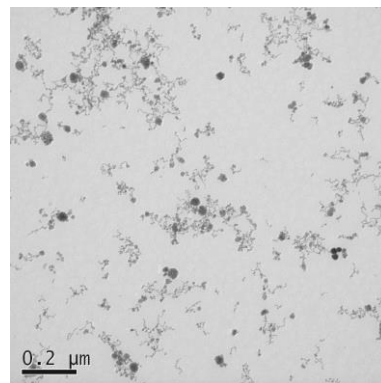


d)

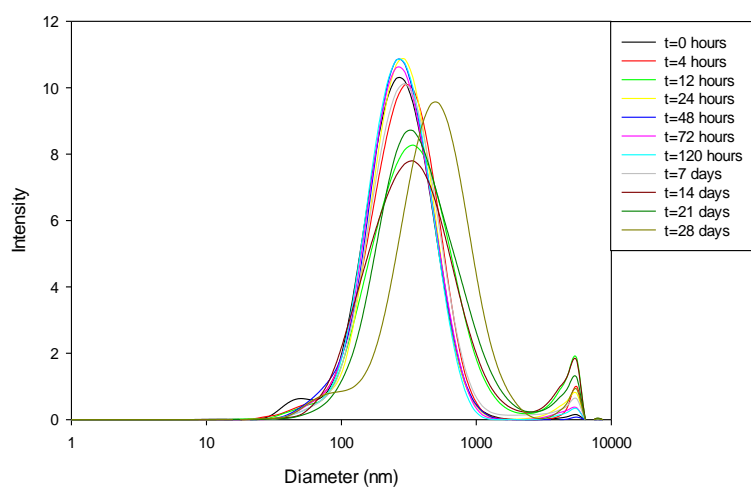
Figure 5.4 c) and d) Size distribution graphs (left) and TEM images (right) for 360 K PVP ceria samples exposed to c) 65 °C and d) 80 °C as a function of time.



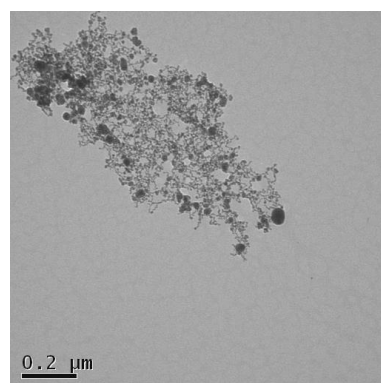
a)



a)

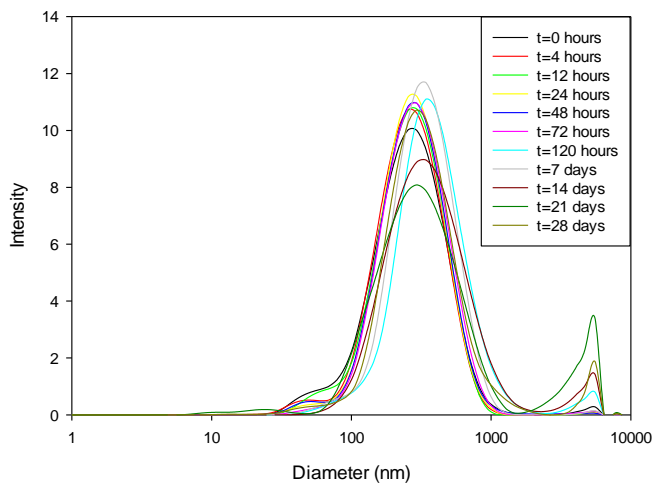


b)

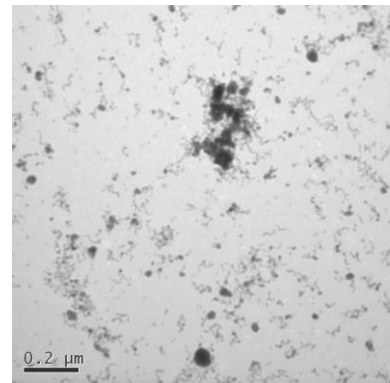


b)

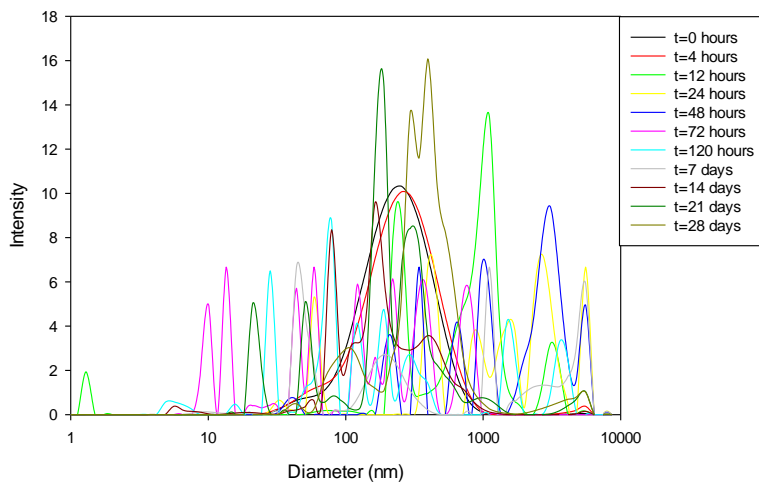
Figure 5.5 Size distribution graphs (left) and TEM images (right) for Commercial ceria samples exposed to a) 25 °C, b) 45 °C, c) 65 °C and d) 80 °C as a function of time.



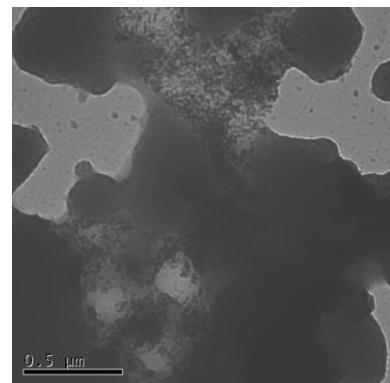
c)



c)

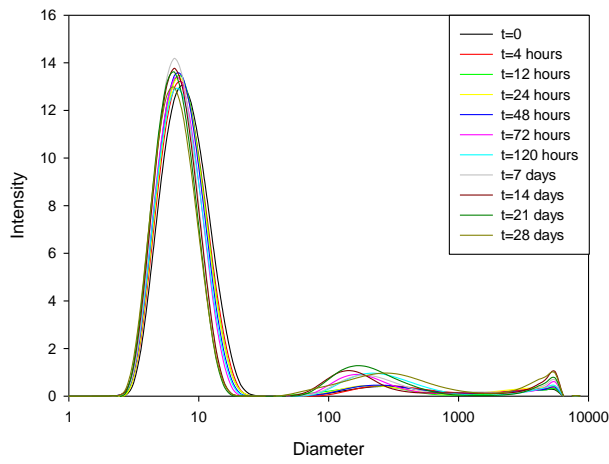


d)

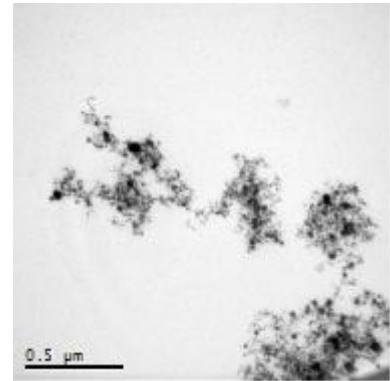


d)

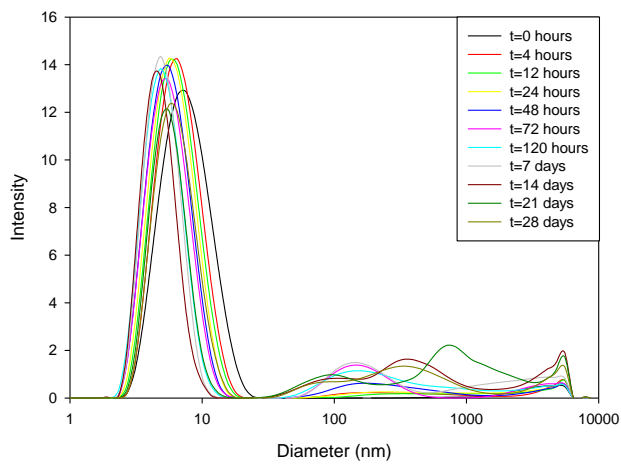
Figure 5.5 Size distribution graphs (left) and TEM images (right) for Commercial ceria samples exposed to a) 25 °C, b) 45 °C, c) 65 °C and d) 80 °C as a function of time.



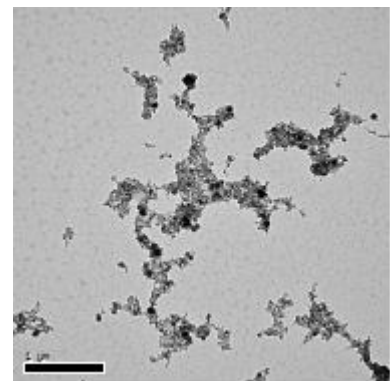
a)



a)

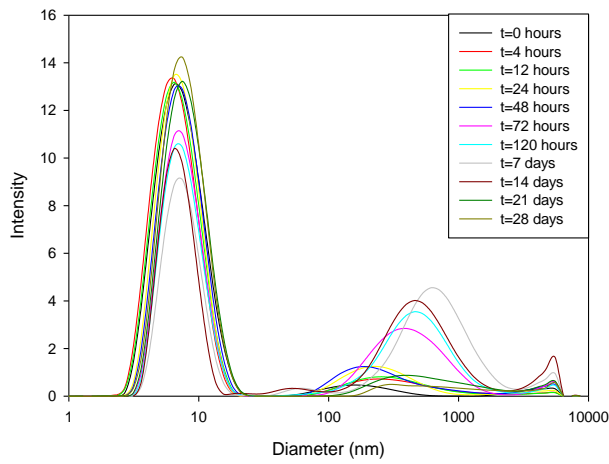


b)

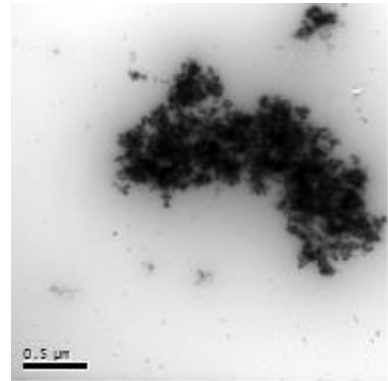


b)

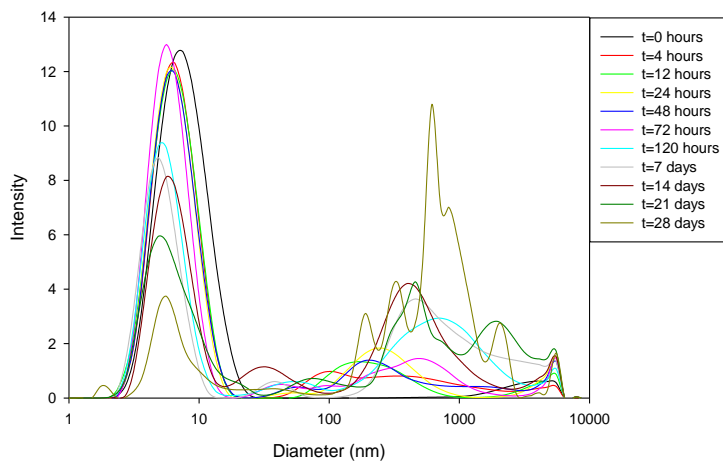
Figure 5.6 a) and b) Size distribution graphs (left) and TEM images (right) for 10 K PVP capped copper oxide samples exposed to a) 25 °C and b) 45 °C as a function of time.



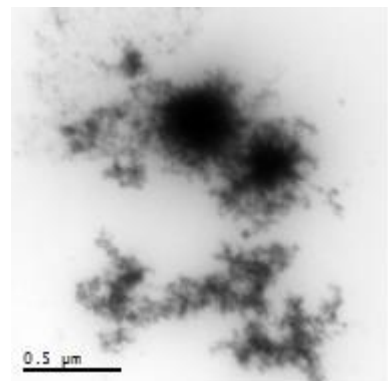
c)



c)

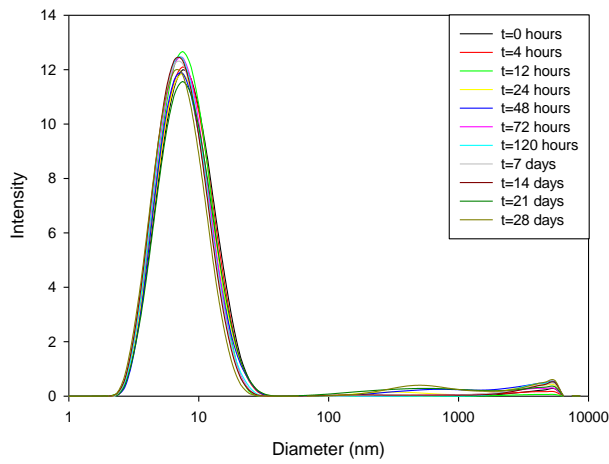


d)

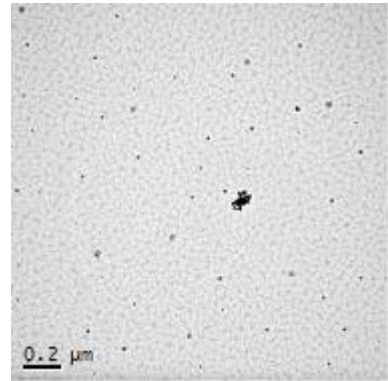


d)

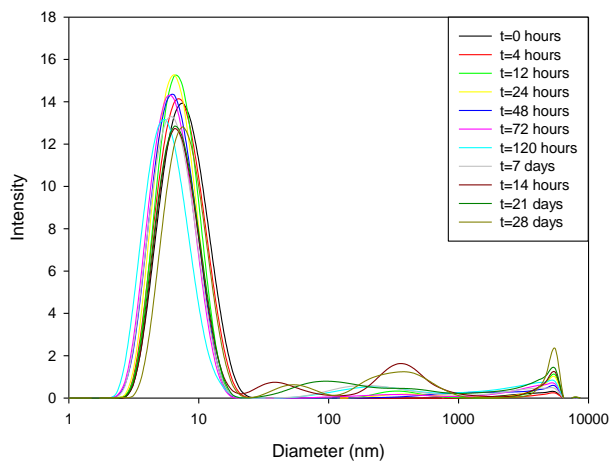
Figure 5.6 c) and d) Size distribution graphs (left) and TEM images (right) for 10 K PVP capped copper oxide samples exposed to a) 25 °C, b) 45 °C, c) 65 °C and d) 80 °C as a function of time.



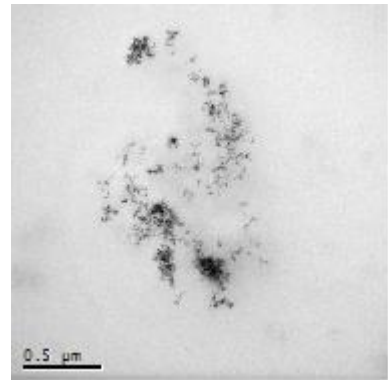
a)



a)

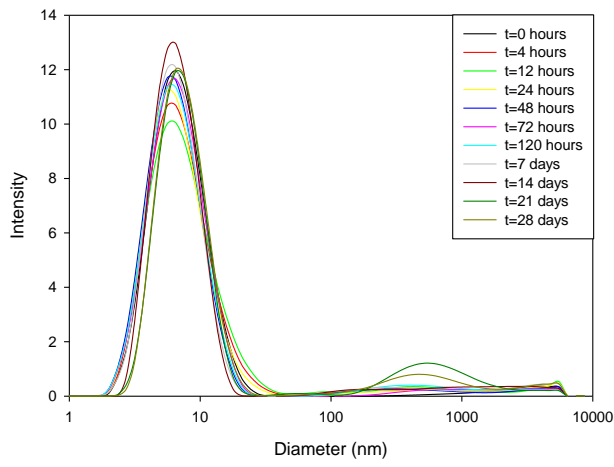


b)

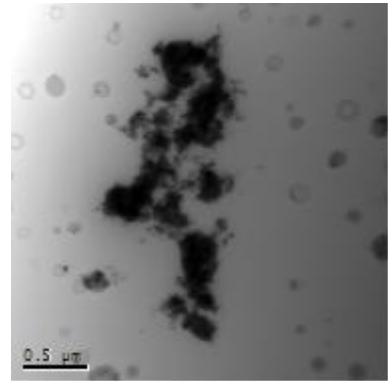


b)

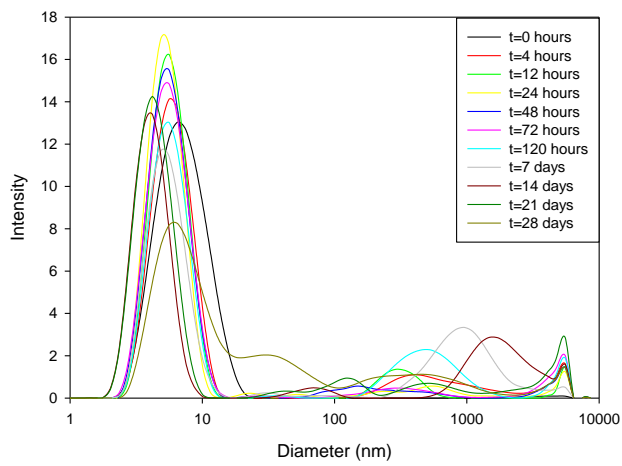
Figure 5.7 a) and b) Size distribution graphs (left) and TEM images (right) for 10 K PVP capped zinc oxide samples exposed to a) 25 °C and b) 45 °C as a function of time.



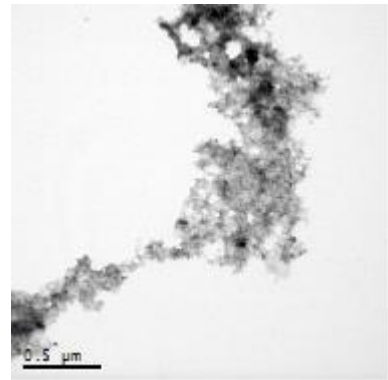
c)



c)



d)



d)

Figure 5.7 c) and d) Size distribution graphs (left) and TEM images (right) for 10 K PVP capped zinc oxide samples exposed to c) 65 °C and d) 80 °C as a function of time.

5.7 Monitoring Chemical Changes

5.7.1 Surface Charge

The thermal influence on the surface charge of the samples was measured by means of DLS zeta potential analysis. Prior to the analysis the pH of the samples was measured. All PVP containing samples had a pH of c.6 whilst the commercial ceria samples had a pH of 7. Following this it was assumed that the pH of the samples did not change over time.

The data, plotted in Figures 5.8-5.14, represent the change in average zeta potential at different temperatures as a function of time. Results have shown behaviour differs for PVP sample and the NM samples, capped and uncapped NMs and for NMs with varying core composition indicating that the presence of the capping agent, the capping and core interaction and the core composition are all factors that are affected differently by temperature and all play a role in zeta potential values.

Noticeable changes over time for the different temperatures were only observed in the case of the PVP samples, the commercial ceria NMs and the PVP capped zinc oxide NMs.

The PVP samples (used for reference) which have an original zeta potential value close to 0 mV due to PVP steric stabilisation (Section 4.7.1) show changes over time which are most noticeable at 80 °C (Figure 5.8). These changes involve a decrease of a maximum of c. 12 mV and an increase of c. 2 mV from this value.

Clearly, of all the NMs, the commercial ceria NMs' surface charge was that influenced most by temperature (Figure 5.12). The fact that the NMs' surface was not

protected by a capping agent meant that no steric stabilisation was present to stabilise the dispersion and the change in surface charge is what brings about the aggregation. Therefore, this results in more aggregation taking place at a faster rate than in the case of the PVP protected samples.

The change in zeta potential was most influenced at 80 °C with a significant drop in zeta potential to values very close to 0 mV indicating that the NMs are no longer stable and as a result aggregation may be taking place. This was in fact observed in the DLS and TEM results seen in Section 5.6.1. Furthermore, the greater the exposure temperature the greater the associated error (i.e. the error bars) became. It is most probably likely to more interactions occurring between the NMs as the temperature increased.

In the case of PVP capped zinc oxide (Figure 5.14) changes fluctuated over a greater zeta potential range than the other PVP samples fluctuating from -3 mV to + 2.5 mV. Despite this the values obtained at different temperatures only became significant amongst one another on the very last measurement taken on day 28.

All the other samples, namely 10 K, 40 K and 360 K PVP capped ceria and 10 K PVP capped copper oxide, seen in Figures 5.9-5.11 and 5.13 respectively, show no significant change in average zeta potential over time regardless of the exposure temperature. In the case of these samples the average zeta potential values remains similar to the original value which is around 0 mV due to PVP steric stabilisation as discussed in Section 4.7.1 in Chapter 4. Despite this the discrepancy in the behaviour of the PVP samples and the PVP capped metal oxide NM samples, which involves the PVP samples showing more changes in zeta potential over time than the PVP capped metal oxide NMs, indicates that the presence of the NM core results in the surface charge is effected differently by temperature. As a result the rate of aggregation is also different as it is

dependent on the surface charge. TEM and DLS results discussed in Section 5.6.1 indicate that aggregation is occurring and therefore the reason that the zeta potential values are found at around 0 mV are likely to be influenced by this decrease in stability.

A quick side study was carried out whereby the zeta potential of mixtures containing varying amounts of PVP mixed with the commercial ceria NMs revealed that the zeta potential value of the solution decreases to approach 0 as the amount of PVP mixed in is increased. Additionally, mixing of the PVP does not ensure capping of the NMs therefore it is very likely that in the case of the temperature ageing work the PVP capping is not working as effectively as previously confirmed through the TEM and DLS. Nevertheless the zeta potential remained unchanged due to the excessive amount of PVP still present within the solution.

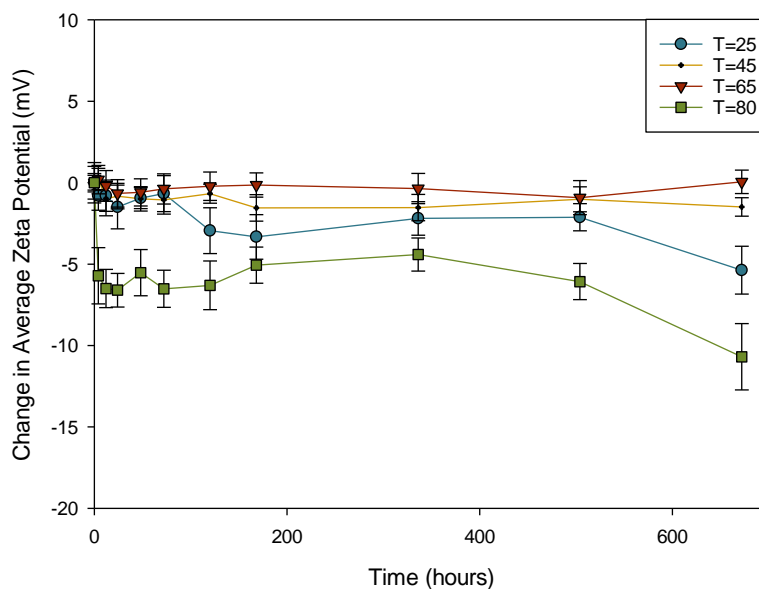


Figure 5.8 Change in average zeta potential (mV) as a function of time for 10 K PVP samples at 25, 45, 65 and 80 °C.

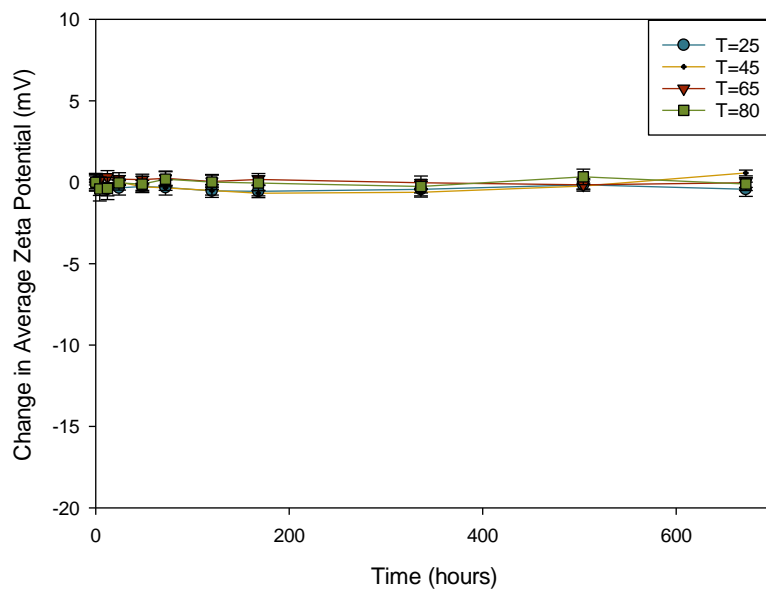


Figure 5.9 Change in average zeta potential (mV) as a function of time for 10 K PVP capped ceria samples at 25, 45, 65 and 80 °C.

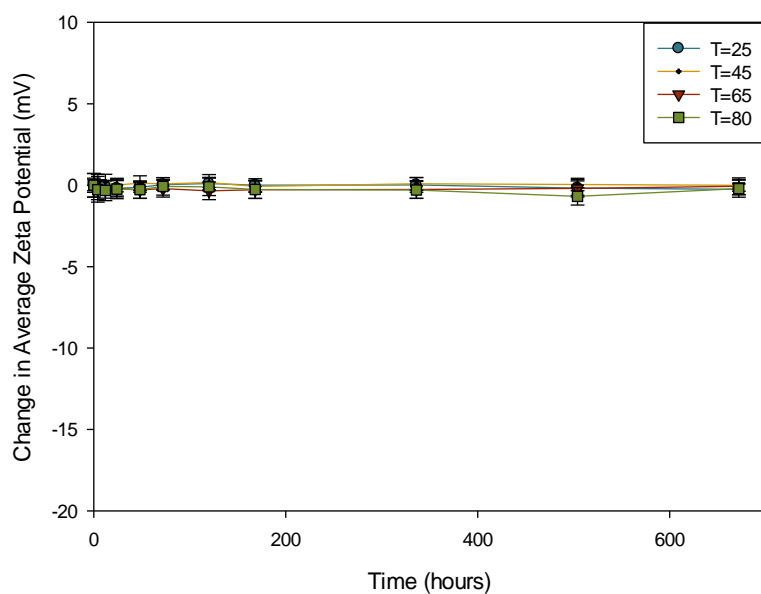


Figure 5.10 Change in average zeta potential (mV) as a function of time for 40 K PVP capped ceria samples at 25, 45, 65 and 80 °C.

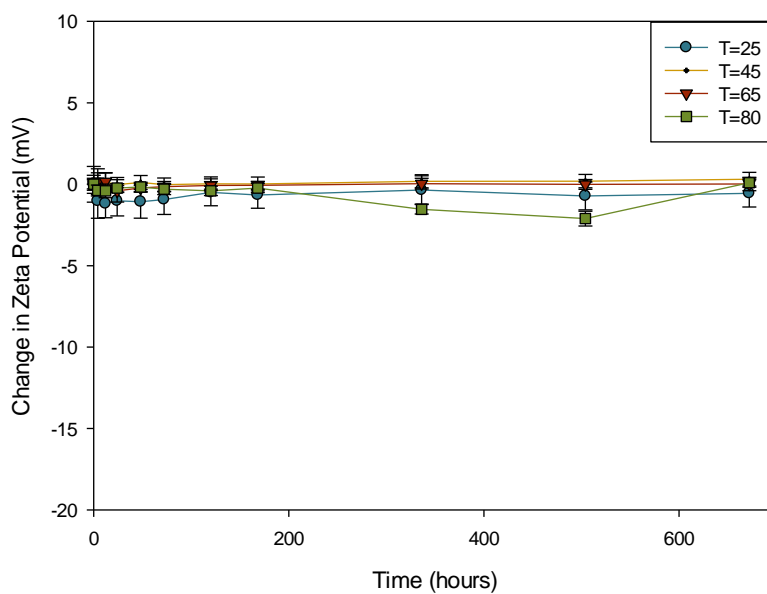


Figure 5.11 Change in average zeta potential (mV) as a function of time for 360 K PVP capped ceria samples at 25, 45, 65 and 80 °C.

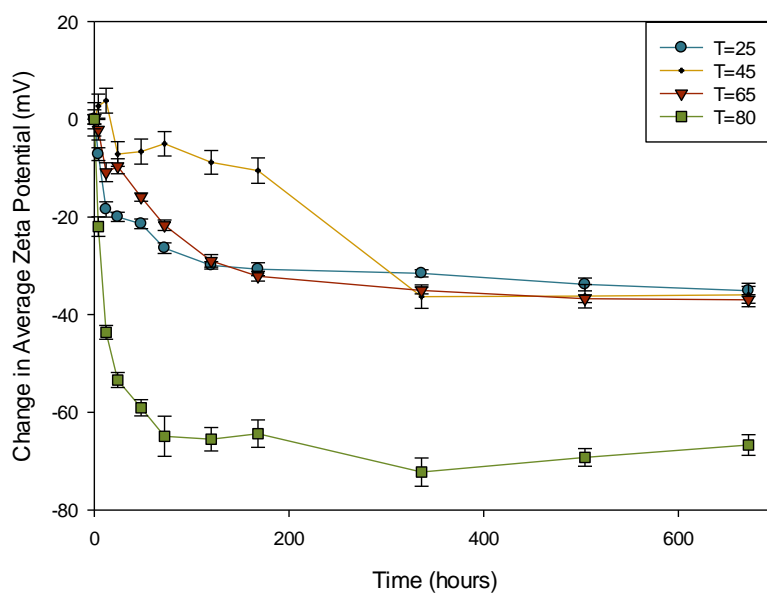


Figure 5.12 Change in average zeta potential (mV) as a function of time for commercial ceria samples at 25, 45, 65 and 80 °C.

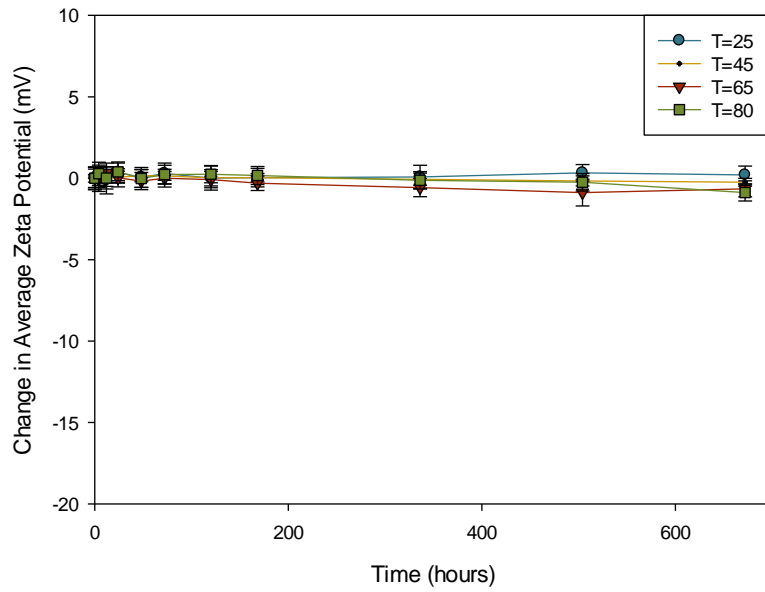


Figure 5.13 Change in average zeta potential (mV) as a function of time for 10 K PVP capped copper oxide samples at 25, 45, 65 and 80 °C.

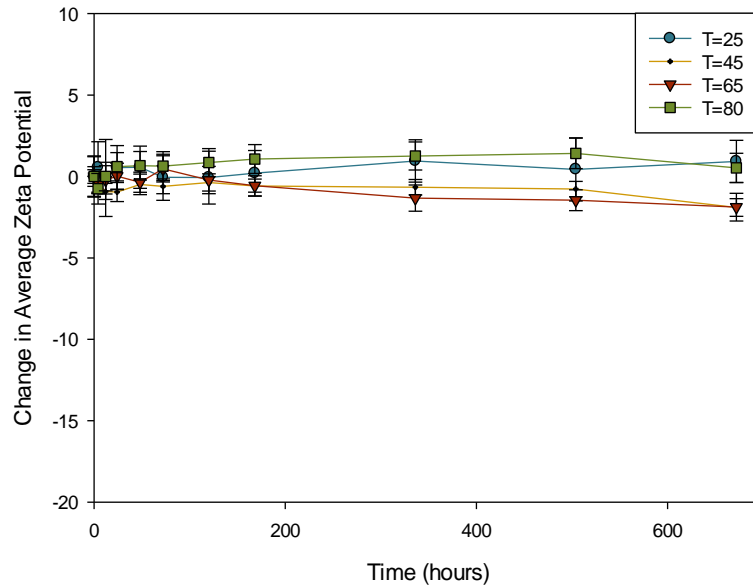


Figure 5.14 Change in average zeta potential (mV) as a function of time for 10 K PVP capped zinc oxide samples at 25, 45, 65 and 80 °C.

5.7.2 Chemical Composition

5.7.2.1 X-ray Photoelectron Spectroscopy

XPS analysis was carried out to study the influence, if any, of temperature on the oxidation state of the NM surfaces. The spectra obtained after 28 days of exposure can be seen in Figures 5.15 – 5.21. The data for the as prepared samples is taken from the data obtained in Chapter 4 and all spectra were referenced to the C1s peak (C-C, C-H) at 285.0 eV binding energy.

The spectra of the PVP capped zinc oxide NMs show no significant change, those of the commercial ceria NMs show minimal changes, and the PVP capped ceria NMs and PVP capped copper oxide samples show significant changes. The latter two show variations in the metal oxidation state. This is an important feature to study as it has been suggested that oxidative stress could play an important role in toxicity due to the formation of reactive oxygen species (ROS) (Aydın et al., 2012).

In general the changes noted from the XPS spectra amongst the PVP capped NMs decreased from ceria to copper oxide to zinc oxide. This correlates with the rate of change in size discussed in Section 5.6.1 whereby the rate of size changes looks to be greatest for PVP capped ceria to copper oxide to zinc oxide. This shows that the behaviour of the NMs and the influence of temperature on the NMs are dependent on the core chemical composition.

Kim et al. (2012) report Ce^{3+} having XPS peaks at 885.0 and 903.5 eV whilst Ce^{4+} has peaks at 882.1, 888.1, 898.0, 900.9, 906.4, and 916.4 eV. The most distinctive feature when observing the XPS spectra of cerium is the presence or absence of a peak at 916 eV which is a characteristic satellite peak of cerium (IV) (Heckert et al., 2008).

The different PVP chain lengths result in different chemical core composition for the as prepared samples as explained in Section 4.7.2.3 in Chapter 4. Furthermore, the PVP capped ceria NMs show significant changes between the spectra at different temperatures. As explained in Section 2.5.2.2, in ceria oxygen vacancy formation occurs when an oxygen atom moves away from its lattice position and hence leaves behind two electrons. These two electrons localise on two neighbouring cerium atoms resulting in the change from Ce (4+) to Ce (3+). This redox cycling behaviour differs for the different types of PVP chain lengths implying that PVP, which acts as an electron donor causing the cerium present in the form of Ce⁴⁺ to gain an electron and hence be reduced to Ce³⁺, plays a role in this reaction. Furthermore, temperature facilitates and affects the rate of these redox reactions.

Changes in core metal oxidation state of the PVP capped ceria NMs show that even though capping stabilises the NMs they are not blocked from external factors such as temperature.

10 K PVP capped ceria, the spectra of which are shown in Figure 5.15, starts off as a mix of Ce³⁺ and Ce⁴⁺ (Section 4.7.2.3). The spectra show that temperature influences the ratio of Ce³⁺ to Ce⁴⁺ as the peaks change intensity, particularly that at 916 eV. At 80 °C the sample is clearly reduced and the presence of Ce⁴⁺ is no longer noticeable. This is concluded from the lack of the presence of the peak at 916 eV.

In the 40 K PVP capped ceria NMs the as prepared XPS spectrum revealed that they were the only PVP capped ceria samples composed solely of Ce³⁺, with no presence of Ce⁴⁺ (Figure 4.36 and Table 4.9). These NMs show no redox changes until the NMs are exposed to 80 °C (Figure 5.15). At this temperature the NMs are oxidised and the sample is composed of a mix of both Ce³⁺ and Ce⁴⁺.

It was not possible to record any spectra for the 360 K PVP capped ceria NMs after exposure to 80 °C as no signal was obtained. The elevated temperature could be causing dissolution and at this highest exposure temperature the samples are likely to have the highest solubility. In fact, what was originally considered the primary DLS peak is nearly non-existent after 28 days (Figure 5.4d).

The spectra seen in Figure 5.17 show that initially the as prepared NMs are composed of both Ce⁴⁺ and Ce³⁺. The samples are reduced to Ce³⁺ at 25 and 45 °C and are once again oxidised to a mix at 65 °C.

For the commercial ceria NMs, seen in Figure 5.18, only some slight changes in peak intensities and ratios can be noticed as a result of exposure to varying temperatures. The presence of Ce⁴⁺ is noted in all spectra. The lack of the PVP capping, which acts as a reducing agent, is probably the reason why the NMs are not as easily reduced as the PVP capped metal oxide NMs.

The binding energy of PVP capped zinc oxide NMs, seen in Figure 5.19, does not seem to vary at the different temperatures. The similar BE energy values of Zn (0) and Zn (II), 1021.7 eV and 1022 eV respectively, make it difficult to determine between the two as mentioned in Section 4.7.2.3 (Thermo Fisher Scientific Inc., 2013b). Hence the need for Auger peaks analyses. In the case of these NMs the LMM Auger line for the kinetic energy was found at c. 988 eV at all temperatures. This confirms the presence of Zn (II) unaffected by temperature.

The spectra for the 10 K PVP capped copper oxide NMs after different temperature exposures, Figure 5.20, show some small changes in peak intensity and width. All spectra show the presence of strong satellite peaks at 943 eV indicating the presence of Cu (II). The as prepared samples and those after exposure at 25, 45 and 65 °C show two peaks at

above and around 935 eV indicating that both copper (II) and copper (I) species are present. This means that in the samples at 80 °C any Cu (I) present has been completely oxidised to Cu (II).

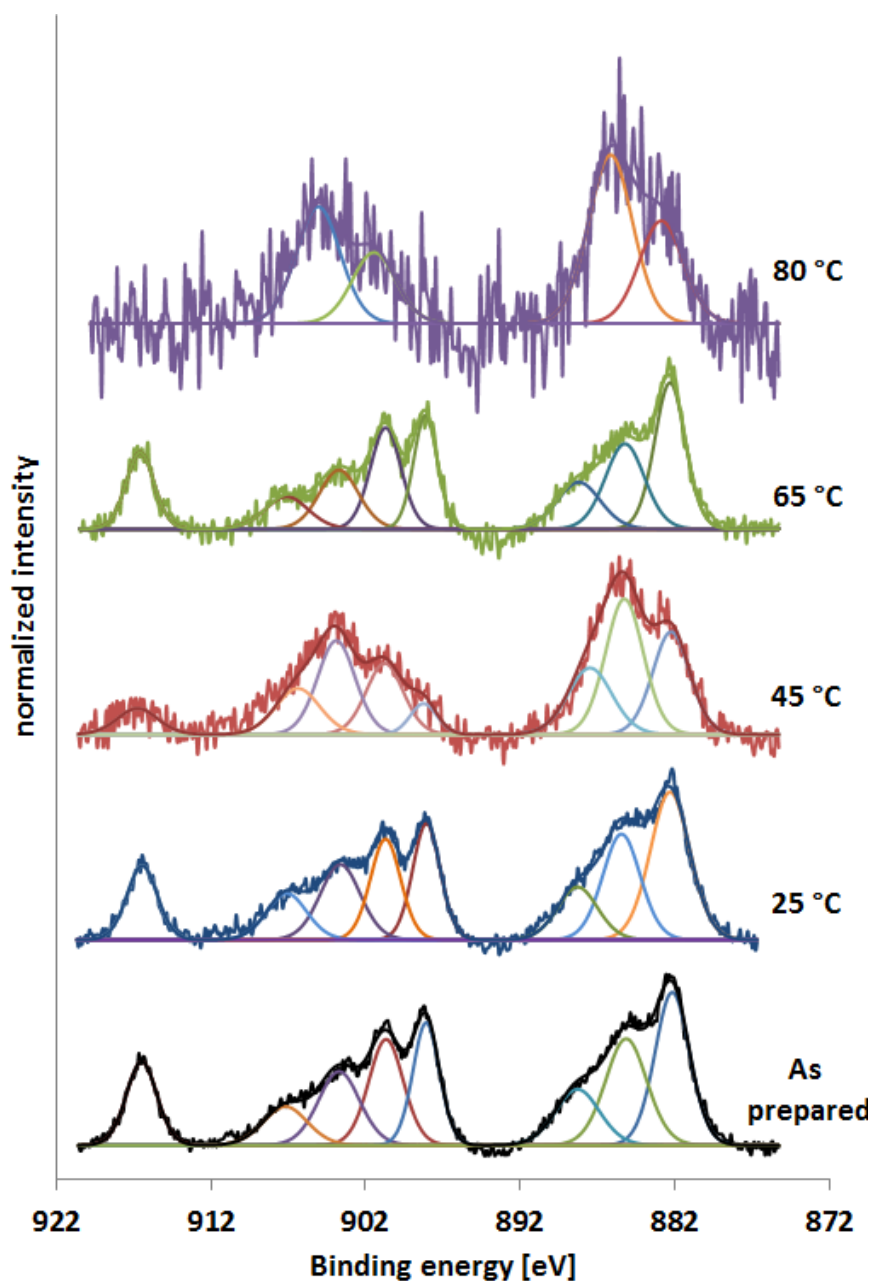


Figure 5.15 XPS Spectra for 10 K PVP capped ceria as prepared and after 28 days at T=25, 45, 65 and 80 °C (from bottom to top).

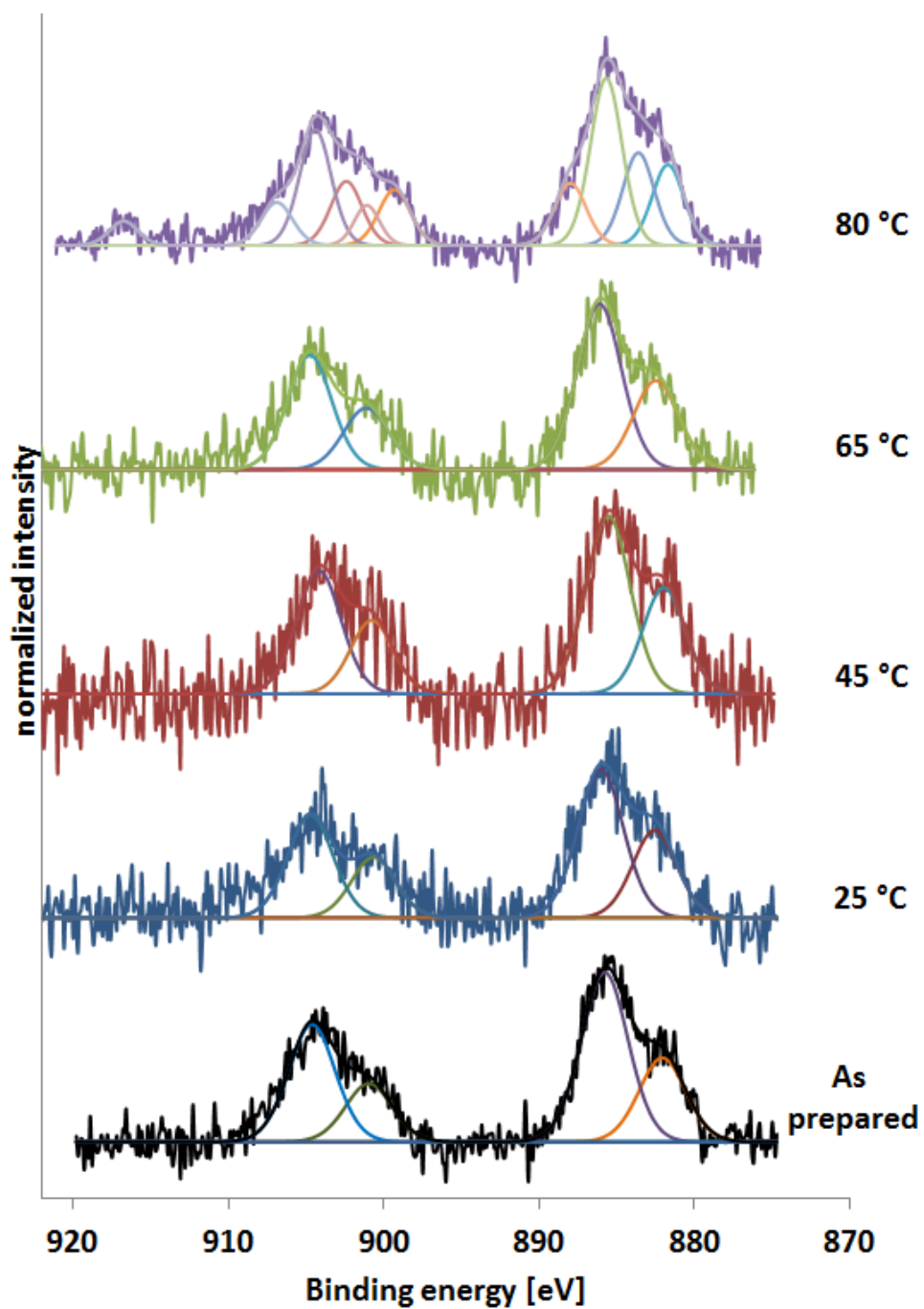


Figure 5.16 XPS Spectra for 40 K PVP capped ceria as prepared and after 28 days at $T=25, 45, 65$ and $80\text{ }^{\circ}\text{C}$ (from bottom to top).

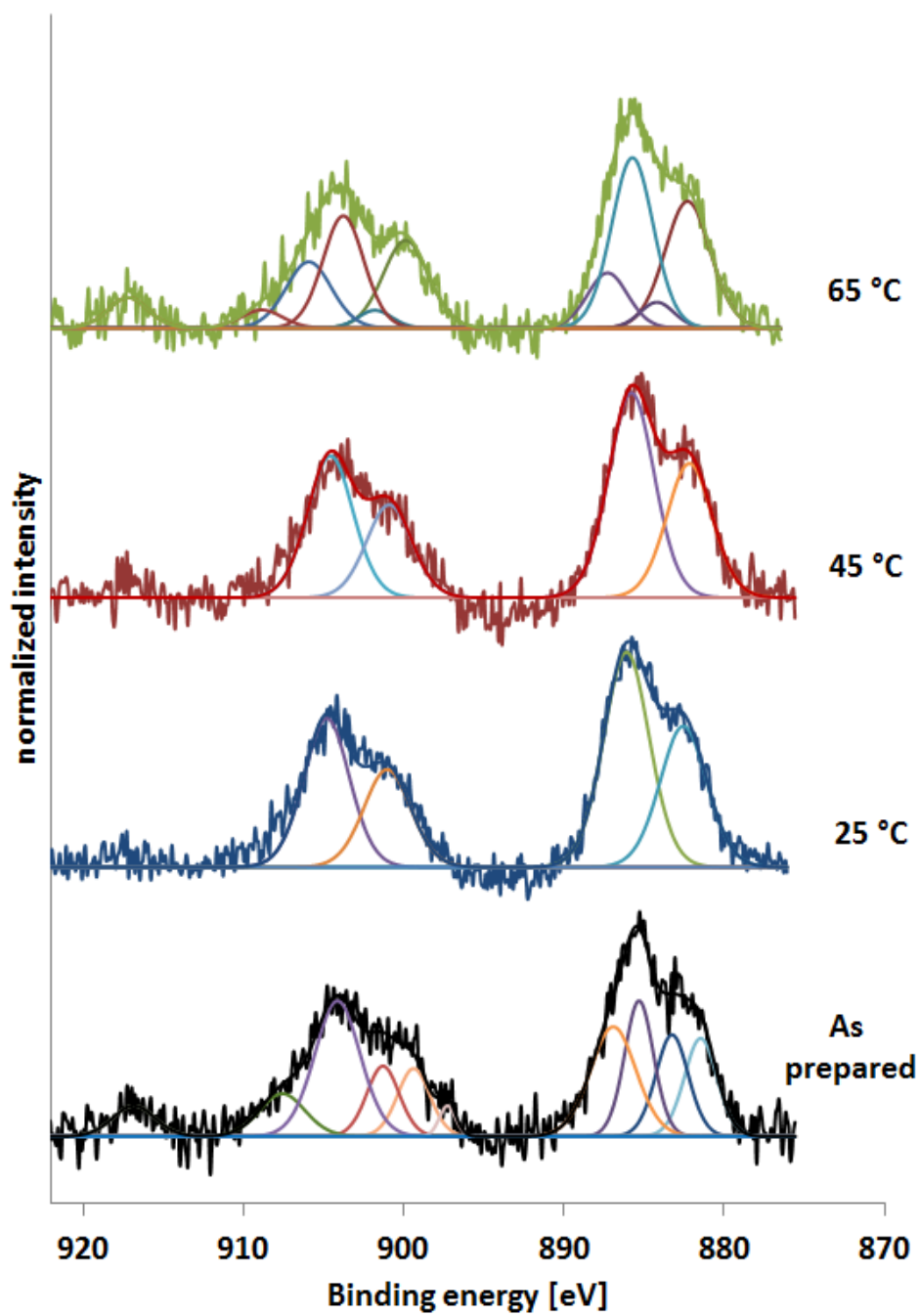


Figure 5.17 XPS Spectra for 360 K PVP capped ceria as prepared and after 28 days at T=25, 45, 65 and 80 °C (from bottom to top).

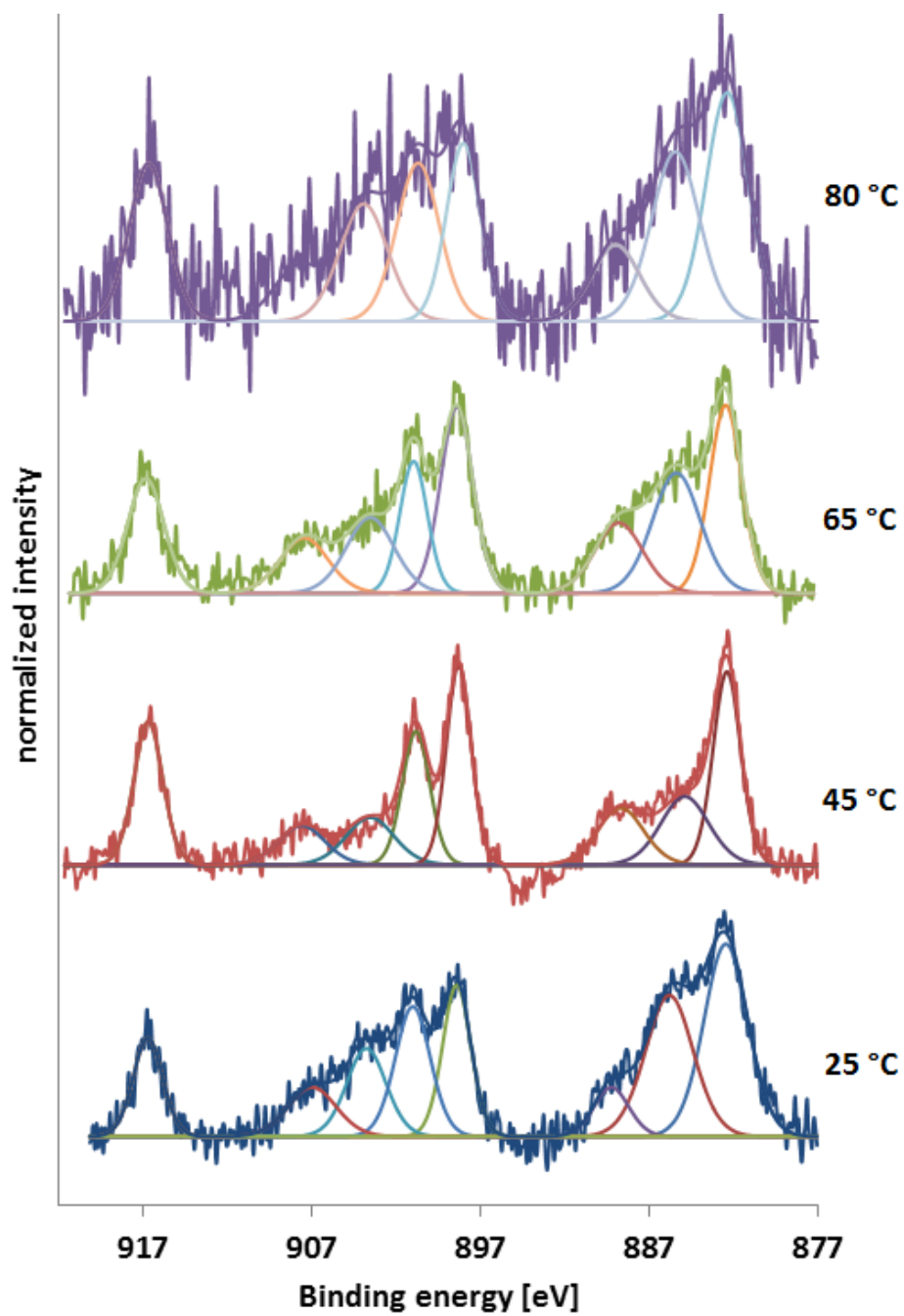


Figure 5.18 XPS Spectra for commercial ceria as prepared and after 28 days at $T=25, 45, 65$ and 80 °C (from bottom to top).

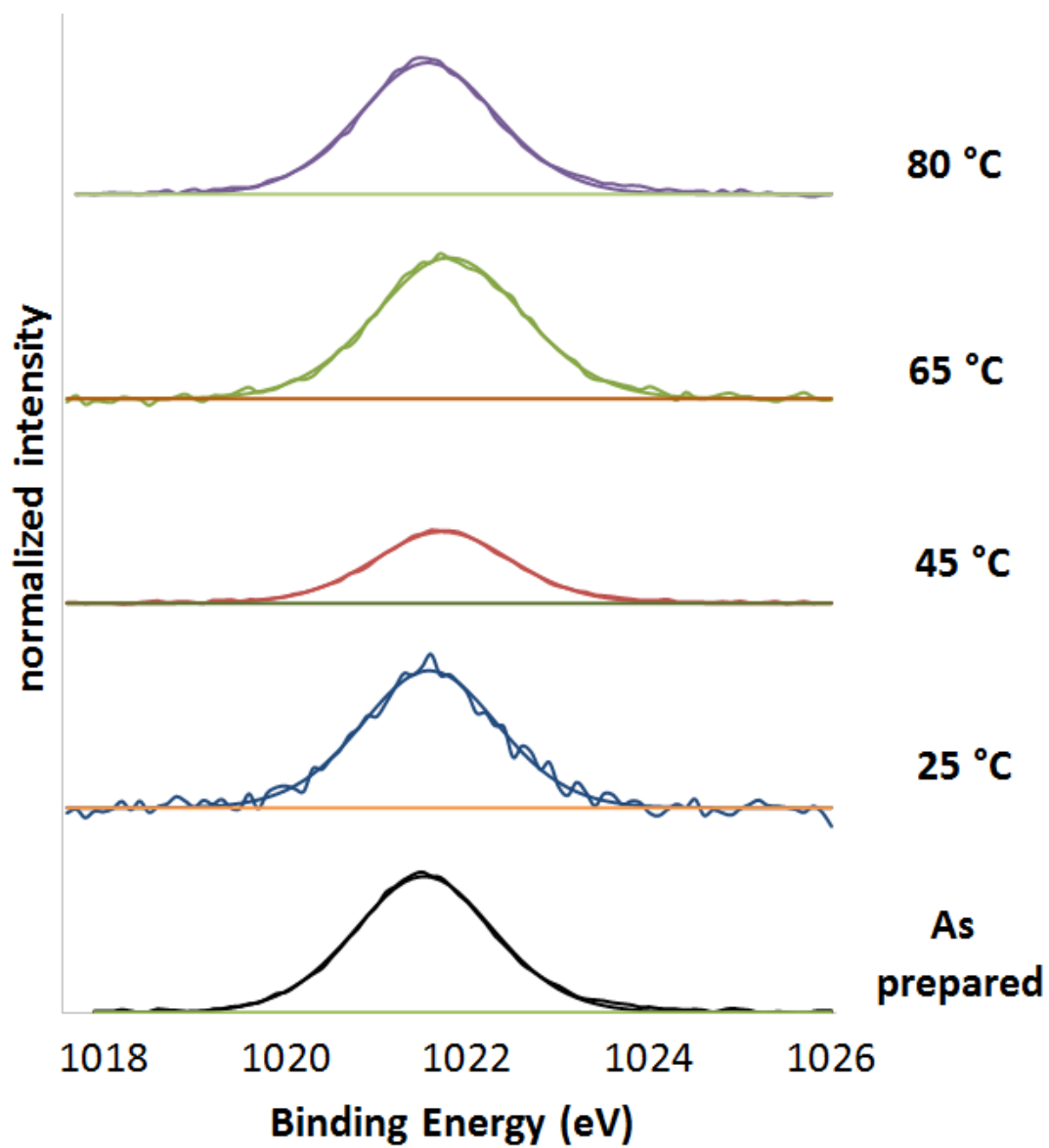


Figure 5.19 XPS Spectra for 10 K PVP capped zinc oxide as prepared and after 28 days at T=25, 45, 65 and 80 °C (from bottom to top).

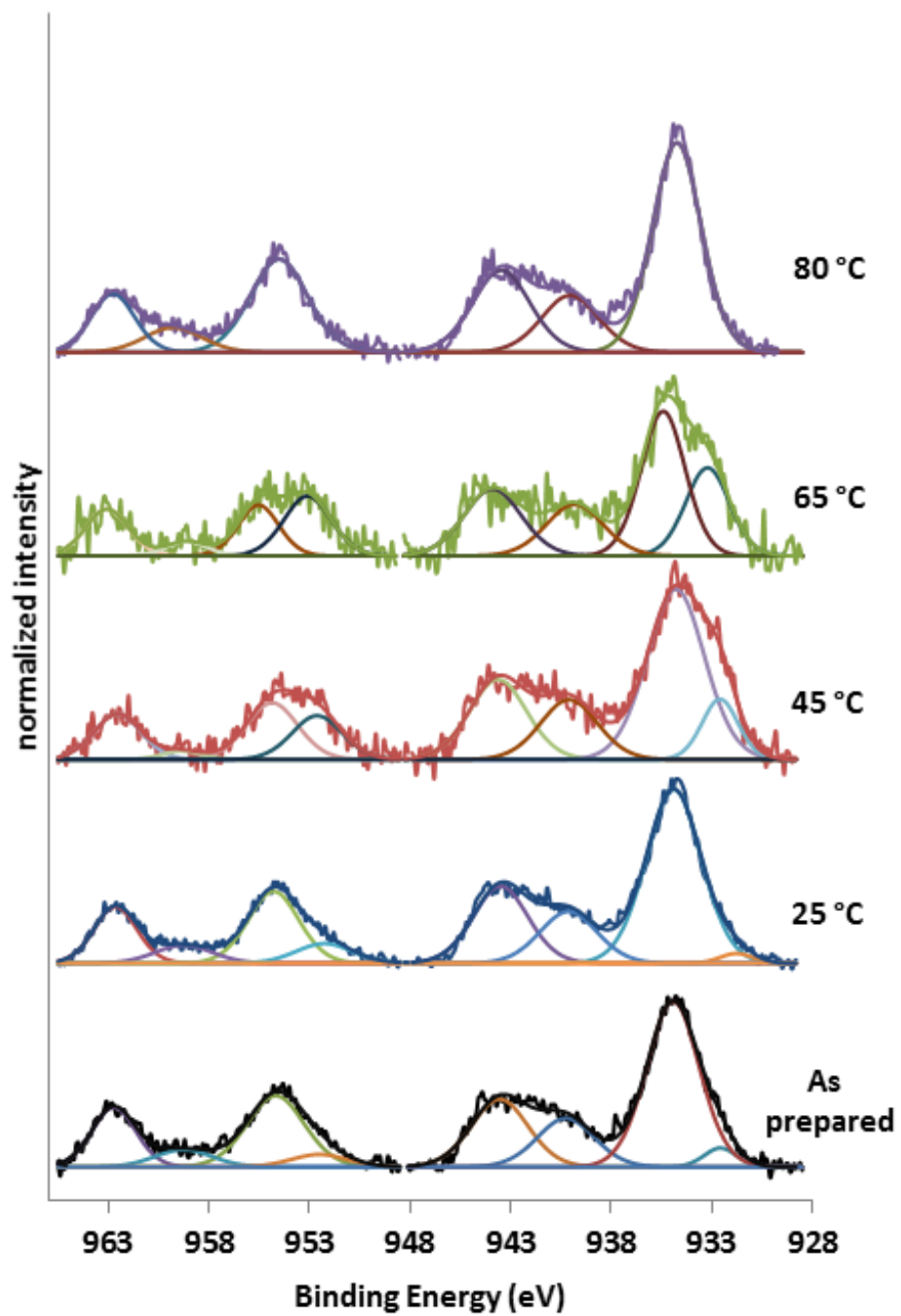


Figure 5.20 XPS Spectra for 10 K PVP capped copper oxide as prepared and after 28 days at $T=25, 45, 65$ and $80\text{ }^{\circ}\text{C}$ (from bottom to top).

5.7.2.2 UV-VIS

UV-VIS analysis revealed information about both the chemical and physical properties of the NMs as well as information about the changes effected by temperatures. The spectra for the PVP samples used for reference and all the NMs at different temperatures as a function of time can be seen in Figures 5.21-5.27.

In general it can be stated that the spectral signal recorded is much weaker at the end of the 28 days. This could imply that dissolution, aggregation or transformation of the NMs is taking place. The rate at which this occurs looks to be influenced by temperature. This decrease in intensity is also seen for the PVP samples (Figure 5.21). Therefore disintegration or disassociation of the capping from the particle could be occurring alongside other changes of the NMs. Furthermore, according to Beer-Lambert's Law (discussed in Section 3.3), absorbance can be directly related to concentration provided that the path length and extinction co-efficient are unchanged. However, in this case, changes in absorbance with time cannot be directly related to the change in concentration of the formed NMs (Hoppe et al., 2006) since, as discussed in Section 5.6.1, size changes are occurring and therefore there is a variation in the extinction co-efficient (Hoppe et al., 2006).

Furthermore, in all the graphs of the samples involving PVP, a peak just below 450 nm can be seen. This peak is not seen for the commercial ceria samples (Figure 5.26). The peak is due to PVP oxidation products as seen in the literature (Hoppe et al., 2006).

Figure 5.22 shows the spectra obtained for 10 K PVP capped ceria NMs. At 25 °C only a single peak attributed mainly to PVP is recorded. This peak decreases in signal intensity over time. At 45 °C, besides decreasing in intensity, this single peak becomes

two peaks; one at 250 nm and one at 300 nm. The former is attributed to PVP as well as cerium (III) as shown from the XPS results (Figure 5.15) whilst the latter can be ascribed to cerium (IV). This shows that the metal oxide NM core is present and that the UV-VIS and XPS spectra correlate. Furthermore, this could mean that the PVP capping is becoming less effective since the ceria UV peak becomes noticeable. Both peaks decrease in intensity over time, suggesting that changes to both the capping and the NM are occurring. At 65 °C the presence of these two peaks once again develops and decreases in intensity over time. At 80 °C only one broader peak is seen. Cerium (IV) could possibly be present until day 14, however day 21 and 28 show a slightly narrower peak that implies that only PVP and cerium (III) are present. This has been confirmed from the XPS spectra (Figure 5.15). The actual time point when the reduction occurred cannot be determined from this data.

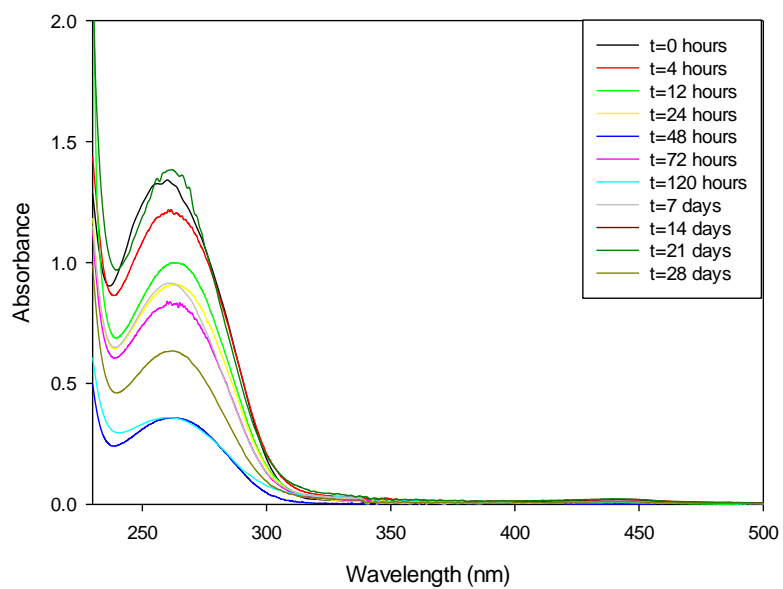
The 40 K PVP capped ceria NMs' UV-VIS spectra (Figure 5.23) look to be less influenced than those of the 10 K PVP capped ceria. One peak (at c. 250 nm) which decreases in intensity is noted in all spectra apart from that at 80 °C for the measurements taken from 14 days onwards where two peaks (at c. 250 nm and 300 nm) are observed. This indicates the presence of cerium in mixed oxidation states as confirmed by XPS (Figure 5.16).

The UV-VIS spectra for the 360 K PVP capped ceria samples can be seen in Figure 5.24. On day 21 at 65 °C the oxidation state of ceria is a mix as two peaks can be observed. At 80 °C no XPS spectrum was obtained. However, UV-VIS detects minimal amount of ceria and shows a clear reduction in the concentration yet indicates that by day 28 a mix of cerium (III) and cerium (IV) is present.

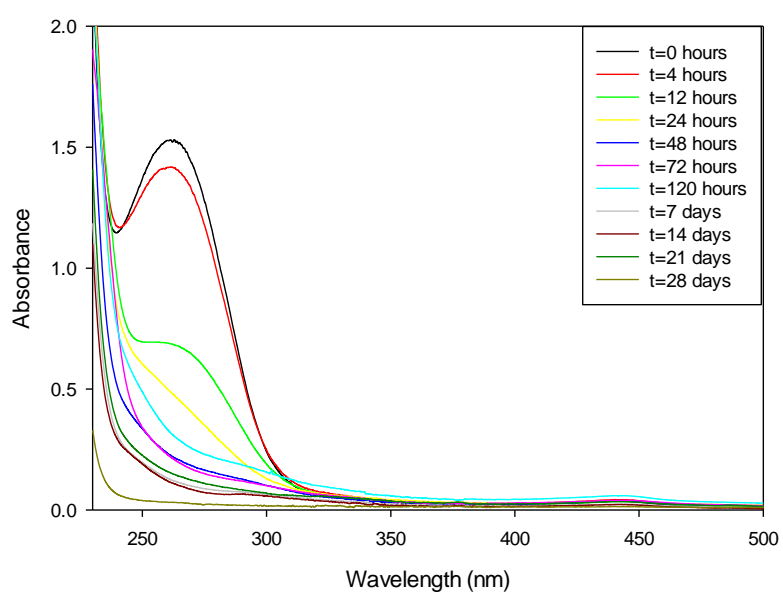
The commercial ceria samples' spectra (Figure 5.25) show a single peak with a maximum intensity at 300 nm. This corresponds to cerium (IV) as also determined from the XPS results (Figure 5.18). These UV spectra show no change in peak position indicating that this ceria sample's initial and final oxidation state is unchanged. The spectra look to imply that no reduction or oxidation take place over the 28 days yet this can only be stated confidently for the time points and temperatures at which the measurements were taken. The only variation noted is a decrease in intensity over time and the rate of which looks to be influenced by temperature.

In Figure 5.26 the UV-VIS spectra for 10 K PVP capped zinc oxide NMs are presented. At 25, 65 and 80 °C one peak that decreases in intensity as a function of time is seen between 220 and 300 nm. At 45 °C this single peak splits into two peaks after 48 hours of temperature exposure. The two peaks are found at 250 nm and just below 300 nm which is lower than that seen in the PVP capped ceria spectra. These are representative of PVP and zinc oxide respectively. Since this behaviour is similar to that seen for the PVP capped ceria NMs it suggests that the PVP capping is in fact becoming less effective.

The final data of UV spectra presented in Figure 5.27 belong to the PVP capped copper oxide NPs and show the typical decrease in signal intensity over time. At 45 °C after 48 hours a slight peak at c. 280 nm, which is characteristic of CuO, can be noted. At 45 and 65 °C the presence of the Cu₂O characteristic peak at 440 nm can also be detected. This is not seen at room temperature.

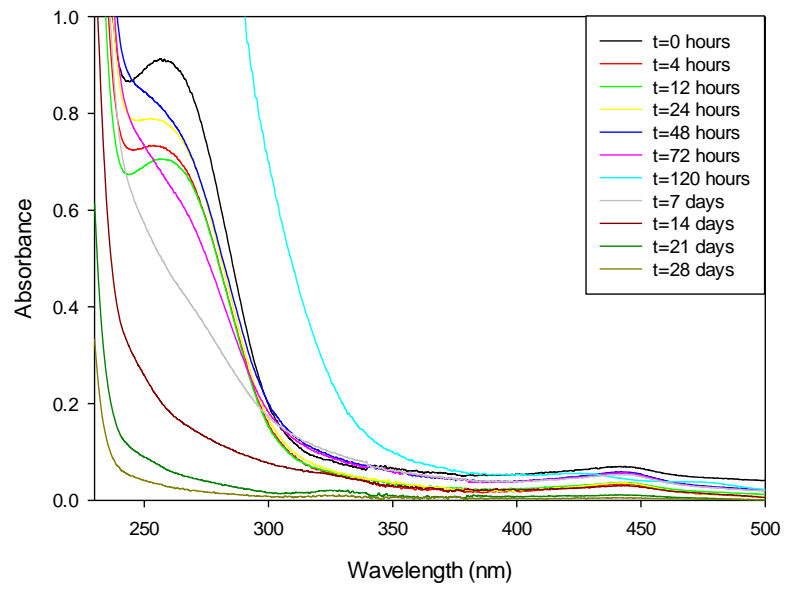


a)

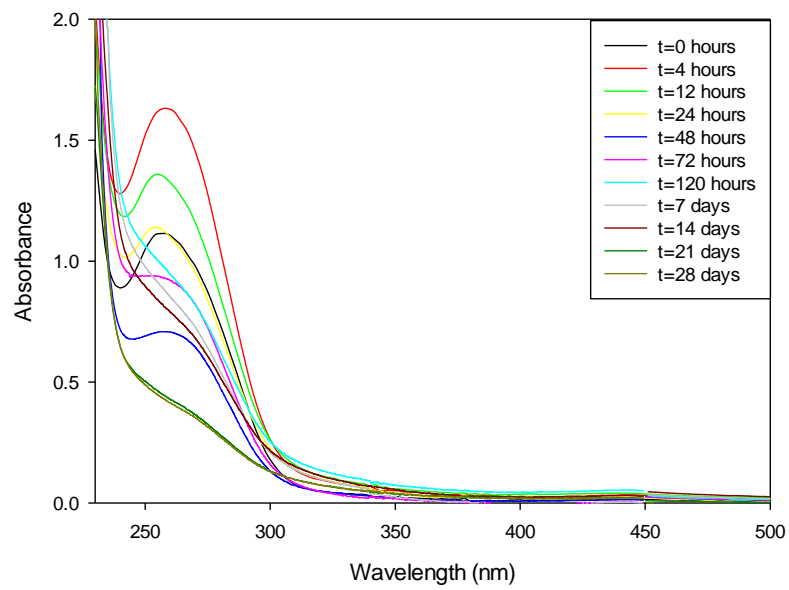


b)

Figure 5.21 a) and b) UV-VIS spectra for 10 K PVP samples exposed to a) 25 and b) 45 °C as a function of time.

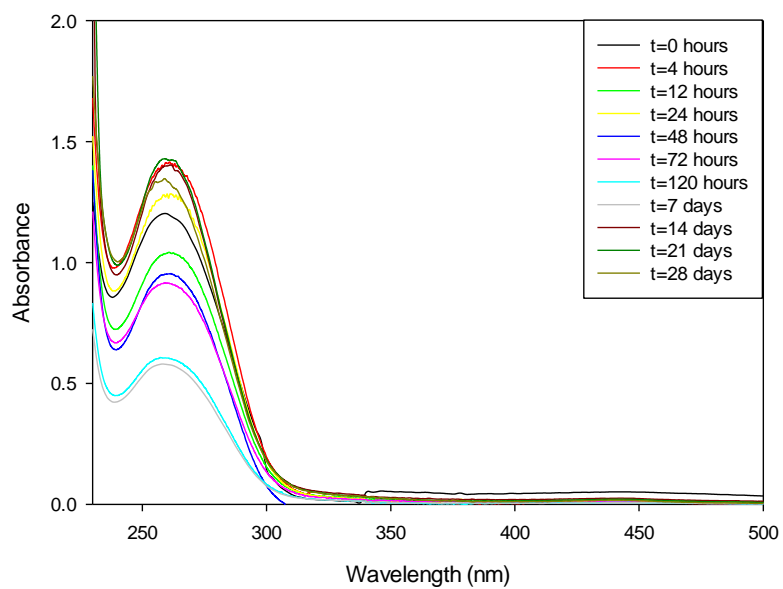


c)

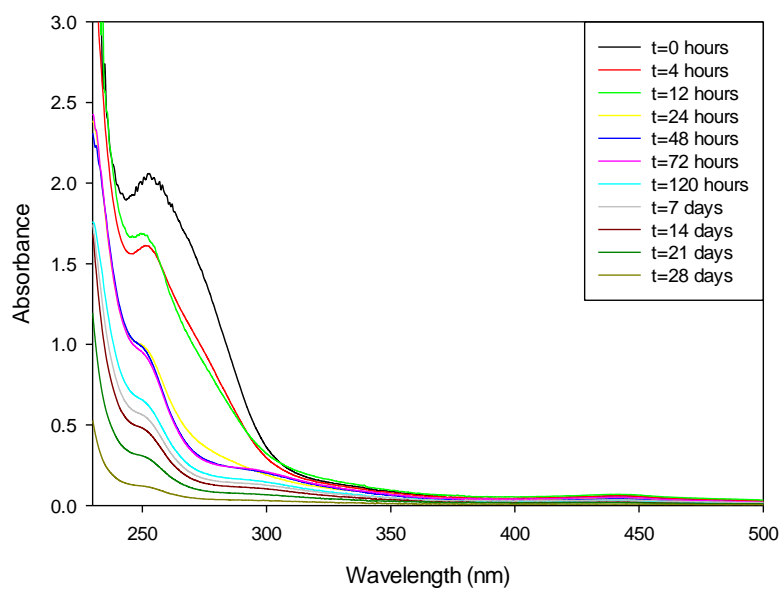


d)

Figure 5.21 c) and d) UV-VIS spectra for 10 K PVP samples exposed to c) 65 and d) 80 °C as a function of time.

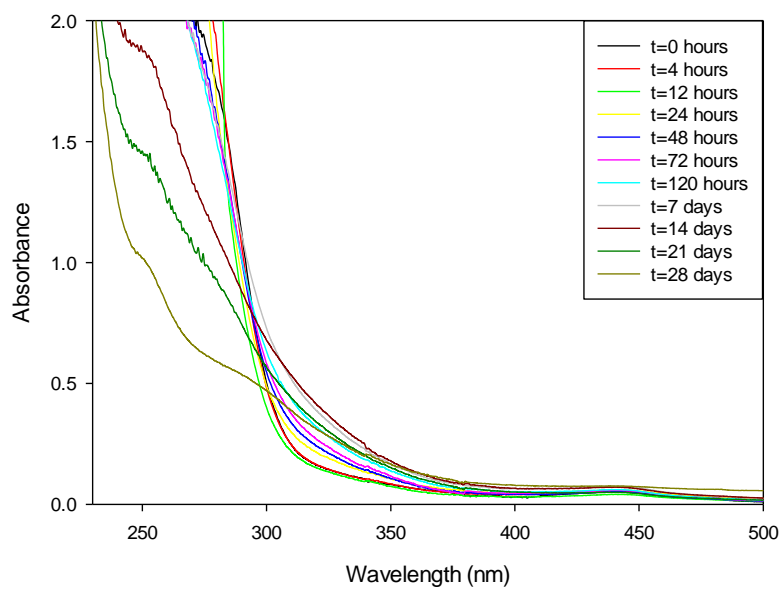


a)

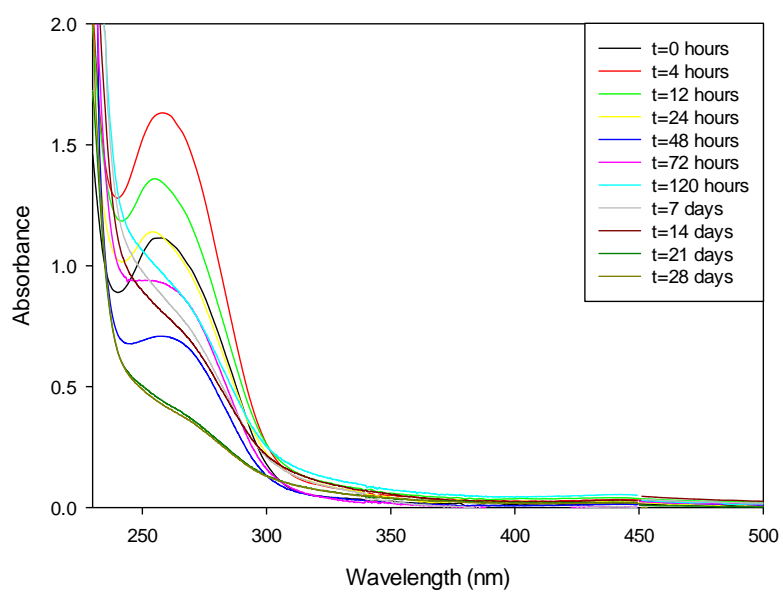


b)

Figure 5.22 a) and b) UV-VIS spectra for 10 K PVP capped ceria exposed to a) 25 and b) 45 °C as a function of time.

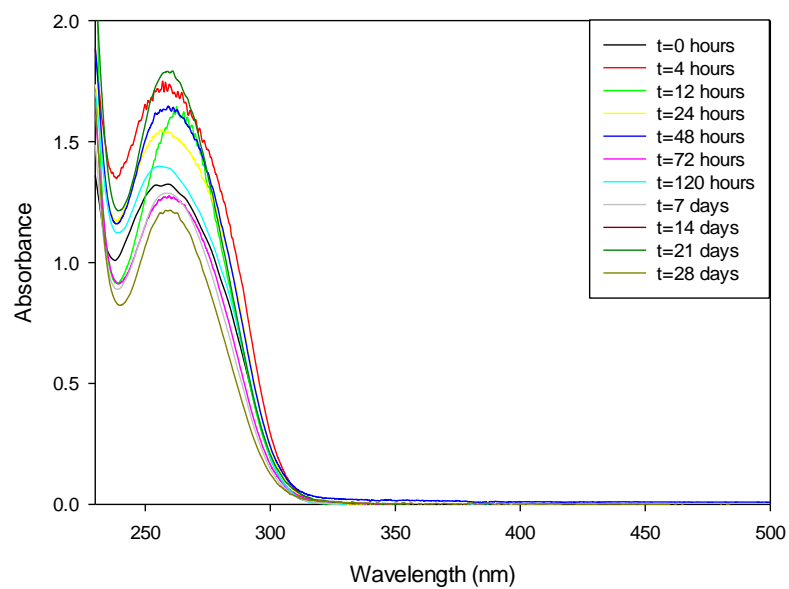


c)

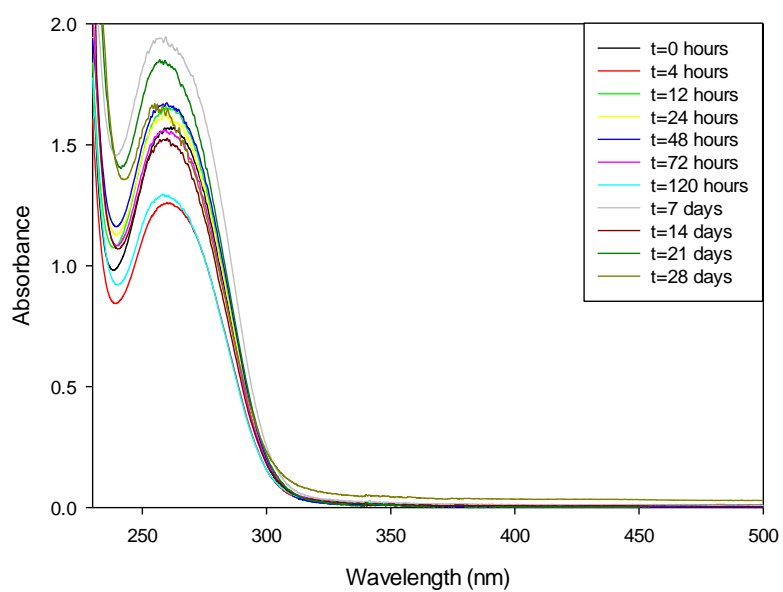


d)

Figure 5.22 c) and d) UV-VIS spectra for 10 K PVP capped ceria exposed to c) 65 and d) 80 °C as a function of time.

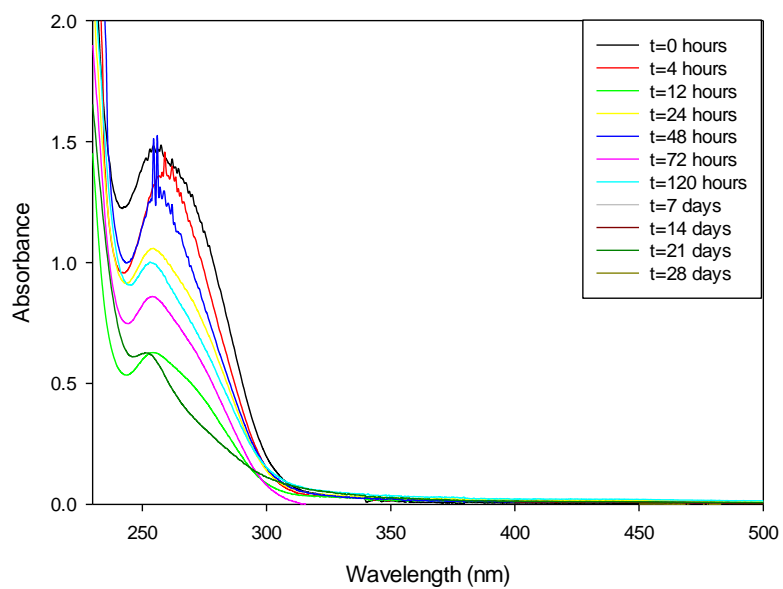


a)

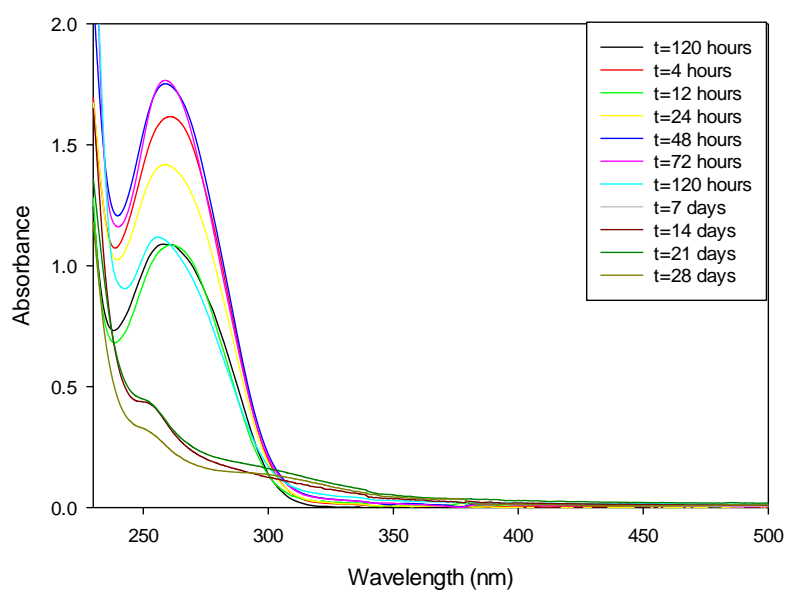


b)

Figure 5.23 a) and b) UV-VIS spectra for 40 K PVP capped ceria exposed to a) 25 and b) 45 °C as a function of time.

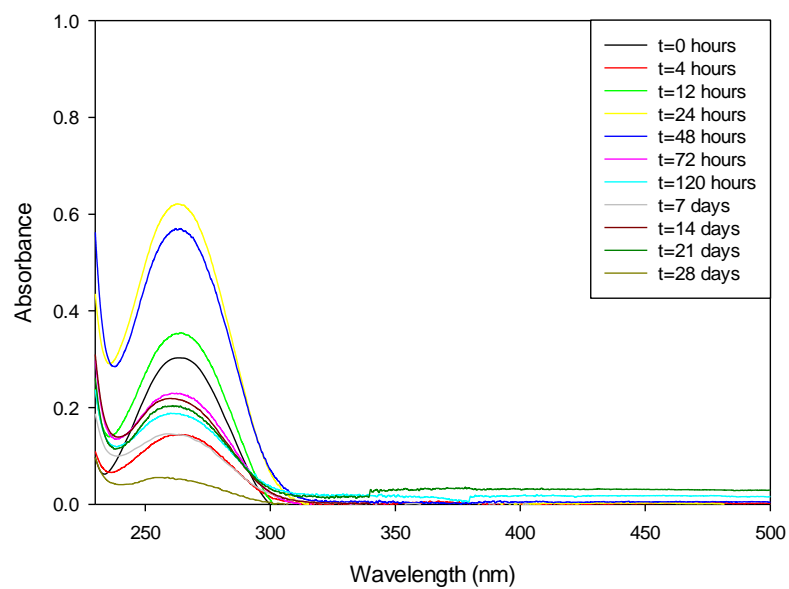


c)

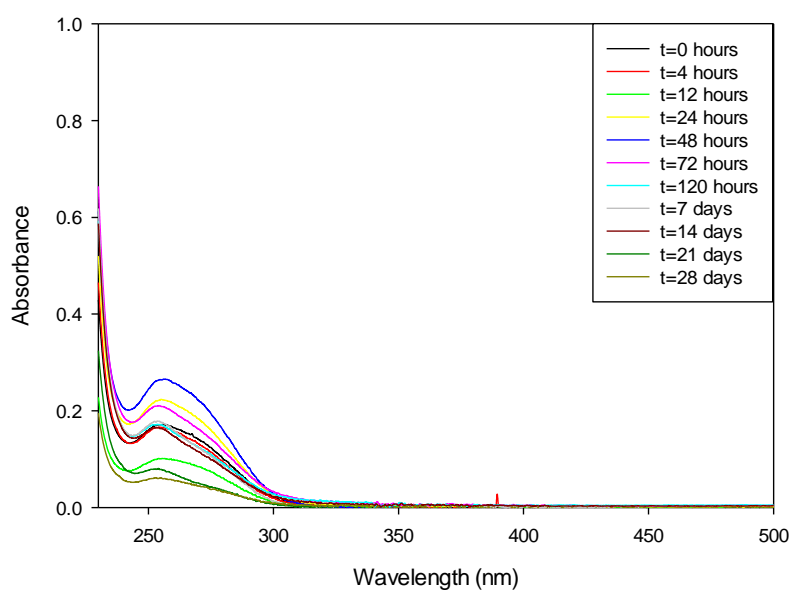


d)

Figure 5.23 UV-VIS spectra for 40 K PVP capped ceria exposed to a) 25, b) 45, c) 65 and d) 80 °C as a function of time.

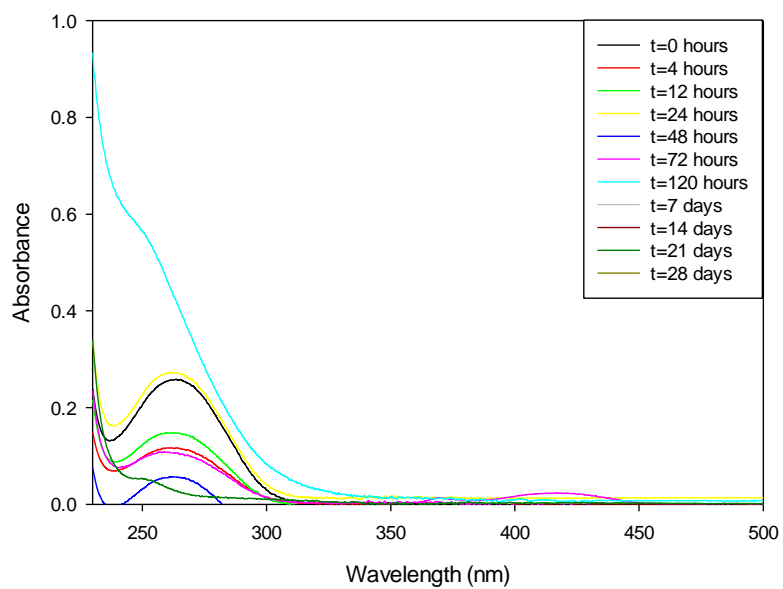


a)

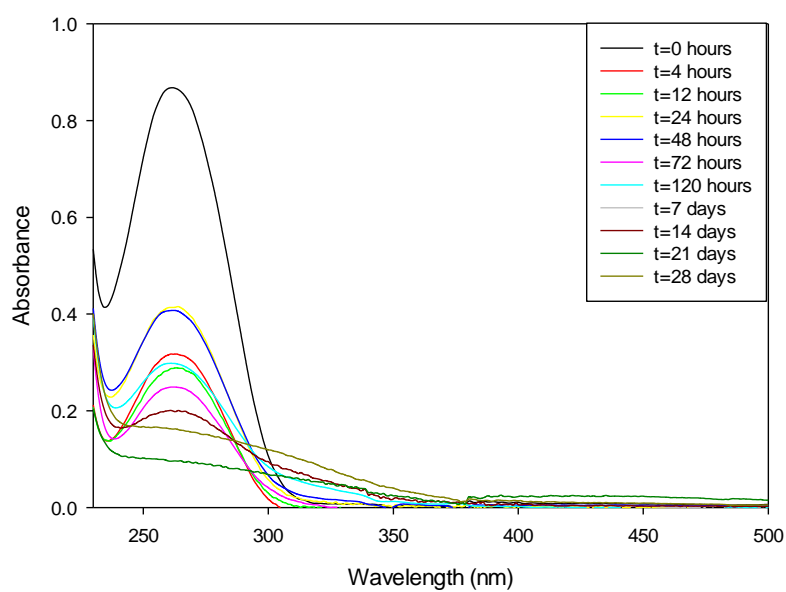


b)

Figure 5.24 a) and b) UV-VIS spectra for 360 K PVP capped ceria exposed to a) 25 and b) 45 °C as a function of time.

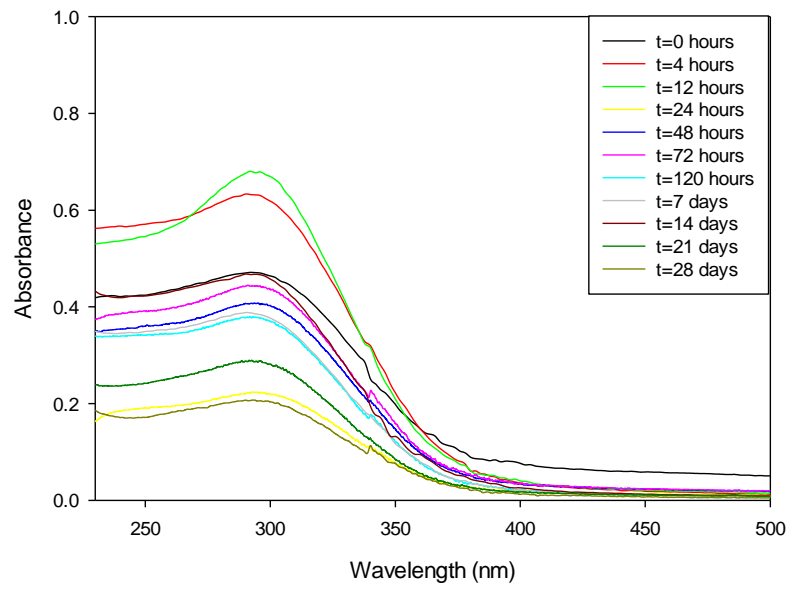


c)

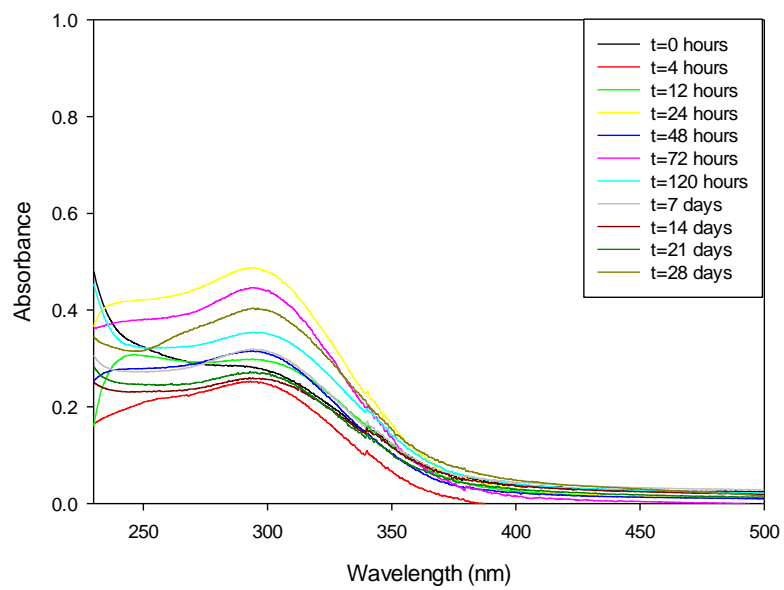


d)

Figure 5.24 c) and d) UV-VIS spectra for 360 K PVP capped ceria exposed to c) 65 and d) 80 °C as a function of time.

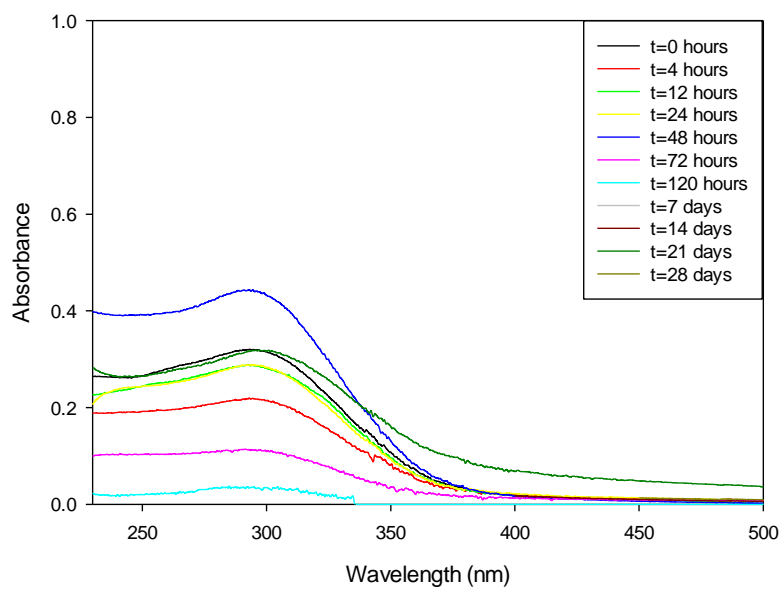


a)

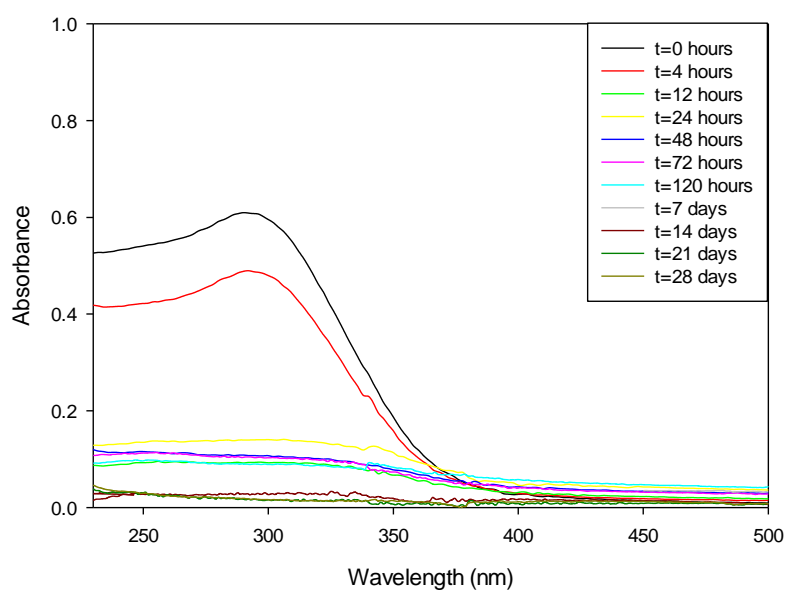


b)

Figure 5.25 a) and b) UV-VIS spectra for Commercial ceria exposed to a) 25 and b) 45 °C as a function of time.

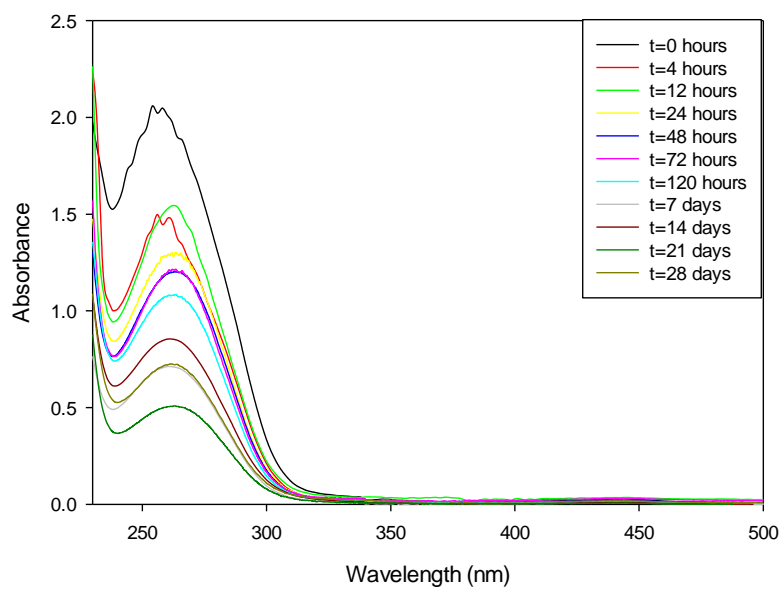


c)

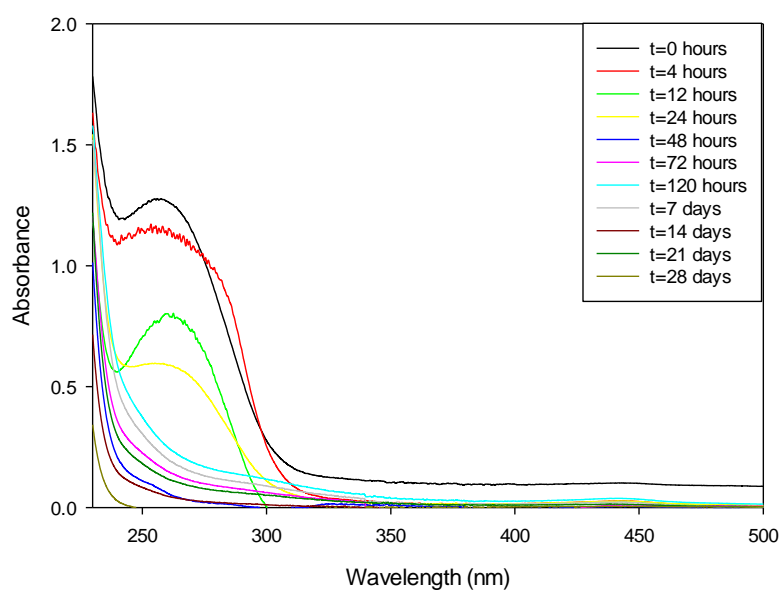


d)

Figure 5.25 c) and d) UV-VIS spectra for Commercial ceria exposed to c) 65 and d) 80 °C as a function of time.

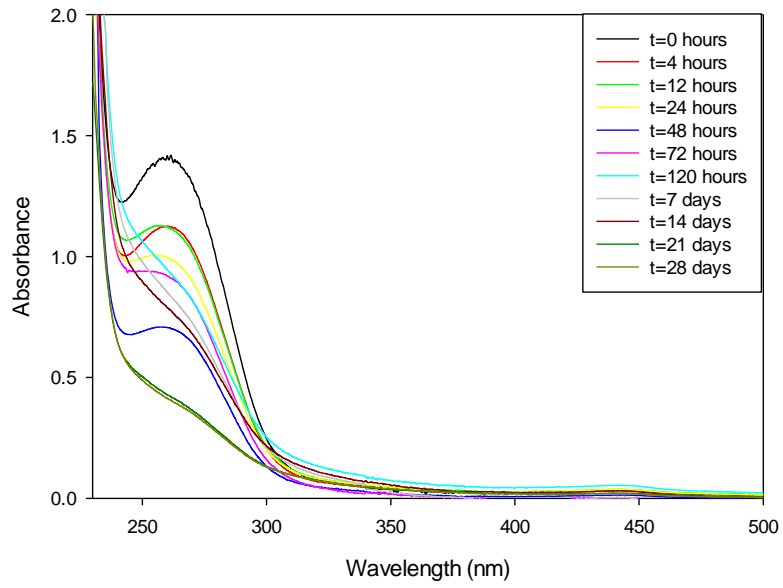


a)

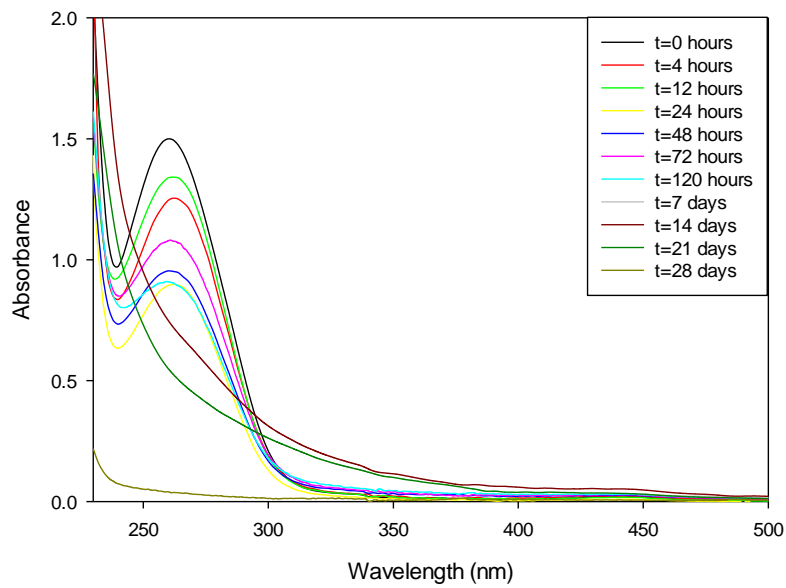


b)

Figure 5.26 a) and b) UV-VIS spectra for 10 K PVP capped zinc oxide exposed to a) 25 and b) 45 °C as a function of time.

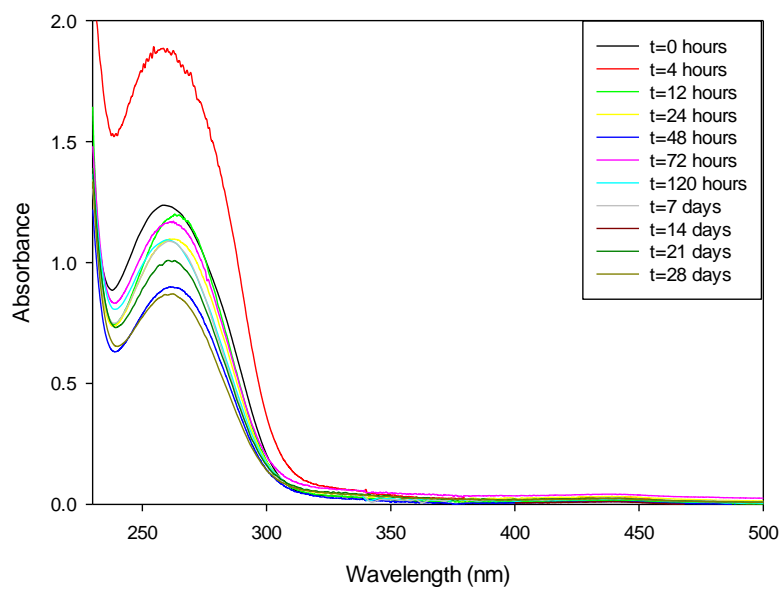


c)

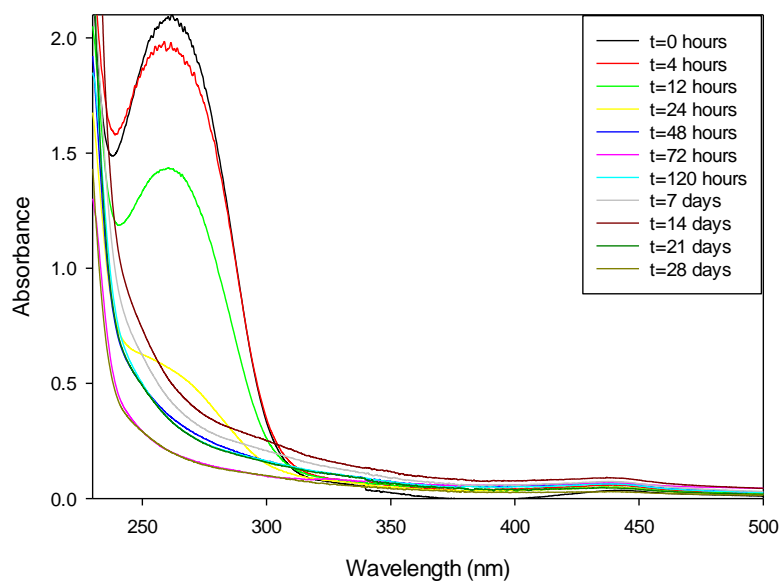


d)

Figure 5.26 c) and d) UV-VIS spectra for 10 K PVP capped zinc oxide exposed to c) 65 and d) 80 °C as a function of time.

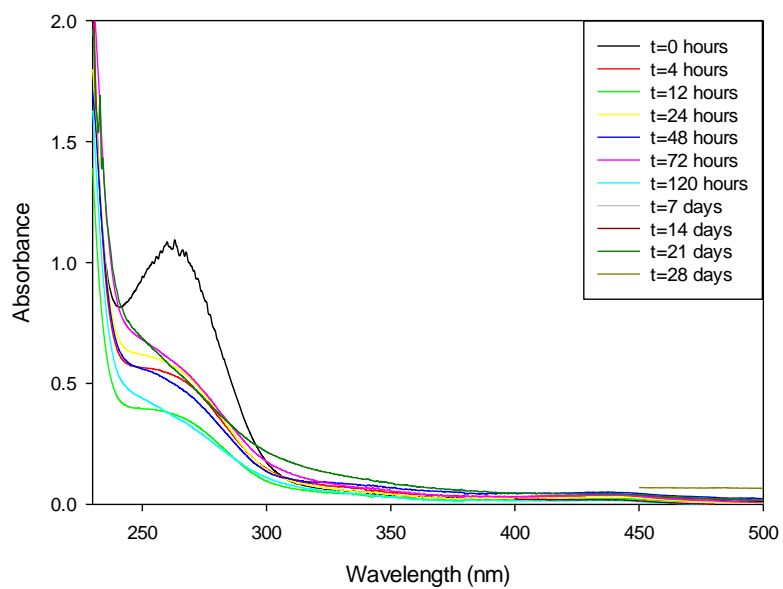


a)

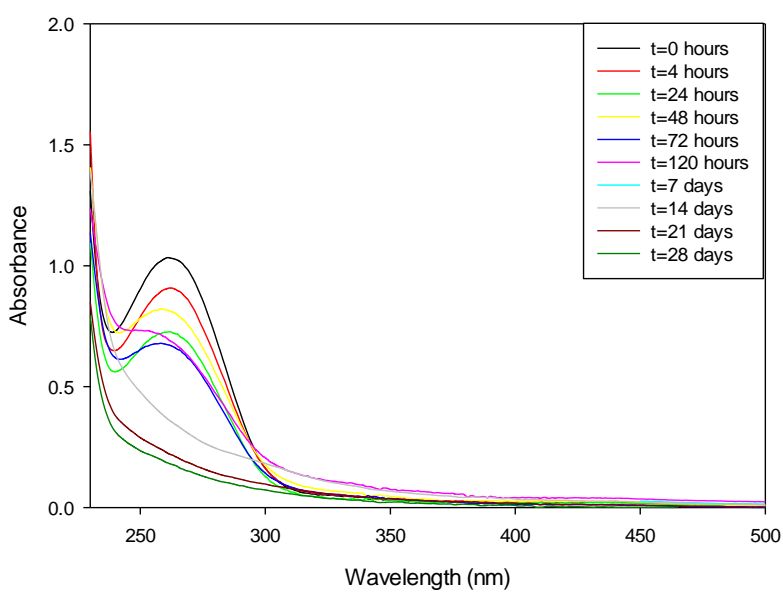


b)

Figure 5.27 a) and b) UV-VIS spectra for 10 K PVP capped copper oxide exposed to a) 25 and b) 45 °C as a function of time



c)



d)

Figure 5.27 c) and d) UV-VIS spectra for 10 K PVP capped copper oxide exposed to c) 65 and d) 80 °C as a function of time

5.8 Conclusions

Studying the behaviour of NMs in different environments reveals important information that can influence a NM's toxicity. This work allowed for the study of thermal transformations of NMs, as a proxy for ageing, revealing significant characteristic physical and chemical property behaviours, including size and metal core valency changes, for PVP capped metal oxide NM and a commercial ceria NM.

Size and appearance analysis were carried out by DLS and TEM. A general trend was noted for all samples. This involved a decrease in the primary size of the NMs and the development of a second peak at a larger size indicating aggregation, which was clearly seen by TEM, for all samples. As the temperature increased the rate of change and aggregation in size increased. Differences in these changes and rate of changes were revealed amongst the PVP sample, capped and uncapped NM samples. In the case of the ceria samples as the PVP chain length increases the changes in size at different temperatures look to decrease. The rate of size change varies for the different nanoparticle cores, ceria > copper oxide > zinc oxide, revealing that the core composition also plays a role in influencing the rate of aggregation. Furthermore the presence of PVP is not restricting aggregation. It is however minimising it and influencing the behaviour as the commercial ceria NMs are significantly affected particularly at 80 °C. This indicates that a threshold temperature has been exceeded and the NMs are significantly physically transformed.

Additionally, the Pearson product-moment correlation coefficient (PCC) was calculated for the temperature, size, primary peak intensity and time of the different samples. This investigation revealed that, although some similarities were noticed, there

were no trends noticeable for the whole sample range. This highlights the complexity of transformations and how environment specific the behaviour of NMs can be.

Based on the zeta potential measurements as a function of time and temperature the surface charge of all the capped NMs show very little change. The values are all found around 0 due to PVP steric stabilisation. The PVP samples show changes (decrease of c. 12 mV to increase of c. 2 mV) over time. These are most noticeable at 80 °C. Of all the NMs the zeta potential of the commercial ceria NMs was most significantly influenced by temperature due to the lack of capping agent.

Chemical changes were monitored by XPS and UV-VIS. The results obtained from these techniques correlate for all samples analysed. The XPS spectra of PVP capped zinc oxide indicate no significant changes in chemical composition. The commercial ceria show some slight changes in peak intensity, which could be attributed to oxidation state changes. The PVP capped ceria NMs and PVP capped copper oxide samples both display variations in the metal oxidation state, an important feature affecting toxicity. This demonstrates that despite the capping stabilising the NMs, they can remain reactive and thus be affected by external factors. In general the changes noted from the XPS spectra amongst the PVP capped NMs decreased from ceria to copper oxide to zinc oxide as also seen for the changes in size.

UV-VIS indicates the probability of dissolution, aggregation and/or transformation of the NMs and PVP due to a decrease in peak intensity. The rate at which this occurs looks to be influenced by temperature. The PVP capping looks to be becoming less effective as a function of time and temperature and, as for the PVP capped metal oxide NMs, multiple peaks become noticeable. These peaks are characteristic of the respective

metal oxide cores and the PVP ceria. Despite this the PVP remains present in dispersion and the zeta potential values are not affected.

In conclusion the NM behaviour looks to differ based on both internal factors, including NM properties, and external factors which in this case is temperature. Both the physical and chemical properties play a determining role. In this study these features included core composition, capping, capping and core interaction and NM size. Moreover, in spite of the PVP capping stabilising the NMs, this does not ensure that they are not affected by external factors.

These findings reveal two possible aspects in NMs' life cycle. These are their effects over a short time period in different temperature environments and their estimate or "predict" potential long-term behaviour. The latter is revealed through the studies at elevated temperature, speeding up the processes taking place and therefore allowing temperature to be used as a proxy of time. Although as yet we cannot directly link the accelerated ageing testing to real-life studies due to the lack of real prolonged environmental data, this study shows that environmental changes are likely to occur and therefore it is probable that, in fact, it is not the pristine NMs that are present in the environment but one that we may have transformed. This highlights the importance of carrying out toxicity and behavioural studies on the aged nanomaterials as well as the pristine ones in order to fully understand their behaviour in the environment. Furthermore, this emphasises the complex features influencing the life-cycle of nanomaterials.

Chapter 6: Phosphate induced Transformations of Ceria based Nanomaterials

6.1 Introduction

During their life cycle many manufactured nanomaterials (MNMs) undergo significant transformations. Assessing the environmental and human health implications of MNMs requires an understanding of the potential exposure routes (Figure 6.1) that can induce biological transformations, interactions with macromolecules, physical and chemical transformation and in turn influence toxicology behaviours and effects (Lowry et al., 2012). Details of various transformations have been discussed in Chapter 2. The transformations taking place vary depending on the NM and the environmental exposure scenario. Temperature can also induce transformations, as seen in Chapter 5, and may serve as a proxy for time. An important aspect of life cycle analysis is the understanding of how transformations are effected over time. This is therefore the reason why ageing investigations are so important.

Possible Life-Cycle Transformations
(During Production, Storage, Use, Disposal and Environmental release)

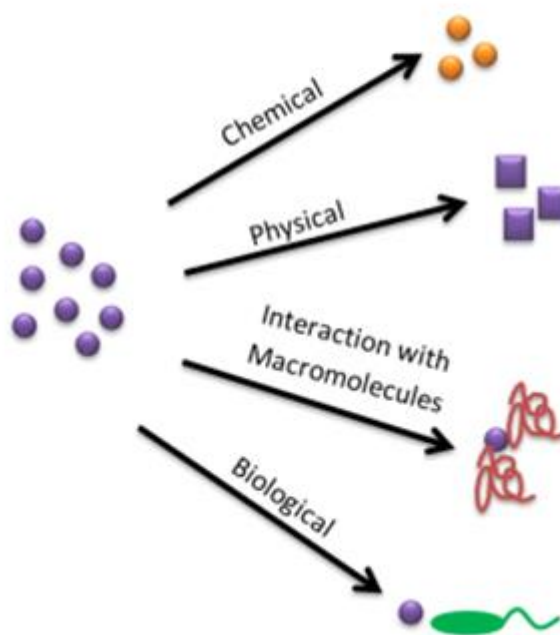
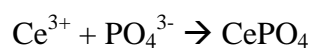


Figure 6.1 Possible Nanoparticle Transformations.

This Chapter describes a phosphate ageing scenario. Phosphate has a high affinity for cerium (Singh et al., 2011). The equation for this reaction can be seen in Equation 6.1.



Equation 6.1

It is well known that CeO₂ NPs are more soluble under acidic conditions and Ce (III) ions have high binding affinity to phosphate groups, which can change their ultimate fate and toxicity (Li et al., 2014, Zhang et al., 2012).

Furthermore there is the high probability of this reaction occurring in the environment because of the natural presence of phosphorus and its compounds (EPA, 2012). Phosphorus is an essential nutrient for the plants and animals that make up the aquatic food web. Phosphorus cycles through the environment changing form as it does so (EPA, 2012). Phosphates enter waterways from human and animal waste, phosphorus rich bedrock, laundry, cleaning, industrial effluents, and fertilizer runoff (Oram, 2014).

In this Chapter, the range of ceria NP samples selected for the phosphate ageing scenario are discussed, including both the laboratory prepared 10 K PVP capped ceria, the commercial ceria used in the previous chapter and a number of zirconium doped ceria MNMs, that will be introduced more fully in the next section. The synthesis and characterisation details for the 10 K PVP capped ceria NMs can be found in Chapter 4. As for the commercially available ceria, this sample along with the 10 K PVP capped ceria sample has already been used for the thermal study described in Chapter 5. This Chapter explains the ageing process, the characterisation analysis and the results. The characterisation techniques used have been discussed in Chapter 3. The results of this chapter are divided into three subsections to discuss: (a) a pilot study involving the exposure of 10 K PVP capped ceria samples to a laboratory prepared phosphate solution, (b) the exposure of the commercial ceria and zirconium doped ceria series to a laboratory prepared phosphate solution, and (c) the exposure of ceria NMs to a naturally occurring phospholipid.

Literature has shown that rare earth oxides (REOs) transform biologically on exposure to phosphate compounds at a low pH (Li et al., 2014). Zhang et al. (2012) investigated the biotransformation of ceria in cucumber plants and observed that organic acids (e.g., citric acids) promoted CeO_2 dissolution and reducing substances (e.g., ascorbic

acids) played a key role in the transformation process, generating Ce (III) ions which then reacted with the phosphate present in the media. CeO₂ NPs were transformed to CePO₄ and Ce-carboxylates despite the very low solubility of CeO₂. CeO₂ NP uptake was also observed in cilantro, but the CeO₂ NPs were not transformed (Morales et al., 2013).

Li et al. (2014) discuss their investigation of the interactions of cellular phosphates with rare earth oxides (REO). Li et al. (2014) observed a pH dependent biological transformation process that results in phosphate deposition on the particle surface and stripping of phosphate groups from the lysosomal membrane lipids. In their study however, unlike other REO nanoparticles studied, CeO₂ remained substantially non-transformed, the reason being that CeO₂ exhibits a higher K_{sp} (10^{-53}) in water than other REOs (K_{sp} , 10^{-21}), and is highly insoluble at both pH 7 and 4.5 (Abreu and Morais, 2010).

Evidence in the literature suggests that rare earth oxides (REOs) transform on exposure to phosphate compounds at a low pH however this transformation of ceria has not always been observed or studied in depth (Li et al., 2014, Zhang et al., 2012, Rui et al., 2015). It is well known that CeO₂ NPs are more soluble under acidic conditions and Ce (III) ions have high binding affinity to phosphate groups, which can change their ultimate fate and toxicity (Li et al., 2014, Zhang et al., 2012). This work aims to study the physical and chemical changes occurring to the particles on exposure to a laboratory prepared phosphate solution and a naturally occurring phospholipid.

Phosphate ageing using a laboratory prepared phosphate solution was carried out by modifying an existing method that studies the transformation of ceria nanoparticles in plant systems in order to replicate the scenario (Zhang et al., 2012). The original 1 mM solution concentration used by Zhang et al. (2012) was used. Additionally, another

solution concentration having a fivefold concentration to that in the original publication was used so as to induce a faster and more complete transformation of the ceria NMs.

Phosphate ageing using a naturally occurring phospholipid was carried out using a solution of L- α -phosphatidylcholine. This was done with the aim of replicating a scenario within the human body. L- α -phosphatidylcholine is a phospholipid component of bile. Phospholipids contain phosphate components (Figure 6.2) that could result in ceria transformations. This interaction considers particles interacting with particles rather than particles reacting with molecule as in the previous scenarios.

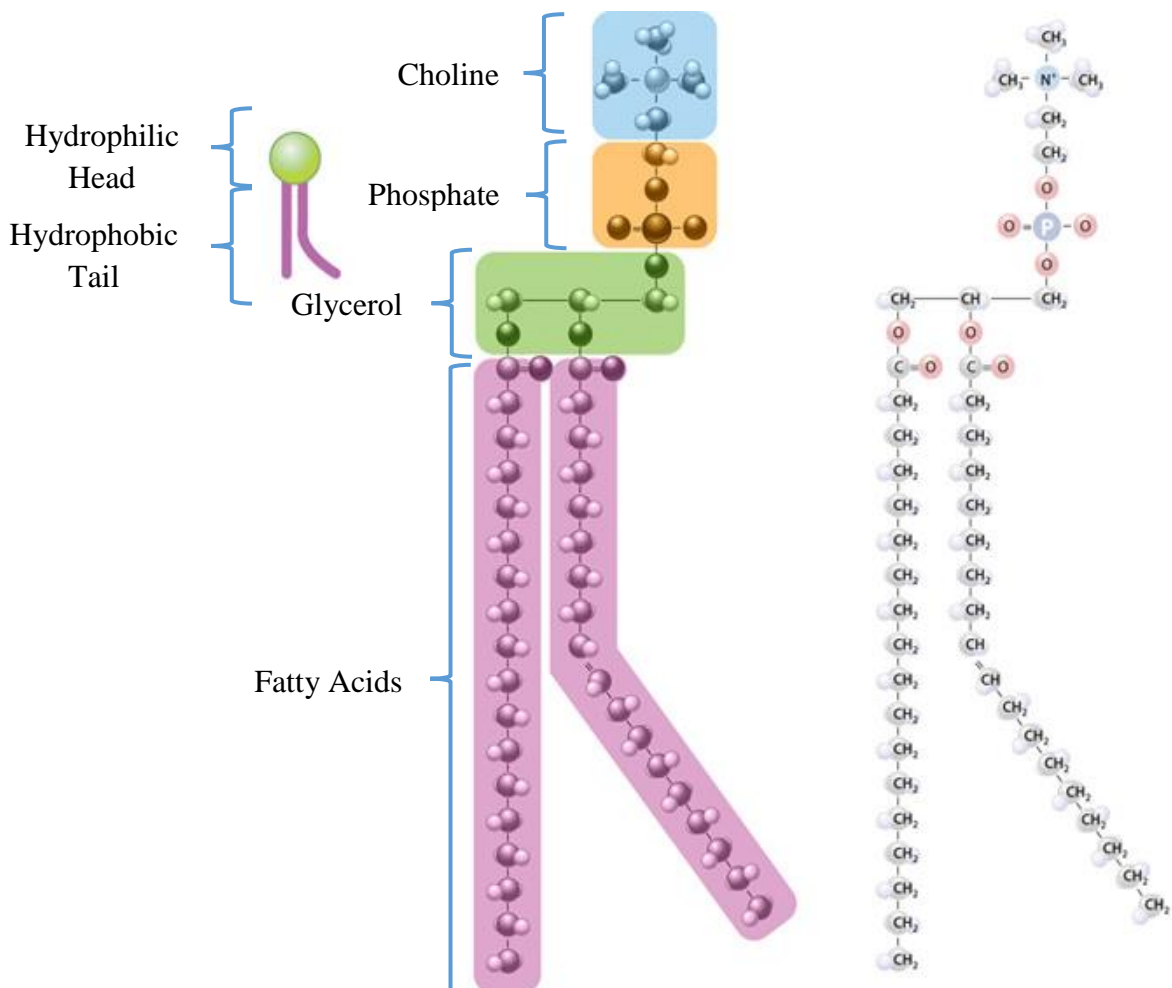


Figure 6.2 Phospholipid structure (Miko, 2014).

Bile is very complex and varies according to the nutritional state of the individual. The main components include bile acids (also called bile salts), phospholipids (mainly phosphatidylcholine), cholesterol, bilirubin (mostly in its conjugated form), inorganic salts (potassium, sodium and bicarbonate), together with very small amounts of copper and other metals (Figure 6.3) (Farina, 2009). The pH of bile is slightly acidic with a pH of about 5 to 6 (The Editors of Encyclopædia Britannica Online, 2015). This pH creates the ideal environment for transformation in the presence of phosphate to take place. Bile's function is to digest fats in the duodenum, the first part of the small intestine (Farina, 2009).

Bile is a greenish yellow secretion produced in the liver and passed to the gallbladder for concentration to about 5 times (and sometimes as high as 18 times) the original secretion, storage or transport into the duodenum (The Editors of Encyclopædia Britannica Online, 2015). About 800 to 1,000 ml of bile (before concentration) are produced daily by the liver (The Editors of Encyclopædia Britannica Online, 2015). These quantities and those from Figure 6.3 were used to determine the quantities used for the phosphate ageing.

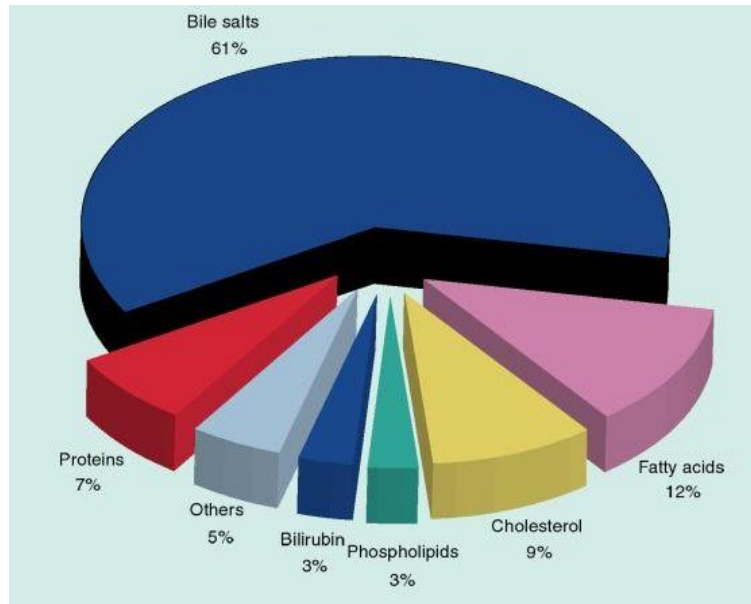


Figure 6.3 Chemical composition of bile. Percentages represent ratio to total solute concentration (mg/ml)
(Farina, 2009)

Furthermore, the study was carried out at 37 °C to represent the temperature of the human body. The process taken for food to travel through the digestive tract from when it comes in contact with bile in the small intestine until it is egested can take a maximum of 89 hours (Science Learning Hub, 2014). This is the reason for the chosen duration of the experiment exposure being 96 hours.

6.2 Laboratory prepared phosphate solution

6.2.1 Samples selected for phosphate ageing using a laboratory prepared phosphate solution

The following samples were exposed to the laboratory prepared phosphate solution:

- 10 K PVP capped ceria
- Commercial Cerium (IV) oxide NMs (Sample A)
- $\text{Ce}_{0.9}\text{Zr}_{0.1}\text{O}_2$ NMs (Sample B)
- $\text{Ce}_{0.75}\text{Zr}_{0.25}\text{O}_2$ NMs (Sample C)
- $\text{Ce}_{0.48}\text{Zr}_{0.52}\text{O}_2$ NMs (Sample D)
- $\text{Ce}_{0.25}\text{Zr}_{0.75}\text{O}_2$ NMs (Sample E)
- $\text{Ce}_{0.1}\text{Zr}_{0.9}\text{O}_2$ NMs (Sample F)
- Zirconium (IV) oxide NMs (Sample G)

The first NM sample listed was taken from the NM library developed and discussed in Chapter 4. The other seven samples were commercially available zirconium doped ceria samples ranging from pure ceria (Sample A) to pure zirconium (IV) oxide (Sample G). The 10 K PVP capped ceria and sample A were the samples used for the thermal ageing studies discussed in Chapter 5. The reasons for selecting these samples were to compare:

1. PVP capped ceria with uncapped ceria samples.
2. Zirconium doped ceria samples with varying compositions of zirconium and cerium ranging from pure cerium (IV) oxide to pure zirconium (IV) oxide. This library was created in order to investigate the effects of doping on the ROS generation and furthermore the effects on toxicity.

6.2.2 Sample preparation

The 10 K PVP capped ceria NMs were prepared as explained in Section 4.4 and used as such. The commercially available zirconium doped ceria (Sample A to G) NMs were acquired from Promethean Particles Ltd. (Nottingham) as dispersions in deionised water and were used as obtained.

6.2.3 Laboratory prepared Phosphate solution preparation

The laboratory prepared phosphate solution method was based on that of Zhang et al (2012). A 1 mM and 5 mM solution of monopotassium phosphate, citric acid and ascorbic acid were prepared using the quantities shown in Table 6.1. The pH of the phosphate solution was adjusted to c. 5.5 and measured using a pH meter.

Table 6.1. Quantities used to prepare a 1 mM and 5 mM phosphate solution

	1 mM solution	5 mM solution
Citric Acid (g)	0.0420	0.210
Ascorbic Acid (g)	0.0350	0.175
Monopotassium phosphate (g)	0.0272	0.136

6.2.4 Phosphate exposure method

6.2.4.1 10 K PVP Capped Ceria NMs phosphate pilot

exposure

10 K PVP capped ceria NMs were synthesised as explained in Section 4.4.1. These NMs were exposed to a pH adjusted (c.5.5) 5 mM phosphate solution which was prepared as explained in Section 6.2.3. Three different exposure scenarios were set up with varying volumes of NM dispersion, 5 mM phosphate solution and milliQ water as shown in Table 6.2. The first is the same as one of the zirconium doped ceria NMs exposure mixtures (Table 6.3 Scenario A) discussed below whilst the other two vary. The reason for the different scenario quantities was that of studying the changed effect of the ratio of the phosphate to the cerium on the transformation. The samples were subsequently left to stand in the dark for 21 days.

Table 6.2 Three different phosphate exposure scenarios prepared for 10 K PVP capped ceria NMs with varying volumes of NM dispersion, 5 mM phosphate solution and milliQ water.

Scenario	NM Dispersion (mL)	5 mM Phosphate Solution (mL)	MilliQ Water (mL)
A	1	4	N/A
B	4	1	N/A
C	1	1	3

6.2.4.1.1 Characterisation

Pristine, 7 day old and 21 day old samples were characterised by means of DLS, both sizing and zeta potential (Section 3.2), UV-VIS (Section 3.3) and TEM (Section 3.7).

6.2.4.2 Zirconium doped ceria NMs phosphate exposure

1 mL or 0.08 mL aliquots of the commercial zirconium doped ceria (Samples A – G) NM dispersions were respectively added to 4 mL or 4.92 mL volumes of 1 mM or 5 mM phosphate solutions. Table 6.3 shows the volumes of each component added to prepare the mixture of NMs and phosphate solution. The samples containing less NMs were merely used for observation purposes and UV-VIS analysis. The 1:4 ratio of NM to phosphate solution (Scenario A) was chosen to include the highest phosphate concentration possible whilst being comparable to the pilot study carried out on the 10 K PVP capped ceria NMs (Section 6.2.4.1). A total of four different mixtures were prepared

for each sample (Samples A – G) resulting in a total of 28 sample vials. The samples were then left to stand in the dark for 21 days.

Table 6.3 Volumes of NM dispersions and 1 or 5 mM phosphate solutions required to prepare each of the zirconium doped ceria phosphate exposure samples.

Scenario	NM Dispersion (mL)	1 mM solution (mL)	5 mM solution (mL)
A	1	N/A	4
D	1	4	N/A
E	0.08	N/A	4.92
F	0.08	4.92	N/A

6.2.4.2.1 Characterisation

The phosphate exposed zirconium doped ceria samples (Samples A-G) (Section 6.2.4.1) were characterised by means of DLS, both sizing and zeta potential (Section 3.2), and UV-VIS (Section 3.3) before phosphate solution addition (pristine), immediately after phosphate solution addition, after 7 days of exposure and 21 days of exposure. Pristine, 7 day old and 21 day old samples were further characterised by means of XRD (Section 3.6), FT-IR (Section 3.5), TEM (Section 3.7) and EDX (Section 3.9).

6.3 Naturally occurring phospholipid exposure

6.3.1 Samples selected for phosphate ageing using a naturally occurring phospholipid

The commercial cerium (IV) oxide NMs (Sample A) were selected for exposure to the naturally occurring phospholipid. These NMs, which were used for the temperature ageing studies, were chosen from the list of those used for exposure to the laboratory phosphate solution for comparative purposes. Furthermore these NMs are not from one of the doped samples, that is they are simply composed of ceria without any additional compositional component. Lastly they are uncapped and therefore it was thought that the ceria would be more easily accessible for the phosphate group.

6.3.2 Samples preparation

The commercial cerium (IV) oxide (Sample A) NMs were acquired from Promethean Particles Ltd. (Nottingham) as dispersions in deionised water. Details on their characterisation can be found in Appendix 5. They were used as obtained.

6.3.3 Naturally occurring phospholipid solution preparation

A naturally occurring phospholipid solution was prepared using L- α -phosphatidylcholine. The solutions prepared had a concentration of 3 mg/mL, representing the quantity of phospholipid in bile as produced prior to concentration and 15 mg/mL, representing the quantity of phospholipid in bile concentrated to 5 times. The pH

of the solution was adjusted to a pH of 5.5. Following this two NM and phospholipid sample solutions were prepared by adding 4 mL of the 3 mg/mL or 15 mg/mL L- α -phosphatidylcholine solution to 1 mL of NM dispersion. The details for the exposure sample solution quantities are shown in Table 6.4. The exposure samples were incubated in a Grant-bio Orbital Shaker-Incubator ES-20. The incubator was set at 37 °C and 80 rpm and the samples were left for 96 hours.

Table 6.4 Quantities used to prepare natural occurring phospholipid exposure.

Scenario	NM Dispersion (mL)	L-α-phosphatidylcholine concentration (mg/mL)	Volume of L-α-phosphatidylcholine (mL)
G	1	3	4
H	1	15	4

6.5.2.2.3 Characterisation

Characterisation was carried out by means of DLS, both sizing and zeta potential (Section 3.2), UV-VIS (Section 3.3), TEM analysis (Section 3.7), XRD (Section 3.4) and FT-IR (Section 3.5). Measurements were taken at time 0 and after 96 hours.

6.4 Laboratory phosphate ageing of 10 K PVP capped ceria pilot study

This section presents and discusses the characterisation results obtained from the pilot phosphate exposure study where laboratory synthesised 10 K PVP capped ceria were exposed to phosphate containing solutions (Section 6.2).

6.4.1 Physical properties

6.4.1.1 Shape and Size

6.4.1.1.1 Dynamic Light Scattering

The size distribution graphs for the 10 K PVP capped ceria NMs exposed to the phosphate solutions as a function of time are shown in Figure 6.4. The study was carried out for 21 days however the graphs also show an additional reading taken after 13 months.

The initial NM size and PDI for the specific batch of PVP capped ceria NMs exposed to phosphate ageing were found to be 5.470 ± 0.1443 nm and 0.207 ± 0.013 respectively. As a result of the ageing drastic changes in both these values occur with significant changes in Z-Average size values, multiple peaks observed and samples becoming very polydisperse.

As mentioned in Section 6.2.4.1 the reason for the different scenario quantities was to study the effect of the ratio of the phosphate to the cerium on the transformation. On immediate phosphate solution addition to the mixture with a final composition of 1 part NM suspension (resulting in a concentration of 0.0004 mg/mL), 1 part phosphate solution and 3 parts (Scenario C) water a drastic increase in Z-Average to 2541 ± 677.1 nm was noted along with the presence of multiple peaks. The PDI value also shows an increase. After 7 days peaks are noted at a slightly larger size than for the pristine particles (c. 6 nm) and then at a much larger size (multiple peaks greater than 100 nm). After 21 days results reveal that the samples are not stable. Multiple peaks at sizes greater than 100 nm are observed and these are most likely due to aggregation. After 13 months the primary peak

size is just below 10 nm and the size distribution graph looks to have less aggregation peaks, that is, peaks at much higher size values.

For the solution composed of 4 parts of NM dispersion (resulting in a concentration of 0.0016 mg/mL) and 1 part phosphate solution (Scenario B), addition of the phosphate solution shows an immediate decrease in particle size to around 2 nm and an increase in PDI value from 0.190 ± 0.006 to 0.422 ± 0.194 . After 7 days there is a significant increase in size and a decrease in count rate, the two observations combined indicating the occurrence of sedimentation. At 21 days a similar feature is noted for the Scenario C sample after 7 days. This involves the presence of peaks around the original size (c. 6 nm) and much larger (greater than 100 and 1000 nm). Finally, after 13 months, the size measurements obtained are much larger and the Z-Average value is 3439 ± 87.90 nm.

The final solution, composed of 1 part NM dispersion (resulting in a concentration of 0.0004 mg/mL) and 4 parts phosphate solution (Scenario A), shows a radical increase in PDI to the maximum value given by the instrument, a value of 1.000 ± 0.000 . This is the maximum PDI value that can be obtained and represents a strong amount of polydispersity. The Z-average at time 0 is 1750 ± 530.9 nm. A primary peak within the same size range of the pristine particles is noticeable however multiple peaks are also seen at larger sizes. After 7 days the primary size looks to have decreased and the size of the larger particles has increased. 21 days of exposure results in a high PDI value of 0.835 ± 0.240 and after 13 months the polydispersity continues increasing with the Z-Average found to be 2221 ± 570.9 nm.

It is important to keep in mind that DLS measures the hydrodynamic diameter and not the core particle size therefore such large values are a result of the media on the NMs and not realistic of actual size. Furthermore the NMs are settling and aggregating and

therefore DLS is not an ideal size measurement technique necessitating TEM imaging and characterisation. Despite this, DLS still reveals information on the behaviour of the NMs when exposed to phosphate over a period of time.

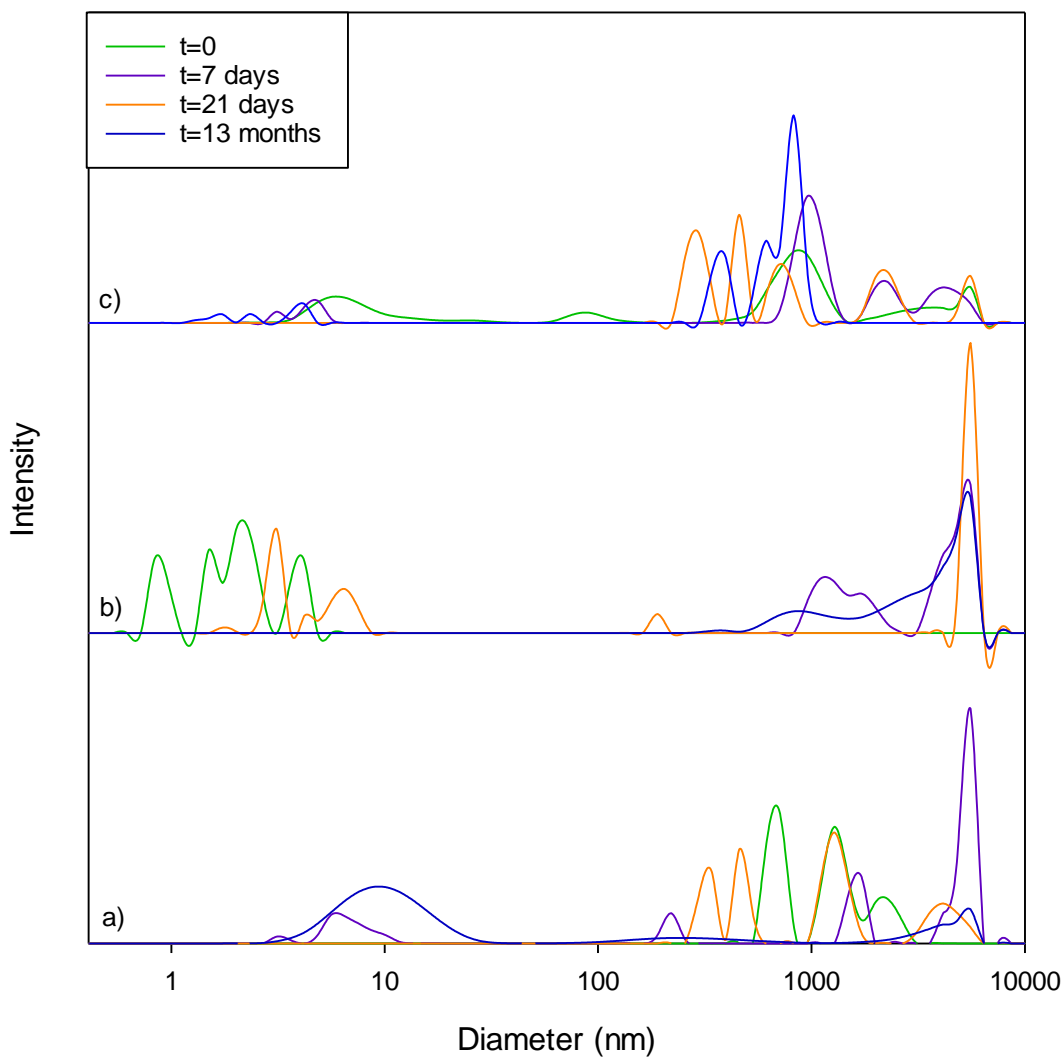
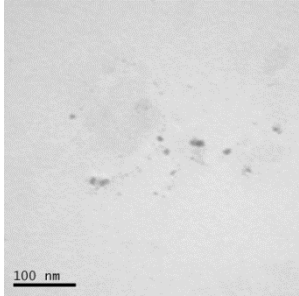
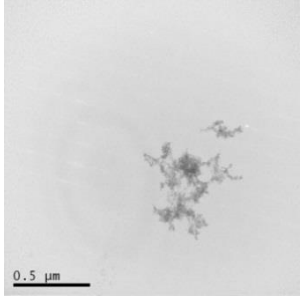
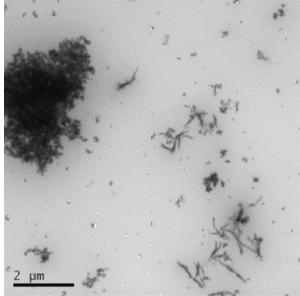
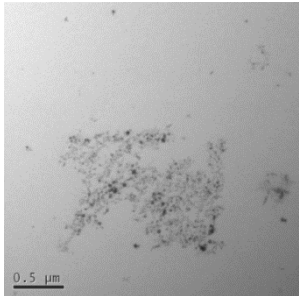
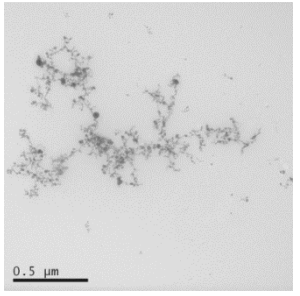
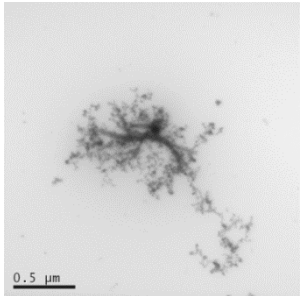
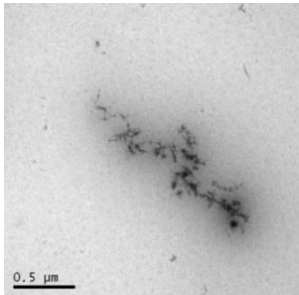
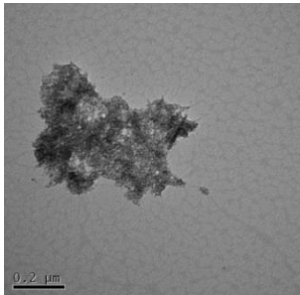
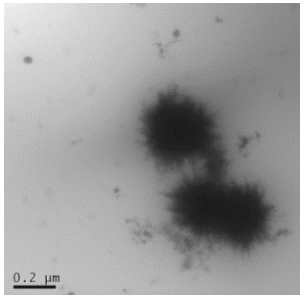


Figure 6.4 DLS size histograms for 10 K PVP capped ceria NM sample exposed to 5 mM phosphate solution as a function of time a) 1 part NM solution, 1 part phosphate solution and 3 parts water, b) 4 parts NM solution and 1 part phosphate solution and c) 1 part NM solution and 4 parts phosphate solution.

6.4.1.1.2 Transmission Electron Microscopy

The TEM images obtained for the as prepared, 1 week and 3 week phosphate aged 10 K PVP capped ceria NMs can be observed in Table 6.5. The images show the pristine particles to be spherical and 7.625 ± 2.595 nm as discussed in Chapter 4 (Section 4.6.2). After one week, the appearance of needles is noted in all images regardless of the exposure scenario. This implies that a physical transformation is taking place. The largest discrepancy between the different exposure solutions is noticeable from the images of the third week. The Scenario C sample shows sea-urchin like structures whilst the other two solutions show needle-like structures. This indicates that the ratio of ceria to the phosphate solution influences the rate of the transformation. Furthermore, the sea-urchin like structures are comparable in size to those seen below for the zirconium doped ceria samples (Table 6.6 and 6.7) despite the initial size of the particles varying. This reveals that there is a tendency for these structures to have a size of c. 200 nm regardless of the initial ceria NM size or composition.

Table 6.5. TEM images for the as prepared, 1 week and 3 week phosphate aged 10 K PVP capped ceria NMs.

Scenario	As prepared	1 week	3 weeks
A (1 NM + 4 phosphate)			
B (4 NM + 1 phosphate)			
C 1 NM + 1 phosphate + 3 H ₂ O)			

6.4.2 Chemical properties

6.4.2.1 Surface Charge

The average zeta potential values of the 10 K PVP capped ceria phosphate exposed samples as a function of time are shown in Figure 6.5. A complete table with all the zeta

potential values plotted can be found in Appendix 7. The original zeta potential value prior to phosphate addition is 1.74 ± 0.136 at pH 6 as shown in Table 4.8 and discussed in Section 4.7.1. This value is very close to the isoelectric point yet the samples are still stable due to steric stabilisation brought about by the PVP capping.

All the samples follow the same trend for the first week yet the rate of change varies for the differing samples. This trend, which involves a drop in average zeta potential followed by an increase, within the first week; beyond that the trend followed depends on the sample. The ratio of the ceria to phosphate changes the behaviour of the transformed particles. This highlights the complexity of ageing processes and the need to be studied in depth for a better understanding of the possible resultant toxicity.

The average zeta potential of the Scenario A sample is the most influenced over time (Figure 6.5), with zeta potential values changing from 1.74 ± 0.14 prior to addition to -14.2 ± 3.42 on addition to -9.81 ± 3.11 after 13 months. This is possibly due to more cerium phosphate forming due to the higher phosphate concentration. This in turn results in greater aggregation brought about by the phosphate solution as seen in Table 6.5. The values are also associated with the largest error. In Figure 6.5 it can be seen that after the first 7 days the average zeta potential drops once again and by 13 months shows an increase.

The values of the sample composed of Scenario B are the least influenced by time. After the first 7 days the average zeta potential continues to drop from 3.66 ± 0.5240 mV to 3.61 ± 0.291 mV. After 13 months the average zeta potential, 1.24 ± 0.101 mV, is similar to the original value. This could imply that the samples were least influenced or transformed by the phosphate solution and this can be seen in the TEM images in Table 6.5.

The final Scenario C solution made up of 1 part NP dispersion, 1 part phosphate solution and 3 parts water shows an increase in average zeta potential between day 7 and day 21 and a significantly reasonably sized decrease by 13 months.

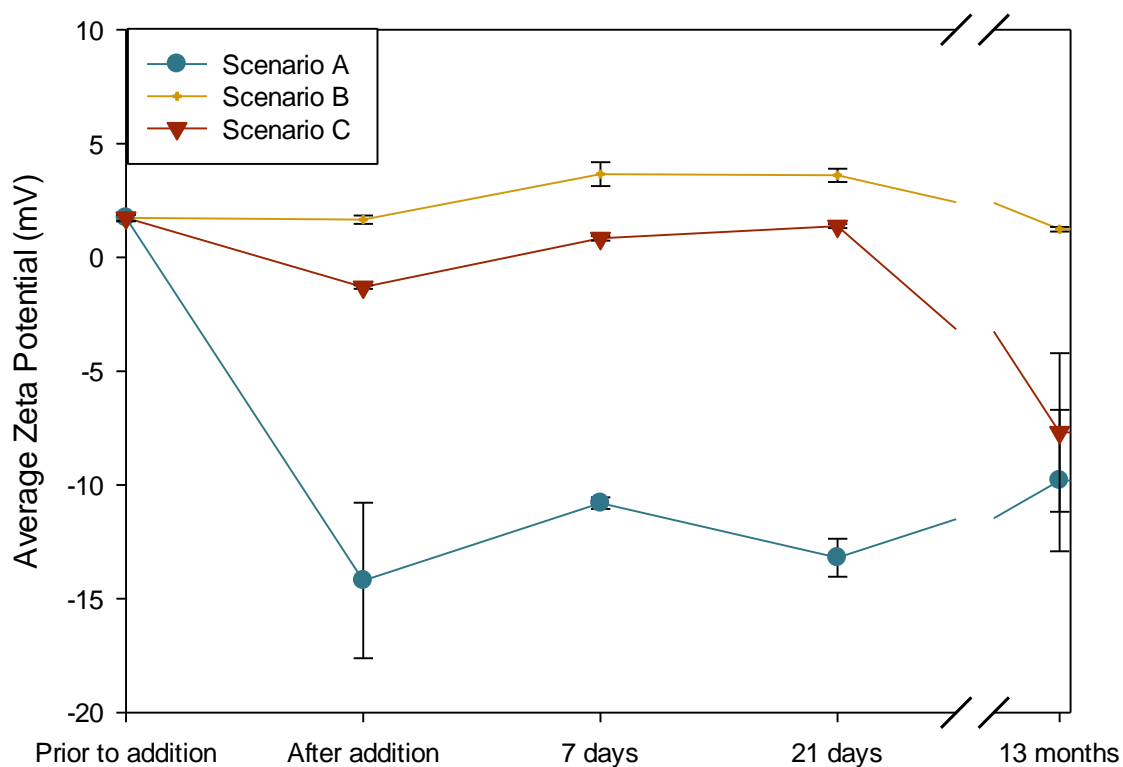


Figure 6.5 Zeta Potential for all 10 K PVP capped ceria phosphate exposed samples as a function of time.

6.4.2.2 Chemical Composition

In order to determine whether any chemical compositional transformations took place it would have been beneficial to carry out XRD analysis. However due to the small size of the particles and the excessive presence of the PVP capping, no XRD spectrum could be obtained. Therefore it was attempted to determine chemical changes by means of UV-VIS.

6.4.2.2.1 UV-VIS

The 10 K PVP capped ceria NMs show a strong UV-VIS absorbance peak at c. 270 nm regardless of the ratio of particles to phosphate solution. This can be seen from Figures 6.6-6.8. This peak is most likely to be due to the ascorbic acid present within the phosphate solution (Table 6.1) which reportedly has an absorbance at 265 nm (Tóth et al., 2002). This peak is shadowing the PVP absorption peak which has been found to be at c. 250 nm and the cerium (III) peak found between 230 and 260 nm. The intensity of this peak is similar for both the Scenario B and C exposed samples. The peak has a greater intensity for the sample exposed to Scenario A (the scenario with the highest phosphate concentration). This confirms that the peak is due to a component of the phosphate solution, namely ascorbic acid, and not the NMs. The intensity of this peak decreases over time due to the ascorbic acid reducing the ceria and hence becoming oxidised to dehydroascorbic acid which does not show a peak in the recorded range (Root-Bernstein et al., 2016).

Furthermore as the intensity of this peak decreases there are some instances where another peak is seen at 300 nm as seen for the sample from Scenario B after 21 days. This peak is characteristic of cerium (IV), which is expected from the evidence presented in Chapter 4 of a mixed valency state (III and IV) for the 10 K PVP capped ceria NMs. Since Ce (IV) is still present after 21 days this implies that, provided there are still enough organic acids and phosphate ions present, the transformation will continue to take place past the predetermined experimentation period of 21 days.

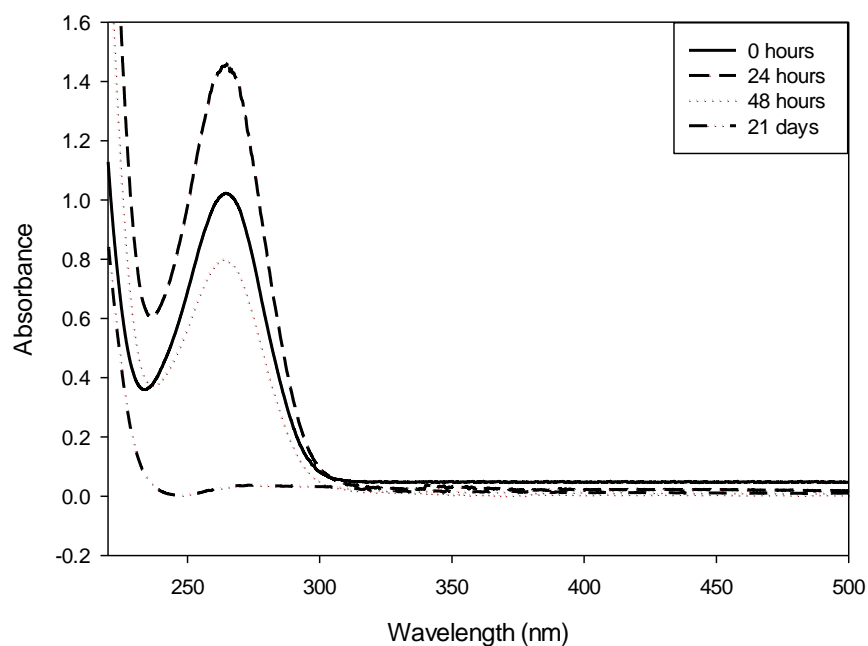


Figure 6.6 UV-VIS spectra for sample from Scenario A (1 part NM + 4 parts phosphate) as a function of time.

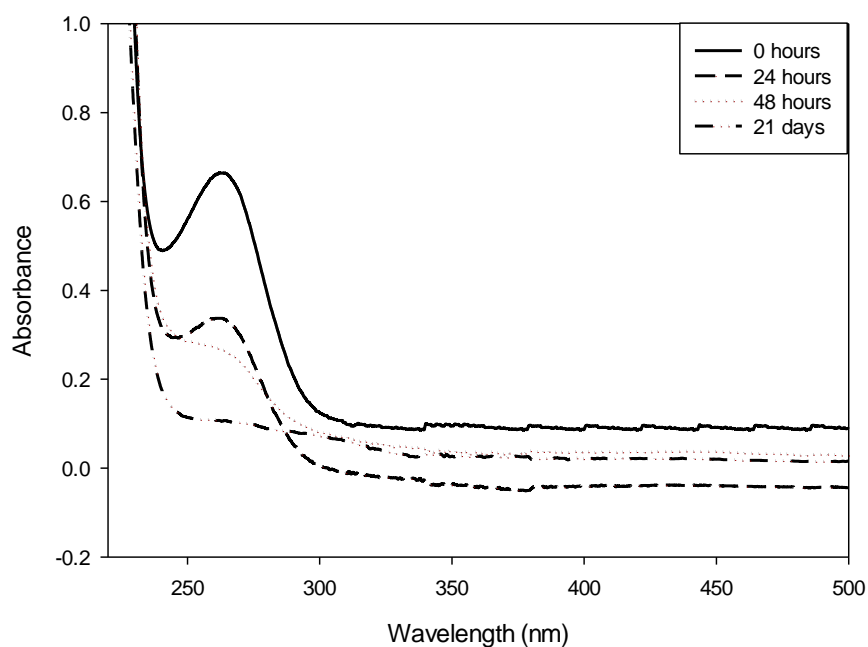


Figure 6.7 UV-VIS spectra for sample from Scenario B (4 parts NM + 1 part phosphate) as a function of time.

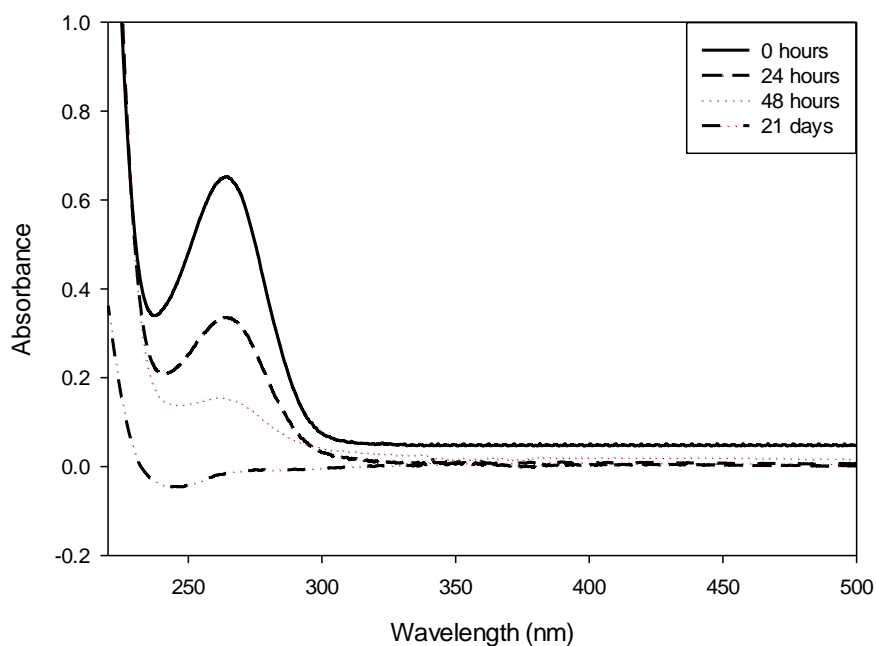


Figure 6.8 UV-VIS spectra for sample from Scenario C (1 part NM + 1 part phosphate + 3 parts H₂O) as a function of time.

6.5 Laboratory phosphate ageing of zirconium doped ceria

This section presents and discusses the characterisation results obtained from the study where the NM series A-G (as described in 6.2.1) were exposed to phosphate containing solutions (Section 6.2). The design for the experiments below was informed from the pilot study presented earlier.

6.5.1 Physical properties

6.5.1.1 Appearance

In this section the results of the visual inspection of the ceria and zirconium doped ceria samples during the laboratory phosphate ageing process described above are presented. Photographs of the samples were taken following: (1) immediate exposure to the phosphate solution, (2) after 7 days and (3) after 21 days of continuous exposure. In general, on addition of 4 mL of the phosphate solution, whether at 1 mM (Scenario D) or 5 mM (Scenario A) concentration, the NM suspensions appear to undergo an immediate and noticeable colour change. However, when 4.92 mL of phosphate solution were added 80 μ L of NM sample, resulting in more phosphate solution added to less NM than Scenarios A and D, no noticeable colour change was noted. The weaker NM concentration was probably the reason for this.

Samples A-G exposed to 4 mL of 5 mM phosphate solution was added to 1 mL of NM solution (Scenario A). The immediate colour change on phosphate addition resulted in the samples having a colour range from purple-grey to white (Figure 6.9). As the amount of ceria present within the zirconium doped ceria samples decreased the colour changed from purple-grey to white. Over time the samples changed colour and at the end of the 21 days all the samples looked yellowish (Figure 6.10).

Samples A-G as a function of time where 4 mL of 1 mM phosphate solution was added to 1 mL of NM solution (Scenario D) showed the lower phosphate concentration produced lighter coloured samples. Significant settling was noticed after 7 days (Figure 6.11) and increased over the 21 days implying that the precipitate formed was unstable.

The colour of the samples varied as the amount of ceria present within the zirconium doped ceria samples varied.

Phosphate addition to samples A-G as a function of time where 4.92 mL of 5 mM phosphate solution were added 80 μ L of NM solution (Scenario E) showed no immediate colour changes were noted. However, samples B-G became yellow in colour over time. Sample A showed the presence of a sedimentation layer at the bottom of the vial. The use of 1 mM (Scenario F) rather than 5 mM phosphate solution resulted in some samples gaining a pink tinge rather than a yellow colour over time.

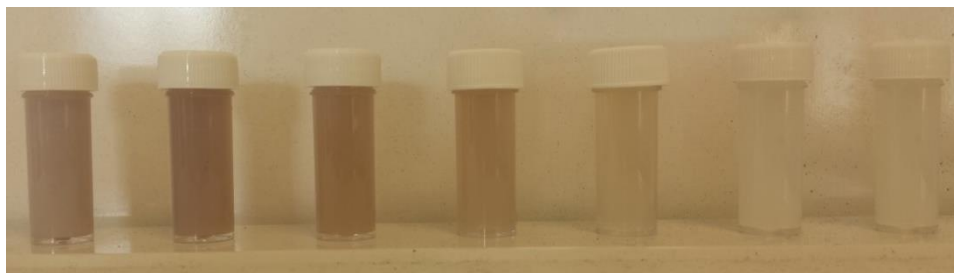


Figure 6.9 Samples A-G (left to right) after immediate addition of 4 mL of 5 mM phosphate solution to 1 mL of NM solution (Scenario A).



Figure 6.10 Samples A-G (left to right) after 21 days exposed to Scenario A.

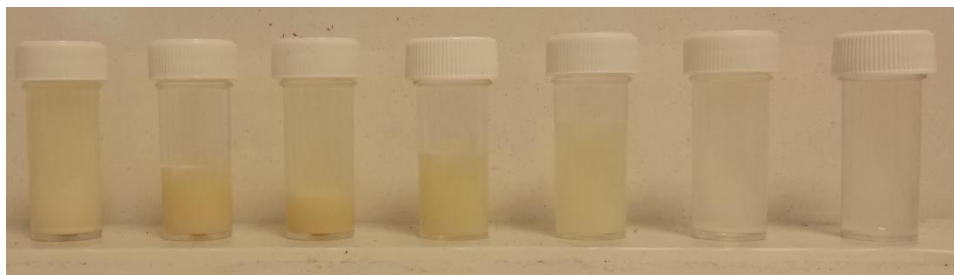


Figure 6.11 Samples A-G (left to right) after 7 days exposed to Scenario D.

6.5.1.2 Shape and Size

6.5.1.2.1 Dynamic Light Scattering

DLS was used to measure the hydrodynamic diameter of NMs in the suspensions. Table 6.6 shows the Z-Average obtained for pristine and aged zirconium doped ceria samples A-G. The size distribution graphs are shown in Figures 6.12 and 6.13 for 1 mM (Scenario D) and 5 mM (Scenario A) phosphate solutions respectively.

It is immediately noticeable that, on addition of the phosphate solution, regardless of the concentration, the pristine particle size which ranges from 260 nm to 360 nm for the samples, decreases for all samples except for sample A exposed to 1 mM phosphate solution where an increase in Z-Average is recorded. This change is likely to be due to the influence of the ionic concentration on the different NMs. The phosphate ions have a greater effect on the hydrodynamic diameter of the zirconium doped ceria samples rather than the pure ceria NMs.

The general trend for both 1 mM and 5 mM phosphate exposed samples is that the Z-Average value decreases on immediate phosphate addition followed by an increase in size. The size increase was due to transformations taking place. The extent of the increase varies depending on the sample. As the zirconium concentration increases, that is from

sample A to G, the size changes occurring over time after addition of phosphate are less significant. This appears to be the result of lesser or no transformations taking place. In fact sample G, which is composed of zirconium oxide, showed minimal changes over the 21 days following the decrease in Z-Average on phosphate addition.

Sample A, which is composed of cerium dioxide, shows the most significant changes out of all the samples. Furthermore the changes are more pronounced for the 5 mM exposure compared to the 1 mM exposure with the size distribution for the 1 mM exposure becoming bimodal by day 21 and the 5 mM exposure becoming multimodal by day 7. This implies that the phosphate concentration plays a role in the transformation. This was further supported by Sample B, where the changes in Z-Average were more distinct for the 5 mM exposure than the 1 mM exposure. Samples C and D were consistent with the trend of a decrease in Z-Average on immediate addition followed by an increase over the 21 days. Samples E and F showed very little Z-Average value changes over the 21 day period after the initial decrease. Once again the changes are more prominent for the 5 mM exposure rather than the 1 mM exposure.

Table 6.6 Z-Average (nm) values obtained for pristine and aged zirconium doped ceria samples.

Sample	Pristine	Day 0		Day 7		Day 21	
		1 mM	5 mM	1 mM	5 mM	1 mM	5 mM
Sample A	269.5 ± 8.979	285.5 ± 3.519	266.2 ± 3.175	702.5 ± 19.43	6477 ± 1911	2268 ± 239.6	5706 ± 582.0
Sample B	330.4 ± 4.509	152.9 ± 1.849	329.6 ± 8.848	192.3 ± 2.703	579.7 ± 19.06	224.6 ± 2.068	830.0 ± 14.81
Sample C	297.5 ± 4.032	139.1 ± 2.438	165.9 ± 2.693	155.7 ± 1.447	311.3 ± 5.357	239.8 ± 2.176	276.9 ± 5.806
Sample D	315.7 ± 5.200	93.02 ± 1.294	91.37 ± 1.322	112.5 ± 0.6904	136.6 ± 1.865	123.6 ± 3.068	209.6 ± 6.052
Sample E	358.3 ± 6.424	73.50 ± 1.079	77.44 ± 1.520	72.66 ± 0.829	77.41 ± 0.0931	74.43 ± 0.979	104.3 ± 2.096
Sample F	341.0 ± 10.93	113.4 ± 2.381	128.6 ± 2.994	118.6 ± 1.226	114.4 ± 1.339	121.7 ± 2.137	126.1 ± 3.755
Sample G	304.0 ± 13.05	122.4 ± 1.427	127.5 ± 1.246	119.5 ± 1.561	125.3 ± 1.914	128.9 ± 10.66	101.8 ± 1.346

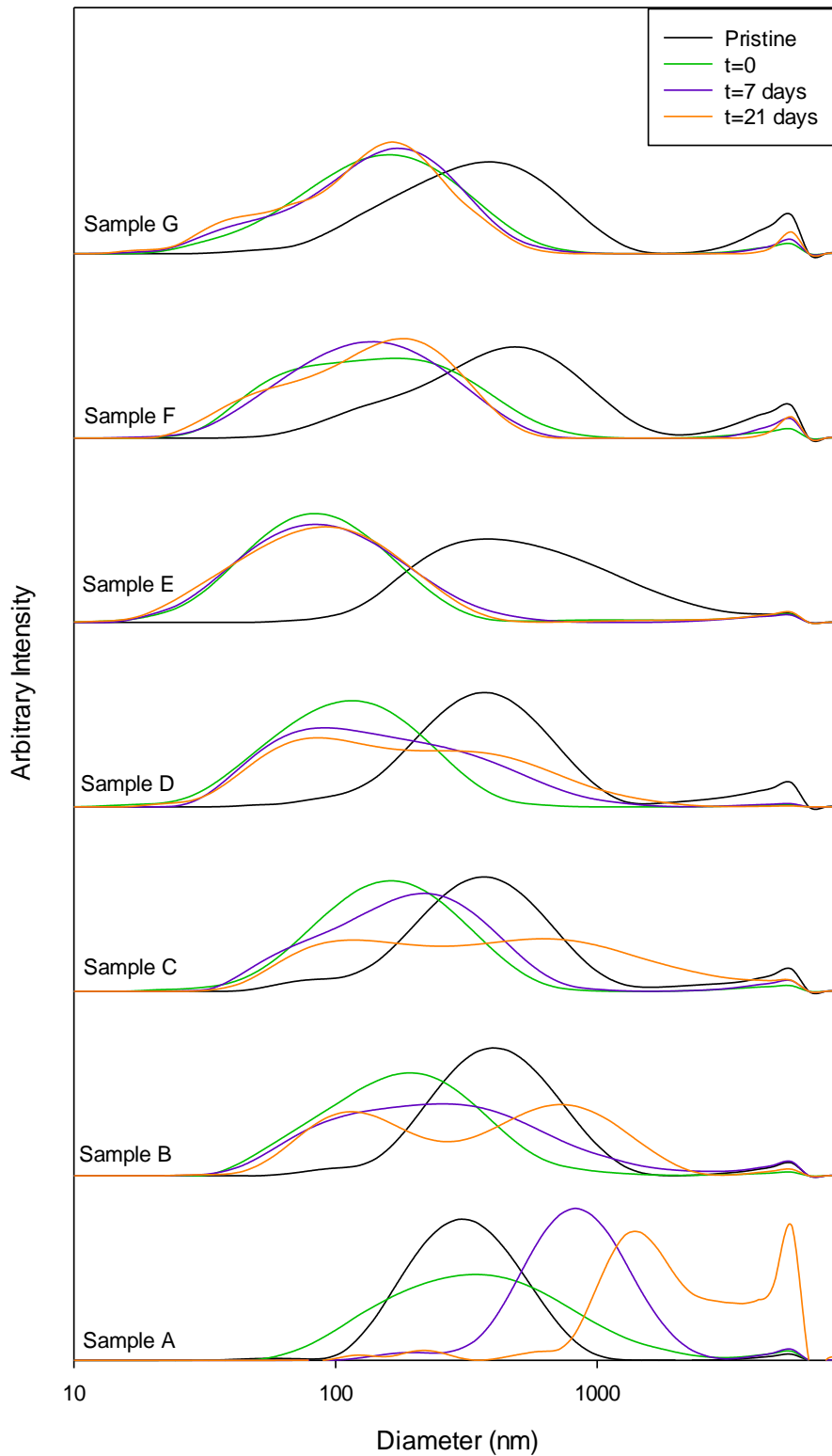


Figure 6.12 DLS size histograms for zirconium doped ceria samples A-G exposed to 1 mM phosphate solution (Scenario D) as a function of time.

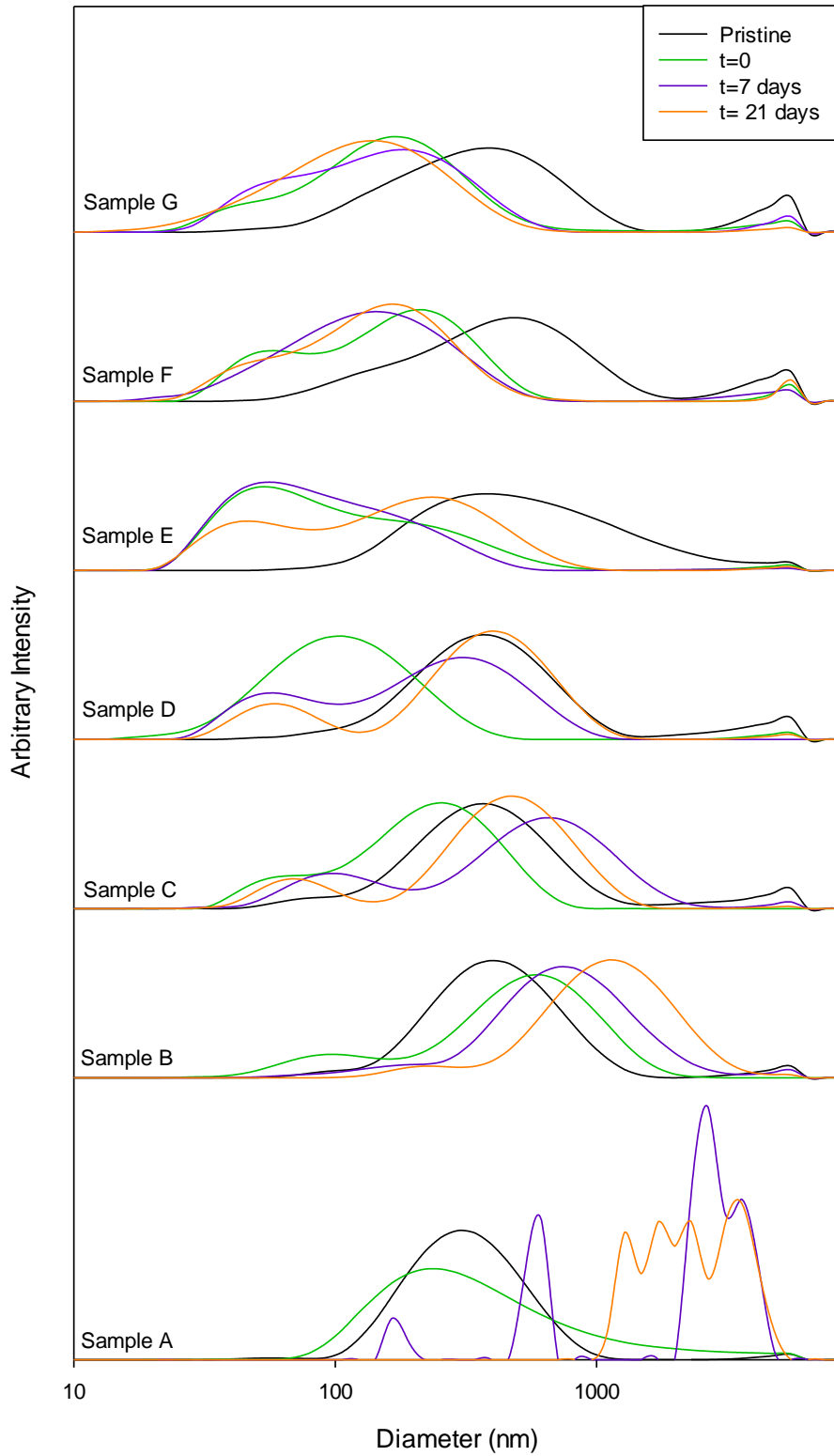


Figure 6.13 DLS size histograms for zirconium doped ceria samples A-G exposed to 5 mM phosphate solution (Scenario A) as a function of time.

6.5.1.2.2 Transmission Electron Microscopy

The TEM images obtained, shown in Table 6.7, reveal the physical transformations that took place over time on exposure of the NMs to the phosphate solutions. TEM images of the pristine particles show that the particle size is smaller than that obtained by DLS. The primary pristine particle size is much smaller than that recorded by DLS, and is, in fact, within the nanorange (< 100 nm). STEM analysis carried out elsewhere (as part of the NanoMILE project – <http://nanomile.eu-vri.eu>) revealed the NPs' sizes to be c. 5 nm. The reason for this discrepancy in size is that DLS measures the hydrodynamic diameter rather than the actual diameter of individual particles. Additionally, in the case of agglomerates as seen here, the DLS size values will be more true to the agglomerate size. This is the case with samples A-G where the DLS Z-Average was found to be greater than 200 nm and comparable to the agglomerate size (Section 6.5.1.2.1).

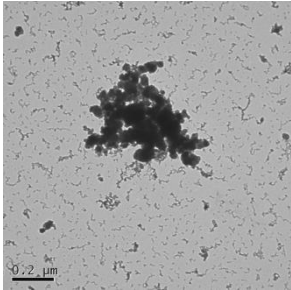
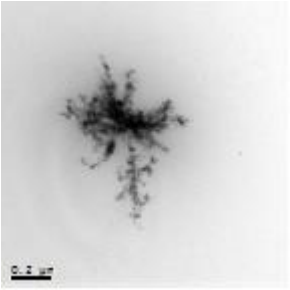
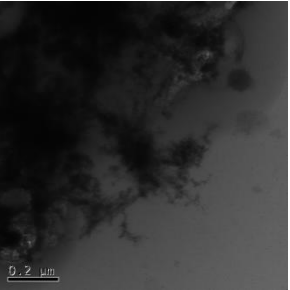
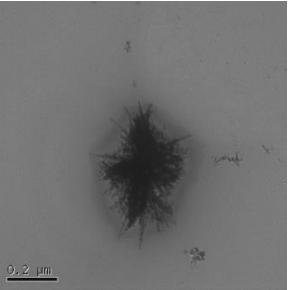
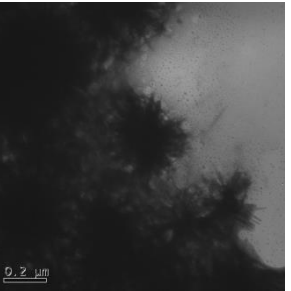
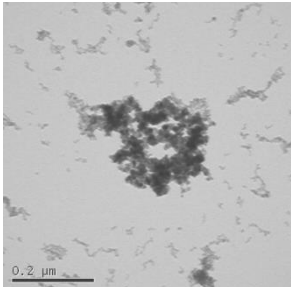
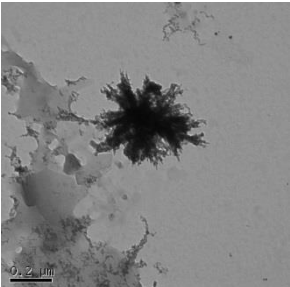
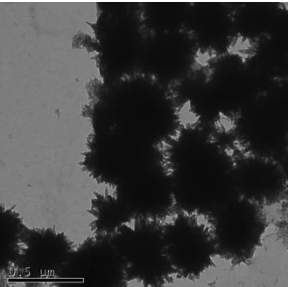
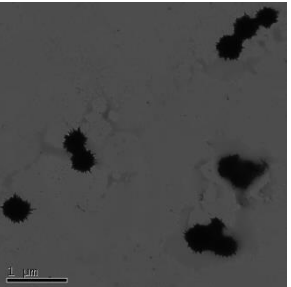
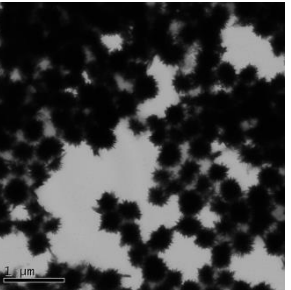
The exposure of the zirconium doped ceria nanoparticle samples A-G to the phosphate solution resulted in structural changes with the formation of sea-urchin/needle-like structures. Samples A to F all showed some form of this physical transformation. The degree and rate of transformations decreased from sample A to sample G. This correlates with deductions made from the DLS results. The degree and rate of transformation varied depending on the quantity of ceria present within the sample. With the decrease in ceria, transformations decreased from sea-urchins to needles to no transformation in the case of sample G where no ceria was present. In fact sample G simply showed some slight aggregation. This shows that the transformations occurring are due to the cerium oxide. Furthermore, the 5 mM phosphate solution transformations occurred faster than those for

the 1 mM. This is particularly noticeable when comparing the 7 days images for both concentrations.

The sea-urchin formation looks to take place in a number of steps. Firstly the primary particles appear to decrease in size. This could be due to CeO₂ dissolution and reduction in the presence of citric and ascorbic acid. In fact Zhang et al. (2012) highlight that organic acids (e.g., citric acid) promoted CeO₂ dissolution and reducing substances (e.g., ascorbic acid) played a key role in the transformation process, generating Ce (III) ions which then reacted with the phosphate present in the media. The smaller particles seem to form needles, as seen in sample A 1 mM after 7 days, which then come together in clusters to form larger sea-urchin like structures having a size of c. 200 nm. These sea-urchin shaped materials gather together. The abundance of these structured materials decreases from sample A to G and hence is dependent on the cerium concentration of the sample.

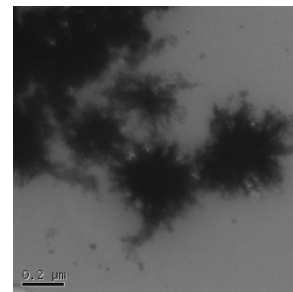
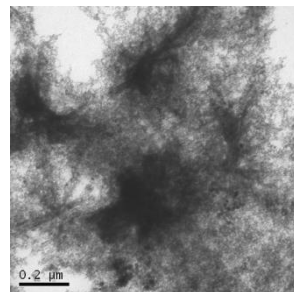
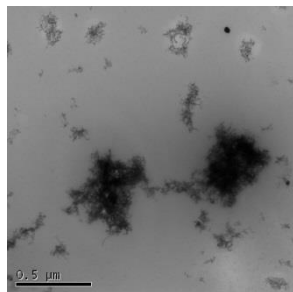
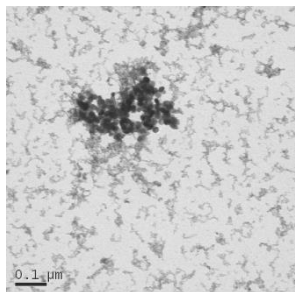
The resultant particles have a larger surface area than the original particles. This change in surface structure increases the surface area of the particles which in turn can affect reactivity and possible NM interactions in the environment or human body.

Table 6.7 TEM images for (from left to right) Pristine, 7 day old 1 mM phosphate exposed samples, 21 day old 1 mM phosphate exposed samples, 7 day old 5 mM phosphate exposed samples and 21 day old 5 mM phosphate exposed samples A-G (from top to bottom).

Sample	Pristine	1 mM 7 days	1 mM 21 days	5 mM 7 days	5 mM 21 days
Sample A Cerium(IV) oxide					
Sample B $Ce_{0.9}Zr_{0.1}O_2$					

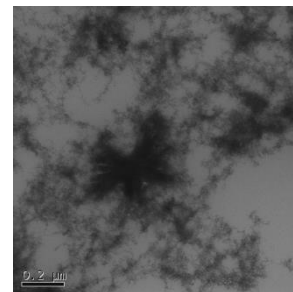
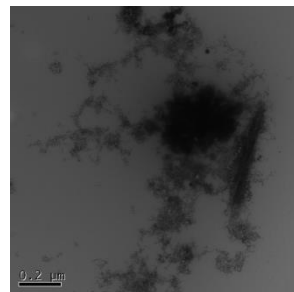
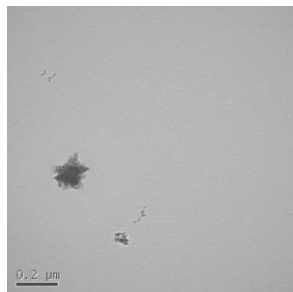
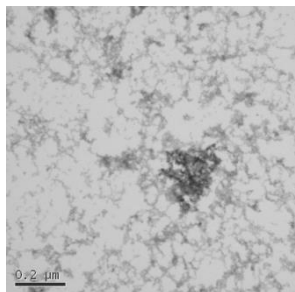
Sample C

$\text{Ce}_{0.75}\text{Zr}_{0.25}\text{O}_2$



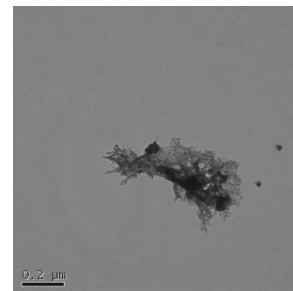
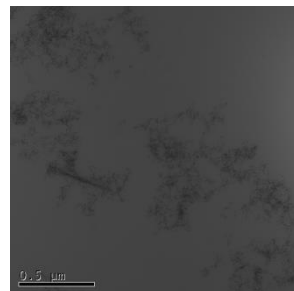
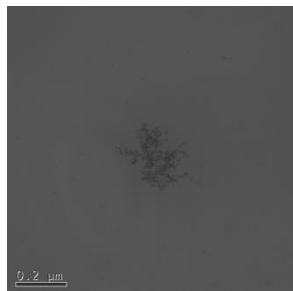
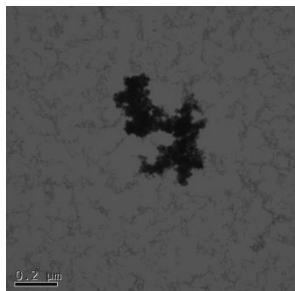
Sample D

$\text{Ce}_{0.48}\text{Zr}_{0.52}\text{O}_2$

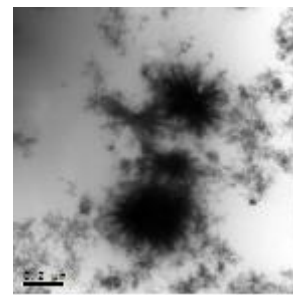
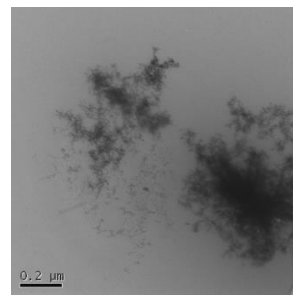
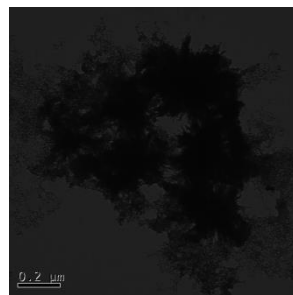
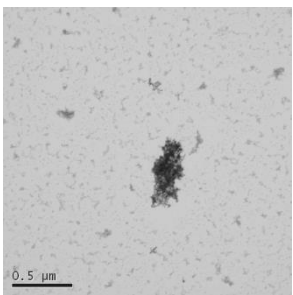


Sample E

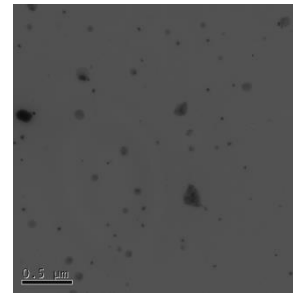
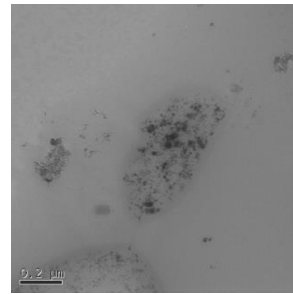
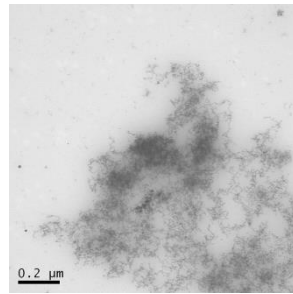
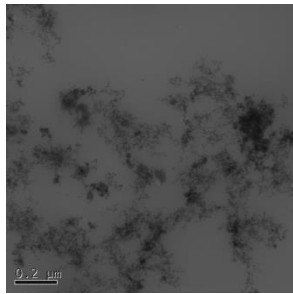
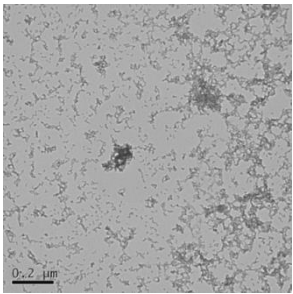
$\text{Ce}_{0.25}\text{Zr}_{0.75}\text{O}_2$



Sample F
 $\text{Ce}_{0.1}\text{Zr}_{0.9}\text{O}_2$



Sample G
Zirconium
(IV) oxide



6.5.2 Chemical properties

6.5.2.1 Surface Charge

Zeta potential gives an indication of the stability of the system and is important for electrochemical surface properties. These in turn can affect the behaviour and toxicity of NMs. Figures 6.14 and 6.15 show the zeta potential of the zirconium doped ceria samples A-G exposed to 1 mM and 5 mM phosphate solution respectively as a function of time. Both graphs show that, on immediate addition of the phosphate solution, the zeta potential values change from a positive stable values of 34 – 53 mV to negative stable values of -36 – -43 mV for the 1 mM solution and -38 – -49 mV for the 5 mM solution. Both sets of values are considered stable because they are more positive than +30 mV or more negative than -30 mV (Malvern, 2013b). Factors affecting zeta potential are pH, conductivity and concentration of the formulation components (Malvern, 2013b). The change in zeta potential is due to the change in environment. The dissociation of acidic groups on the surface of a particle give rise to a negatively charged surface (Malvern, 2013b). The phosphate ions increase the surface charge density and change the charge of the oxide surface (Brookhaven Instruments, 2016, Nelson et al.). Furthermore, the phosphate environment results in a change in electrolyte concentration and pH (c. 5.5).

Between $t=0$ and $t=7$ days very little change is seen for all samples exposed to both 1 mM and 5 mM except for the cerium dioxide sample A exposed to 5 mM phosphate solution. For this sample the zeta potential value increases significantly towards 0. At 21 days of exposure, there is more of an effect on the zeta potential values of the samples, implying that time is an influencing transformational and behavioural factor. In the case of

the 5 mM solution only samples C and F are stable. Samples A, B, D, E and G have zeta values close to zero which is the isoelectric point and the point where the colloidal system is least stable. This leads to aggregation of the particles. In fact the TEM images, particularly those for sample A and B, show the presence of aggregation. In the case of the 1 mM solution only samples B and D are stable. Samples A, C, E, F and G have zeta values close to zero which correlates to the aggregation seen in the TEM images.

In general samples A, E and G follow the same trend regardless of the phosphate concentration. Samples B and D remain stable in the 1 mM solution but not the 5 mM solution implying that the increased concentration results in faster particle transformations. It is possible that, if left for longer, the zeta potential for these samples in the 1 mM solution would also approach zero. Samples C and F are unstable after 21 days with the 1 mM solution but stable in the 5 mM solution. This further proves that it is not simply the phosphate concentration that influences the transformation but also the sample composition and the relationship between the two.

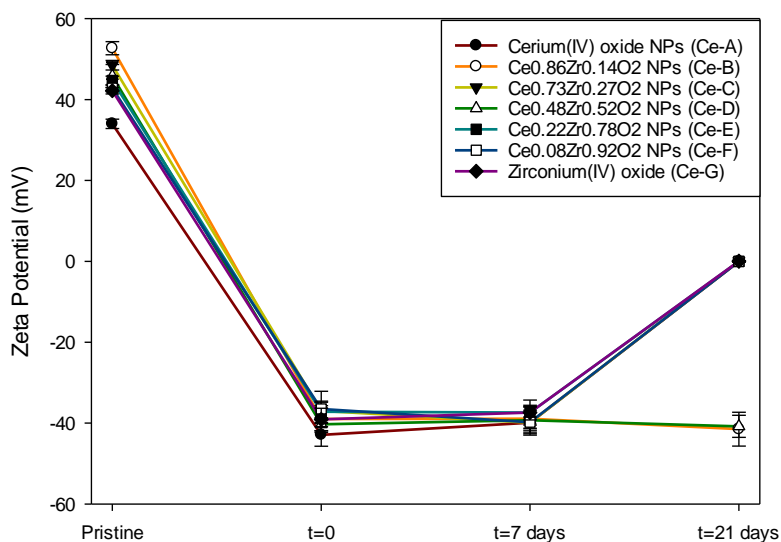


Figure 6.14 Zeta Potential of zirconium doped ceria samples A-G exposed to 1 mM phosphate solution as a function of time.

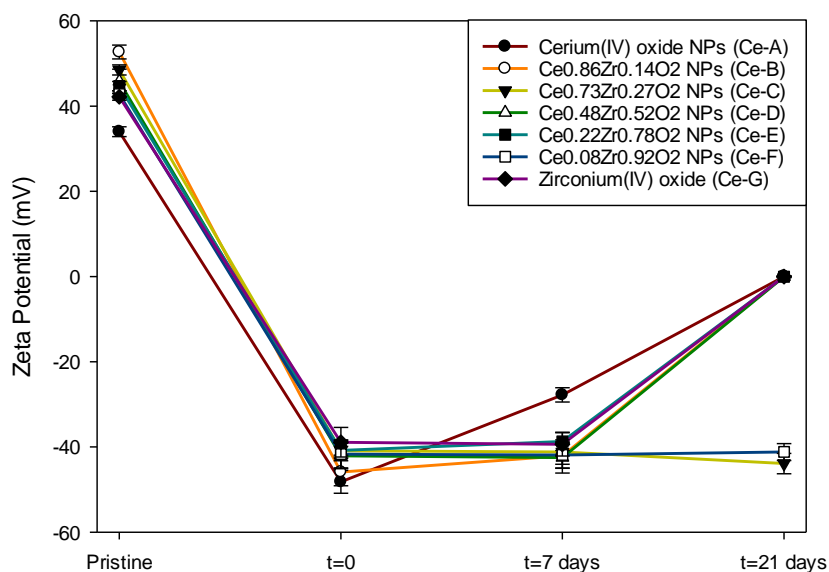


Figure 6.15 Zeta Potential of zirconium doped ceria samples A-G exposed to 5 mM phosphate solution as a function of time.

6.5.2.2 Chemical Composition

6.5.2.2.1 FT-IR

Figure 6.16 shows the spectra for samples A-G (top to bottom) in their pristine state (left) and after 21 days exposed to a 5 mM phosphate solution (right). The spectra for the samples after 7 days and those exposed to a 1 mM phosphate solution after 7 and 21 days can be found in Appendix 8.

A number of the spectra show a broad peak above 3000 cm^{-1} which results from O-H stretching (Reusch, 2013) occurring due to the presence of water showing that even though samples were dried before analysis some moisture was still present. Furthermore, the strong peak seen just below 3000 cm^{-1} is due to C-H stretching (Reusch, 2013). Strong

peaks around 2000 cm^{-1} can be seen in both the pristine and exposed sample spectra. These can be attributed to nitrogen dioxide and carbon dioxide from the atmosphere.

Following exposure the stretching peak for P-O can be seen in the spectrum of sample A indicating a change of cerium dioxide to cerium phosphate. The peak is found at c. 960 cm^{-1} , a slightly lower value than that quoted in literature (Rajesh et al., 2004), probably due to interactions with cerium. This peak is shadowed in samples B-G due to a peak seen in all zirconium containing spectra. This could be the -OH bending peak which has been reported to be found at c. 937 cm^{-1} (Reusch, 2013). The weak peak seen for the exposed samples at 1153 cm^{-1} can be attributed to P=O stretching which in literature has a value between 1100 and 1200 cm^{-1} (Reusch, 2013). This peak is not observed for sample G. In fact no spectral differences are noted for the pristine and exposed sample G implying no chemical transformation took place. Samples B-F show features resembling both sample A and sample G. This is due to the fact that they are samples composed of a mixed phase cerium (sample A being the end member) and zirconium dioxide (sample G being the end member).

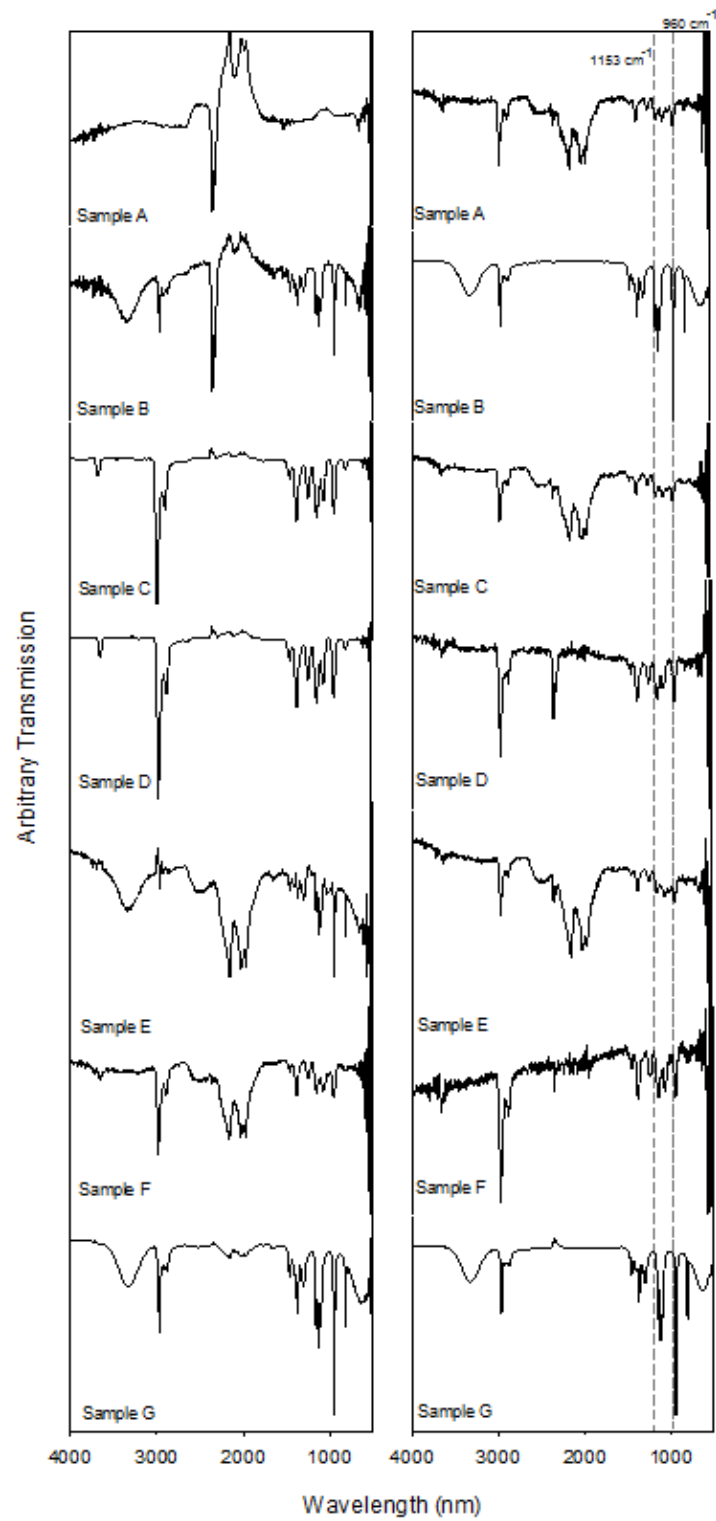


Figure 6.16 FT-IR spectra for pristine (left) and 21 day 5 mM phosphate exposed samples A-G (top to bottom).

6.5.2.2.2 UV-VIS

The UV-VIS spectra for the pristine, immediately exposed, 7 days and 21 days exposed samples to 1 mM and 5 mM phosphate solutions are presented in Figures 6.17 and 6.18 respectively. The major difference between the two graphs is the intensity of the major peak on Day 0 as otherwise the trends are the same for both the 1 mM and 5 mM exposure scenarios.

On analysing the pristine spectra sample A clearly shows the cerium (IV) absorbance peak which occurs in the 300 to 400 nm range and is due to the charge-transfer transition between O $2p$ and Ce $4f$ bands (Herrling, 2013, Tsunekawa et al., 2000). The intensity of this peak decreases to non-existent across samples B-G as the cerium concentration decreases to nil in sample G, zirconium dioxide. Pristine sample G shows a spectrum characteristic of zirconium dioxide. The spectrum has a peak at c. 240 which literature has attributed to both tetragonal and monoclinic zirconium dioxide (Ranga Rao and Sahu, 2001) and a peak near 290 nm which can be attributed to interstitial Zr^{3+} ions in the monoclinic lattice (Kumari et al., 2009).

On addition of the phosphate solution a strong peak occurs immediately at c. 270 nm. This peak is most likely to be due to ascorbic acid which reportedly has an absorbance at 265 nm (Tóth et al., 2002). This peak shows a slight blue shift (a decrease in wavelength) from samples A to G probably due to the interaction with other peaks belonging to cerium and zirconium phosphates and oxides found in the same region, likely to be shadowing. The intensity of this peak increases from samples A to G. The reason for this is the amount of ascorbic acid present increases from samples A-G as the amount needed for reducing the cerium decreases due to the decrease in ceria concentration from

samples A to G. This peak is less prominent for the 1 mM phosphate exposed samples due to the fact that less ascorbic acid is present than in the more concentrated 5 mM solution. Furthermore, this peak shows the presence of a shoulder at a higher wavelength c. 300 nm, which decreases in intensity from samples A to G. This peak is most likely due to cerium (IV).

Day 7 shows a drastic decrease in intensity and a weak peak is seen just above 300 nm for 1 mM and a slightly lower wavelength for 5 mM. The low intensity was probably the result of a detection reduction brought about by the settling of particles seen in the images presented in Section 6.5.1.1. Between day 7 and 21 only differences in intensity were noticed and no significant peak position changes were recorded.

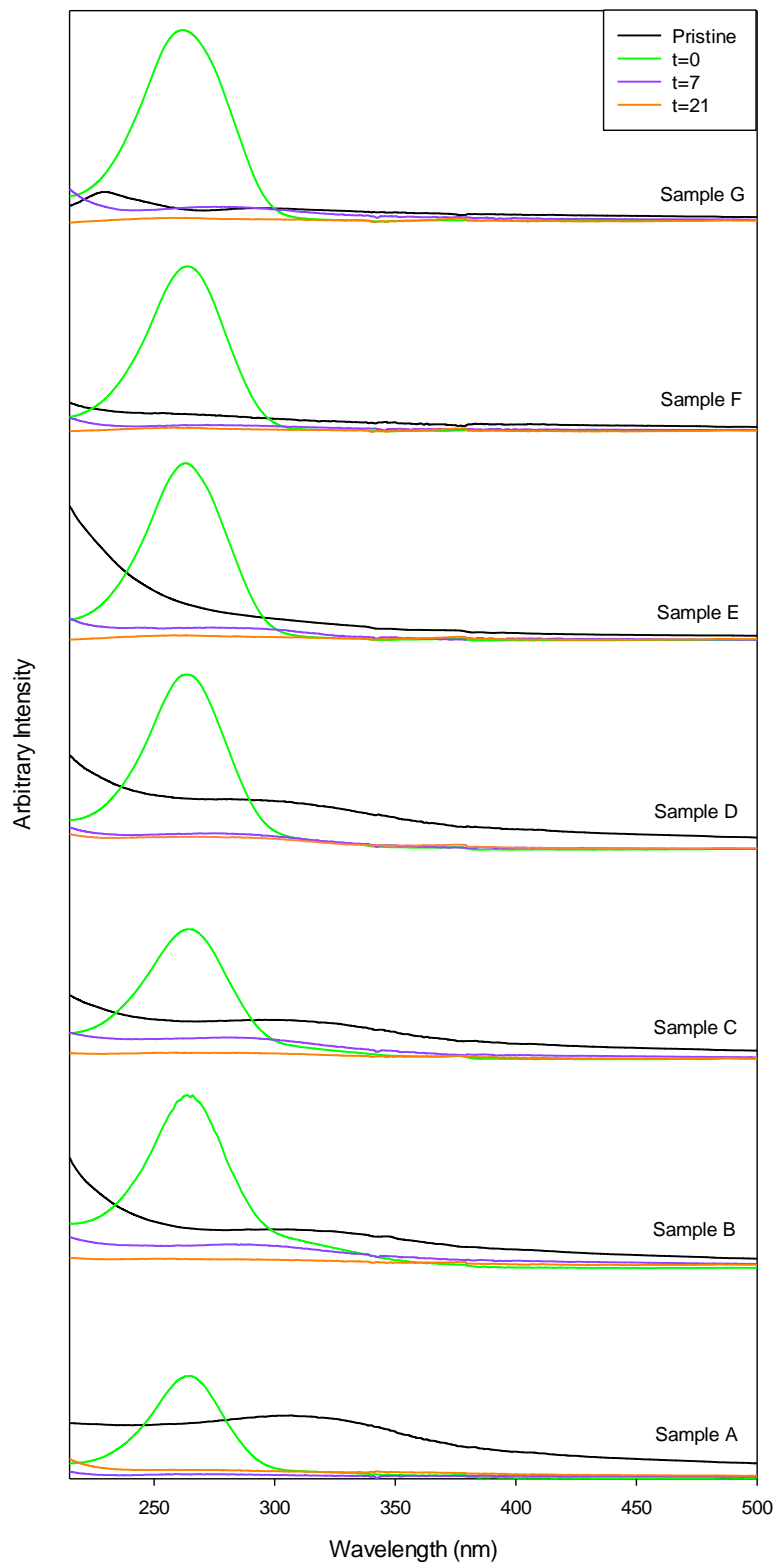


Figure 6.17 UV-VIS spectra for pristine, immediately exposed, 7 and 21 days exposed samples exposed to 1 mM phosphate solution.

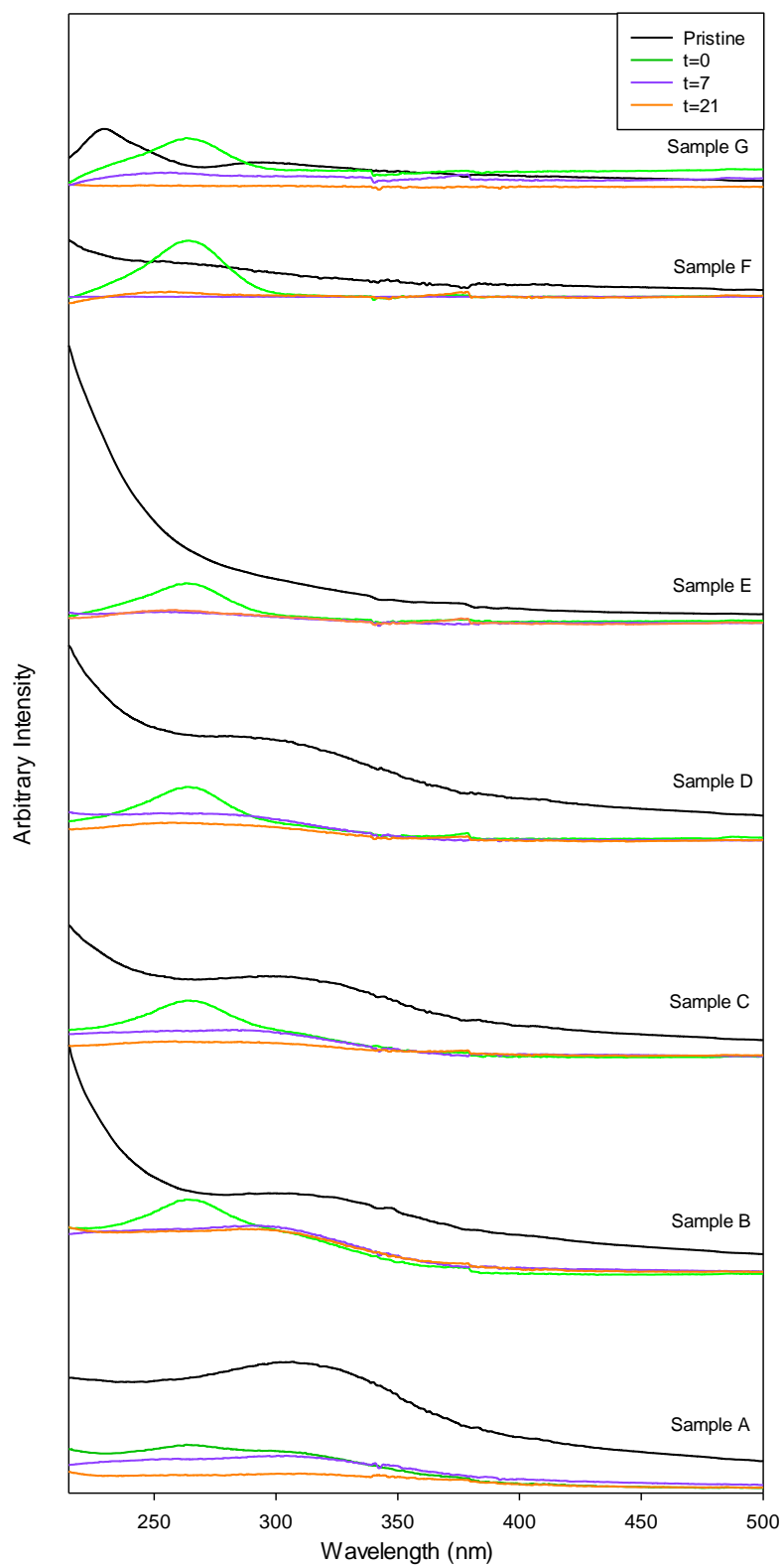


Figure 6.18 UV-VIS spectra for pristine, immediately exposed, 7 and 21 days exposed samples exposed to 5 mM phosphate solution.

6.5.2.2.3 XRD

XRD was carried out to study the sample structures and composition before and after exposure to the phosphate solutions. Figure 6.19 shows spectra for the pristine and 21 day 5 mM phosphate exposed samples. The spectra for the 5 mM samples after 7 days and 1 mM samples after 21 days can be found in Appendix 9.

The spectrum for pristine sample A, cerium dioxide, shows peaks at $2\theta = 28, 47$ and 56° representing Miller indices (111), (220) and (311) respectively (Lawrence et al., 2011b). Sample G, zirconium oxide, at the other end of the sample spectrum was identified as having a monoclinic structure with peaks observed at $2\theta = 28.2, 33.8, 35.1, 50.3$ and 57.7° representing Miller indices (111), (002), (200), (122) and ($2\bar{2}2$) respectively (Joint Committee on Powder Diffraction Standards, 2001). This was expected as zirconium oxide adopts a monoclinic crystal structure at room temperature and changes to tetragonal and cubic structures with elevated temperatures (Stevens, 1986). The drying temperature was not high enough to induce these changes. Pristine samples B-F showed features pertaining to both samples A and G since they are composed of zirconium doped cerium oxide. The features similar to sample A decreased from samples B to F as the concentration of ceria within the sample decreased, whilst those resembling sample G increased as the amount of zirconium within the sample increased.

XRD revealed and confirmed the chemical transformations following exposure to the phosphate solution (right spectra in Figure 6.19). After the 21 days the samples look to be more crystalline than the pristine samples. Samples A-F, all cerium containing samples, all show peaks attributed to cerium phosphate indicating that the transformation is not simply physical as seen by TEM (Section 6.5.1.2.2), but also chemical. The cerium

phosphate monazite peaks are most clearly seen for sample A. These are found at $2\theta = 25, 27, 28, 41$ and 48.5° representing Miller indices (020), (200), (120), (013) and (103) respectively. The cerium phosphate peaks become less obvious from sample A-F. This implies that the transformation varies depending on the cerium dioxide quantity as seen from TEM (Section 6.5.1.2.2) and DLS (Section 6.5.1.2.1). Sample G shows peaks belonging to potassium phosphate, the starting reagent, and zirconium oxide. No transformation is observed for the zirconium oxide. This proves that it is the ceria that is transforming on contact with the phosphate solution and not the zirconium oxide. Furthermore, despite not changing, the zirconium oxide does not appear to inhibit the transformation of the ceria within the doped sample.

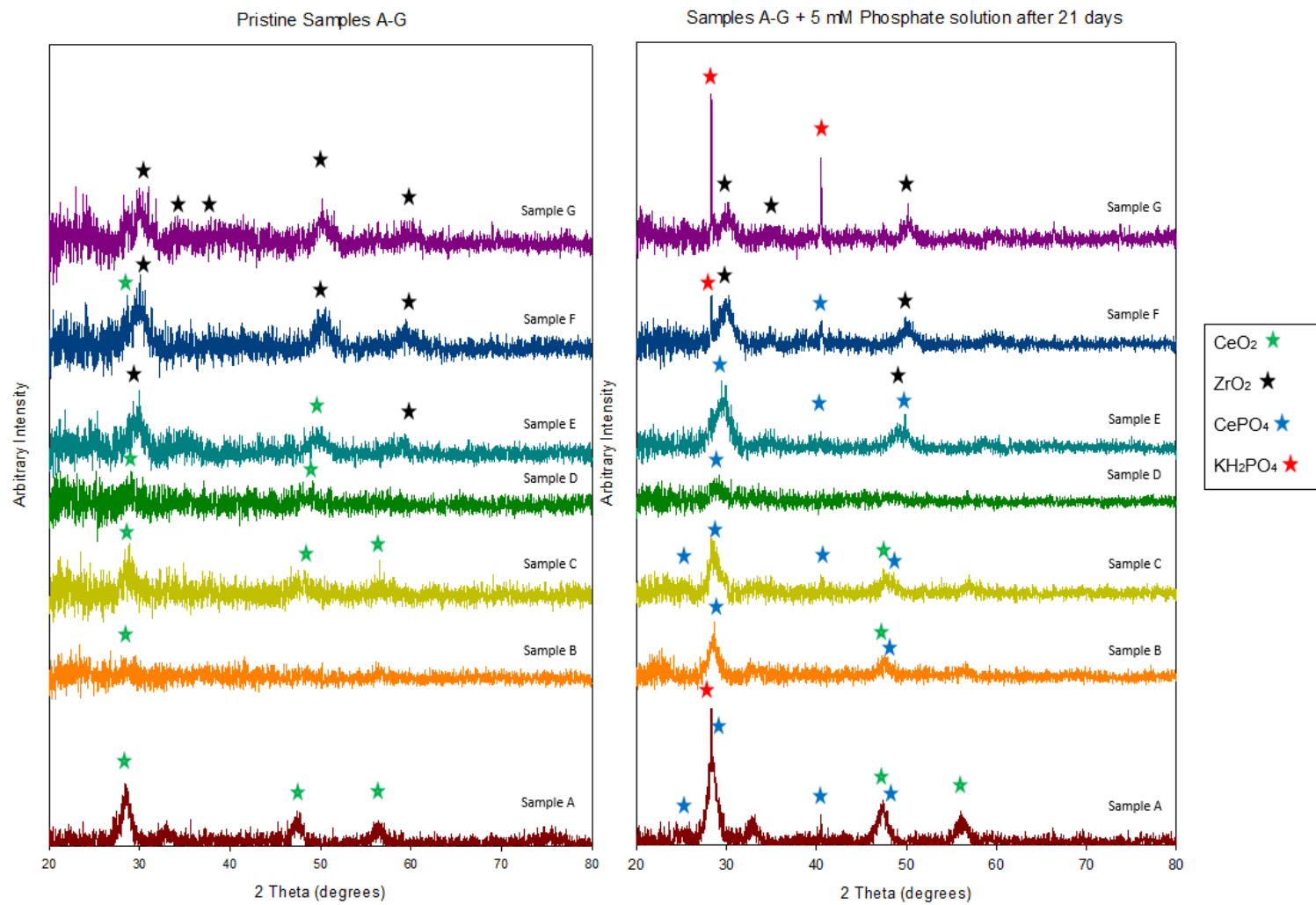


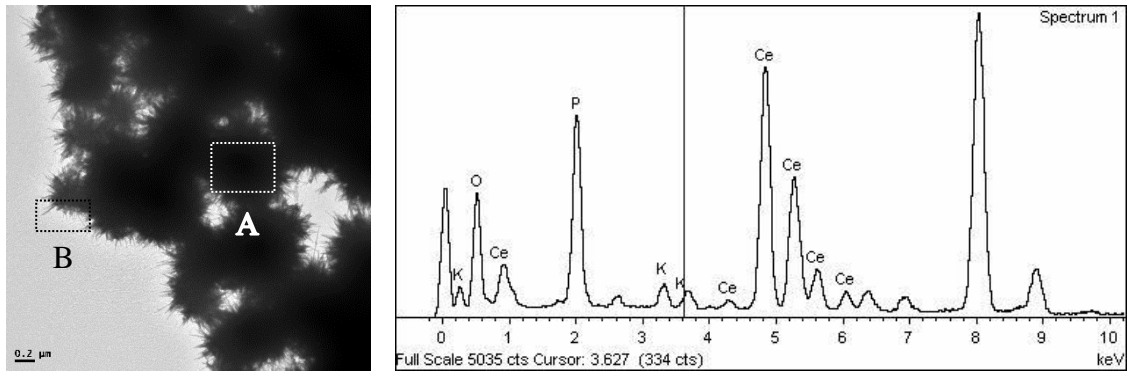
Figure 6.19 XRD patterns for the pristine (left) and 21 day 5 mM phosphate exposed samples A-G (bottom to top).

6.5.2.2.4 EDX

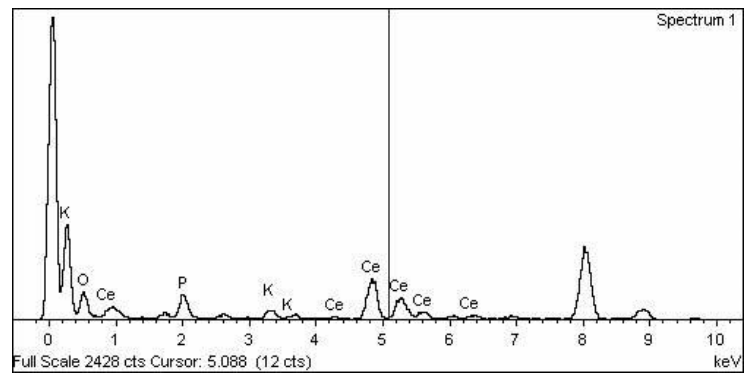
The chemical composition of the samples was determined by EDX. Figures 6.20-6.26 show the TEM images and spectra obtained for samples A-G respectively. The TEM images once again show the physical transformations that occurred. The sea urchin density decreases from sample A to G where G shows no needle-like or sea-urchin structures.

All the spectra show the presence of copper due to the copper grids on which the samples were mounted for analysis. Sample A, as expected, shows no presence of zirconium. EDX picks up potassium, cerium, phosphorus and oxygen. These are most likely due to potassium phosphate, the salt used to make up the phosphate solution, cerium dioxide, possibly due to some unreacted nanoparticles and cerium phosphate due to the chemical transformation taking place whereby phosphate reacts easily with cerium ions to form cerium phosphate. Samples B-F show the presence of all the same components as sample A with the addition of zirconium as the samples were initially composed of zirconium doped ceria. The spectrum for sample G shows no cerium since it is composed of zirconium oxide. EDX identifies potassium, zirconium, phosphorus and oxygen. These are most likely due to the potassium phosphate, the salt used to make up the phosphate solution and zirconium oxide NMs.

The needles and core of the sea-urchin structures do not differ in compositional components as seen from the spectra of samples A and B in Figure 6.20. There is a slight difference in signal intensity with the core having a stronger signal for phosphorus and cerium implying that the chemical transformation results in the formation of cerium phosphate.

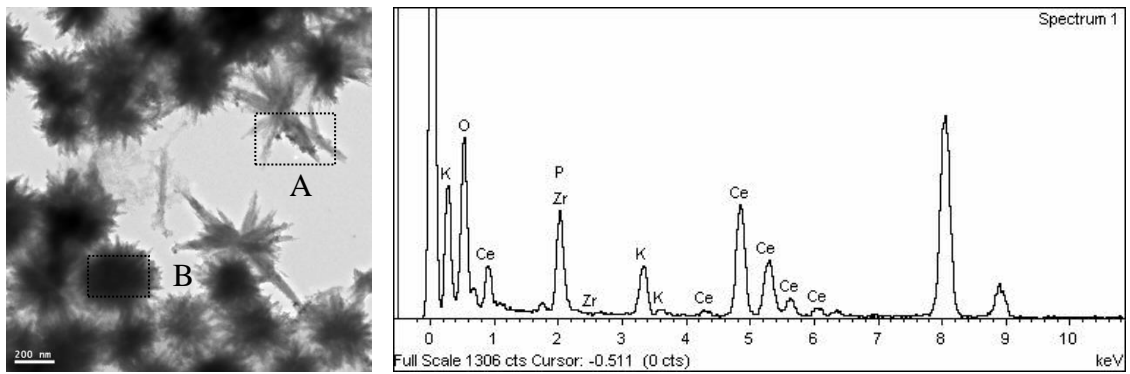


(A)

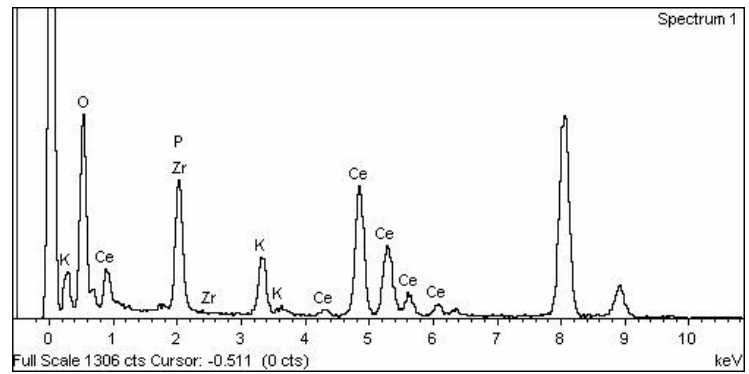


(B)

Figure 6.20 TEM image and EDX spectra of sample B exposed to 5 mM phosphate solution for 21 days where (A) shows the core NM and (B) shows the edge spectrum.



(A)



(B)

Figure 6.21 TEM image and EDX spectra of sample B exposed to 5 mM phosphate solution for 21 days where (A) shows the needles and (B) shows the core NM spectrum.

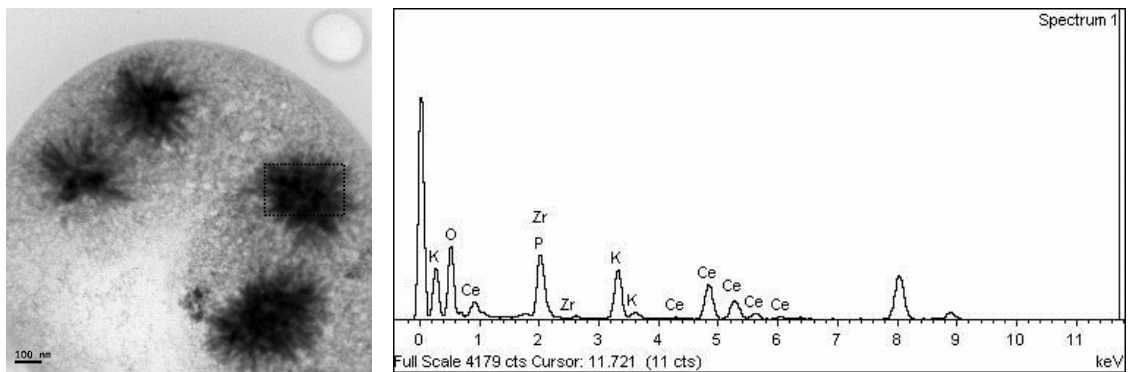


Figure 6.22 TEM image and EDX spectrum of sample C exposed to 5 mM phosphate solution for 21 days.

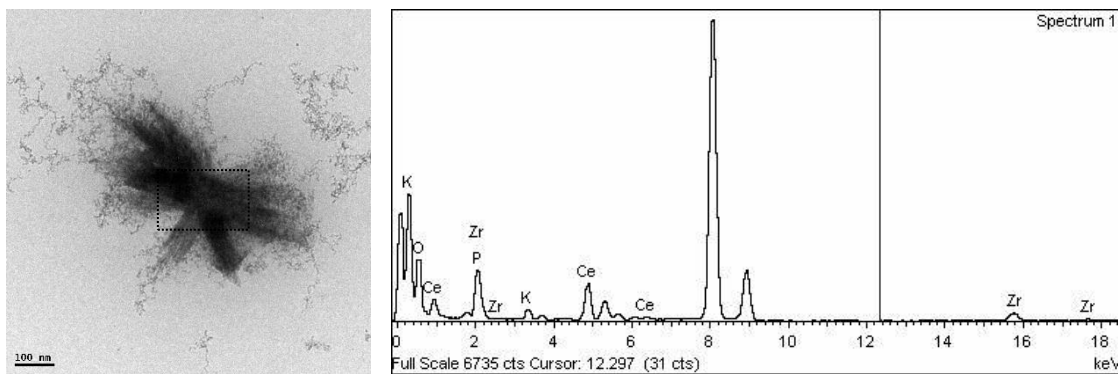


Figure 6.23 TEM image and EDX spectrum of sample D exposed to 5 mM phosphate solution for 21 days.

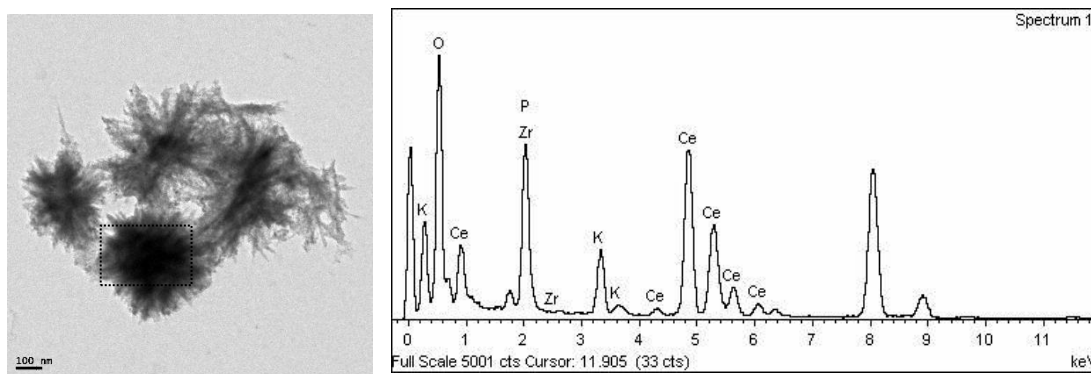


Figure 6.24 TEM image and EDX spectrum of sample E exposed to 5 mM phosphate solution for 21 days.

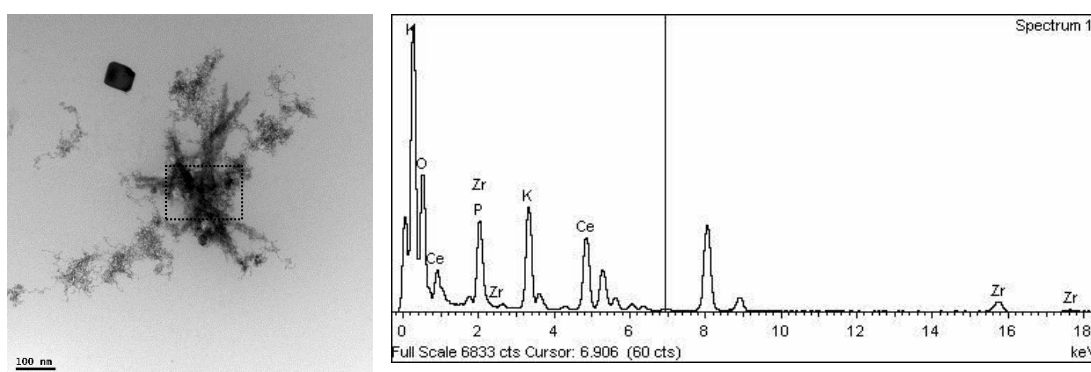


Figure 6.25 TEM image and EDX spectrum of sample F exposed to 5 mM phosphate solution for 21 days.

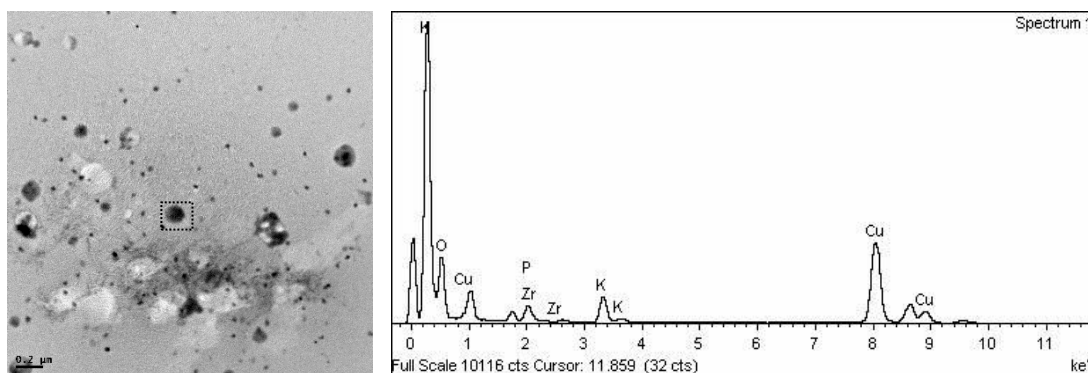


Figure 6.26 TEM image and EDX spectrum of sample G exposed to 5 mM phosphate solution for 21 days.

6.6 Phosphate ageing of ceria nanomaterials using a naturally occurring phospholipid

This section presents and discusses the characterisation results obtained from the exposure of commercial ceria NMs (Sample A) to solutions containing 3 mg/mL or 15 mg/mL L- α -phosphatidylcholine (Section 6.3).

6.6.1 Physical properties

6.6.1.1 Appearance

On addition of the commercial ceria NMs to the phospholipid solution a milky solution forms with a brown coloured precipitate indicating a significant transformation of the pristine particles. After the 96 hour exposure period the precipitate is found to settle. The colour variation, precipitate formation and precipitate settling are more pronounced for the more concentrated sample (15 mg/mL) rather than the less concentrated solution (3 mg/mL).

6.6.1.2 Shape and Size

6.6.1.2.1 Dynamic Light Scattering

The pristine hydrodynamic diameter Z-Average was found to be 172.1 ± 1.705 nm. This is larger than the actual diameter measured by TEM discussed in Section 6.5.1.2.2 below as it represents the hydrodynamic particle size (explained more fully in Section 3.2 in Chapter 3).

The addition of the phospholipid solution to the commercial ceria NMs results in an increase in polydispersity from the original value of 0.272 ± 0.009 . This is shown by the multiplicity of peaks in Figure 6.27 for both concentrations. This indicates that some form of physical transformation is taking place. Furthermore, in the case of the more concentrated sample (15 mg/mL), the PDI value increases to a larger extent than the less concentrated sample (3 mg/mL). The latter has a value of 0.576 ± 0.109 whilst the former a value of 1.000 ± 0.000 , the maximum PDI value possible. This indicates that the phospholipid concentration affects any changes occurring. Additionally, the primary peak of the 15 mg/mL solution is found in the same region as that of the pristine particle. The primary peak of the 3 mg/mL solution is however found at a larger size.

After 96 hours of exposure no size distribution can be seen for the 15 mg/mL sample. This is due to the rapid settling of the sample which does not allow enough time for the instrument to obtain the distribution. The 3 mg/mL solution size distribution after 96 hours resembles that of $t=0$ just shifted to a larger size. This shift is probably due to aggregation which is most likely due to the particle-particle interactions. The size

distribution graphs of these two samples after 96 hours further reveals that the NM behaviour varies depending on the phospholipid concentration.

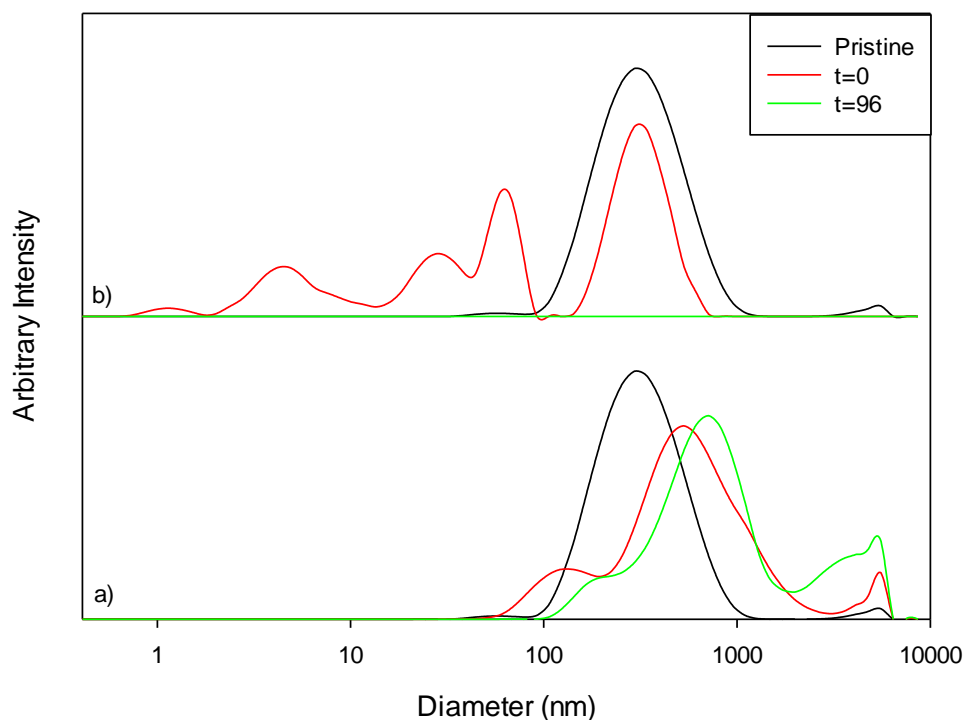


Figure 6.27 DLS size histograms for commercial ceria NMs exposed to a) 3 mg/mL and b) 15 mg/mL phospholipid solution as a function of time.

6.6.1.2.2 Transmission Electron Microscopy

The results obtained from TEM analysis of the pristine ceria NMs and phospholipid exposed NMs are shown in Table 6.8 and Figures 6.28-6.32. It is immediately evident that no needle-like or sea-urchin shaped structures are present implying that cerium phosphate was not formed. This was confirmed by means of XRD discussed in Section 6.5.2.2.1. Despite this the spherical particles are seen to undergo changes in size as a result of phospholipid exposure and as a function of time.

The average size obtained is similar for all the samples except those exposed to the 15 mg/mL solution for 96 hours, where a smaller size is measured. In all cases the average size value is associated with a large standard deviation. This is due to aggregation taking place and reflects the large polydispersity value obtained from DLS (discussed in Section 6.5.1.2.1).

The mode shows the most common size obtained. That for the pristine NMs was 4.097 nm. On exposure to 3 mg/mL of phospholipid this is seen to increase to 6.597 nm and slightly decrease to 6.547 nm after 96 hours. The histograms for the NM size following exposure to the 3 mg/mL solution, Figures 6.38b and 6.39b, reveal the peak shifting to the right representing a larger size as a function of time. This indicates aggregation taking place.

Exposure of the ceria NMs to the 15 mg/mL phospholipid solution resulted in a similar modal trend with an increase in size to 5.719 nm followed by a decrease to 3.192 nm. The histograms for the NM size following exposure to the 15 mg/mL solution, Figures 6.40b and 6.41b, also reveal this trend. The increase in size is due to aggregation whilst the decrease could be due to a chemical change occurring possibly the first step of the transformation as mentioned in XRD below (Section 6.6.2.2.1).

Table 6.8 TEM size values obtained for commercial ceria samples and phospholipid exposed commercial ceria samples.

Sample	Size (nm)	Standard Deviation	Median	Mode
Sample A	15.383	17.126	8.233	4.097
Exposed to 3 mg/mL at t=0	16.569	12.670	12.793	6.597
Exposed to 3 mg/mL at t=96	16.490	10.867	13.511	6.547
Exposed to 15 mg/mL at t=0	16.069	13.272	11.049	5.719
Exposed to 15 mg/mL at t=96	7.358	6.649	4.8875	3.192

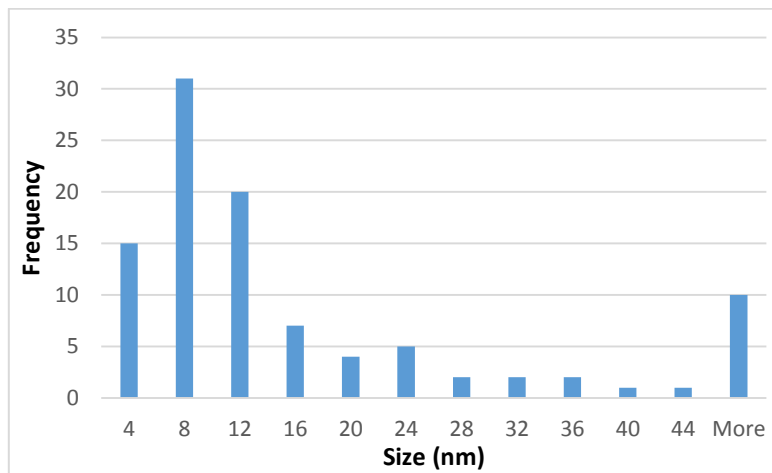
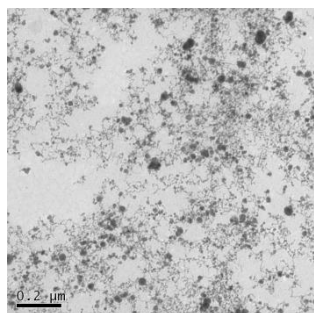


Figure 6.28 a) TEM image and b) Histogram depicting size (nm) versus frequency for Sample A.

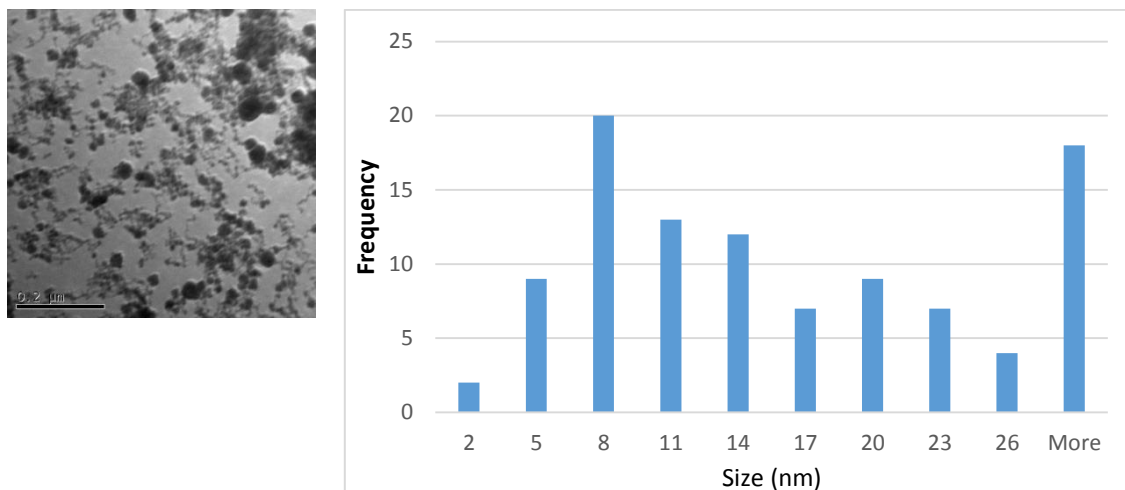


Figure 6.29 a) TEM image and b) Histogram depicting size (nm) versus frequency for NMs exposed to 3 mg/mL phospholipid solution at time 0.

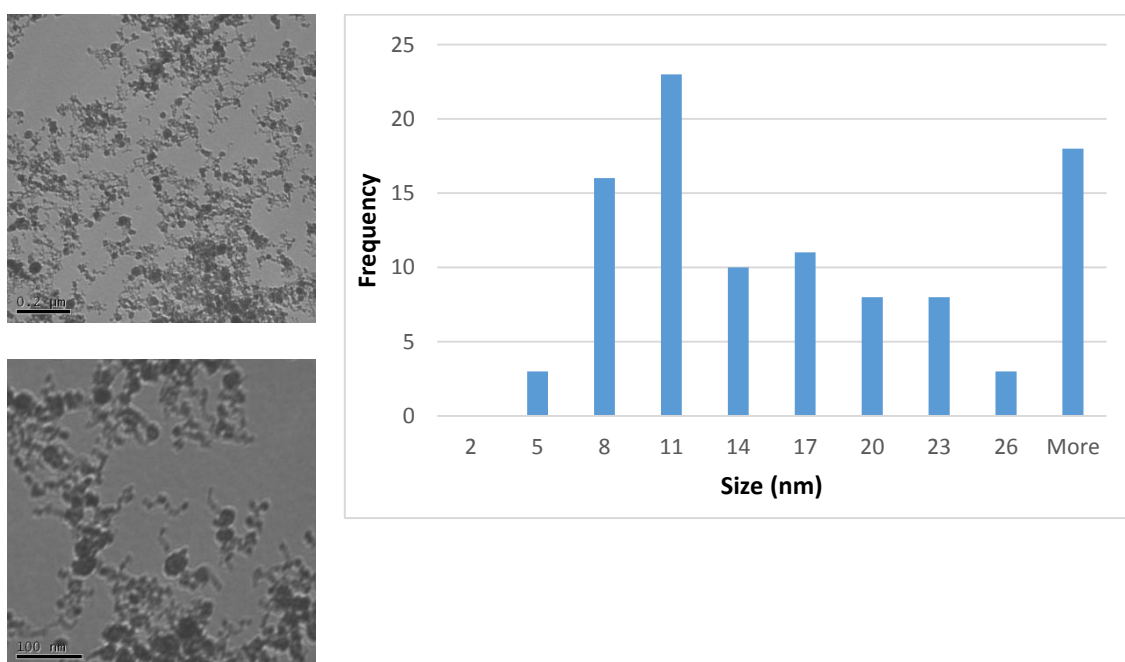


Figure 6.30 a) TEM images and b) Histogram depicting size (nm) versus frequency for NMs exposed to 3 mg/mL phospholipid solution after 96 hours.

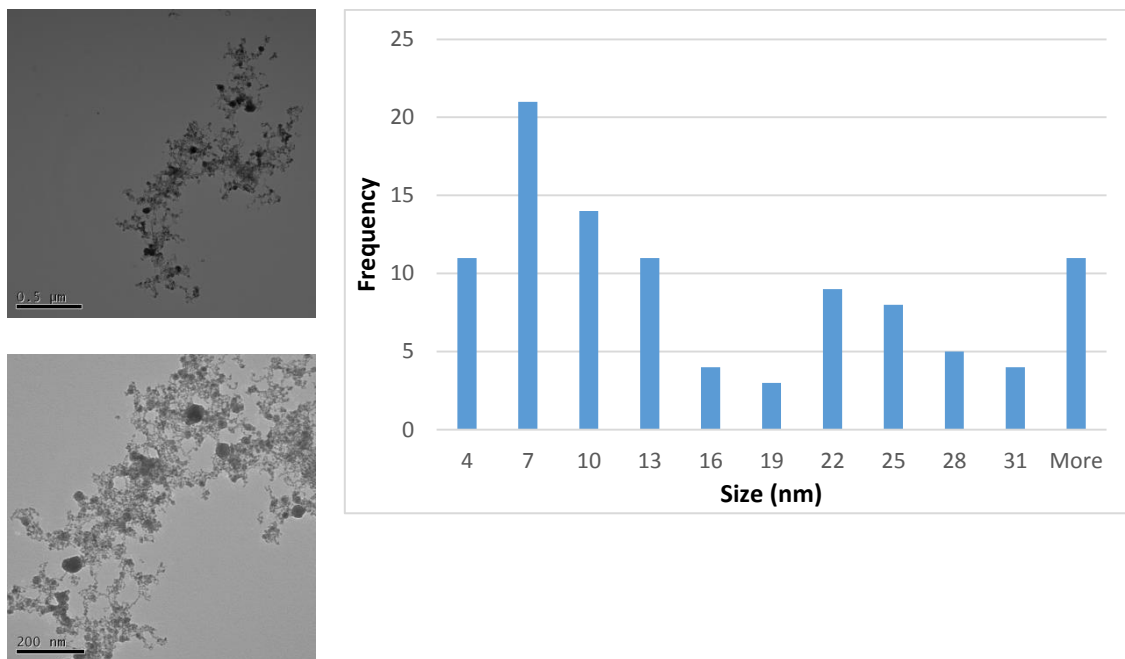


Figure 6.31 a) TEM image and b) Histogram depicting size (nm) versus frequency for NMs exposed to 15 mg/mL phospholipid solution at time 0.

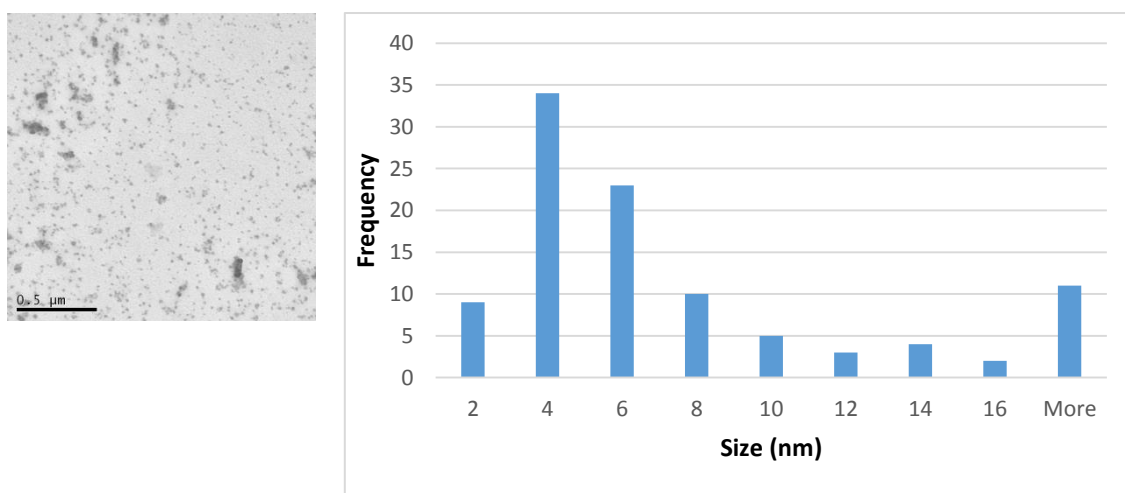


Figure 6.32 a) TEM images and b) Histogram depicting size (nm) versus frequency for NMs exposed to 15 mg/mL phospholipid solution after 96 hours.

6.6.2 Chemical properties

6.6.2.1 Surface Charge

Figure 6.33 depicts the average zeta potential (at pH 5.5) of the ceria NMs exposed to the different concentrations of phospholipid solutions as a function of time. A complete table with all the zeta potential values plotted can be found in Appendix 10. The results show differences based on both concentration and time.

On immediate addition, the NM suspension exposed to the less concentrated phospholipid solution shows a drastic decrease in zeta potential as a result of a different environment. After 96 hours the zeta potential value increases to a stable positive value of 49.8 ± 3.86 mV.

The NMs exposed to the more concentrated phospholipid solution show minimal change on addition of the solution. This is different to the behaviour seen for the NPs exposed to the 3 mg/mL solution and is due to the different ionic strength present within the solutions. However, after 96 hours a drop in average zeta potential to a value near neutral is seen.

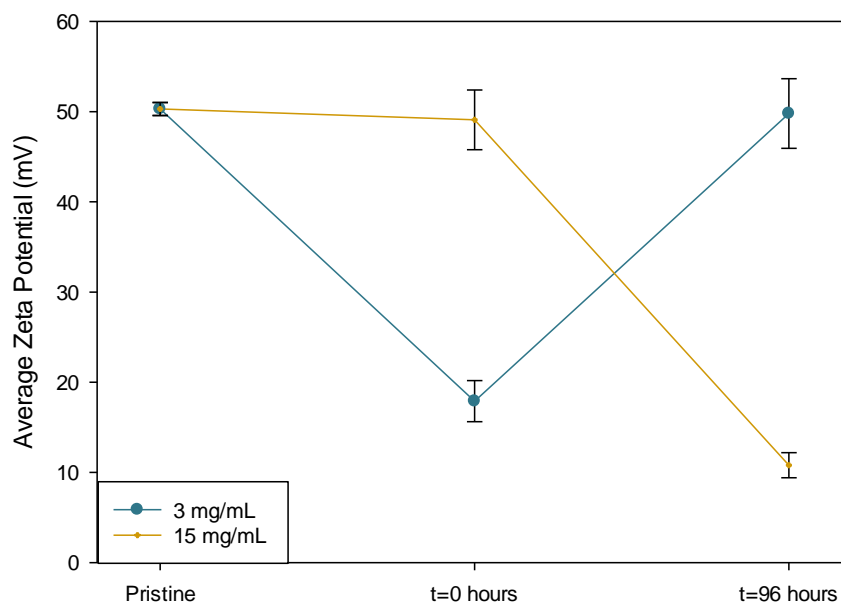


Figure 6.33 Average zeta potential for commercial ceria NMs (Sample A) exposed to 3 mg/mL and 15 mg/mL phospholipid solution as a function of time.

6.6.2.2 Chemical Composition

6.6.2.2.1 XRD

XRD was carried out to study the sample structures and composition before and after exposure to the phospholipid solutions. Figure 6.34 shows spectra for the pristine and the exposed samples. The spectrum for pristine ceria NMs is the same as that of sample A from the series of the zirconium doped ceria NMs. The spectrum is discussed in Section 6.5.2.2.3. It is representative of cerium dioxide and shows peaks at $2\theta = 28, 47$ and 56° representing Miller indices (111), (220) and (311) respectively (Lawrence et al., 2011a). The exposed samples show a similar pattern indicating that no chemical transformation occurred. However, it is possible that these peaks are shadowing those of

Ce_2O_3 which are found at $2\theta = 29$ and 56° representing Miller indices (002) and (112) respectively (Lawrence et al., 2011a). In fact the NMs exposed to the 15 mg/mL solution show a broader and stronger peak just below $2\theta = 30^\circ$ and below $2\theta = 60^\circ$. This could imply that the first step of the transformation, which is the reduction, is in fact beginning to occur.

Unlike the samples exposed to the organic acid and phosphate containing solution, where the XRD spectrum showed a chemical transformation and the presence of cerium phosphate (Figure 6.19) following exposure, no cerium phosphate peaks were observed here. There are three possible reasons for the lack of the presence of cerium phosphate. Firstly the lack of the organic acids present within the phospholipid solution which could have resulted in a slower dissolution and reduction reaction of the ceria nanoparticles taking place. Fatty acid may not be as efficient in dissolution and reduction as citric and ascorbic acid are. Secondly, the exposure duration may have been too short for the transformation to occur. Despite this a longer exposure period would have not been realistically representative of how long bile is in the body before being discarded. A final reason could be that the complexity of the phospholipid molecule did not allow easy access to the phosphate group to allow a reaction for a transformation to take place.

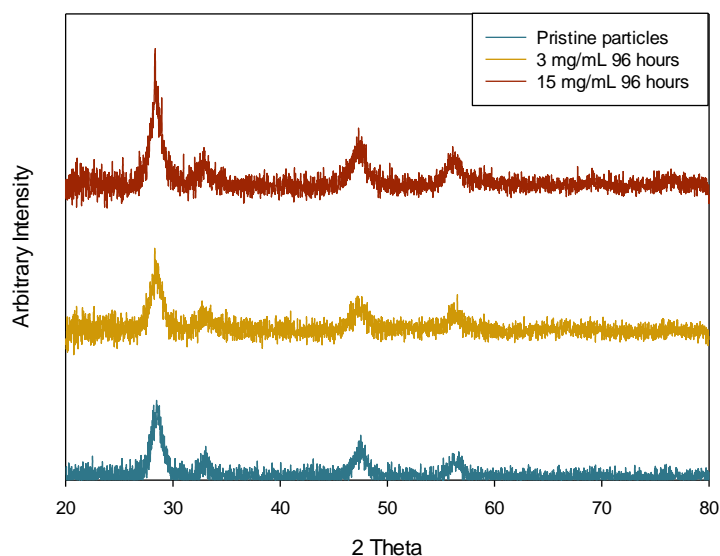


Figure 6.34 XRD patterns of pristine commercial ceria NMs prior to exposure, NMs exposed to 3 mg/mL phospholipid solution for 96 hours and NMs exposed to 15 mg/mL phospholipid solution for 96 hours.

6.7 Understanding the Phosphate Induced Transformations

Ceria and ceria-rich samples underwent chemical and physical transformations when exposed to a mixture containing citric acid, ascorbic acid and monopotassium phosphate. The transformation taking place depicted in Figure 6.35, involved the following four steps:

1. Dissolution of CeO_2 by citric acid.
2. Reduction of Ce^{4+} to Ce^{3+} by ascorbic acid.
3. Reaction of Ce (III) ions with the phosphate present in the media.
4. Formation of needle-shaped Ce(III)-phosphate phase.

5. Clustering of needles around a core and formation of larger sea-urchin like structures.

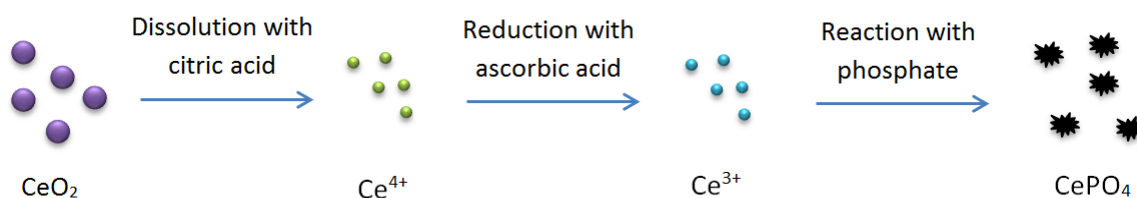


Figure 6.35 Transformation of ceria and ceria-rich nanoparticles in the presence of a mixture of organic acids and phosphate.

The exposure of the ceria NMs to the naturally occurring phospholipid showed no characteristic phosphate ageing transformations. The lack of a reducing phase, timing and/or phosphate could explain why this transformation did not take place.

6.8 Conclusions

6.8.1 Pilot phosphate ageing of 10 K PVP capped ceria NMs

On exposure of the 10 K PVP capped ceria NMs to three different strengths of phosphate solutions major transformations were observed, despite the NMs being capped with PVP; the capping, therefore, does not prevent the transformation from taking place.

As a result of the phosphate exposure, drastic changes in both the Z-Average and PDI values were noted with multiple peaks observed and the samples becoming very polydisperse. The different nanoparticle to phosphate ratio resulted in differing trends yet no generalisation can be drawn from the results due to the extensive aggregation occurring.

TEM revealed the spherical ceria nanoparticles having transformed to needle-like/sea-urchin cerium phosphate characteristic structures. These clearly indicate the transformation occurring. UV-VIS showed a strong peak at 270 nm which is due to ascorbic acid and shadowing that of PVP and cerium (III). The intensity of this peak is similar for the samples from Scenario B (4 parts NP and 1 part phosphate solution) and Scenario C (1 part NM, 1 part phosphate and 3 parts water solution). The peak has a greater intensity for the 1 part NM and 4 part phosphate solution. This confirms that the peak is due to a component of the phosphate solution, namely ascorbic acid, and not the nanoparticles. Furthermore, it is believed that the transformation mechanism involves the organic acids (e.g., citric acids) promoting CeO_2 dissolution and the reducing substances (e.g., ascorbic acids) generating Ce (III) ions. The generation of these ions, that have a high binding affinity to phosphate groups, enable the phase transformation.

6.8.2 Phosphate ageing of zirconium doped ceria

The exposure of zirconium doped ceria NMs to environmentally realistic phosphate solutions resulted in physical and chemical transformations for all ceria-containing samples. These were studied by means of various characterisation techniques.

Ceria and cerium-rich samples showed the Z-Average value decreases on immediate phosphate addition followed by an increase in size. These particles grew into characteristic sea urchin/needle-like structures which were observed by means of TEM. Smaller particles seem to form needles, these needles growing into clusters to form larger sea-urchin like structures having a size of c. 200 nm. These sea-urchin shaped particles gather together.

Ceria and cerium-rich samples also underwent compositional transformation to phosphate-bearing phases. The chemical transformation was monitored and confirmed by means of FT-IR, UV-VIS, XRD and EDX. The stretching peak for P-O can be seen in the spectrum of pure cerium dioxide but is shadowed in the other spectra. Despite this the P=O peak can be seen for all ceria containing samples 1153 cm^{-1} . The UV-VIS spectra show a strong peak at c. 270 nm. This is due to the presence of ascorbic acid which increases in intensity from samples A to G as the amount needed for reducing the ceria decreases as a result of the decrease in ceria concentration from samples A to G.

XRD revealed that samples A-F, all cerium containing samples, all show peaks attributed to cerium phosphate (monazite structure). EDX picked up potassium, cerium, phosphorous and oxygen for sample A. Samples B-F show the presence of all the same components as sample A with the addition of zirconium. The needles and core of the sea-urchin structures do not differ in compositional components. The spectrum for sample G shows no cerium since it is composed of zirconium oxide.

Sample G, the zirconium oxide NMs, showed no transformation to phosphate. This indicates that it is the cerium that is transforming on contact with the phosphate solution and not the zirconium. Despite the presence of the zirconium within the doped samples, transformations, both chemical and physical, still took place as revealed through the characterisation results obtained. Therefore the presence of the dopant, the zirconium, did not prevent the cerium within the sample from reacting with the organic acids and phosphate and transforming.

The transformations were dependent on time, ceria concentration and phosphate to cerium concentration. The degree to which the transformation takes place varied depending on the cerium to zirconium ratio and the phosphate solution concentration. The

greater the cerium content and the phosphate concentration, the more significant and noticeable the transformations were.

The transformation mechanism involved an organic acid (e.g., citric acid) promoting CeO₂ dissolution and a reducing substance (e.g., ascorbic acid) generating Ce (III) ions. The generation of these ions, that have a high binding affinity to phosphate groups, enable the formation of cerium phosphate.

6.8.3 Phosphate ageing of ceria nanomaterials using a naturally occurring phospholipid

The exposure of the ceria NMs to a naturally occurring phospholipid revealed minimal physical and chemical changes. No characteristic phosphate ageing transformations were observed.

Addition of the NMs to the phospholipid solution resulted in a precipitate. TEM showed no needle-like or sea-urchin shaped structures present in the precipitate or suspended particles implying that cerium phosphate was not formed. Despite this the spherical particles are seen to undergo changes in size as a result of phospholipid exposure and as a function of time. DLS showed an increase in both polydispersity and size most likely brought about by aggregation. TEM revealed that the average size obtained is similar for all the samples except those exposed to the 15 mg/mL solution for 96 hours, where a smaller size is measured possibly implying dissolution of the samples. In all cases the average size value is associated with a large standard deviation due to aggregation resulting in polydispersity. Changes were more pronounced for the more concentrated phospholipid solution (15 mg/mL) rather than for the less concentrated one (3 mg/mL).

Time also influences these changes. Surface charge behaviour differed depending on the phospholipid solution concentration. Only slight changes were determined by XRD possibly implying some presence of Ce_2O_3 . No characteristic cerium phosphate peaks were noted indicating that the transformation seen on exposure to phosphate solution was not observed here.

There are three possible reasons for the lack of phosphate induced ageing as seen using the phosphate solution. Firstly the lack of ascorbic acid or equivalent substance resulted in no reduction of the cerium. Secondly the 96 hour exposure duration, though realistically representative of a scenario, may have in fact been too short for the transformation to occur. Finally, the complexity of the phospholipid molecule may have hindered access of the nanoparticles to the phosphate group and thus not allow a reaction for a transformation to take place.

Chapter 7: Conclusions

The first aim was to synthesise a new nanomaterial library and characterise its components by means of a multi-method approach.

This goal was achieved as PVP capped metal oxide nanomaterials, where the core was composed of ceria, zinc oxide or copper oxide, were successfully synthesised, scaled-up and characterised by means of various characterisation techniques. Techniques included DLS, Zeta potential, UV-VIS, TEM, STEM, EELS, EDX, XAS, FT-IR, XPS, ICP-OES. The synthesis was easily adaptable, reliable and repeatable.

TEM and DLS results revealed comparably sized PVP capped metal oxide NMs of c. 5, 7 or 20 nm for 10 K, 40 K and 360 K PVP respectively. STEM showed smaller size values with the 10 K PVP capped metal oxide NM core having a size of c. 3-4 nm. The surface charge of all NM dispersions was found to be close to zero due to steric stabilisation brought about by the PVP capping.

Chemical characterisation confirmed the presence of the metal oxide NMs and determined that, where the metal had more than one stable oxidation state, which is in the case of cerium and copper, the oxide cores were composed of mixed valency states. UV-VIS, EDX and EELS would have not been sufficient enough for valency state analysis and XPS was needed to back up and develop the results interpretation. XPS revealed 10 K and 360 K PVP capped ceria NMs to be mixed with the latter having a greater ratio percentage of Ce (III) and the former a greater ratio percentage of Ce (IV). 40 K PVP capped ceria was shown to be composed of Ce (III) oxide. Furthermore XPS showed all copper oxide samples to contain both Cu (I) and Cu (II), with Cu (II) being the more dominant species

for 10 K and 360 K PVP capped copper oxide and Cu (I) the more dominant for the 40 K PVP capped.

PVP has been found to play a significant role in the synthesis of the NMs as well as being an influencing factor in determining both the NMs' physical properties, including appearance and size, as well as the NMs' chemical properties including surface charge, concentration and oxidation state.

The importance of the library is that it provided the development of a set of particles with systematically varied properties. These allow for hypothesis driven toxicity studies, whereby the effect of a specific property (size, composition) can be assessed whilst other properties remain unchanged. This library is already being used in toxicity studies, e.g. for high throughput screening as part of the NanoMILE project as well as for an algae toxicity study in collaboration with Universidad Autónoma de Madrid.

The second aim was to study any chemical or physical alterations to nanomaterials, particularly the developed PVP capped nanomaterial library, resulting from temperature ageing studies.

The purpose of this part of the project was to study the chemical and physical transformations, induced by the thermal treatment of the library nanomaterials described in Chapter 5. This thermal treatment was implemented as a proxy for ageing of nanomaterials in order to enable prediction of longer term transformations that would be experimentally unfeasible to test.

The transformations were investigated by means of a multi-method characterisation approach. Samples were analysed at various time points by DLS – size and zeta potential

analysis, TEM, UV-VIS and XPS. Results showed that NM behaviour was influenced by both internal factors, including core composition, capping and core interaction and size, and external factors, in this case temperature.

DLS and TEM revealed a general trend involving a decrease in the primary size of the NMs and the development of a second peak at a larger size indicating aggregation as seen also by TEM, as a function of temperature and time. Differences in these changes and rate of changes were revealed amongst the PVP used as a reference, capped and uncapped samples. In the case of the ceria samples as the PVP chain length increases the changes in size at different temperatures look to decrease. The rate of size change varies for the different nanoparticle cores, ceria > copper oxide > zinc oxide, revealing that the core composition also plays a role in influencing the rate of aggregation. Furthermore, it is important to note that the presence of PVP is not restricting aggregation. The commercial ceria (uncapped) sample seemed to have a threshold temperature at 80 °C, beyond which the particles' size and aggregation were significantly affected.

The surface charge of all the capped particles shows very little change as a function of time regardless of the temperature, as indicated by the zeta potential measurements. The PVP samples used for reference showed some slight changes. However, due to the lack of capping, the most significant changes were noted for the commercial ceria (Sample A), particularly at 80 °C.

Chemical analysis, studied by XPS and UV-VIS, confirmed metal core oxidation states. PVP capped zinc oxide showed no changes. Sample A NMs showed minimal changes and the lack of the PVP capping, which acts as a reducing agent, is probably the reason why the particles are not as easily reduced as the PVP capped metal oxide NMs. The PVP capped copper oxide and ceria NMs showed changes in oxidation. For the 10 K

PVP capped copper oxide NMs up until 65 °C both copper (II) and copper (I) species are present yet at 80 °C any Cu (I) present has been completely oxidised to Cu (II). 10 K PVP capped ceria started off in a mixed valency state and at 80 °C the sample is clearly reduced. 40 K PVP capped ceria NMs show that the NM cores become oxidised and exist in a mixed valency state. No spectrum was obtained for the 360 K PVP capped ceria NMs after exposure to 80 °C as no signal was obtained. The elevated temperature could be causing dissolution or faster dissolution of the NMs. The core composition valency state is an important feature that could influence toxicity. Changes in valency state were noted as a function of temperature and time and dependent on the influence of temperature, core chemistry and/or PVP reducing ability on the core.

Furthermore, UV-VIS indicates the probability of dissolution, aggregation and/or transformation of the particles and PVP due to a decrease in peak intensity over the 28 days and the development of a second peak. The rate of change is influenced by temperature and increasing with increasing temperature.

The PVP capping, despite stabilising the NMs, did not isolate them from external factors and therefore the particles underwent physical and chemical changes. Additionally the capping looked to be becoming less effective as a function of time and temperature. This was evidenced by the presence of aggregation observed by DLS and TEM as well as through UV-VIS where the metal peak originally shadowed by the PVP peak becomes noticeable particularly in the case of the ceria NMs.

This study shed light on the complexity of ageing. Furthermore it shows how specific NM behaviour is to NM properties, both physical and chemical, the environment, and the interaction between the two. In this study core composition, capping, capping and core interaction and NM size all influenced the behaviour. Moreover, in spite of the PVP

capping stabilising the NMs, this does not ensure that they are not affected by external factors.

The third aim was to study any chemical or physical alterations to ceria and ceria containing nanomaterials, resulting from phosphate induced ageing.

When released into the environment ceria and ceria containing NMs are able to come in contact with phosphate bearing molecules and media both in the environment and within the human body. The aim here was to study the possible transformations of commercial ceria (Sample A), zirconium doped ceria and laboratory synthesised 10 K PVP capped ceria NMs in the presence of phosphate containing solutions. These samples were chosen in order to compare PVP capped and uncapped ceria NMs and a range of zirconium doped ceria samples with varying compositions of zirconium to cerium ranging from pure cerium (IV) oxide to pure zirconium (IV) oxide. Following various exposure scenarios the NMs' physical and chemical properties were characterised by DLS, zeta potential, UV-VIS, TEM, EDX, XRD and FT-IR.

Phosphate ageing of a series of zirconium doped ceria nanoparticles, ranging from pure ceria to pure zirconium dioxide, was carried out. This was done using a 5 mM pH adjusted solution of potassium phosphate, ascorbic acid and citric acid and resulted in physical and chemical transformations for all ceria-containing samples. Ceria and ceria-rich samples underwent transformation to larger particles growing into characteristic “sea urchin”/needle-like structures. Furthermore these samples underwent compositional transformation to phosphate-bearing phases. The transformation, discussed in detail in Section 6.7, occurred as a result of the reaction of Ce (III) ions, from the dissolution of the

CeO₂ by citric acid followed by the reduction of Ce (IV) to Ce (III) by ascorbic acid, with phosphate groups present within the media. The transformations were dependent on time, ceria concentration and phosphate to ceria ratios. The degree to which the transformation took place varied depending on the cerium to zirconium ratio and the phosphate solution concentration and was proportional to the cerium content and the phosphate concentration. The zirconium oxide particles showed no transformation to phosphate. However, the presence of zirconium within the doped samples did not inhibit these transformations.

10 K PVP capped ceria NMs showed similar transformations as those observed for the zirconium doped ceria NMs. The transformations were once again dependent on time, ceria concentration and phosphate to ceria concentration and most likely occurred in the same way.

Exposure of ceria sample A NMs to a pH adjusted solution of a naturally occurring phospholipid, which was set up in such a way to be as representative of a real-life scenario as possible, revealed minimal physical and chemical changes. Changes involved size and polydispersity increments due to aggregation, as well as surface charge changes due to the altered environment. On exposure of these materials to the phosphate solution no characteristic phosphate ageing transformations were observed. There could be three possible reasons for this. First of these is the lack of a phase to aid the reduction of the ceria. Secondly, the 96 hour exposure duration may be too short for the transformation to occur since XRD spectrum for the NPs exposed to the 15 mg/mL phospholipid solution did in fact show peaks, implying that the first step of the transformation, which is the reduction, was in fact beginning to occur. Finally there is the possibility that the access of the NMs to the phosphate group of the phospholipid molecule was hindered by the bulkiness of the phospholipid molecule.

This study, focusing on synthesis, characterisation and, behavioural and transformation understanding acts as the vital preliminary basis for toxicity studies. This work has shown that NM transformations are complex and dependent on a number of internal and external, physical and chemical NM properties in order to occur. It further highlights the important need for thorough understanding of the exposure of pristine NMs and their behaviour once transformed. It is hoped that the well-characterised NM library samples, temperature aged NMs and transformed NMs will continue to be used for various toxicity studies.

Chapter 8: Future Work

This work has focussed on the synthesis, characterisation and behavioural and transformation understanding of a library of PVP capped metal oxide NMs and commercially available ceria based NMs. This library can act as a preliminary basis for future work. As mentioned in the conclusion these particles have already begun to be used for toxicity studies. Ideally this work continues to develop and the NMs continue to be used for more extensive toxicity studies such as *in vitro* studies and daphnia toxicity work to test the hypothesis that core chemistry is a primary toxicity-controlling factor.

Complimentary to the toxicity work, additional studies can be carried out on the particles of the NM library to further understand their core composition chemistry. It would be useful to acquire the proportion of alternative valency states and detailed information about the bonding environment for all NMs in order to explain on-going and already obtained toxicity results. Proposed XAS Synchrotron work, which is pending, would allow for this.

Additionally the behaviour of the NM library in different scenarios and environments may be looked into. This could include stability and dissolution studies in various media such as those of freshwater or daphnia. Furthermore other ageing studies, such as UV exposure and other transformation studies, can be performed on the NM library samples.

In the case of phosphate ageing, this could be carried out in a more environmentally or biologically realistic scenario. Moreover the exposure of the ceria or ceria containing NMs to the phosphate solution could be extended from 21 days to investigate what would happen over longer periods of time. An attempt could be made to

study the kinetics of the reaction by monitoring the rate of formation of the cerium phosphate by possibly using ICP as a technique.

Another interesting aspect which future research should address is the expansion of the PVP capped metal oxide library. This can be done by trying a range of different starting reagents similar to cerium nitrate, zinc nitrate and copper nitrate in order to determine whether they also produce PVP capped NMs having comparable properties. Moreover attempts can be made to synthesise PVP capped mixed metal oxide core NMs by adapting the initial amount of metal nitrate used for the synthesis when using a combination of metal nitrates. Any new library NMs or doped library NMs, after extensively characterised, should also have their behaviour and toxicity studied.

Appendix 1

Table A.1.1 Average Zeta Potential Values for PVP capped metal oxide nanoparticle and scaled-up nanoparticle dispersions.

Sample	Average Zeta Potential (mV)
10 K PVP reference sample	-1.81 ± 0.20
40 K PVP reference sample	-0.90 ± 0.09
360 K PVP reference sample	-3.63 ± 0.26
10 K PVP capped ceria x1	1.74 ± 0.14
10 K PVP capped ceria x3	0.28 ± 0.29
10 K PVP capped ceria x6	0.43 ± 0.03
40 K PVP capped ceria x1	0.06 ± 0.07
40 K PVP capped ceria x3	-0.64 ± 0.72
40 K PVP capped ceria x6	0.62 ± 0.06
360 K PVP capped ceria x1	0.07 ± 0.16
360 K PVP capped ceria x3	-1.02 ± 0.14
360 K PVP capped ceria x6	-0.52 ± 0.25
10 K PVP capped zinc oxide x1	-0.89 ± 0.22
10 K PVP capped zinc oxide x3	-0.20 ± 0.15
10 K PVP capped zinc oxide x6	0.04 ± 0.007
40 K PVP capped zinc oxide x1	0.05 ± 0.57
40 K PVP capped zinc oxide x3	-0.15 ± 0.16
40 K PVP capped zinc oxide x6	-0.29 ± 0.52

360 K PVP capped zinc oxide x1	-0.08 ± 0.08
360 K PVP capped zinc oxide x3	-0.44 ± 0.14
360 K PVP capped zinc oxide x6	-0.40 ± 0.23
10 K PVP capped copper oxide x1	-0.29 ± 0.27
10 K PVP capped copper oxide x3	0.01 ± 0.13
10 K PVP capped copper oxide x6	0.21 ± 0.02
40 K PVP capped copper oxide x1	-0.16 ± 0.11
40 K PVP capped copper oxide x3	-0.56 ± 0.38
40 K PVP capped copper oxide x6	0.28 ± 0.38
360 K PVP capped copper oxide x1	-0.02 ± 0.15
360 K PVP capped copper oxide x3	-0.87 ± 0.27
360 K PVP capped copper oxide x6	-0.59 ± 0.07

Appendix 2

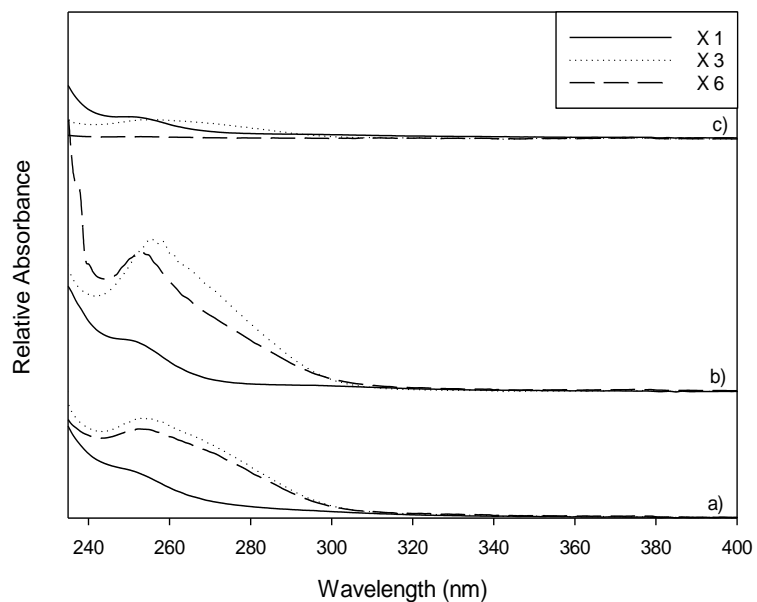


Figure A.2.1. UV-VIS spectra for scaled-up PVP capped ceria as prepared, x3 and x6 for a) 10 K PVP, b) 40 K PVP and c) 360 K PVP

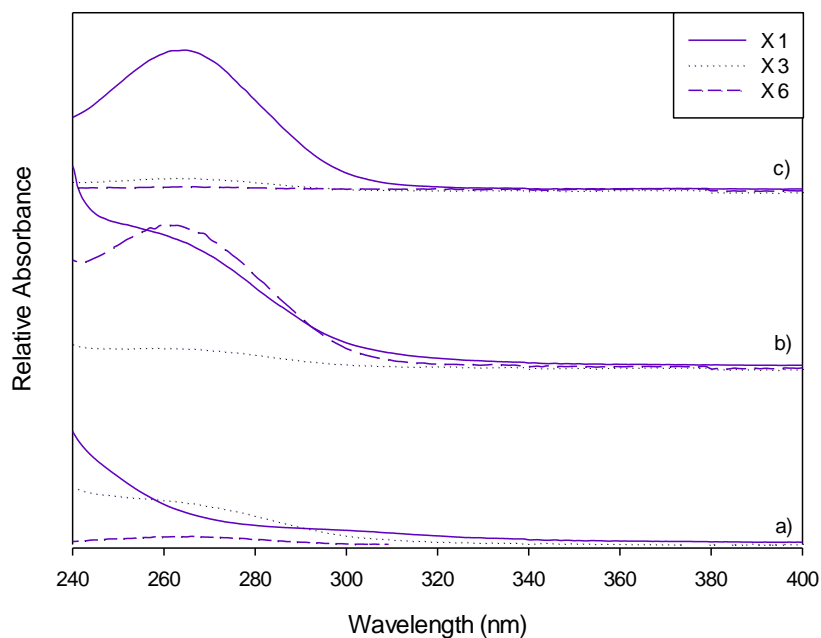


Figure A.2.2. UV-VIS spectra for scaled-up PVP capped zinc oxide as prepared, x3 and x6 for a) 10 K PVP, b) 40 K PVP and c) 360 K PVP

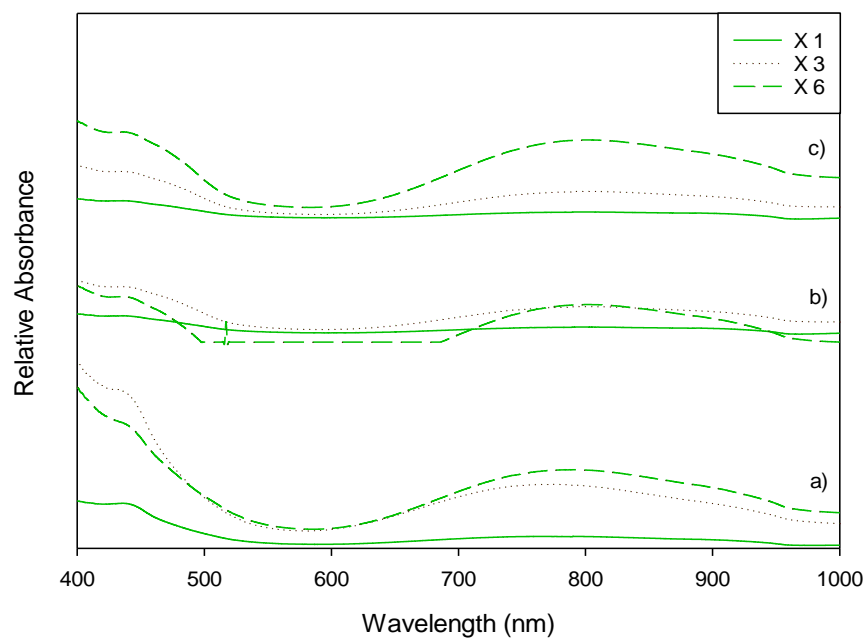


Figure A.2.3. UV-VIS spectra for scaled-up PVP capped copper as prepared, x3 and x6 for a) 10 K PVP, b) 40 K PVP and c) 360 K PVP

Appendix 3

Table A.3.1 ICP-OES Concentration Values obtained for PVP capped metal oxide nanoparticle and scaled-up nanoparticle dispersions

Sample	Reading 1 (mg/L)	Standard deviation 1	Reading 2 (mg/L)	Standard deviation 2	Reading 3 (mg/L)	Standard deviation 3	Average Reading (mg/L)	Standard deviation
Ce 10 x1 1	1.438	0.025	/	/	1.369	0.034	1.404	0.049
Ce 10 x1 2	2.205	0.016	2.050	0.027	2.223	0.032	2.159	0.095
Ce 10 x1 3	2.607	0.019	2.647	0.038	2.329	0.019	2.528	0.173
Ce 10 x3 1	13.160	0.168	9.909	0.019	15.690	0.271	12.920	2.898
Ce 10 x3 2	11.710	0.135	11.540	0.491	11.910	0.134	11.720	0.185
Ce 10 x3 3	9.713	0.105	8.677	0.041	10.090	0.731	9.493	0.732
Ce 10 x6 1	17.430	0.249	18.440	0.030	14.820	0.098	16.897	1.868
Ce 10 x6 2	8.494	0.138	14.900	0.105	15.670	0.035	13.021	3.940
Ce 10 x6 3	18.320	0.256	10.210	0.202	22.400	0.422	16.977	6.205

Ce 40 x1 1	1.342	0.010	1.316	0.015	1.135	0.015	1.264	0.113
Ce 40 x1 2	1.168	0.003	1.687	0.039	1.708	0.013	1.521	0.306
Ce 40 x1 3	2.068	0.014	1.833	0.032	2.102	0.031	2.001	0.146
Ce 40 x3 1	11.750	0.162	7.354	0.064	8.958	0.138	9.354	2.225
Ce 40 x3 2	6.499	0.119	7.119	0.136	6.813	0.121	6.810	0.310
Ce 40 x3 3	10.040	0.120	10.180	0.201	5.233	0.054	8.484	2.817
Ce 40 x6 1	18.380	0.565	19.390	0.013	22.230	0.187	20.000	1.996
Ce 40 x6 2	11.360	0.220	11.620	0.362	10.080	0.210	11.020	0.824
Ce 40 x6 3	26.270	0.288	10.390	0.016	10.330	0.124	15.663	9.186
Ce 360 x1 1	0.215	0.014	0.275	0.005	0.189	0.004	0.226	0.044
Ce 360 x1 2	0.243	0.008	0.273	0.002	0.219	0.002	0.245	0.027
Ce 360 x1 3	0.291	0.006	0.179	0.004	0.241	0.003	0.237	0.056
Ce 360 x3 1	1.494	0.010	4.503	0.065	4.210	0.086	3.402	1.659
Ce 360 x3 2	3.521	0.091	3.409	0.007	3.117	0.040	3.349	0.209

Ce 360 x3 3	3.786	0.127	2.735	0.016	2.441	0.025	2.987	0.707
Ce 360 x6 1	6.593	0.125	/	/	6.344	0.058	6.469	0.176
Ce 360 x6 2	9.598	0.163	4.902	0.152	7.835	0.064	7.445	2.372
Ce 360 x6 3	2.583	0.065	2.341	0.029	1.230	0.009	2.051	0.722
Zn 10 x1 1	1.223	0.011	0.848	0.006	0.841	0.005	0.971	0.014
Zn 10 x1 2	0.813	0.009	0.842	0.001	0.776	0.002	0.810	0.009
Zn 10 x1 3	0.954	0.011	0.864	0.001	0.992	0.005	0.937	0.012
Zn 10 x3 1	3.196	0.276	3.008	0.009	3.075	0.018	3.093	0.277
Zn 10 x3 2	3.314	0.005	2.440	0.004	2.472	0.007	2.742	0.009
Zn 10 x3 3	4.933	0.060	3.331	0.027	3.446	0.022	3.903	0.069
Zn 10 x6 1	7.224	0.078	5.284	0.070	5.186	0.075	5.898	0.128
Zn 10 x6 2	13.060	0.291	9.150	0.145	5.851	0.026	9.354	0.326
Zn 10 x6 3	9.686	0.169	6.868	0.056	3.868	0.015	6.807	0.179
Zn 40 x1 1	0.934	0.003	0.917	0.006	1.019	0.009	0.957	0.011
Zn 40 x1 2	0.773	0.007	0.705	0.002	1.007	0.010	0.828	0.012

Zn 40 x1 3	0.703	0.005	0.904	0.009	0.744	0.001	0.784	0.010
Zn 40 x3 1	1.926	0.017	1.827	0.008	1.769	0.013	1.841	0.023
Zn 40 x3 2	2.485	0.030	4.123	0.019	2.323	0.039	2.977	0.053
Zn 40 x3 3	2.798	0.038	2.256	0.026	2.286	0.012	2.447	0.048
Zn 40 x6 1	5.666	0.092	5.854	0.073	4.346	0.011	5.289	0.118
Zn 40 x6 2	5.360	0.074	10.550	0.238	7.593	0.086	7.834	0.264
Zn 40 x6 3	8.522	0.135	5.783	0.020	5.392	0.011	6.566	0.137
Zn 360 x1 1	0.103	0.002	0.027	0.001	0.109	0.003	0.080	0.004
Zn 360 x1 2	0.159	0.003	0.198	0.001	0.135	0.001	0.164	0.003
Zn 360 x1 3	0.184	0.003	0.140	0.001	0.335	0.002	0.220	0.004
Zn 360 x3 1	0.658	0.001	0.776	0.003	0.423	0.001	0.619	0.004
Zn 360 x3 2	0.408	0.003	0.637	0.000	0.559	0.005	0.535	0.006
Zn 360 x3 3	0.801	0.004	0.707	0.009	0.602	0.008	0.703	0.012
Zn 360 x6 1	1.691	0.014	0.710	0.005	0.536	0.007	0.979	0.017
Zn 360 x6 2	3.684	0.019	2.505	0.026	2.467	0.009	2.885	0.034

Zn 360 x6 3	2.214	0.018	1.060	0.010	1.493	0.011	1.589	0.023
Cu 10 x1 1	1.026	0.020	1.411	0.019	1.328	0.018	1.255	0.203
Cu 10 x1 2	1.282	0.023	1.375	0.027	1.841	0.014	1.499	0.300
Cu 10 x1 3	1.557	0.015	1.538	0.010	1.606	0.027	1.567	0.035
Cu 10 x3 1	5.372	0.032	3.030	0.024	2.997	0.055	3.800	1.362
Cu 10 x3 2	2.411	0.017	4.509	0.034	3.310	0.137	3.410	1.053
Cu 10 x3 3	3.346	0.019	2.361	0.055	2.938	0.039	2.882	0.495
Cu 10 x6 1	5.530	0.023	4.745	0.094	5.135	0.008	5.137	0.393
Cu 10 x6 2	4.374	0.032	3.443	0.065	2.909	0.024	3.575	0.741
Cu 10 x6 3	4.246	0.052	4.241	0.045	3.836	0.176	4.108	0.235
Cu 40 x1 1	0.997	0.006	0.898	0.031	0.859	0.009	0.918	0.071
Cu 40 x1 2	1.064	0.001	0.766	0.014	0.842	0.014	0.891	0.155
Cu 40 x1 3	0.463	0.017	0.488	0.006	0.632	0.026	0.528	0.091
Cu 40 x3 1	1.826	0.040	2.538	0.044	1.675	0.052	2.013	0.461
Cu 40 x3 2	1.820	0.026	1.996	0.003	1.764	0.010	1.860	0.121

Cu 40 x3 3	1.717	0.019	2.081	0.062	1.822	0.027	1.873	0.187
Cu 40 x6 1	7.153	0.151	9.295	0.049	5.643	0.059	7.364	1.835
Cu 40 x6 2	6.571	0.226	4.945	0.079	8.832	0.351	6.783	1.952
Cu 40 x6 3	3.346	0.050	4.683	0.049	5.878	0.126	4.636	1.267
Cu 360 x1 1	0.157	0.001	0.305	0.012	0.226	0.003	0.229	0.074
Cu 360 x1 2	0.198	0.002	0.188	0.005	0.206	0.002	0.197	0.009
Cu 360 x1 3	0.333	0.010	0.236	0.007	0.199	0.002	0.256	0.069
Cu 360 x3 1	0.693	0.009	0.492	0.018	0.764	0.018	0.650	0.141
Cu 360 x3 2	0.039	0.002	0.371	0.003	0.308	0.003	0.239	0.176
Cu 360 x3 3	0.831	0.017	1.181	0.009	0.870	0.006	0.961	0.192
Cu 360 x6 1	2.178	0.030	1.198	0.045	0.656	0.045	1.344	0.771
Cu 360 x6 2	1.587	0.017	1.694	0.012	1.299	0.015	1.527	0.204
Cu 360 x6 3	3.158	0.072	3.802	0.054	2.173	0.018	3.044	0.820

Appendix 4

Figure A.4.1 shows the DLS size distributions obtained for 10 K PVP capped ceria NMs at room temperature for a period of six months.

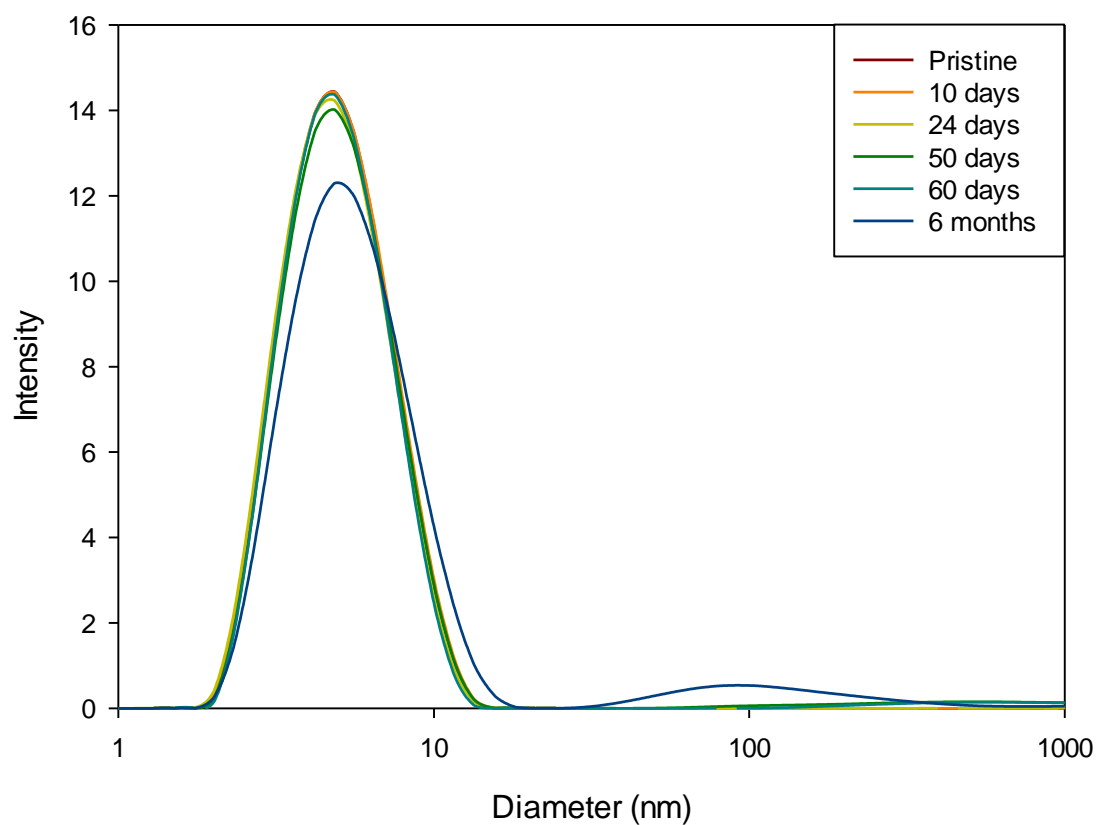


Figure A.4.1 DLS size distribution graphs for 10 K PVP capped ceria NMs at room temperature over 6 months.

Appendix 5

The characterisation data for the commercial ceria NMs (Sample A) were taken from the NanoMILE characterisation deliverable. Tables A.5.1-A.5.4 show the STEM, DLS, zeta potential and UV-VIS results respectively.

Table A.5.1 STEM Characterisation data of commercial ceria NMs.

Parameter	Details
Instrument name	JEOL JEM2100F
Accelerating voltage	200 keV
Substrate for sample support	cumesh400 holey carbon film
Description of sample preparation method	Samples were prepared by partially drying a drop of the particle solution on a cumesh400 holey carbon film (Agar scientific) at room temperature The grid was washed thoroughly with UHP water and re-dried.
Number of particles analysed (≥ 100)	140
Size of sample (nm)	4.7
Standard deviation of sample (nm)	1.4

Figures

(size distribution, images,
diffraction pattern)

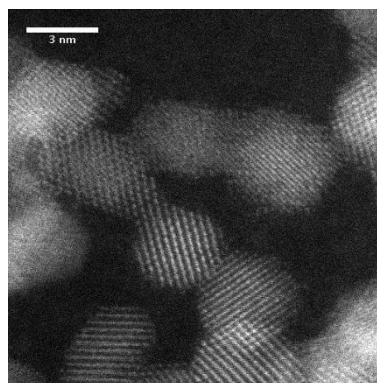
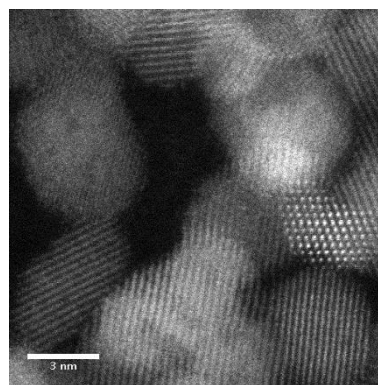
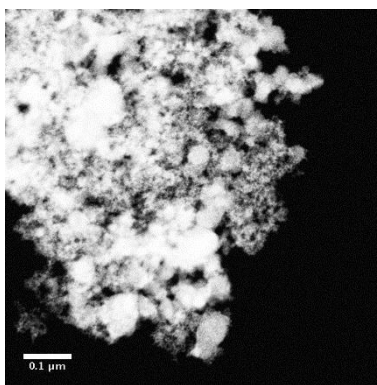
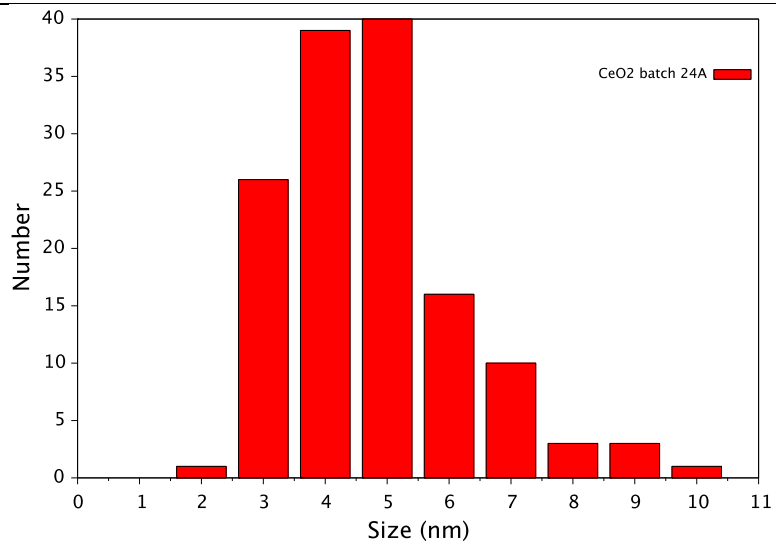


Table A.5.2 DLS Characterisation data of commercial ceria NMs.

Parameter	Details
Instrument Name	Malvern Zetasizer 5000
Cuvette Type	low volume disposable cuvettes (polystyrene) (glass, polystyrene)
Sample volume (mL)	1ml
Scattering angle	173°
Laser wavelength	633 nm
Medium refractive index	0.2
Size (nm)	172.1 ± 1.705
PDI	0.272 ± 0.009
Size distribution graph	

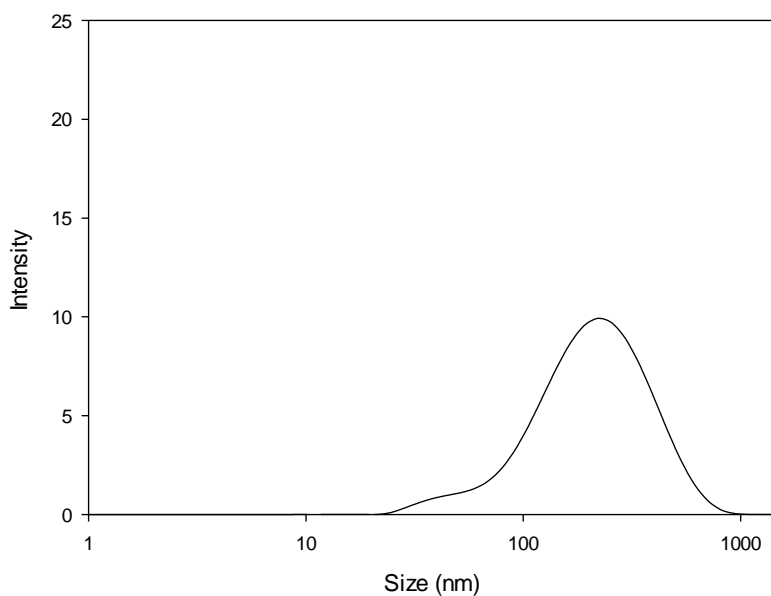


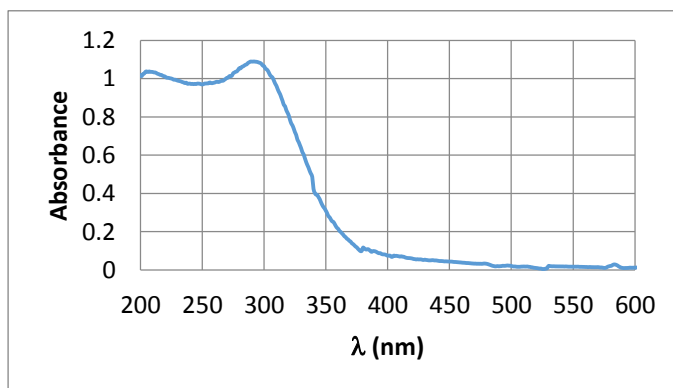
Table A.5.3 Zeta Potential Characterisation data of commercial ceria NMs.

Parameter	Details
Instrument name	Malvern Zetasizer 5000
Cuvette Type	Disposable folded capillary cells
pH of the suspension	7
Voltage selection (<i>automatic, manual</i>)	automatic
Ionic strength of dispersant	Close to zero
Average zeta potential (mV)	50.3 mV \pm 0.719
Average electrophoretic mobility	3.641 \pm 0.05149

Table A.5.4 UV-VIS Characterisation data of commercial ceria NMs.

Parameter	Details
Instrument name	6800 Jenway double beam UV-VIS spectrophotometer
Measurement range	200 – 800nm
Cuvette material	Quartz
Cuvette size	10 cm
Reference sample	water
Sample dispersant	water

Figure



Appendix 6

Table A.6.1 shows the statistical data obtained for the PCC analysis of the size data obtained by means of DLS. 44 data samples were analysed for each sample except the commercial ceria (PROM Ce) not including T=80 °C where 33 samples were analysed.

Table A.6.1 PCC statistical analysis data.

			Intensity	Temperature	Size
REF10	Correlation Co-efficient	Time	-0.320	0.000	0.112
	P Value		0.0342	1.000	0.470
	Correlation Co-efficient	Intensity		-0.516	-0.389
	P Value			0.000333	0.00898
	Correlation Co-efficient	Temperature			0.161
	P Value				0.297
Ce10	Correlation Co-efficient	Time	-0.675	0.000	-0.0617
	P Value		0.00000049	1.000	0.691
	Correlation Co-efficient	Intensity		-0.378	0.434
	P Value			0.0113	0.00322
	Correlation Co-efficient	Temperature			-0.497
	P Value				0.000601
Ce40	Correlation Co-efficient	Time	-0.206	0.000	0.376
	P Value		0.179	1.000	0.0120
	Correlation Co-efficient	Intensity		-0.717	-0.179
	P Value			0.0000000437	0.244

	Correlation Co-efficient	Temperature			0.333
	P Value				0.0270
Ce360	Correlation Co-efficient	Time	-0.282	0.000	0.00355
	P Value		0.0633	1.000	0.982
	Correlation Co-efficient	Intensity		0.405	0.807
	P Value			0.00639	3.796E-011
	Correlation Co-efficient	Temperature			0.550
	P Value				0.000108
Commercial	Correlation Co-efficient	Time	0.240	0.000	0.186
I					
Ce	P Value		0.116	1.000	0.227
Including	Correlation Co-efficient	Intensity		-0.177	0.0576
T=80	P Value			0.252	0.710
	Correlation Co-efficient	Temperature			0.0338
	P Value				0.828
PROM Ce	Correlation Co-efficient	Time	-0.276	0.000	0.529
Not	P Value		0.120	1.000	0.00154
including					
T=80	Correlation Co-efficient	Intensity		0.0765	-0.277
	P Value			0.672	0.119
	Correlation Co-efficient	Temperature			0.267
	P Value				0.134
Zn10	Correlation Co-efficient	Time	-0.301	0.000	-0.0270
	P Value		0.0472	1.000	0.862
	Correlation Co-efficient	Intensity		0.168	-0.361

	P Value		0.277		0.0160
	Correlation Co-efficient	Temperature			-0.761
	P Value				0.00000000204
Cu10	Correlation Co-efficient	Time	-0.355	0.000	-0.197
	P Value		0.0182	1.000	0.200
	Correlation Co-efficient	Intensity		-0.558	0.254
	P Value			0.0000831	0.0964
	Correlation Co-efficient	Temperature			-0.209
	P Value				0.174

Appendix 7

The average zeta potential values of the 10 K PVP capped ceria NMs exposed to different phosphate solutions as a function of time are shown in Table A.7.1.

Table A.7.1 Average zeta potential values of the phosphate exposed 10 K PVP capped ceria NMs.

	Scenario A	Scenario B	Scenario C
	1 part NP and 4 parts phosphate solution (mV)	4 parts NM and 1 part phosphate solution (mV)	1 part NM, 1 part phosphate solution & 3 parts water (mV)
Prior to addition	1.74 ± 0.14	1.74 ± 0.14	1.74 ± 0.14
After addition	-14.2 ± 3.42	1.66 ± 0.182	-1.30 ± 0.0781
After 7 days	-10.8 ± 0.252	3.66 ± 0.524	0.846 ± 0.102
After 21 days	-13.2 ± 0.833	3.61 ± 0.291	1.38 ± 0.0929
After 13 months	-9.81 ± 3.11	1.24 ± 0.101	-7.69 ± 3.49

Appendix 8

The FT-IR spectra for 7 day 5 mM, 7 day 1 mM and 21 day 1 mM phosphate exposed zirconium doped ceria samples (A-G) are shown in Figures A.8.1 and A.8.2.

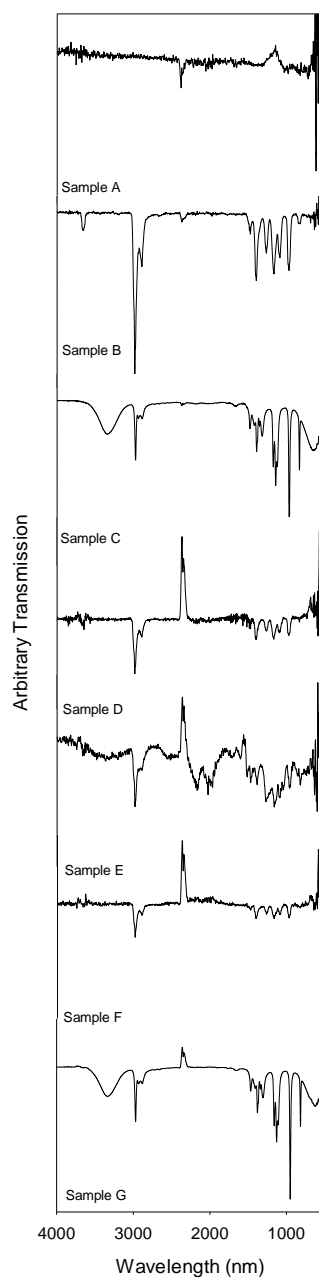


Figure A.8.1 FT-IR spectra for 7 day 5 mM phosphate exposed samples A-G (top to bottom).

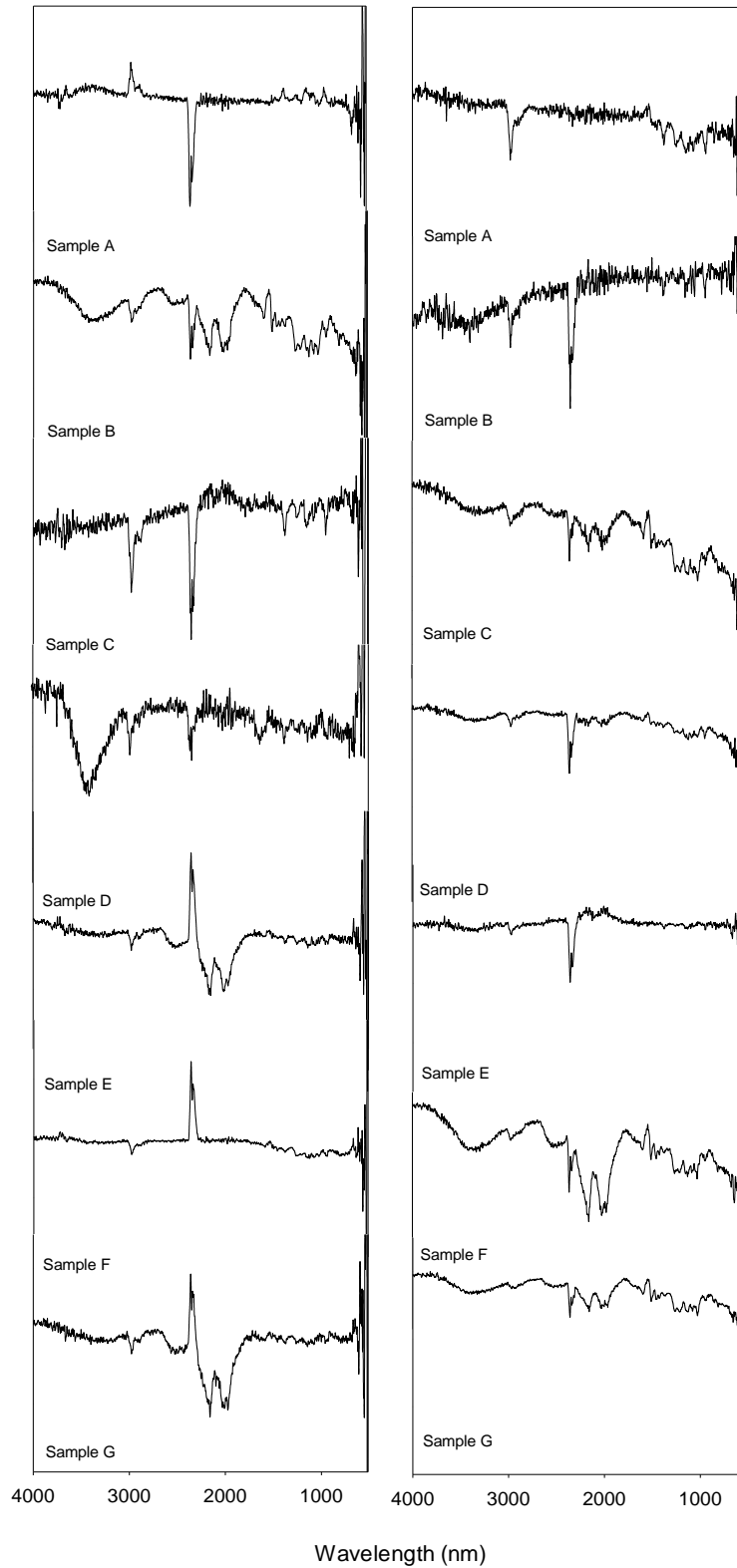


Figure A.8.2 FT-IR spectra for 7 day (left) and 21 day (right) 1 mM phosphate exposed samples A-G (top to bottom).

Appendix 9

The XRD patterns for the 7 day 5 mM and 21 day 1 mM phosphate exposed zirconium doped ceria samples (A-G) are shown in Figures A.8.1 and A.8.2 respectively.

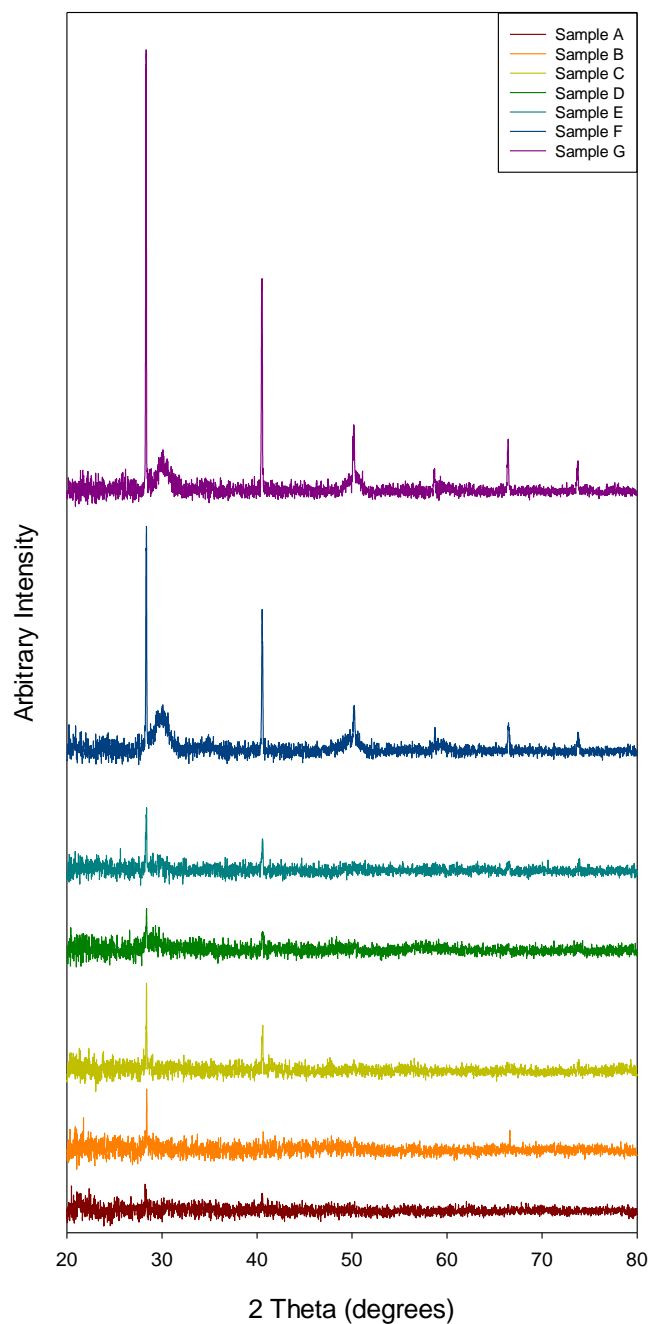


Figure A.9.1 XRD pattern for the 21 day 1 mM phosphate exposed samples A-G (bottom to top).

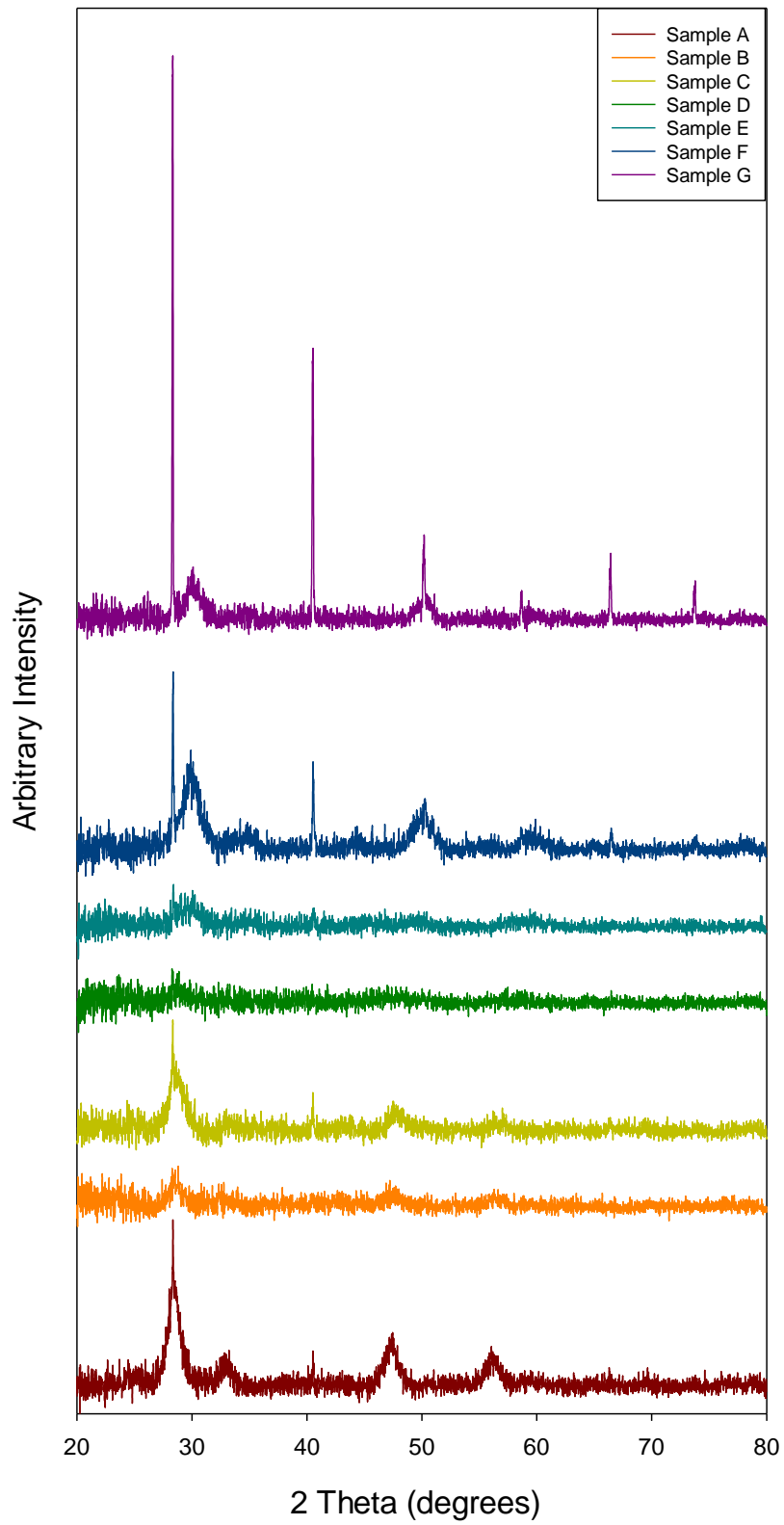


Figure A.9.2 XRD pattern for the 7 day 5 mM phosphate exposed samples A-G (bottom to top).

Appendix 10

The average zeta potential values of the commercial ceria NMs exposed to the different concentrated phospholipid solutions as a function of time are shown in Table A.10.1.

Table A.10.1 Average zeta potential values of the phospholipid exposed commercial ceria NMs.

Sample	Pristine (mV)	t=0 (mV)	t=96 (mV)
3 mg/mL	50.3 ± 0.719	17.9 ± 2.27	49.8 ± 3.86
15 mg/mL	50.3 ± 0.719	49.1 ± 3.31	10.8 ± 1.39

Appendix 11

Journal Publications

S. M. Briffa, I. Lynch, V. Trouillet, M. Bruns, D. Hapiuk, J. Liu, R. E. Palmer and E. Valsami-Jones, “*Development of scalable and versatile nanomaterial libraries for nanosafety studies: Polyvinylpyrrolidone (PVP) Capped Metal Oxide Nanoparticles*”, RSC Advances. 2017. 7. DOI:10.1039/C6RA25064E.

S. M. Briffa, I. Lynch and E. Valsami-Jones, “*Physical and chemical phosphate transformations of Zirconium doped Ceria nanoparticles - A better understanding of engineered nanomaterial possible environmental behaviour*”. In preparation.

I., Romer, **S. M. Briffa**, Y. A. R. Dasilva, , D. Hapiuk, R. E. Palmer and E. Valsami-Jones, “*Impact of phosphate concentration and pH on the phosphate induced biotransformations of different cerium dioxide nanoparticles*”. In preparation.

Oral Presentations

S. M. Briffa, I. Lynch, V. Trouillet, M. Bruns, D. Hapiuk, J. Liu, R. E. Palmer, K. Ignatyev, Z. Shi and E. Valsami-Jones, “*Importance of Multi-method Characterisation Approach in the Development and Behavioural Understanding of nanomaterial libraries for nanosafety studies: Polyvinylpyrrolidone (PVP) capped Metal Oxide Nanoparticles*”,

New Tools and Approaches for Nanomaterial Safety Assessment, Malaga 7-9 February, 2017.

S. M. Briffa, I. Lynch and E. Valsami-Jones, “*Physical & Chemical Phosphate Transformations of Zirconium doped Ceria Nanoparticles*”, 2nd Nanosafety Forum for Young Scientists , Visby, Sweden, September 15-16, 2016.

S. M. Briffa, I. Lynch and E. Valsami-Jones, “*Importance of nanoparticle libraries for toxicity studies – The synthesis and characterisation of a PVP capped metal oxide nanoparticle library*”, Postgraduate Symposium on Nanotechnology, Birmingham, 15 December 2015.

S. M. Briffa, I. Lynch and E. Valsami-Jones, “*Thermal Transformations of Manufactured Nanoparticles (MNPs) as a Proxy for Ageing*”, 10th International Conference on the Environmental Effects of Nanoparticles and Nanomaterials, Vienna, 6-10 September 2015.

S. M. Briffa, I. Lynch, V. Trouillet, M. Bruns, D. Hapiuk, Z. Y. Dang, R. E. Palmer, N. Sano and E. Valsami-Jones, “*Development of nanomaterial libraries for nanosafety studies: PVP capped Metal Oxide Nanoparticles*”, International Congress on Safety of Engineered Nanoparticles and Nanotechnologies (SENN 2015), Helsinki, 12-15 April 2015.

S. M. Briffa, I. Lynch and E. Valsami-Jones, “*Synthesis & Characterisation of Polyvinylpyrrolidone (PVP) Capped Metal Oxide Nanoparticles for Ageing Studies*”, NanoSafety Forum for Young Scientists, Syracuse, 8-9 October 2014.

Poster Presentations

S. M. Briffa, I. Lynch, V. Trouillet, M. Bruns, D. Hapiuk, J. Liu, R. E. Palmer, K. Ignatyev, Z. Shi and E. Valsami-Jones, “*Importance of Multi-method Characterisation Approach in the Development of nanomaterial libraries for nanosafety studies: Polyvinylpyrrolidone (PVP) Capped Metal Oxide Nanoparticles*”, Nanoparticle Characterisation Challenges for the Community, IOP, London, 4 July 2016.

S. M. Briffa, I. Lynch and E. Valsami-Jones, “*Phosphate induced transformations of zirconium doped ceria nanoparticles – A better understanding of engineered nanomaterial environmental behaviour*”, Postgraduate Symposium on Nanotechnology, Birmingham, 15 December 2015.

I. Römer, **S. M. Briffa** and E. Valsami-Jones, “*Transformations of Ceria nanoparticles as a result of phosphate ageing studies*”, 10th International Conference on the Environmental Effects of Nanoparticles and Nanomaterials, Vienna, 6-10 September 2015.

References

- Malvern - Innovative solutions in material characterisation*. [Online]. Available: <http://www.malvern.com/> [Accessed 22 / 04 / 2012].
- ABREU, R. D. & MORAIS, C. A. 2010. Purification of rare earth elements from monazite sulphuric acid leach liquor and the production of high-purity ceric oxide. *Minerals Engineering*, 23, 536-540.
- AGILENT TECHNOLOGIES 2012. Agilent Resolutions pro. 5.2 ed.
- AI, Y., ZHANG, M., JOO, S. W., CHENEY, M. A. & QIAN, S. 2010. Effects of Electroosmotic Flow on Ionic Current Rectification in Conical Nanopores. *The Journal of Physical Chemistry C*, 114, 3883-3890.
- ALAGARSI, A. 2011. *Introduction to Nanomaterials* [Online]. Available: <https://nccr.iitm.ac.in/2011.pdf> [Accessed 23/11/2015].
- ANDERSON, J. & CHRIS, G. V. D. W. 2009. Fundamentals of zinc oxide as a semiconductor. *Reports on Progress in Physics*, 72, 126501.
- ANEGGI, E., BOARO, M., LEITENBURG, C. D., DOLCETTI, G. & TROVARELLI, A. 2006. Insights into the redox properties of ceria-based oxides and their implications in catalysis. *Journal of Alloys and Compounds*, 408–412, 1096-1102.
- ANON 2011. The dose makes the poison. *Nat Nano*, 6, 329-329.
- ANSARI, A. A., ALHOSHAN, M., ALSALHI, M. S. & ALDWAYYAN, A. S. 2010. Prospects of Nanotechnology in Clinical Immunodiagnosics. *Sensors (Basel, Switzerland)*, 10, 6535-6581.

- ANSARI, A. A., SOLANKI, P. R. & MALHOTRA, B. D. 2009. Hydrogen peroxide sensor based on horseradish peroxidase immobilized nanostructured cerium oxide film. *Journal of Biotechnology*, 142, 179-184.
- ANTONIO, M. R. 1992. Structure Determination by Diffraction and Scattering. In: BRUNDLE, C. R., EVANS, C. A., JR. & WILSON, S. (eds.) *Encyclopedia of Materials Characterization - Surfaces, Interfaces, Thin Films*. Elsevier.
- ARORA, S. K., DEVI, A., JASWAL, V. S., SINGH, J., KINGER, M. & GUPTA, V. D. Synthesis and characterization of ZnO nanoparticles. *Oriental Journal of Chemistry*, 30, 1671-1679.
- ASSOCIATION, I. Z. 2011. *Zinc Oxide Properties* [Online]. Available: http://www.zinc.org/info/zinc_oxide_properties [Accessed 30/04/2014].
- ATKINS, P. W. 2006. Atkins' Physical chemistry. In: DE PAULA, J. (ed.) *Physical chemistry*. 8th ed. / Peter Atkins, Julio de Paula. ed. Oxford: Oxford University Press.
- ATTA, A. M., EL-GHAZAWY, R. A., FARAG, R. K. & ELSAEED, S. M. 2011. Synthesis and characterization of pH-sensitive PAMPS/PVP nanogels in aqueous media. *Polymers for Advanced Technologies*, 22, 732-737.
- AUFFAN, M., BERTIN, D., CHAURAND, P. ET AL., 2013. Role of molting on the biodistribution of CeO₂ nanoparticles with *Daphnia pulex*. *Water Research*, 3921-3930.
- AUFFAN, M., PEDEUTOUR, M., ROSE, J., MASION, A., ZIARELLI, F., BORSCHNECK, D., CHANEAC, C., BOTTA, C., CHAURAND, P., LABILLE, J. & BOTTERO, J. Y. 2010. Structural degradation at the surface of a TiO₂-based

- nanomaterial used in cosmetics. *Environmental Science and Technology*, 44, 2689-2694.
- AUFFAN, M., ROSE, J., BOTTERO, J.-Y., LOWRY, G. V., JOLIVET, J.-P. & WIESNER, M. R. 2009. Towards a definition of inorganic nanoparticles from an environmental, health and safety perspective. *Nat Nano*, 4, 634-641.
- AYDIN, A., SIPAHI, H. & CHAREHSAZ, M. 2012. *Nanoparticles Toxicity and Their Routes of Exposures*.
- BAALOUSHA, M., HOW, W., VALSAMI-JONES, E. & LEAD, J. R. 2014. Chapter 1 - Overview of Environmental Nanoscience. *In: JAMIE, R. L. & EUGENIA, V.-J. (eds.) Frontiers of Nanoscience*. Elsevier.
- BAALOUSHA, M., JU-NAM, Y., COLE, P. A., GAISER, B., FERNANDES, T. F., HRILJAC, J. A., JEPSON, M. A., STONE, V., TYLER, C. R. & LEAD, J. R. 2012. Characterization of cerium oxide nanoparticles—Part 1: Size measurements. *Environmental Toxicology and Chemistry*, 31, 983-993.
- BAE, S., HWANG, Y. S., LEE, Y.-J. & LEE, S.-K. 2013. Effects of Water Chemistry on Aggregation and Soil Adsorption of Silver Nanoparticles. *Environ Health Toxicol*, 28, e2013006.
- BAER, D. R., AMONETTE, J. E., ENGELHARD, M. H., KUCHIBHATLA, S., NACHIMUTHU, P., WANG, C. M., NURMI, J. T., SARATHY, V., TRATNYEK, P. G., KARAKOTI, A. & SEAL, S. 2013. Effects of the Environment and Time on Properties of Nanoparticles in Solution.
- BAER, D. R., MUNUSAMY, P., KARAKOTI, A., KUCHIBHATLA, S., SEAL, S. & THEVUTHASAN, S. 2012. Ceria Nanoparticles: Planned and Unplanned preparation and Environmental Impacts on Particle Properties.

- BAKAND, S. & HAYES, A. 2016. Toxicological Considerations, Toxicity Assessment, and Risk Management of Inhaled Nanoparticles. *Int J Mol Sci*, 17.
- BALZANI, V. 2008. Nanoscience and nanotechnology: The bottom-up construction of molecular devices and machines. *Pure and Applied Chemistry*.
- BAMWENDA, G. R. & ARAKAWA, H. 2000. Cerium dioxide as a photocatalyst for water decomposition to O₂ in the presence of Ceaq⁴⁺ and Feaq³⁺ species. *Journal of Molecular Catalysis A: Chemical*, 161, 105-113.
- BARISIK, M., ATALAY, S., BESKOK, A. & QIAN, S. 2014. Size Dependent Surface Charge Properties of Silica Nanoparticles. *The Journal of Physical Chemistry C*, 118, 1836-1842.
- BAUER, M. & BERTAGNOLLI, H. 2012. X-Ray Absorption Spectroscopy – the Method and Its Applications. *Methods in Physical Chemistry*. 1st Edition ed. Weinheim, Germany: Weinheim, Germany: Wiley-VCH Verlag GmbH & Co. KGaA.
- BEHRENS, S. H., CHRISTL, D. I., EMMERZAEL, R., SCHURTENBERGER, P. & BORKOVEC, M. 2000. Charging and Aggregation Properties of Carboxyl Latex Particles: Experiments versus DLVO Theory. *Langmuir*, 16, 2566-2575.
- BENN, T. M. & WESTERHOFF, P. 2008. Nanoparticle silver released into water from commercially available sock fabrics. *Environ Sci Technol*, 42, 4133-9.
- BERGIN, I. L. & WITZMANN, F. A. 2013. Nanoparticle toxicity by the gastrointestinal route: evidence and knowledge gaps. *International journal of biomedical nanoscience and nanotechnology*, 3, 10.1504/IJBNN.2013.054515.
- BERNE, B. J. & PECORA, R. 1976. *Dynamic Light Scattering: With Applications to Chemistry, Biology, and Physics*, Dover Publications.

- BERTRAND, F., GERMAN, S.-A., ANWAR, A., IRUNE, V., GEMMA, B., YOLANDA, R. D. M. & LENNART, B. 2013. Dispersion and surface functionalization of oxide nanoparticles for transparent photocatalytic and. *Science and Technology of Advanced Materials*, 14, 023001.
- BOGNER, A., JOUNEAU, P. H., THOLLET, G., BASSET, D. & GAUTHIER, C. 2007. A history of scanning electron microscopy developments: Towards “wet-STEM” imaging. *Micron*, 38, 390-401.
- BONDARENKO, O., JUGANSON, K., IVASK, A., KASEMETS, K., MORTIMER, M. & KAHRU, A. 2013. Toxicity of Ag, CuO and ZnO nanoparticles to selected environmentally relevant test organisms and mammalian cells in vitro: a critical review. *Archives of Toxicology*, 87, 1181-1200.
- BOSTROM, A. & LÖFSTEDT, R. E. 2010. Nanotechnology Risk Communication Past and Prologue. *Risk Analysis*, 30, 1645-1662.
- BOTTA, C., LABILLE, J., AUFFAN, M., BORSCHNECK, D., MICHE, H., CABIÉ, M., MASION, A., ROSE, J. & BOTTERO, J.-Y. 2011. TiO₂-based nanoparticles released in water from commercialized sunscreens in a life-cycle perspective: Structures and quantities. *Environmental Pollution*, 159, 1543-1550.
- BRAGG, W. H. & BRAGG, W. L. 1913. The Reflection of X-rays by Crystals. *Proceedings of the Royal Society of London A: Mathematical, Physical and Engineering Sciences*, 88, 428-438.
- BRIFFA, S. M., LYNCH, I., TROUILLET, V., BRUNS, M., HAPIUK, D., LIU, J., PALMER, R. E. & VALSAMI-JONES, E. 2017. Development of scalable and versatile nanomaterial libraries for nanosafety studies: polyvinylpyrrolidone (PVP) capped metal oxide nanoparticles. *RSC Advances*, 7, 3894-3906.

- BROOKHAVEN INSTRUMENTS. 2016. *Colloid Stability in Aqueous Suspensions* [Online]. Available: <http://www.brookhaveninstruments.com/literature/library/colloidal-stability-in-aqueous-suspensions> [Accessed 14/04/2016].
- BROWNING, N. D. & PENNYCOOK, S. J. 2000. *Valence band electron energy loss spectroscopy (EELS) of oxide superconductors*, Cambridge, Cambridge: Cambridge University Press.
- BRUCE, P. G., SCROSATI, B. & TARASCON, J.-M. 2008. Nanomaterials for Rechargeable Lithium Batteries. *Angewandte Chemie International Edition*, 47, 2930-2946.
- BRUCHEZ, M., JR., MORONNE, M., GIN, P., WEISS, S. & ALIVISATOS, A. P. 1998. Semiconductor nanocrystals as fluorescent biological labels. *Science*, 281, 2013-6.
- BRUKER. 2016. *EVA Software - The next era in phase analysis* [Online]. Available: <https://www.bruker.com/products/x-ray-diffraction-and-elemental-analysis/x-ray-diffraction/xrd-software/eva/overview.html> [Accessed].
- BRUNDLE, C. R., EVANS, C. A. & WILSON, S. 1992. *Encyclopedia of Materials Characterization: Surfaces, Interfaces, Thin Films*, Butterworth-Heinemann.
- BRYDSON, R. & HONDOW, N. 2011. Electron Energy Loss Spectrometry and Energy Dispersive X-ray Analysis. In: BRYDSON, R. (ed.) *Aberration-Corrected Analytical Electron Microscopy*. Chichester, UK: Chichester, UK: John Wiley & Sons, Ltd.
- BSI, B. S. I. 2011. Nanoparticles vocabulary. . London: PAS 71:2011.
- BULCKE, F., THIEL, K. & DRINGEN, R. 2014. Uptake and toxicity of copper oxide nanoparticles in cultured primary brain astrocytes. *Nanotoxicology*, 8, 775-785.

- BURKE, J. E. 1966. *Progress in Ceramic Science*, Elsevier Science.
- BUZEA, C., PACHECO BLANDINO, I. & ROBBIE, K. 2007. Nanomaterials and nanoparticles: Sources and toxicity. *Biointerphases*, 2, MR17-MR172.
- CAMPBELL, C. T. & PEDEN, C. H. F. 2005. Oxygen Vacancies and Catalysis on Ceria Surfaces. *Science*, 309, 713-714.
- CAYROL, C., SARRAUTE, J., TARROUX, R., REDOULES, D., CHARVERON, M. & GALL, Y. 1999. A mineral sunscreen affords genomic protection against ultraviolet (UV) B and UVA radiation: in vitro and in situ assays. *Br. J. Dermatol.*, 141, 250-258.
- CBNI. 2014. *Centre for BioNano Interactions launches €7 million EU FP7 FutureNanoNeeds Project* [Online]. Available: <http://www.ucd.ie/cbni/newsevents/cbni-in-the-news/name,196987,en.html> [Accessed].
- CERVINI-SILVA, J., FOWLE, D. A. & BANFIELD, J. 2005. Biogenic dissolution of a soil cerium-phosphate mineral. *American Journal of Science*, 305, 711-726.
- CHAE, S.-R., HUNT, D. E., IKUMA, K., YANG, S., CHO, J., GUNSCH, C. K., LIU, J. & WIESNER, M. R. 2014. Aging of fullerene C60 nanoparticle suspensions in the presence of microbes. *Water Research*, 65, 282-289.
- CHAMBERS, C. & HOLLIDAY, A. K. 2013. *Inorganic Chemistry: Butterworths Intermediate Chemistry*, Elsevier Science.
- CHAN, W. C. & NIE, S. 1998. Quantum dot bioconjugates for ultrasensitive nonisotopic detection. *Science*, 281, 2016-8.
- CHAPPLE, M. 2003. *Complete A-Z Physics Handbook*, Hodder Arnold.

- CHAVEZ, J. J. 2011. *X-ray Photoelectron Spectroscopy (XPS)* [Online]. Available: <https://wiki.utep.edu/pages/viewpage.action?pageId=51217144> [Accessed 29/04/2015].
- CHEMIASOFT. 2014. *Inductively Coupled Plasma Optical Emission Spectrometry (ICP-OES)* [Online]. Available: <http://www.chemiasoft.com/chemd/node/52> [Accessed 29/04/2015].
- CHEN, C.-Y. & CHANG, K.-H. 2012. Temperature independent resistive oxygen sensor prepared using zirconia-doped ceria powders. *Sensors and Actuators B: Chemical*, 162, 68-75.
- CHEN, H.-I. & CHANG, H.-Y. 2005. Synthesis of nanocrystalline cerium oxide particles by the precipitation method. *Ceramics International*, 31, 795-802.
- CHEN, K. L. & ELIMELECH, M. 2008. Interaction of fullerene (C₆₀) nanoparticles with humic acid and alginate coated silica surfaces: measurements, mechanisms, and environmental implications. *Environ Sci Technol*, 42, 7607-14.
- CHEN, W., CHEN, J., FENG, Y.-B., HONG, L., CHEN, Q.-Y., WU, L.-F., LIN, X.-H. & XIA, X.-H. 2012. Peroxidase-like activity of water-soluble cupric oxide nanoparticles and its analytical application for detection of hydrogen peroxide and glucose. *Analyst*, 137, 1706-1712.
- CHEN, X., LOU, Y., DAYAL, S., QIU, X., KROLICKI, R., BURDA, C., ZHAO, C. & BECKER, J. 2005. Doped Semiconductor Nanomaterials. *Journal of Nanoscience and Nanotechnology*, 5, 1408-1420.
- CHEN, Y.-C., CHEN, K.-B., LEE, C.-S. & LIN, M. C. 2009. Direct Synthesis of Zr-Doped Ceria Nanotubes. *The Journal of Physical Chemistry C*, 113, 5031-5034.

- CHEN, Z., WESTERHOFF, P. & HERCKES, P. 2008. Quantification of C60 fullerene concentrations in water. *Environmental Toxicology and Chemistry*, 27, 1852-1859.
- CHO, E. C., ZHANG, Q. & XIA, Y. 2011. The effect of sedimentation and diffusion on cellular uptake of gold nanoparticles. *Nat Nano*, 6, 385-391.
- CHRISTIAN, G. D. 2004. *Analytical chemistry / Gary D. Christian*, Hoboken, N.J., Hoboken, N.J. : John Wiley & Sons, Inc.
- CHRISTIAN, P., VON DER KAMMER, F., BAALOUSHA, M. & HOFMANN, T. 2008. Nanoparticles: structure, properties, preparation and behaviour in environmental media. *Ecotoxicology*, 17, 326-343.
- CHUA, S. 2016. *Organic Chemistry – What is Reflux?* [Online]. Available: <http://www.alevelh2chemistry.com/organic-chemistry-what-is-reflux/> [Accessed 01/07/16].
- COLE, P. 2011. *Nanoparticles in aqueous environments : a physicochemical and ecotoxicological study of cerium dioxide / by Paula Cole*. Thesis (PhD.)--University of Birmingham, School of Geography, Earth and Environmental Sciences, College of Life and Environmental Sciences.
- CORY, H., JANET, L., ALEX, P., REDDY, K. M., ISAAC, C., ANDREW, C., KEVIN, F. & DENISE, W. 2008. Preferential killing of cancer cells and activated human T cells using ZnO nanoparticles. *Nanotechnology*, 19, 295103.
- CRAWFORD, S. L. 2006. Correlation and Regression. *Circulation*, 114, 2083-2088.
- CROSS, S. E., INNES, B., ROBERTS, M. S., TSUZUKI, T., ROBERTSON, T. A. & MCCORMICK, P. 2007. Human skin penetration of sunscreen nanoparticles: in-vitro assessment of a novel micronized zinc oxide formulation. *Skin Pharmacol Physiol*, 20, 148-54.

- CUMBERLAND, S. A. & LEAD, J. R. 2009. Particle size distributions of silver nanoparticles at environmentally relevant conditions. *Journal of Chromatography A*, 1216, 9099-9105.
- CUSHEN, M., KERRY, J., MORRIS, M., CRUZ-ROMERO, M. & CUMMINS, E. 2012. Nanotechnologies in the food industry – Recent developments, risks and regulation. *Trends in Food Science & Technology*, 24, 30-46.
- DE MARZI, L., MONACO, A., DE LAPUENTE, J., RAMOS, D., BORRAS, M., DI GIOACCHINO, M., SANTUCCI, S. & POMA, A. 2013. Cytotoxicity and Genotoxicity of Ceria Nanoparticles on Different Cell Lines in Vitro. *International Journal of Molecular Sciences*, 14, 3065-3077.
- DECALUWE, S. C. & UNIVERSITY OF MARYLAND, C. P. M. E. 2009. *Quantifying the Role of Ceria as a Catalyst in Solid Oxide Fuel Cell Anodes*, University of Maryland, College Park.
- DECIEDRO, P. 2011. *What in the World is Laser?* [Online]. Available: <http://filipinofreethinkers.org/2011/05/18/what-in-the-world-is-laser-part-3-of-3/> [Accessed 25/02/2014].
- DEMIR, I., OZDEN, Y. S. & YILMAZ, K. 2004. Accelerated ageing test of aubergine, cucumber and melon seeds in relation to time and temperature variables. *Seed Science and Technology*, 32, 851-855.
- DERJAGUIN, B. & LANDAU, L. 1993. Theory of the stability of strongly charged lyophobic sols and of the adhesion of strongly charged particles in solutions of electrolytes. *Progress in Surface Science*, 43, 30-59.
- DESGRENIERS, S. 1998. High-density phases of ZnO: Structural and compressive parameters. *Physical Review B*, 58, 14102-14105.

- DI MONTE, R., FORNASIERO, P., GRAZIANI, M. & KAŠPAR, J. 1998. Oxygen storage and catalytic NO removal promoted by CeO₂-containing mixed oxides. *Journal of Alloys and Compounds*, 275–277, 877-885.
- DIAMOND LIGHT SOURCE. 2014. *Beamline Schematic* [Online]. Available: <http://www.diamond.ac.uk/Beamlines/Spectroscopy/I18/Specification.html> [Accessed 07/03/2016].
- DJURIČIĆ, B. & PICKERING, S. 1999. Nanostructured cerium oxide: preparation and properties of weakly-agglomerated powders. *Journal of the European Ceramic Society*, 19, 1925-1934.
- DOMÈNECH, B., BASTOS-ARRIETA, J., ALONSO, A., MUÑOZ, M., MURAVIEV, D. N. & MACANÁS, J. 2012. *Bifunctional Polymer-Metal Nanocomposite Ion Exchange Materials*.
- DOMINGOS, R. F., BAALOUSHA, M., JU-NAM, Y., REID, M. M., TUFENKJI, N., LEAD, J., LEPPARD, G. G. & WILKINSON, K. J. 2009. Characterizing Manufactured Nanoparticles in the Environment: Multimethod Determination of Particle Sizes.
- EAG. 2014. *ICP-OES vs ICP-MS: A Comparison* [Online]. Available: <http://www.eag.com/mc/icp-oes-vs-icp-ms.html> [Accessed 29/04/2015].
- EL NAGGAR, A. M. A., GOBARA, H. M. & NASSAR, I. M. 2015. Novel nano-structured for the improvement of photo-catalyzed hydrogen production via water splitting with in-situ nano-carbon formation. *Renewable and Sustainable Energy Reviews*, 41, 1205-1216.
- ELSAESSER, A. & HOWARD, C. V. 2012. Toxicology of nanoparticles. *Advanced Drug Delivery Reviews*, 64, 129-137.

- ENGELHARD, M. H. 2015. *X-ray Photoelectron Spectroscopy XPS* [Online]. Available: http://www.emsl.pnl.gov/emslweb/sites/default/files/engelhard_xps.pdf [Accessed 21/04/2015].
- ENSOL INSTRUMENTS LTD. *Nano Particle Size and Zeta Potential Measurement* [Online]. Available: http://www.iensol.co.kr/product/view.php?product_seq=7 [Accessed 17/06/2015].
- ENVIRONMENTAL PROTECTION AGENCY 2007. *Nanotechnology White Paper*, . Washington DC.
- EPA. 2012. *Phosphorous* [Online]. Available: <http://water.epa.gov/type/rsl/monitoring/vms56.cfm> [Accessed 27/08/2014].
- EUROPEAN COMMISSION. 2011. *Nanotechnology* [Online]. Available: http://ec.europa.eu/nanotechnology/policies_en.html [Accessed 29/10/13].
- EUROPEAN COMMISSION. 2013. *Nanotechnologies: Principles, Applications, Implications and Hands-on Activities* [Online]. Available: https://ec.europa.eu/research/industrial_technologies/pdf/nano-hands-on-activities_en.pdf [Accessed 03/12/2015].
- EUROPEAN COMMISSION. 2015. *Legislation* [Online]. Available: http://ec.europa.eu/growth/sectors/cosmetics/legislation/index_en.htm [Accessed 05/12/2015].
- FAR, A. H. 2014. *Dynamic Light Scattering (DLS)* [Online]. Available: <http://www.slideshare.net/ardalanhayatifar/dynamic-light-scattering-dls> [Accessed 08/01/2016].
- FARAJI, A. H. & WIPF, P. 2009. Nanoparticles in cellular drug delivery. *Bioorganic & Medicinal Chemistry*, 17, 2950-2962.

- FARINA, A., DUMONCEAU, J., LESCUYER, P. 2009. *Expert Rev Proteomics.*, 6, 285-301.
- FARRÉ, M., SANCHÍS, J. & BARCELÓ, D. 2011. Analysis and assessment of the occurrence, the fate and the behavior of nanomaterials in the environment. *TrAC Trends in Analytical Chemistry*, 30, 517-527.
- FAVARO, M., MENDICHI, R., OSSOLA, F., RUSSO, U., SIMON, S., TOMASIN, P. & VIGATO, P. A. 2006. Evaluation of polymers for conservation treatments of outdoor exposed stone monuments. Part I: Photo-oxidative weathering. *Polymer Degradation and Stability*, 91, 3083-3096.
- FEI. 2015. *An Introduction to Electron Microscopy* [Online]. Available: <http://www.fei.com/introduction-to-electron-microscopy/stem/> [Accessed 28/12/2015].
- FELLER, R. L. 1995. *Accelerated Aging: Photochemical and Thermal Aspects*, Getty Conservation Institute.
- FENG, X., CHEN, A., ZHANG, Y., WANG, J., SHAO, L. & WEI, L. 2015. Central nervous system toxicity of metallic nanoparticles. *International Journal of Nanomedicine*, 10, 4321-4340.
- FEYNMAN, R. 1959. *There's plenty of room at the bottom*. [Online]. Available: <http://www.zyvex.com/nanotech/feynman.html> [Accessed 15/11/2013].
- FLEGER, Y. & ROSENBLUH, M. 2009. Surface Plasmons and Surface Enhanced Raman Spectra of Aggregated and Alloyed Gold-Silver Nanoparticles. *Research Letters in Optics*, 2009, 5.
- FOOTHILL COLLEGE. 2014. *Transmission Electron Microscopy* [Online]. Available: <http://fgamedia.org/faculty/rdcormia/NANO53/TEM.htm> [Accessed 15/06/2015].

- FORNASIERO, P., DIMONTE, R., RAO, G. R., KASPAR, J., MERIANI, S., TROVARELLI, A. & GRAZIANI, M. 1995. Rh-Loaded CeO₂-ZrO₂ Solid-Solutions as Highly Efficient Oxygen Exchangers: Dependence of the Reduction Behavior and the Oxygen Storage Capacity on the Structural-Properties. *Journal of Catalysis*, 151, 168-177.
- FRANSMAN, W., BUIST, H., KUIJPERS, E., WALSER, T., MEYER, D., ZONDERVAN-VAN DEN BEUKEN, E., WESTERHOUT, J., KLEIN ENTINK, R. H. & BROUWER, D. H. 2016. Comparative Human Health Impact Assessment of Engineered Nanomaterials in the Framework of Life Cycle Assessment. *Risk Analysis*, n/a-n/a.
- FREDERICKSON, C. J., KOH, J. Y. & BUSH, A. I. 2005. The neurobiology of zinc in health and disease. *Nat Rev Neurosci*, 6, 449-62.
- FU, Q., SALTSBURG, H. & FLYTZANI-STEPHANOPOULOS, M. 2003. Active Nonmetallic Au and Pt Species on Ceria-Based Water-Gas Shift Catalysts. *Science*, 301, 935-938.
- GAISER, B. K., FERNANDES, T. F., JEPSON, M. A., LEAD, J. R., TYLER, C. R., BAALOUSHA, M., BISWAS, A., BRITTON, G. J., COLE, P. A., JOHNSTON, B. D., JU-NAM, Y., ROSENKRANZ, P., SCOWN, T. M. & STONE, V. 2012. Interspecies comparisons on the uptake and toxicity of silver and cerium dioxide nanoparticles. *Environmental Toxicology and Chemistry*, 31, 144-154.
- GALHARDI, C. M., DINIZ, Y. S., RODRIGUES, H. G., FAINE, L. A., BURNEIKO, R. C., RIBAS, B. O. & NOVELLI, E. L. 2005. Beneficial effects of dietary copper supplementation on serum lipids and antioxidant defenses in rats. *Ann Nutr Metab*, 49, 283-8.

- GARVIE, L. A. J. & BUSECK, P. R. 1999. Determination of Ce⁴⁺/Ce³⁺ in electron-beam-damaged CeO₂ by electron energy-loss spectroscopy. *Journal of Physics and Chemistry of Solids*, 60, 1943-1947.
- GATAN CORPORATE. 2016. *Cerium* [Online]. Available: <http://www.eels.info/atlas/cerium> [Accessed 26/07/2016].
- GAUR, A. & SHRIVASTAVA, B. D. 2011. A Comparative Study of the Methods of Speciation Using X-ray Absorption Fine Structure. *Acta Physica Polonica A*, 121, 647-652.
- GEDDES, C. D. 2016. *Reviews in Plasmonics 2015*, Springer International Publishing.
- GLATZEL, P. & JUHIN, A. 2013. X-ray Absorption and Emission Spectroscopy. *Local Structural Characterisation*. John Wiley & Sons, Ltd.
- GOENKA, S., SANT, V. & SANT, S. 2014. Graphene-based nanomaterials for drug delivery and tissue engineering. *Journal of Controlled Release*, 173, 75-88.
- GOODWIN, J. 2004. *Colloids and interfaces with surfactants and polymers; an introduction.*, John Wiley and Sons Ltd.
- GOTTSCHALK, F., LASSEN, C., KJOELHOLT, J., CHRISTENSEN, F. & NOWACK, B. 2015. Modeling Flows and Concentrations of Nine Engineered Nanomaterials in the Danish Environment. *International Journal of Environmental Research and Public Health*, 12, 5581-5602.
- GUO, L., YANG, S., YANG, C., YU, P., WANG, J., GE, W. & WONG, G. K. L. 2000. Synthesis and Characterization of Poly(vinylpyrrolidone)-Modified Zinc Oxide Nanoparticles. *Chemistry of Materials*, 12, 2268-2274.
- GUSEV, A. I. 2011. *Glossary of Nanotechnology and related terms* [Online]. Available: <http://eng.thesaurus.rusnano.com/wiki/article1371> [Accessed 06/05/2014].

- HAMMOND, C. 2015. *The Basics of Crystallography and Diffraction*, Oxford University Press.
- HANDY, R., OWEN, R. & VALSAMI-JONES, E. 2008. The ecotoxicology of nanoparticles and nanomaterials: current status, knowledge gaps, challenges, and future needs. *Ecotoxicology*, 17, 315-325.
- HANNINK, R. H. J. A. A. J. H. 2006. *Nanostructure control of materials*. , Cambridge, England,, Woodhead publishing limited.
- HANSEN, T., CLERMONT, G., ALVES, A., ELOY, R., BROCHHAUSEN, C., BOUTRAND, J. P., GATTI, A. M. & KIRKPATRICK, C. J. 2006. Biological tolerance of different materials in bulk and nanoparticulate form in a rat model: sarcoma development by nanoparticles. *J. R. Soc. Interface*, 3, 767-775.
- HARIFI, T. & MONTAZER, M. 2012. Past, present and future prospects of cotton cross-linking: New insight into nano particles. *Carbohydrate Polymers*, 88, 1125-1140.
- HARRISON, B. S. & ATALA, A. 2007. Carbon nanotube applications for tissue engineering. *Biomaterials*, 28, 344-353.
- HARTRIDGE, A. & BHATTACHARYA, A. K. 2002. Preparation and analysis of zirconia doped ceria nanocrystal dispersions. *Journal of Physics and Chemistry of Solids*, 63, 441-448.
- HASSELLÖV, M. A. R. K. 2009. *Analysis and Characterization of Manufactured Nanoparticles in Aquatic Environments. Environmental and Human Health Impacts of Nanotechnology*, , John Wiley & Sons, Ltd: .
- HECKERT, E. G., KARAKOTI, A. S., SEAL, S. & SELF, W. T. 2008. The role of cerium redox state in the SOD mimetic activity of nanoceria. *Biomaterials*, 29, 2705-9.

- HEINLAAN, M., IVASK, A., BLINOVA, I., DUBOURGUIER, H.-C. & KAHRU, A. 2008. Toxicity of nanosized and bulk ZnO, CuO and TiO₂ to bacteria *Vibrio fischeri* and crustaceans *Daphnia magna* and *Thamnocephalus platyurus*. *Chemosphere*, 71, 1308-1316.
- HELLER, W. & PUGH, T. L. 1960. "Steric" stabilization of colloidal solutions by adsorption of flexible macromolecules. *Journal of Polymer Science*, 47, 203-217.
- HERRLING, T., SEIFERT, M., JUNG, K. 2013. Cerium Dioxide: Future UV-filter in Sunscreen? *SOWF*, 139, 10-15.
- HIRANO, M. & INAGAKI, M. 2000. Preparation of monodispersed cerium() oxide particles by thermal hydrolysis: influence of the presence of urea and Gd doping on their morphology and growth. *Journal of Materials Chemistry*, 10, 473-477.
- HISCHIER, R. & WALSER, T. 2012. Life cycle assessment of engineered nanomaterials: state of the art and strategies to overcome existing gaps. *Science of the Total Environment*, 425, 271-282.
- HOECKE, K. V., QUIK, J. T. K., MANKIEWICZ-BOCZEK, J., SCHAMPHELAERE, K. A. C. D., ELSAESSER, A., MEEREN, P. V. D., BARNES, C., MCKERR, G., HOWARD, C. V., MEENT, D. V. D., RYDZYŃSKI, K., DAWSON, K. A., SALVATI, A., LESNIAK, A., LYNCH, I., SILVERSMIT, G., SAMBER, B. R. D., VINCZE, L. & JANSSEN, C. R. 2009. Fate and Effects of CeO₂ Nanoparticles in Aquatic Ecotoxicity Tests. *Environmental Science & Technology*, 43, 4537-4546.
- HOET, P., BRÜSKE-HOHLFELD, I. & SALATA, O. 2004. Nanoparticles & known and unknown health risks. *Journal of Nanobiotechnology*, 2, 12.

- HONG, R. Y., LI, J. H., CHEN, L. L., LIU, D. Q., LI, H. Z., ZHENG, Y. & DING, J. 2009. Synthesis, surface modification and photocatalytic property of ZnO nanoparticles. *Powder Technology*, 189, 426-432.
- HOPPE, C. E., LAZZARI, M., PARDIÑAS-BLANCO, I. & LÓPEZ-QUINTELA, M. A. 2006. One-Step Synthesis of Gold and Silver Hydrosols Using Poly(N-vinyl-2-pyrrolidone) as a Reducing Agent. *Langmuir*, 22, 7027-7034.
- HOU, W.-C. & JAFVERT, C. T. 2009. Photochemical Transformation of Aqueous C60 Clusters in Sunlight. *Environmental Science & Technology*, 43, 362-367.
- HSIAO, I. L. & HUANG, Y.-J. 2011. Effects of various physicochemical characteristics on the toxicities of ZnO and TiO₂ nanoparticles toward human lung epithelial cells. *Science of the Total Environment*, 409, 1219-1228.
- HU, J., WANG, D., WANG, J. & WANG, J. 2012. Bioaccumulation of Fe₂O₃(magnetic) nanoparticles in *Ceriodaphnia dubia*. *Environmental Pollution*, 162, 216-222.
- HUNTER, R. J. 1981. *Zeta potential in colloid science : principles and applications*, London; New York, Academic Press.
- HUSSAINOVA, I. 06/05/2014. *Fundamentals of nanomaterials* [Online]. Available: https://www.ttu.ee/public/m/Mehaanikateaduskond/Instituudid/Materjalitehnika_instituut/MTX9100/Lecture5_NanomatFundamentals.pdf [Accessed 06/05/2014].
- HUTCHISON, J. 2007. Nanocharacterisation. In: KIRKLAND, A. (ed.). Cambridge: Cambridge : Royal Society of Chemistry.
- IBRAHIM, N. A. 2015. Chapter 12 - Nanomaterials for Antibacterial Textiles. In: KON, M. R. (ed.) *Nanotechnology in Diagnosis, Treatment and Prophylaxis of Infectious Diseases*. Boston: Academic Press.

- INSTITUTE OF PHYSICS. 2015. *Episode 530: X-Ray Diffraction* [Online]. Available: http://tap.iop.org/atoms/xray/530/page_47297.html [Accessed 05/06/2015].
- INTERMOLECULAR FORCES 2014. Intermolecular Forces.
- ISMAIL, H. M. 1991. A thermoanalytic study of metal acetylacetonates. *Journal of analytical and applied pyrolysis*, 21, 315-326.
- ISO 2008. Nanotechnologies - Terminology and definitions for nano-objects - Nanoparticle, nanofibre and nanoplate.
- ISO 2010a. *DD ISO/TS 80004-1:2010 - Nanotechnologies. Vocabulary. Core terms.*
- ISO 2010b. Nanotechnologies—vocabulary—part 1: Core Terms (2010). ISO/TS 80004-1:2010.
- ISPAS, C., ANDREESCU, D., PATEL, A., GOIA, D. V., ANDREESCU, S. & WALLACE, K. N. 2009. Toxicity and Developmental Defects of Different Sizes and Shape Nickel Nanoparticles in Zebrafish. *Environ. Sci. Technol.*, 43, 6349-6356.
- IUPAC. COMPENDIUM OF CHEMICAL TERMINOLOGY, N. E. T. G. B. 1997. Oxford Blackwell Scientific Publications,. Available: <http://goldbook.iupac.org/O04348.html> [Accessed 06/05/2014].
- JING, X., PARK, J. H., PETERS, T. M. & THORNE, P. S. 2015. Toxicity of copper oxide nanoparticles in lung epithelial cells exposed at the air–liquid interface compared with in vivo assessment. *Toxicology in Vitro*, 29, 502-511.
- JOINT COMMITTEE ON POWDER DIFFRACTION STANDARDS 2001. Diffraction Data File no. 37-1484. *International Centre for Diffraction Data*
- JRC. 2010. *Considerations on a Definition of Nanomaterial for Regulatory Purposes* [Online]. Available:

https://ec.europa.eu/jrc/sites/default/files/jrc_reference_report_201007_nanomaterials.pdf [Accessed 03/12/2015].

- JU-NAM, Y. & LEAD, J. R. 2008. Manufactured nanoparticles: An overview of their chemistry, interactions and potential environmental implications. *Science of The Total Environment*, 400, 396-414.
- KALLAY, N. & ZALAC, S. 2002. Stability of nanodispersions: A model for kinetics of aggregation of nanoparticles. *J. Colloid Interface Sci.*, 253, 70-76.
- KARAKOTI, A., SINGH, S., DOWDING, J. M., SEAL, S. & SELF, W. T. 2010. Redox-active radical scavenging nanomaterials. *Chem Soc Rev*, 39, 4422-32.
- KARAKOTI, A. S., MUNUSAMY, P., HOSTETLER, K., KODALI, V., KUCHIBHATLA, S., ORR, G., POUNDS, J. G., TEEGUARDEN, J. G., THRALL, B. D. & BAER, D. R. 2012. Preparation and characterization challenges to understanding environmental and biological impacts of ceria nanoparticles. *Surface and Interface Analysis*, 44, 882-889.
- KARLSSON, H. L., CRONHOLM, P., GUSTAFSSON, J. & MÖLLER, L. 2008. Copper Oxide Nanoparticles Are Highly Toxic: A Comparison between Metal Oxide Nanoparticles and Carbon Nanotubes. *Chemical Research in Toxicology*, 21, 1726-1732.
- KASZUBA, M., MCKNIGHT, D., CONNAH, M., MCNEIL-WATSON, F. & NOBBMANN, U. 2008. Measuring sub nanometre sizes using dynamic light scattering. *An Interdisciplinary Forum for Nanoscale Science and Technology*, 10, 823-829.
- KELLER, A. A., MCFERRAN, S., LAZAREVA, A. & SUH, S. 2013. Global life cycle releases of engineered nanomaterials. *Journal of Nanoparticle Research*, 15, 1692.

- KELLY, K. L., CORONADO, E., ZHAO, L. L. & SCHATZ, G. C. 2002. The Optical Properties of Metal Nanoparticles: The Influence of Size, Shape, and Dielectric Environment. *The Journal of Physical Chemistry B*, 107, 668-677.
- KIM, C. K., KIM, T., CHOI, I. Y., SOH, M., KIM, D., KIM, Y. J., JANG, H., YANG, H. S., KIM, J. Y., PARK, H. K., PARK, S. P., PARK, S., YU, T., YOON, B. W., LEE, S. H. & HYEON, T. 2012. Ceria nanoparticles that can protect against ischemic stroke. *Angew Chem Int Ed Engl*, 51, 11039-43.
- KIM, K. T., KLAINE, S. J., CHO, J., KIM, S.-H. & KIM, S. D. 2010. Oxidative stress responses of *Daphnia magna* exposed to TiO₂ nanoparticles according to size fraction. *Science of The Total Environment*, 408, 2268-2272.
- KING, R. C., MOULDER, J. F. & CHASTAIN, J. 1995. *Handbook of x-ray photoelectron spectroscopy : a reference book of standard spectra for identification and interpretation of XPS data*, Eden Prairie, Minn., Physical Electronics.
- KLINGSHIRN, C. 2007a. ZnO: From basics towards applications. *physica status solidi (b)*, 244, 3027-3073.
- KLINGSHIRN, C. 2007b. ZnO: Material, Physics and Applications. *ChemPhysChem*, 8, 782-803.
- KNAAPEN, A. M., BORM, P. J. A., ALBRECHT, C. & SCHINS, R. P. F. 2004. Inhaled particles and lung cancer. Part A: Mechanisms. *International Journal of Cancer*, 109, 799-809.
- KNOLL, M. & RUSKA, E. 1932. The Electron Microscope. *Zeitschrift Fur Physik*, 78, 318-319.

- KOBAYASHI, M., JUILLERAT, F., GALLETTO, P., BOWEN, P. & BORKOVEC, M. 2005. Aggregation and Charging of Colloidal Silica Particles: Effect of Particle Size. *Langmuir*, 21, 5761-5769.
- KOPELIOVICH, D. 2013. *Stabilisation of colloids* [Online]. Available: http://www.substech.com/dokuwiki/doku.php?id=stabilization_of_colloids [Accessed 06/05/2014].
- KRATOS ANALYTICAL LTD. 2015. *X-ray Photoelectron Spectroscopy (XPS)* [Online]. Available: <http://www.kratos.com/applications/techniques/x-ray-photoelectron-spectroscopy> [Accessed 06/01/2015].
- KREIBIG, U. 1995. Optical properties of metal clusters / Uwe Kreibig, Michael Vollmer. *In: VOLLMER, M. (ed.). Berlin: Springer.*
- KUCHIBHATLA, S. V. N. T., KARAKOTI, A. S., BAER, D. R., SAMUDRALA, S., ENGELHARD, M. H., AMONETTE, J. E., THEVUTHASAN, S. & SEAL, S. 2012. Influence of Aging and Environment on Nanoparticle Chemistry: Implication to Confinement Effects in Nanocerium. *The Journal of Physical Chemistry C*, 116, 14108-14114.
- KUCHIBHATLA, S. V. N. T., KARAKOTI, A. S., THEVUTHASAN, S., SEAL, S. & BAER, D. R. Influence of aging on the properties of cerium oxide nanoparticles - implications to quantum confinement effect. *Nanotechnology (IEEE-NANO)*, 2011 11th IEEE Conference on, 15-18 Aug. 2011 2011. 646-650.
- KUMAR, S., VENKATESWARLU, P., RAO, V. & RAO, G. 2013. Synthesis, characterization and optical properties of zinc oxide nanoparticles. *International Nano Letters*, 3, 1-6.

- KUMARI, L., LI, W. Z., XU, J. M., LEBLANC, R. M., WANG, D. Z., LI, Y., GUO, H. & ZHANG, J. 2009. Controlled Hydrothermal Synthesis of Zirconium Oxide Nanostructures and Their Optical Properties. *Crystal Growth & Design*, 9, 3874-3880.
- KUNTSCHKE, J., HORST, J. C. & BUNJES, H. 2011. Cryogenic transmission electron microscopy (cryo-TEM) for studying the morphology of colloidal drug delivery systems. *International Journal of Pharmaceutics*, 417, 120-137.
- LABILLE, J., FENG, J., BOTTA, C., BORSCHNECK, D., SAMMUT, M., CABIE, M., AUFFAN, M., ROSE, J. & BOTTERO, J.-Y. 2010. Aging of TiO₂ nanocomposites used in sunscreen. Dispersion and fate of the degradation products in aqueous environment. *Environmental Pollution*, 158, 3482-3489.
- LARNER, F., DOGRA, Y., DYBOWSKA, A., FABREGA, J., STOLPE, B., BRIDGESTOCK, L. J., GOODHEAD, R., WEISS, D. J., MOGER, J., LEAD, J. R., VALSAMI-JONES, E., TYLER, C. R., GALLOWAY, T. S. & REHKÄMPER, M. 2012. Tracing Bioavailability of ZnO Nanoparticles Using Stable Isotope Labeling. *Environmental Science & Technology*, 46, 12137-12145.
- LAWRENCE, N. J., JIANG, K. & CHEUNG, C. L. 2011a. Formation of a porous cerium oxide membrane by anodization. *Chemical Communications*, 47, 2703-2705.
- LAWRENCE, N. J., JIANG, K. & CHEUNG, C. L. 2011b. Formation of a porous cerium oxide membrane by anodization. *Chem Commun (Camb)*, 47, 2703-5.
- LAZZARI, M. & CHIANTORE, O. 2000. Thermal-ageing of paraloid acrylic protective polymers. *Polymer*, 41, 6447-6455.
- LE CHATELIER, H. L. 1884. Sur un énoncé général des lois des équilibres chimiques. *Comptes rendus*, 99, 786-789.

- LEE, H. J., YEO, S. Y. & JEONG, S. H. 2003. Antibacterial effect of nanosized silver colloidal solution on textile fabrics. *Journal of Materials Science*, 38, 2199-2204.
- LEE, J. & DONAHUE, N. M. 2011. Secondary Organic Aerosol Coating of Synthetic Metal-Oxide Nanoparticles. *Environmental Science & Technology*, 45, 4689-4695.
- LENG, Y. 2008. X-Ray Spectroscopy for Elemental Analysis. John Wiley & Sons (Asia) Pte Ltd.
- LENGLET, M., KARTOUNI, K. & DELAHAYE, D. 1991. Characterization of copper oxidation by linear potential sweep voltammetry and UV-Visible-NIR diffuse reflectance spectroscopy. *Journal of Applied Electrochemistry*, 21, 697-702.
- LI, J.-H., LIU, X.-R., ZHANG, Y., TIAN, F.-F., ZHAO, G.-Y., YU, Q.-L.-Y., JIANG, F.-L. & LIU, Y. 2012a. Toxicity of nano zinc oxide to mitochondria. *Toxicology Research*, 1, 137-144.
- LI, R., JI, Z., CHANG, C. H., DUNPHY, D. R., CAI, X., MENG, H., ZHANG, H., SUN, B., WANG, X., DONG, J., LIN, S., WANG, M., LIAO, Y.-P., BRINKER, C. J., NEL, A. & XIA, T. 2014. Surface Interactions with Compartmentalized Cellular Phosphates Explain Rare Earth Oxide Nanoparticle Hazard and Provide Opportunities for Safer Design. *ACS Nano*, 8, 1771-1783.
- LI, X., LENHART, J. J. & WALKER, H. W. 2012b. Aggregation kinetics and dissolution of coated silver nanoparticles. *Langmuir*, 28, 1095-104.
- LIANG, Q., WU, X., WENG, D. & LU, Z. 2008. Selective oxidation of soot over Cu doped ceria/ceria-zirconia catalysts. *Catalysis Communications*, 9, 202-206.
- LIN, D. & XING, B. 2008. Root Uptake and Phytotoxicity of ZnO Nanoparticles. *Environmental Science & Technology*, 42, 5580-5585.

- LIN, K.-F., CHENG, H.-M., HSU, H.-C., LIN, L.-J. & HSIEH, W.-F. 2005. Band gap variation of size-controlled ZnO quantum dots synthesized by sol-gel method. *Chemical Physics Letters*, 409, 208-211.
- LIN, W., HUANG, Y.-W., ZHOU, X.-D. & MA, Y. 2006. Toxicity of cerium oxide nanoparticles in human lung cancer cells. *International Journal of Toxicology*, 25, 451-457.
- LOGOTHETIDIS, S., PATSALAS, P. & CHARITIDIS, C. 2003. Enhanced catalytic activity of nanostructured cerium oxide films. *Materials Science and Engineering: C*, 23, 803-806.
- LOMBI, E., DONNER, E., TAHERI, S., TAVAKKOLI, E., JÄMTING, Å. K., MCCLURE, S., NAIDU, R., MILLER, B. W., SCHECKEL, K. G. & VASILEV, K. 2013. Transformation of four silver/silver chloride nanoparticles during anaerobic treatment of wastewater and post-processing of sewage sludge. *Environmental Pollution*, 176, 193-197.
- LOUIE, S. M., MA, R. & LOWRY, G. V. 2014. Chapter 2 - Transformations of Nanomaterials in the Environment. In: JAMIE, R. L. & EUGENIA, V.-J. (eds.) *Frontiers of Nanoscience*. Elsevier.
- LOURENCO, C., TEIXEIRA, M., SIMÕES, S. & GASPAR, R. 1996. Steric stabilization of nanoparticles: Size and surface properties. *International Journal of Pharmaceutics*, 138, 1-12.
- LOWRY, G. V., GREGORY, K. B., APTE, S. C. & LEAD, J. R. 2012. Transformations of Nanomaterials in the Environment. *Environmental Science & Technology*, 46, 6893-6899.

- LUKEHART, C. M. & SCOTT, R. A. 2013. *Nanomaterials: Inorganic and Bioinorganic Perspectives*, Wiley.
- LYNCH, I., DAWSON, K. A., LEAD, J. R. & VALSAMI-JONES, E. 2014. Chapter 4 - Macromolecular Coronas and Their Importance in Nanotoxicology and Nanoecotoxicology. In: JAMIE, R. L. & EUGENIA, V.-J. (eds.) *Frontiers of Nanoscience*. Elsevier.
- MA, J. Y. C., YOUNG, S. H., MERCER, R. R., BARGER, M., SCHWEGLER-BERRY, D., MA, J. K. & CASTRANOVA, V. 2014a. Interactive effects of cerium oxide and diesel exhaust nanoparticles on inducing pulmonary fibrosis. *Toxicology and Applied Pharmacology*, 278, 135-147.
- MA, R., LEVARD, C., JUDY, J. D., UNRINE, J. M., DURENKAMP, M., MARTIN, B., JEFFERSON, B. & LOWRY, G. V. 2014b. Fate of Zinc Oxide and Silver Nanoparticles in a Pilot Wastewater Treatment Plant and in Processed Biosolids. *Environmental Science & Technology*, 48, 104-112.
- MÄDLER, L., STARK, W. J. & PRATSINIS, S. E. 2002. Flame-made Ceria Nanoparticles. *Journal of Materials Research*, 17, 1356-1362.
- MALAM, Y., LOIZIDOU, M. & SEIFALIAN, A. M. 2009. Liposomes and nanoparticles: nanosized vehicles for drug delivery in cancer. *Trends in Pharmacological Sciences*, 30, 592-599.
- MALVERN 2013a. *Malvern Zetasizer User Manual*, UK.
- MALVERN. 2013b. *Zeta Potential - An Introduction in 30 Minutes* [Online]. Available: <http://www3.nd.edu/~rroeder/ame60647/slides/zeta.pdf> [Accessed 04/02/2014].

- MALVERN. 2015a. *Dynamic Light Scattering - common terms defined* [Online]. Available: <http://www.malvern.com/en/support/resource-center/Whitepapers/WP111214DLSTermsDefined.aspx> [Accessed 10/12/2015].
- MALVERN. 2015b. *Dynamic Light Scattering: An Introduction in 30 minutes* [Online]. Available: <http://www.malvern.com/en/support/resource-center/technical-notes/TN101104DynamicLightScatteringIntroduction.aspx> [Accessed 12/23/2015].
- MALVERN INSTRUMENTS LTD 2014. Zetasizer Software.
- MALVERN PERSONAL COMMUNICATION. 2012. *RE: Particle Size Analysis*.
- MALVIJA, R. K., VERMA, M. & YADAV, V. 2013. Preparation and characterization of zinc oxide nanofluid in organic components. *Science Technology and Management Journal By AISECT University*.
- MANIER, N., GARAUD, M., DELALAIN, P., AGUERRE-CHARIOL, O. & PANDARD, P. Behaviour of ceria nanoparticles in standardized test media - influence on the results of ecotoxicological tests. Nanosafe2010: International Conference on Safe Production and Use of Nanomaterials, 2012.
- MANOUBI, T., COLLIEX, C. & REZ, P. 1990. Quantitative electron energy loss spectroscopy on M45 edges in rare earth oxides. *Journal of Electron Spectroscopy and Related Phenomena*, 50, 1-18.
- MANSOORI, G. A. & SOELAIMAN, T. A. F. 2005. Nanotechnology - An introduction for the standards community. *Journal of ASTM International*, 2, 17-38.
- MARTIROSYAN, A. & SCHNEIDER, Y.-J. 2014. Engineered Nanomaterials in Food: Implications for Food Safety and Consumer Health. *International Journal of Environmental Research and Public Health*, 11, 5720-5750.

- MASUI, T., FUJIWARA, K., MACHIDA, K.-I., ADACHI, G.-Y., SAKATA, T. & MORI, H. 1997. Characterization of Cerium(IV) Oxide Ultrafine Particles Prepared Using Reversed Micelles. *Chemistry of Materials*, 9, 2197-2204.
- MATERIALS EVALUATION AND ENGINEERING INC. 2009. *X-ray Photoelectron Spectroscopy* [Online]. Available: <http://mee-inc.com/xray-photo.html> [Accessed 05/04/2014].
- MATIJEVIĆ, E. & HSU, W. P. 1987. Preparation and properties of monodispersed colloidal particles of lanthanide compounds: I. Gadolinium, europium, terbium, samarium, and cerium(III). *Journal of Colloid and Interface Science*, 118, 506-523.
- MAURER-JONES, M. A., GUNSOLUS, I. L., MURPHY, C. J. & HAYNES, C. L. 2013. Toxicity of Engineered Nanoparticles in the Environment. *Analytical chemistry*, 85, 3036-3049.
- MERRIFIELD, R. C., WANG, Z. W., PALMER, R. E. & LEAD, J. R. 2013. Synthesis and Characterization of Polyvinylpyrrolidone Coated Cerium Oxide Nanoparticles. *Environmental Science & Technology*, 47, 12426-12433.
- MEYSSAMY, H., RIWOTZKI, K., KORNOWSKI, A., NAUSED, S. & HAASE, M. 1999. Wet-Chemical Synthesis of Doped Colloidal Nanomaterials: Particles and Fibers of LaPO₄:Eu, LaPO₄:Ce, and LaPO₄:Ce,Tb. *Advanced Materials*, 11, 840-844.
- MIKO, I. 2014. *Cell Membranes* [Online]. Nature Education,. Available: <http://www.nature.com/scitable/topicpage/cell-membranes-14052567> [Accessed 09/07/2016].
- MITRANO, D., NOWACK, B., MOTELLIER, S. & S., C. 2014. Report on environmental transformation reactions.

- MITRANO, D. M., MOTELLIER, S., CLAVAGUERA, S. & NOWACK, B. 2015. Review of nanomaterial aging and transformations through the life cycle of nano-enhanced products. *Environment International*, 77, 132-147.
- MOEZZI, A., MCDONAGH, A. M. & CORTIE, M. B. 2012. Zinc oxide particles: Synthesis, properties and applications. *Chemical Engineering Journal*, 185–186, 1-22.
- MOGENSEN, K. B. & KNEIPP, K. 2014. Size-Dependent Shifts of Plasmon Resonance in Silver Nanoparticle Films Using Controlled Dissolution: Monitoring the Onset of Surface Screening Effects. *The Journal of Physical Chemistry C*, 118, 28075-28083.
- MONTAZER, M. & SEIFOLLAHZADEH, S. 2011. Enhanced Self-cleaning, Antibacterial and UV Protection Properties of Nano TiO₂ Treated Textile through Enzymatic Pretreatment. *Photochemistry and Photobiology*, 87, 877-883.
- MONTES, M. O., HANNA, S. K., LENIHAN, H. S. & KELLER, A. A. 2012. Uptake, accumulation, and biotransformation of metal oxide nanoparticles by a marine suspension-feeder. *Journal of Hazardous Materials*, 225-226, 139-145.
- MORALES, M. I., RICO, C. M., HERNANDEZ-VIEZCAS, J. A., NUNEZ, J. E., BARRIOS, A. C., TAFOYA, A., FLORES-MARGES, J. P., PERALTA-VIDEA, J. R. & GARDEA-TORRESDEY, J. L. 2013. Toxicity Assessment of Cerium Oxide Nanoparticles in Cilantro (*Coriandrum sativum* L.) Plants Grown in Organic Soil. *Journal of Agricultural and Food Chemistry*, 61, 6224-6230.
- MORIMOTO, Y., IZUMI, H., YOSHIURA, Y., TOMONAGA, T., OYABU, T., MYOJO, T., KAWAI, K., YATERA, K., SHIMADA, M., KUBO, M., YAMAMOTO, K., KITAJIMA, S., KURODA, E., KAWAGUCHI, K. & SASAKI, T. 2015.

- Pulmonary toxicity of well-dispersed cerium oxide nanoparticles following intratracheal instillation and inhalation. *Journal of Nanoparticle Research*, 17, 1-16.
- MORRIS, V., FLEMING, P. G., HOLMES, J. D. & MORRIS, M. A. 2013. Comparison of the preparation of cerium oxide nanocrystallites by forward (base to acid) and reverse (acid to base) precipitation. *Chemical Engineering Science*, 91, 102-110.
- MOSELEY, H. G. J. 1913. XCIII. The high-frequency spectra of the elements. *Philosophical Magazine Series 6*, 26, 1024-1034.
- MTX9100. 06/05/2014. *Fundamentals of nanomaterials* [Online]. Available: https://www.ttu.ee/public/m/Mehaanikateaduskond/Instituudid/Materjalitehnika_instituut/MTX9100/Lecture5_NanomatFundamentals.pdf [Accessed 06/05/2014].
- MUDUNKOTUWA, I. A., PETTIBONE, J. M. & GRASSIAN, V. H. 2012. Environmental Implications of Nanoparticle Aging in the Processing and Fate of Copper-Based Nanomaterials. *Environmental Science & Technology*, 46, 7001-7010.
- MURUGANANTHAM CHELLIAH, J. B. B. R. A. U. M. K., . 2012. Synthesis and Characterization of Cerium Oxide Nanoparticles by Hydroxide Mediated Approach. *Journal of Applied Sciences*, 12, 1734-1737.
- NAIR, S., SASIDHARAN, A., RANI, V. V. D., MENON, D., MANZOOR, K. & RAINA, S. 2009. Role of size scale of ZnO nanoparticles and microparticles on toxicity toward bacteria and osteoblast cancer cells. *J. Mater. Sci.-Mater. Med.*, 20, 235-241.
- NANOTECHNOLOGIES, T. P. O. E. 2013. *Inventory Finds Increase in Consumer Products Containing Nanoscale Materials* [Online]. Available: <http://www.nanotechproject.org/news/archive/9242/> [Accessed 15/11/2013].

- NAPPER, D. H. 1977. Steric stabilization. *Journal of Colloid and Interface Science*, 58, 390-407.
- NELSON, B. P., CANDAL, R., CORN, R. M. & ANDERSON, M. A. Control of Surface and ζ Potentials on Nanoporous TiO₂ Films by Potential-Determining and Specifically Adsorbed Ions. *Langmuir*, 16, 6094-6101.
- NIU, Z. & LI, Y. 2013. Removal and Utilization of Capping Agents in Nanocatalysis. *Chemistry of Materials*, 26, 72-83.
- NOWACK, B. & BUCHELI, T. D. 2007. Occurrence, behavior and effects of nanoparticles in the environment. *Environmental Pollution*, 150, 5-22.
- NOWACK, B., GOTTSCHALK, F., MUELLER, N. C. & SOM, C. 2010. Life-Cycle Concepts for Sustainable Use of Engineered Nanomaterials in Nanoproducts. *Handbook of Green Chemistry*. Wiley-VCH Verlag GmbH & Co. KGaA.
- NOWACK, B., RANVILLE, J. F., DIAMOND, S., GALLEGO-URREA, J. A., METCALFE, C., ROSE, J., HORNE, N., KOELMANS, A. A. & KLAINE, S. J. 2012. Potential scenarios for nanomaterial release and subsequent alteration in the environment. *Environmental toxicology and Chemistry*, 31, 50-59.
- OBERDÖRSTER, G., MAYNARD, A., DONALDSON, K., CASTRANOVA, V., FITZPATRICK, J., AUSMAN, K., CARTER, J., KARN, B., KREYLING, W., LAI, D., OLIN, S., MONTEIRO-RIVIERE, N., WARHEIT, D. & YANG, H. 2005. Principles for characterizing the potential human health effects from exposure to nanomaterials: elements of a screening strategy. *Particle and Fibre Toxicology*, 2, 8.

- OBERDORSTER, G., OBERDORSTER, E. & OBERDORSTER, J. 2005. Nanotoxicology: An emerging discipline evolving from studies of ultrafine particles. *Environmental Health Perspectives*, 113, 823-839.
- OMASTOVÁ, M., PODHRADSKÁ, S., PROKEŠ, J., JANIGOVÁ, I. & STEJSKAL, J. 2003. Thermal ageing of conducting polymeric composites. *Polymer Degradation and Stability*, 82, 251-256.
- ONLINE, E. B. 2014. Paracelsus.
- ORAM, B. 2014. *Phosphates in the Environment* [Online]. Water Research Center. Available: <http://www.water-research.net/index.php/phosphates-in-the-environment> [Accessed 27/08/2014].
- OSMOND, M. J. & MCCALL, M. J. 2010. Zinc oxide nanoparticles in modern sunscreens: an analysis of potential exposure and hazard. *Nanotoxicology*, 4, 15-41.
- OZAWA, M., KIMURA, M. & ISOGAI, A. 1993. The application of Ce • Zr oxide solid solution to oxygen storage promoters in automotive catalysts. *Journal of Alloys and Compounds*, 193, 73-75.
- ÖZGÜR, Ü., ALIVOV, Y. I., LIU, C., TEKE, A., RESHCHIKOV, M. A., DOĞAN, S., AVRUTIN, V., CHO, S.-J. & MORKOÇ, H. 2005. A comprehensive review of ZnO materials and devices. *Journal of Applied Physics*, 98, -.
- PARK, B., DONALDSON, K., DUFFIN, R., TRAN, L., KELLY, F., MUDWAY, I., MORIN, J.-P., GUEST, R., JENKINSON, P. & SAMARAS, Z. 2008. Hazard and risk assessment of a nanoparticulate cerium oxide-based diesel fuel additive-a case study. *Inhalation toxicology*, 20, 547-566.
- PARTICLE SCIENCES. 2009. *Considerations in Particle Sizing Part 1: Classification of the Various Sizing Techniques* [Online]. Available:

<http://www.particlesciences.com/news/technical-briefs/2009/considerations-in-particle-sizing-1.html> [Accessed 12/21/2015].

PASUPULETI, S., ALAPATI, S., GANAPATHY, S., ANUMOLU, G., PULLY, N. R. & PRAKHYA, B. M. 2012. Toxicity of zinc oxide nanoparticles through oral route. *Toxicology and Industrial Health*, 28, 675-686.

PAULENOVA, A., CREAGER, S. E., NAVRATIL, J. D. & WEI, Y. 2002. Redox potentials and kinetics of the Ce³⁺/Ce⁴⁺ redox reaction and solubility of cerium sulfates in sulfuric acid solutions. *Journal of Power Sources*, 109, 431-438.

PENG, S., MCMAHON, J. M., SCHATZ, G. C., GRAY, S. K. & SUN, Y. 2010. Reversing the size-dependence of surface plasmon resonances. *Proceedings of the National Academy of Sciences of the United States of America*, 107, 14530-14534.

PENNER-HAHN, J. E. 2001. X-ray Absorption Spectroscopy. *eLS*. John Wiley & Sons, Ltd.

PENNER-HAHN, J. E. 2016. *X-ray Absorption Spectroscopy* [Online]. University of Michigan. Available: https://www.elsevier.com/__data/promis_misc/622954sc1.pdf [Accessed 06/07/2016].

PENNYCOOK, S. J., LUPINI, A. R., VARELA, M., BORISEVICH, A., PENG, Y., OXLEY, M. P., VAN BENTHEM, K. & CHISHOLM, M. F. 2007. Scanning Transmission Electron Microscopy for Nanostructure Characterization. In: ZHOU, W. & WANG, Z. (eds.) *Scanning Microscopy for Nanotechnology*. Springer New York.

PEREIRA, R., ROCHA-SANTOS, T. A. P., ANTUNES, F. E., RASTEIRO, M. G., RIBEIRO, R., GONÇALVES, F., SOARES, A. M. V. M. & LOPES, I. 2011. Screening evaluation of the ecotoxicity and genotoxicity of soils contaminated with

- organic and inorganic nanoparticles: The role of ageing. *Journal of Hazardous Materials*, 194, 345-354.
- PERELSHTEIN, I., RUDERMAN, E., PERKAS, N., TZANOV, T., BEDDOW, J., JOYCE, E., MASON, T. J., BLANES, M., MOLLA, K., PATLOLLA, A., FRENKEL, A. I. & GEDANKEN, A. 2013. Chitosan and chitosan-ZnO-based complex nanoparticles: formation, characterization, and antibacterial activity. *Journal of Materials Chemistry B*, 1, 1968-1976.
- PERKIN-ELMER CORPORATION. 2013. *Atomic Spectroscopy - A Guide to Selecting the Appropriate Technique and System* [Online]. Available: http://www.perkinelmer.co.uk/PDFS/downloads/bro_worldleaderaaicpmsicpms.pdf [Accessed 29/02/2015].
- PETERS, R. 2000. Fiber optic device for detecting the scattered light or fluorescent light from a suspension. Google Patents.
- PHENRAT, T., LONG, T. C., LOWRY, G. V. & VERONESI, B. 2008. Partial Oxidation (“Aging”) and Surface Modification Decrease the Toxicity of Nanosized Zerovalent Iron. *Environmental Science & Technology*, 43, 195-200.
- PHOLNAK, C., SIRISATHITKUL, C., SUWANBOON, S. & HARDING, D. J. 2014. Effects of precursor concentration and reaction time on sonochemically synthesized ZnO nanoparticles. *Materials Research*, 17, 405-411.
- PICCINNO, F., GOTTSCHALK, F., SEEGER, S. & NOWACK, B. 2012. Industrial production quantities and uses of ten engineered nanomaterials in Europe and the world. *Journal of Nanoparticle Research*, 14, 1-11.

- PINNELL, S. R., FAIRHURST, D., GILLIES, R., MITCHNICK, M. & KOLLIAS, N. 2000. Microfine Zinc Oxide is a Superior Sunscreen Ingredient to Microfine Titanium Dioxide, *Dermatologic Surgery*, 26, 309-314.
- PISARELLO, M. L., MILT, V., PERALTA, M. A., QUERINI, C. A. & MIRÓ, E. E. 2002. Simultaneous removal of soot and nitrogen oxides from diesel engine exhausts. *Catalysis Today*, 75, 465-470.
- POTAPOV, P. L. & SCHRYVERS, D. 2004. Measuring the absolute position of EELS ionisation edges in a TEM. *Ultramicroscopy*, 99, 73-85.
- PROSPECT 2010. Toxicological Review of Nano Cerium Oxide.
- R.W. SIEGEL 1994. *Nanophase Materials, Encyclopedia of Applied Physics* VCH Publishers
- RAJ, S., JOSE, S., SUMOD, U. S. & SABITHA, M. 2012. Nanotechnology in cosmetics: Opportunities and challenges. *Journal of Pharmacy & Bioallied Sciences*, 4, 186-193.
- RAJESH, K., MUKUNDAN, P., PILLAI, P. K., NAIR, V. R. & WARRIER, K. G. K. 2004. High-Surface-Area Nanocrystalline Cerium Phosphate through Aqueous Sol-Gel Route. *Chemistry of Materials*, 16, 2700-2705.
- RAMSDEN, E. N. 2000. *A-Level Chemistry*, Stanley Thornes.
- RANGA RAO, G. & SAHU, H. R. 2001. XRD and UV-Vis diffuse reflectance analysis of CeO₂-ZrO₂ solid solutions synthesized by combustion method. *Journal of Chemical Sciences*, 113, 651-658.
- RASBAND, W. 2015. ImageJ. 1.50b ed.
- RAVEL, B. 2015. Demeter.

- RAY, P. C., YU, H. & FU, P. P. 2009. Toxicity and Environmental Risks of Nanomaterials: Challenges and Future Needs. *Journal of Environmental Science and Health, Part C*, 27, 1-35.
- RAY, P. D., HUANG, B.-W. & TSUJI, Y. 2012. Reactive oxygen species (ROS) homeostasis and redox regulation in cellular signaling. *Cellular signalling*, 24, 981-990.
- REDDY, K. M., FERIS, K., BELL, J., WINGETT, D. G., HANLEY, C. & PUNNOOSE, A. 2007. Selective toxicity of zinc oxide nanoparticles to prokaryotic and eukaryotic systems. *Applied Physics Letters*, 90, -.
- REUSCH, W. 2013. *Infrared Spectroscopy* [Online]. Available: <https://www2.chemistry.msu.edu/faculty/reusch/virttxtjml/Spectrpy/InfraRed/infrared.htm> [Accessed 19/04/2016].
- RICHARDSON, H. W. 2000. Copper Compounds. *Ullmann's Encyclopedia of Industrial Chemistry*. Wiley-VCH Verlag GmbH & Co. KGaA.
- RICKERBY, D. G. & MORRISON, M. 2007. Nanotechnology and the environment: A European perspective. *Science and Technology of Advanced Materials*, 8, 19-24.
- RÖMER, I., GAVIN, A. J., WHITE, T. A., MERRIFIELD, R. C., CHIPMAN, J. K., VIANT, M. R. & LEAD, J. R. 2013. The critical importance of defined media conditions in *Daphnia magna* nanotoxicity studies. *Toxicology Letters*, 223, 103-108.
- ROMER ROCHE, I. 2013. The ecotoxicological and environmental behaviour and transformations of silver nanoparticles. *In*: LEAD, J. R. & VIANT, M. (eds.).
- ROOT-BERNSTEIN, R., FEWINS, J., RHINESMITH, T., KOCH, A. & DILLON, P. F. 2016. Enzymatic recycling of ascorbic acid from dehydroascorbic acid by

- glutathione-like peptides in the extracellular loops of aminergic G-protein coupled receptors. *Journal of Molecular Recognition*, 29, 296-302.
- RORO, K. T., MWAKIKUNGA, B., TILE, N., YALISI, B. & FORBES, A. 2012. Effect of Accelerated Thermal Ageing on the Selective Solar Thermal Harvesting Properties of Multiwall Carbon Nanotube/Nickel Oxide Nanocomposite Coatings. *International Journal of Photoenergy*, 2012, 7.
- ROSSANO, M., HUCHER, N., PICARD, C., COLLETTA, D., LE FOLL, F. & GRISEL, M. 2014. Effects of aging on structure and stability of TiO₂ nanoparticle-containing oil-in-water emulsions. *International Journal of Pharmaceutics*, 461, 89-96.
- ROTOLI, B. M., BUSSOLATI, O., COSTA, A. L., BLOSI, M., DI CRISTO, L., ZANELLO, P. P., BIANCHI, M. G., VISIGALLI, R. & BERGAMASCHI, E. 2012. Comparative effects of metal oxide nanoparticles on human airway epithelial cells and macrophages. *Journal of Nanoparticle Research*, 14, 14.
- ROYAL SOCIETY OF CHEMISTRY. 2015a. *Cerium* [Online]. Available: <http://www.rsc.org/periodic-table/element/58/cerium> [Accessed 16/11/2015 2015].
- ROYAL SOCIETY OF CHEMISTRY. 2015b. *Copper* [Online]. Available: <http://www.rsc.org/periodic-table/element/29/copper> [Accessed 17/11/2015].
- ROYAL SOCIETY OF CHEMISTRY. 2015c. *Zinc* [Online]. Available: <http://www.rsc.org/periodic-table/element/30/zinc> [Accessed 17/11/2015].
- RUI, Y., ZHANG, P., ZHANG, Y., MA, Y., HE, X., GUI, X., LI, Y., ZHANG, J., ZHENG, L., CHU, S., GUO, Z., CHAI, Z., ZHAO, Y. & ZHANG, Z. 2015. Transformation of ceria nanoparticles in cucumber plants is influenced by phosphate. *Environ Pollut*, 198, 8-14.

- SALEH, N. B., PFEFFERLE, L. D. & ELIMELECH, M. 2008. Aggregation Kinetics of Multiwalled Carbon Nanotubes in Aquatic Systems: Measurements and Environmental Implications. *Environmental Science & Technology*, 42, 7963-7969.
- SARATHY, V., TRATNYEK, P. G., NURMI, J. T., BAER, D. R., AMONETTE, J. E., CHUN, C. L., PENN, R. L. & REARDON, E. J. 2008. Aging of Iron Nanoparticles in Aqueous Solution: Effects on Structure and Reactivity. *The Journal of Physical Chemistry C*, 112, 2286-2293.
- SARAVANAN, P., VENKATA RAMANA, G., SRINIVASA RAO, K., SREEDHAR, B., VINOD, V. T. P. & CHANDRASEKARAN, V. 2011. Structural and magnetic properties of self-assembled Sm–Co spherical aggregates. *Journal of Magnetism and Magnetic Materials*, 323, 2083-2089.
- SCENIHR. 2009. *Risk Assessment of Products of Nanotechnologies* [Online]. Available: http://ec.europa.eu/health/ph_risk/committees/04_scenihhr/docs/scenihhr_o_023.pdf [Accessed 23/11/2015].
- SCIENCE LEARNING HUB. 2014. *Timeline-Digestion Chemistry* [Online]. Available: <http://sciencelearn.org.nz/Contexts/Digestion-Chemistry/Timeline> [Accessed 11/07/2015].
- SHARMA, P., JHA, A. B., DUBEY, R. S. & PESSARAKLI, M. 2012. Reactive oxygen species, oxidative damage, and antioxidative defense mechanism in plants under stressful conditions. *Journal of Botany*, 2012.
- SHEFFIELD HALLAM UNIVERSITY. 2015. *UV-Vis Absorption Spectroscopy* [Online]. Available: <http://teaching.shu.ac.uk/hwb/chemistry/tutorials/molspec/uvvisab3.htm> [Accessed 25/2/2014].

- SIGMA-ALDRICH. 2016a. *10 K PVP Product Specification* [Online]. Available: http://www.sigmaaldrich.com/Graphics/COfAInfo/SigmaSAPQM/SPEC/PV/PVP10/PVP10-BULK_____SIAL_____.pdf [Accessed 24/07/2016].
- SIGMA-ALDRICH. 2016b. *40 K PVP Product Specification* [Online]. Available: http://www.sigmaaldrich.com/Graphics/COfAInfo/SigmaSAPQM/SPEC/PV/PVP40/PVP40-BULK_____SIAL_____.pdf [Accessed 24/07/2016].
- SIGMA-ALDRICH. 2016c. *360 K PVP Product Specification* [Online]. Available: http://www.sigmaaldrich.com/Graphics/COfAInfo/SigmaSAPQM/SPEC/PV/PVP360/PVP360-BULK_____SIGMA_____.pdf [Accessed 24/11/2013].
- SILVERSTEIN, R. M., WEBSTER, F. X., KIEMLE, D. J. 2005. *Spectrometric Identification of Organic Compounds.*, USA, John Wiley & Sons, Inc.
- SINGH, S., DOSANI, T., KARAKOTI, A. S., KUMAR, A., SEAL, S. & SELF, W. T. 2011. A phosphate-dependent shift in redox state of cerium oxide nanoparticles and its effects on catalytic properties. *Biomaterials*, 32, 6745-6753.
- SKORODUMOVA, N. V., SIMAK, S. I., LUNDQVIST, B. I., ABRIKOSOV, I. A. & JOHANSSON, B. 2002. Quantum Origin of the Oxygen Storage Capability of Ceria. *Physical Review Letters*, 89, 166601.
- SOLTANI, N., SAION, E., ERFANI, M., REZAEI, K., BAHMANROKH, G., DRUMMEN, G. P. C., BAHRAMI, A. & HUSSEIN, M. Z. 2012. Influence of the Polyvinyl Pyrrolidone Concentration on Particle Size and Dispersion of ZnS Nanoparticles Synthesized by Microwave Irradiation. *International Journal of Molecular Sciences*, 13, 12412-12427.

- SONG, W. Q., KRAUKLIS, P., MOURITZ, A. P. & BANDYOPADHYAY, S. 1995. The effect of thermal ageing on the abrasive wear behaviour of age-hardening 2014 Al/SiC and 6061 Al/SiC composites. *Wear*, 185, 125-130.
- SONSTROM, P. & BAUMER, M. 2011. Supported colloidal nanoparticles in heterogeneous gas phase catalysis: on the way to tailored catalysts. *Phys Chem Chem Phys*, 13, 19270-84.
- SOTIRIOU, G. A. & PRATSINIS, S. E. 2010. Antibacterial Activity of Nanosilver Ions and Particles. *Environmental Science & Technology*, 44, 5649-5654.
- SPEHLING, R. A. & PARAK, W. J. 2010. Surface modification, functionalization and bioconjugation of colloidal inorganic nanoparticles. *Philosophical Transactions of the Royal Society of London A: Mathematical, Physical and Engineering Sciences*, 368, 1333-1383.
- STEBOUNOVA, L., GUIO, E. & GRASSIAN, V. 2011. Silver nanoparticles in simulated biological media: a study of aggregation, sedimentation, and dissolution. *Journal of Nanoparticle Research*, 13, 233-244.
- STEVENS, R. 1986. Introduction to Zirconia. *Magnesium Elektron Publication*, 113.
- STOJEK, Z. 2010. The Electrical Double Layer and Its Structure. In: SCHOLZ, F., BOND, A. M., COMPTON, R. G., FIEDLER, D. A., INZELT, G., KAHLERT, H., KOMORSKY-LOVRIĆ, Š., LOHSE, H., LOVRIĆ, M., MARKEN, F., NEUDECK, A., RETTER, U., SCHOLZ, F. & STOJEK, Z. (eds.) *Electroanalytical Methods*. Springer Berlin Heidelberg.
- SULEIMAN, M., MOUSA, M., HUSSEIN, A., HAMMOUTI, B., HADDA, T. B. & WARAD, I. 2013. Copper(II)-oxide nanostructures: Synthesis, characterizations

- and their applications-review. *Journal of Materials and Environmental Science*, 4, 792-797.
- SUN, Y. & XIA, Y. 2002. Shape-controlled synthesis of gold and silver nanoparticles. *Science*, 298, 2176-9.
- SUNANDAN, B. & JOYDEEP, D. 2009. Hydrothermal growth of ZnO nanostructures. *Science and Technology of Advanced Materials*, 10, 013001.
- SURYANARAYANA, C. & NORTON, M. G. 2013. *X-Ray Diffraction: A Practical Approach*, Springer US.
- TALAPIN, D. V. & YIN, Y. 2011. Themed issue: Chemical transformations of nanoparticles. *Journal of Materials Chemistry*, 21, 11454-11456.
- TANAKA, N. 1992. *Scanning Transmission Electron Microscopy Of Nanomaterials: Basics Of Imaging And Analysis*. Imperial College Press.
- TEJAMAYA, M., RÖMER, I., MERRIFIELD, R. C. & LEAD, J. R. 2012. Stability of Citrate, PVP, and PEG Coated Silver Nanoparticles in Ecotoxicology Media. *Environmental Science & Technology*, 46, 7011-7017.
- THE EDITORS OF ENCYCLOPÆDIA BRITANNICA ONLINE. 2015. *Bile* [Online]. Encyclopædia Britannica Online. Available: <http://www.britannica.com/science/bile> [Accessed 21/09/2015].
- THE HEBREW UNIVERSITY OF JERUSALEM. 2009. *The Zetasizer* [Online]. Available: <http://departments.agri.huji.ac.il/zabam/zetasizer.html> [Accessed 20/05/2014].
- THE PROJECT ON EMERGING NANOTECHNOLOGIES. 2015. *Consumer Products Inventory* [Online]. Available: <http://www.nanotechproject.org/cpi/products/> [Accessed 20/04/2016].

- THERMO FISHER SCIENTIFIC INC. 2013a. *Copper* [Online]. Available: <http://xpssimplified.com/elements/copper.php> [Accessed 20/05/2016].
- THERMO FISHER SCIENTIFIC INC. 2013b. *Zinc* [Online]. Available: <http://xpssimplified.com/elements/zinc.php> [Accessed 25/05/2016].
- THI MY DUNG DANG, T. T. T. L., ERIC FRIBOURG-BLANC AND MAU CHIEN DANG 2011. The influence of solvents and surfactants on the preparation of copper nanoparticles by a chemical reduction method *Advances in Natural Sciences Nanoscience and Nanotechnology*, 2.
- THI MY DUNG DANG, T. T. T. L., ERIC FRIBOURG-BLANC AND MAU CHIEN DANG 2013. UV photochemical synthesis of heparin-coated gold nanoparticles. *Gold Bulletin*.
- THILL, A., ZEYONS, O., SPALLA, O., CHAUVAT, F., ROSE, J., AUFFAN, M. & FLANK, A. M. 2006. Cytotoxicity of CeO₂ Nanoparticles for Escherichia coli. Physico-Chemical Insight of the Cytotoxicity Mechanism. *Environmental Science & Technology*, 40, 6151-6156.
- THWALA, M., MUSEE, N., SIKHWIVHILU, L. & WEPENER, V. 2013. The oxidative toxicity of Ag and ZnO nanoparticles towards the aquatic plant Spirodela punctata and the role of testing media parameters. *Environmental Science-Processes & Impacts*, 15, 1830-1843.
- TOMALIA, D. 2009. In quest of a systematic framework for unifying and defining nanoscience. *Journal of Nanoparticle Research*, 11, 1251-1310.
- TOPNANI, N., KUSHWAHA, S. & ATHAR, T. 2010. Wet Synthesis of Copper Oxide Nanopowder. *International Journal of Green Nanotechnology: Materials Science & Engineering*, 1, M67-M73.

- TÓTH, M., KUKOR, Z. & VALENT, S. 2002. Chemical stabilization of tetrahydrobiopterin by L-ascorbic acid: contribution to placental endothelial nitric oxide synthase activity. *Molecular Human Reproduction*, 8, 271-280.
- TSO, C., ZHUNG, C., SHIH, Y., TSENG, Y., WU, S. & DOONG, R. 2010. Stability of metal oxide nanoparticles in aqueous solutions. *Water Science and Technology*, 61, 127-133.
- TSUNEKAWA, S., FUKUDA, T. & KASUYA, A. 2000. Blue shift in ultraviolet absorption spectra of monodisperse CeO_{2-x} nanoparticles. *Journal of Applied Physics*, 87, 1318-1321.
- ULRICH, A. & WICHSER, A. 2003. Analysis of additive metals in fuel and emission aerosols of diesel vehicles with and without particle traps. *Analytical and bioanalytical chemistry*, 377, 71-81.
- US EPA 2009. Toxicological review of cerium oxide and cerium compounds. Washington, DC
- VAJTAI, R. 2013. *Springer Handbook of Nanomaterials*, Springer Berlin Heidelberg.
- VALSAMI-JONES, E. & LYNCH, I. 2015a. How safe are nanomaterials? *Science*, 350, 388-389.
- VALSAMI-JONES, E. & LYNCH, I. 2015b. NANOSAFETY. How safe are nanomaterials?
- VANCE, M. E., KUIKEN, T., VEJERANO, E. P., MCGINNIS, S. P., HOCELLA, M. F., REJESKI, D. & HULL, M. S. 2015. Nanotechnology in the real world: Redeveloping the nanomaterial consumer products inventory. *Beilstein Journal of Nanotechnology*, 6, 1769-1780.

- VERWEY, E. J. W. 1948. *Theory of the stability of lyophobic colloids : the interaction of sol particles having an electric double layer / by E. J. W. Verwey and J. Th. G. Overbeek, with the collaboration of K. van Nes*, New York, New York : Elsevier Pub. Co.
- WALKER, C. & MORTON, S. 2001. *Auger Parameter Energies - Zinc* [Online]. UK Surface Analysis Forum. Available: <http://www.uksaf.org/data/zn.html> [Accessed 03/03/2016].
- WANG, S., MAMEDOVA, N., KOTOV, N. A., CHEN, W. & STUDER, J. 2002. Antigen/Antibody Immunocomplex from CdTe Nanoparticle Bioconjugates. *Nano Letters*, 2, 817-822.
- WANG, Z. L. 2000. Transmission Electron Microscopy of Shape-Controlled Nanocrystals and Their Assemblies. *The Journal of Physical Chemistry B*, 104, 1153-1175.
- WARREN, B. E. 1989. *X-ray diffraction*, Reading, Mass., Addison-Wesley Pub. Co.
- WENG, X., PERSTON, B., WANG, X. Z., ABRAHAMS, I., LIN, T., YANG, S., EVANS, J. R. G., MORGAN, D. J., CARLEY, A. F., BOWKER, M., KNOWLES, J. C., REHMAN, I. & DARR, J. A. 2009. Synthesis and characterization of doped nano-sized ceria-zirconia solid solutions. *Applied Catalysis B: Environmental*, 90, 405-415.
- WHICH LAB. 2015. *Multifunctional Biopolymers* [Online]. Available: <http://wichlab.com/research/> [Accessed 03/12/2015].
- WILLIAMS, D. B. 1996. Transmission electron microscopy : [textbook for materials science] / [David B. Williams and C. Barry Carter]. 3, Imaging. *In*: CARTER, C. B. (ed.). New York, London: Plenum.

- WÖLL, C. 2007. The chemistry and physics of zinc oxide surfaces. *Progress in Surface Science*, 82, 55-120.
- YAN, C. H., ZHANG, J. & SUN, L.-D. 2004. Zinc Oxide Nanostructures. In: NALWA, H. S. (ed.) *Encyclopedia of Nanoscience and Nanotechnology*. USA: America Scientific Publishers.
- YANG, D., MA, P. A., HOU, Z., CHENG, Z., LI, C. & LIN, J. 2015. Current advances in lanthanide ion (Ln³⁺)-based upconversion nanomaterials for drug delivery. *Chemical Society Reviews*, 44, 1416-1448.
- YANG, X. & RAHAMAN, M. N. 1997. Thin films by consolidation and sintering of nanocrystalline powders. *Journal of the European Ceramic Society*, 17, 525-535.
- YANG, X., YIN, D., SUN, H., WANG, X., DAI, L., CHEN, Y. & CAO, M. 1999. Distribution and bioavailability of rare earth elements in aquatic microcosm. *Chemosphere*, 39, 2443-2450.
- YIN, L., WANG, Y., PANG, G., KOLTYPIN, Y. & GEDANKEN, A. 2002. Sonochemical Synthesis of Cerium Oxide Nanoparticles—Effect of Additives and Quantum Size Effect. *Journal of Colloid and Interface Science*, 246, 78-84.
- YOKEL, R. A., TSENG, M. T., DAN, M., UNRINE, J. M., GRAHAM, U. M., WU, P. & GRULKE, E. A. 2013. Biodistribution and biopersistence of ceria engineered nanomaterials: size dependence. *Nanomedicine-Nanotechnology Biology and Medicine*, 9, 398-407.
- ZHANG, F., CHEN, C.-H., HANSON, J. C., ROBINSON, R. D., HERMAN, I. P. & CHAN, S.-W. 2006a. Phases in Ceria–Zirconia Binary Oxide (1-x)CeO₂-xZrO₂ Nanoparticles: The Effect of Particle Size. *Journal of the American Ceramic Society*, 89, 1028-1036.

- ZHANG, J., LIU, J., PENG, Q., WANG, X. & LI, Y. 2006b. Nearly Monodisperse Cu₂O and CuO Nanospheres: Preparation and Applications for Sensitive Gas Sensors. *Chemistry of Materials*, 18, 867-871.
- ZHANG, L. & WEBSTER, T. J. 2009. Nanotechnology and nanomaterials: Promises for improved tissue regeneration. *Nano Today*, 4, 66-80.
- ZHANG, M., SUN, B. & GU, B. 2016. Accelerated thermal ageing of epoxy resin and 3-D carbon fiber/epoxy braided composites. *Composites Part A: Applied Science and Manufacturing*, 85, 163-171.
- ZHANG, P., MA, Y., ZHANG, Z., HE, X., ZHANG, J., GUO, Z., TAI, R., ZHAO, Y. & CHAI, Z. 2012. Biotransformation of Ceria Nanoparticles in Cucumber Plants. *ACS Nano*, 6, 9943-9950.
- ZHANG, Z., ZHAO, B. & HU, L. 1996. PVP Protective Mechanism of Ultrafine Silver Powder Synthesized by Chemical Reduction Processes. *Journal of Solid State Chemistry*, 121, 105-110.
- ZHAO, J. & CASTRANOVA, V. 2011. Toxicology of Nanomaterials Used in Nanomedicine. *Journal of Toxicology and Environmental Health, Part B*, 14, 593-632.
- ZHIJIAN, W., HAIMING, Z., LIGONG, Z., JINSHAN, Y., SHENGGANG, Y. & CHUNYAN, W. 2003. Low-temperature synthesis of ZnO nanoparticles by solid-state pyrolytic reaction. *Nanotechnology*, 14, 11.
- ZHOU, F., ZHAO, X., XU, H. & YUAN, C. 2007. CeO₂ Spherical Crystallites: Synthesis, Formation Mechanism, Size Control, and Electrochemical Property Study. *The Journal of Physical Chemistry C*, 111, 1651-1657.

ZIETZ, B. P., DIETER, H. H., LAKOMEK, M., SCHNEIDER, H., KESSLER-
GAEDTKE, B. & DUNKELBERG, H. 2003. Epidemiological investigation on
chronic copper toxicity to children exposed via the public drinking water supply.
The Science of the total environment, 302, 127-144.